



universität
wien

DISSERTATION / DOCTORAL THESIS

Titel der Dissertation / Title of the Doctoral Thesis

„Circumstellar Envelopes of Asymptotic Giant Branch
Stars: Evolution and Geometry of Mass-Loss“

verfasst von / submitted by

Magdalena Brunner, Bakk. rer. nat. MSc

angestrebter akademischer Grad / in partial fulfilment of the requirements for the degree of

Doktorin der Naturwissenschaften (Dr. rer. nat.)

Wien, 2018 / Vienna 2018

Studienkennzahl lt. Studienblatt /
degree programme code as it appears on the
student record sheet:

A 796 605 413

Dissertationsgebiet lt. Studienblatt /
field of study as it appears on the student
record sheet:

Astronomie

Betreut von / Supervisor:

ao. Univ.-Prof. Mag. Dr. Franz Kerschbaum

Dedicated to everyone who kept me
(mostly) sane during this journey.

Abstract

At the end of their lives, stars with masses between roughly 0.8 and 8 solar masses (M_{\odot}) enter an evolutionary phase called the asymptotic giant branch (AGB), during which they develop intense stellar winds. AGB stars are important producers of chemical elements, which are created through nucleosynthesis processes in the stellar interior and particularly in thin shells of hydrogen- and helium-burning. The thus created and pre-existing chemical elements can form molecules and subsequently dust grains in the dense and cool layers of the stellar atmosphere. As a result, stellar winds are driven away from the stellar atmosphere by radiation pressure on dust grains, dragging along molecular gas. In return, huge circumstellar envelopes (CSEs) of molecular gas and dust are formed around AGB stars. Variations in the mass-loss rate, interaction of the stellar wind with the surrounding medium or previous winds, and the gravitational influence of binary objects orbiting the star, can all significantly alter the shape of the stellar outflow and CSE. Therefore, CSEs come with quite different geometries, which contain information on the mass-loss history and dynamics of the stellar wind.

The aim of this dissertation is to study the mass-loss evolution and geometry of CSEs from AGB stars in different evolutionary phases and investigate the different scenarios needed to explain the observations of a small sample of AGB stars. The presented observations have been conducted with the Atacama Large Millimeter/submillimeter Array (ALMA), which currently offers the highest possible spatial resolution and sensitivity in this wavelength range. With the use of interferometry we are able to resolve the CSEs of the sample stars with unprecedented spatial resolution and quality, down to the scales of dynamical instabilities in the stellar winds. Our sample of observed AGB stars covers W Aql, TX Psc, R Scl, and U Ant, listed with increasing carbon-to-oxygen (C/O) ratio. This ratio is used to describe the evolutionary sequence of AGB stars, and goes from M- to S- to C-type. We investigate one S-type star (W Aql) and three C-type stars, and particularly focus on the analysis of so-called detached shells, which are so far only found around C-type stars. The ALMA observations are complemented by far-infrared observations with the *Herschel* Space Telescope and single-dish observations in the submillimeter range with the Atacama Pathfinder EXperiment (APEX). To model the observations, we use molecular line radiative transfer modelling (W Aql), geometric models with *Shape* (TX Psc), and dust radiative transfer modelling (R Scl). We find that the molecular abundances around W Aql are in accordance with the chemical models of S-type AGB stars, showing a mixed carbon and oxygen chemistry. Around TX Psc we discover the first elliptical detached shell, which can be explained by significant unexpected stellar rotation, possibly introduced by an orbiting binary object. We model the dust shell mass of the detached shell around R Scl and find that the dust grain geometry influences the mass estimate the most, compared to other dust grain parameters. We present the first high-resolution images of the detached shell around U Ant, which shows intricate fine structure. According to our sample, the observed detached shell morphologies possibly indicate that detached shells get more spatially refined along the C-type AGB star evolution sequence.

Contents

Abstract	v
List of Figures	ix
I Introduction, scientific background, and methods	1
1 Asymptotic giant branch stars	5
1.1 Stellar evolution	5
1.1.1 Evolution from main sequence to AGB	6
1.1.2 Evolution on the AGB	9
1.1.3 Post-AGB evolution	10
1.2 Chemical evolution on the AGB	11
1.2.1 Initial composition, sites of nucleosynthesis, and mixing events . . .	11
1.2.2 Chemical evolution from M- to S- to C-type	13
1.3 Mass-loss evolution and circumstellar envelopes	14
1.3.1 Mass-loss mechanism	14
1.3.2 Chemical composition of CSEs	15
1.3.3 Morphology and evolution of the CSE	16
1.4 The sample of AGB stars covered in this work	17
1.4.1 W Aquilae	18
1.4.2 TX Piscium	20
1.4.3 R Sculptoris	22
1.4.4 U Antliae	24
2 Observational methods	27
2.1 Millimeter/submillimeter interferometry with ALMA	27
2.1.1 ALMA – Atacama Large Millimeter/submillimeter Array	29
2.1.2 Observing techniques	32
2.1.3 Data reduction	33
2.2 Other observational methods	36
2.2.1 Submillimeter photometry with APEX	36
2.2.2 Infrared photometry with <i>Herschel</i>	37
3 Modelling methods	39
3.1 Radiative transfer modelling	39
3.1.1 Molecular line modelling	40
3.1.2 Dust modelling	41

II	Main publications	43
4	The molecule-rich envelope around W Aquilae (Paper I, accepted)	45
5	The elliptical detached shell around TX Piscium (Paper II, submitted)	67
6	The dusty detached shell around R Sculptoris (Paper III)	81
7	The filamentary detached shell around U Antliae (Paper IV)	95
III	Publications with contributions	105
8	The CO envelope around W Aquilae (Paper V)	107
9	The CO envelope around R Sculptoris (Paper VI)	119
10	Measuring the distance to R Sculptoris (Paper VII)	133
IV	Conclusions and outlook	143
11	Conclusions	145
12	Outlook	147
	Acknowledgements / Danksagung	151
	Zusammenfassung	153
	Bibliography	157
A	Appendix	159
A.1	Reprint permission	159
A.2	CV	161

List of Figures

1.1	Hertzsprung-Russel diagram for a sample of stars with different masses . . .	7
1.2	Hertzsprung-Russel diagram with the evolutionary track of a $2 M_{\odot}$ star with solar metallicity	8
1.3	Stellar structure of a $1 M_{\odot}$ AGB star	9
1.4	Schematic view of main-sequence and AGB evolution subject to stellar mass	10
1.5	Schematic view of an AGB circumstellar environment from star to ISM interaction front	15
1.6	High resolution B band HST image of W Aql and the resolved binary	19
1.7	Deconvolved $70 \mu\text{m}$ Herschel PACS image of W Aql	19
1.8	ISO spectra comparison of the C_3 feature between TX Psc and known C-type AGB stars with detached shells	20
1.9	Herschel/PACS observations of the thermal dust emission of TX Psc at $70 \mu\text{m}$	21
1.10	Molecular CO (1–0) and CO (2–1) emission of TX Psc observed with the IRAM 30 m telescope	22
1.11	ALMA observations of the CO(3–2) line in the CSE of R Scl	23
1.12	Comparison between polarised light observations with PolCor, molecular line observations with ALMA, and optical scattered light observations with the <i>Hubble</i> Space Telescope of the CSE around R Scl	24
1.13	Single-dish SEST observations of the molecular CO(1–0) and CO(2–1) emission of the CSE and detached shell around the carbon star U Ant	25
1.14	Dust scattered light observations of the CSE around U Ant, observed with EFOSC2 at the ESO 3-6 m telescope	25
2.1	Schematic figure of simplified interferometer	28
2.2	Simulated ALMA observations of M51	30
2.3	ALMA operation site from above	31
2.4	Schematic view of data collection process with ALMA	34

Part I

Introduction, scientific background, and methods

Introduction

I'd rather learn from one bird how to sing
than teach ten thousand stars how not to dance

E.E. Cummings

Our human lives are busy and restless, mostly centered on ourselves, and governed by the neverending cycle of sunrise and sunset. When we instead turn our heads to look up at the dark night sky, we see the light of countless stars inhabiting our known Universe. They seem still and constant, like insignificant bright dots on a black canvas, never moving and ever present. The same constellations of stars escort us from birth to death, and except from the twinkling light caused by the turbulence of our atmosphere, they never seem to change. But in fact they lead secret lives, from stellar birth to death, full of change and evolution.

Stars are born in dense clouds of interstellar dust and eventually return to interstellar dust. They go through violent deaths of explosions and outbursts of energy, or gentle and slow disintegration through stellar winds. Their immensely long lifespans of billions of years make it virtually impossible to observe these processes from start to beginning during our own short lives. But each individual star of the seemingly infinite number of stars can be seen as one puzzle piece frozen at one particular time in the life cycle, so that we can slowly put the picture together and form coherent theories of stellar evolution.

This thesis is devoted to study the deaths of stars with similar masses as our nearest one, the Sun. These stars are named after the stellar evolutionary phase in which they are, and are called Asymptotic Giant Branch (AGB) stars. Those stars' deaths are not spectacular explosions that for example create pulsars and black holes, but are heralded by the onset of stellar winds, which slowly dissolve the star. During their long lives, AGB stars create countless chemical elements and molecules, which are crucial for the chemical evolution of the Universe and life as we know it. These elements are piled up in circumstellar envelopes (CSEs) around those stars and are ultimately distributed back into the interstellar medium, from which new stars and planets can form.

Especially the last phases of these stellar deaths, which insert a lot of material back into the cosmic cycle of matter, happen on astronomically brief timescales of a few hundred to a few thousand years. Therefore they are very dynamical processes, and we observe stellar winds of many different intensities and shapes. To understand the details of mass loss through stellar winds, high-resolution observations are needed to resolve all dynamical structures that can arise during that process. For this reason, I have focused my research on observations with the world's best millimeter/submillimeter interferometer, called ALMA, which has an unprecedented spatial resolution at those wavelengths.

In the course of this thesis, I present observations of several AGB stars, which show intricate structures within the stellar wind and CSE, and investigate their mass-loss history with respect to their evolutionary stage. In Chapter 1, I summarise the scientific background of AGB stellar evolution. An overview on all studied objects within this dissertation is given in Section 1.4. Chapters 2 and 3 give brief introductions to the observing and modelling methods, respectively, as used in the work for this dissertation. Chapters 4 to 7 present the core publications of this dissertation, and Chapters 8 to 10 present additional publications. Chapter 11 gives a conclusion on the scientific findings of this dissertation, and Chapter 12 gives a brief outlook on future research.

Chapter 1

Sometimes good things fall apart
so better things can fall together.

Marilyn Monroe

Asymptotic giant branch stars

All low- to intermediate-mass stars – our Sun included – will eventually undergo the so-called asymptotic giant branch (AGB) phase, which will be described in various degrees of detail in the following sections of this chapter. AGB stars not only produce significant amounts of heavy elements during their nucleosynthesis processes, but are also subject to complex interplays of dynamic mixing events within the stellar atmosphere, as well as substantial mass loss through stellar winds, which pile up huge circumstellar envelopes (CSEs) around their host stars. I will touch on the most important points of AGB evolution and subsequent observable characteristics, which play an important role in the publications of this thesis, and summarise the current state of research as well as open questions and issues of this broad topic related to my specific projects. Since this thesis is first and foremost a snapshot of my own scientific accomplishments in the scope of a much bigger field of research, I refer to a number of excellent and extensive reviews, which are both a source of information for this chapter as well as a good reference point for further information for the ambitious and curious reader.

A very recent and general review on the mass loss mechanism, its modelling and measurements on the AGB has been published by Höfner & Olofsson (2018). Earlier reviews include the ones of Herwig (2005) on the evolution of AGB stars, Karakas & Lattanzio (2014) on the nucleosynthesis and stellar yields of AGB stars, De Marco & Izzard (2017) on the influence of binarity on AGB stars, and last but not least the very extensive book by Habing & Olofsson (2003) on AGB stars in general.

1.1 Stellar evolution

This section is mostly based on the review by Herwig (2005) and Chapter 2 of the book by Habing & Olofsson (2003), unless another citation is explicitly given.

Stellar evolution as a whole describes all substantial changes within a star on its evolutionary path from birth to death. In this chapter I will summarise the evolutionary path of sun-like stars, which are in the mass range of roughly 0.8 to 8 solar masses (M_{\odot}). Single stars within that mass range will not end their lives in a violent explosion such as supernovae, but evolve through the AGB phase and live through a more gentle end. When talking about stellar evolution, usually one diagram is used to describe the path a star takes depending on its temperature and luminosity: the *Hertzsprung-Russell*¹ diagram. A general Hertzsprung-Russell diagram (HRD), populated with a sample of known stars of different masses, can be found in Figure 1.1.

¹Named after the two scientists who first used this diagram to describe stellar evolution; Ejnar Hertzsprung and Henry Norris Russell.

In this diagram, some example stars with different initial main-sequence masses are plotted with their respective luminosity and surface temperature. Four main regions can be distinguished, showing different evolutionary stages: the main sequence where all stars start their stable lives, giants, supergiants, and white dwarfs. In the following, I will discuss the evolutionary path that leads from the main sequence to (and through) the giant regime to the white dwarfs.

Figure 1.2 shows a specific HRD with the evolutionary track for a star of solar metallicity with an initial main-sequence mass of $2 M_{\odot}$, which I will describe in more detail below. I will only loosely explain the post-AGB evolution until the white dwarf stage and not explicitly focus on the “born-again” evolution track shown in blue in the diagram, but instead focus on the evolution to and on the AGB, which is the main topic of this thesis.

1.1.1 Evolution from main sequence to AGB

When arriving on the main sequence, after being born from dense interstellar clouds, stars quietly burn hydrogen into helium by nucleosynthesis processes in their core (see Section 1.2). These stars consist mainly of hydrogen (H) and helium (He), with a mass percentage of 72 % and 27 % for a solar abundance of H and He, respectively (Asplund et al. 2009). But however large the H supply is, eventually all hydrogen in the stellar core is used up and transformed into helium through nucleosynthesis. Once this happens, the energy production in the stellar core stops and the star turns off the main sequence towards lower temperatures, while the core is gravitationally contracting. At this stage, hydrogen burning continues to exist in a thin shell around the contracting helium core and the star moves to the bottom of the red giant branch (RGB) in the HRD. While the core continues to contract, the outer layers of the star expand and become convective, the luminosity of the hydrogen-burning shell increases, and the temperature decreases: the star ascends the RGB. The convective envelope of the star penetrates into the deeper layers that have been subject to partial hydrogen burning earlier, and nuclear processed material is mixed outwards. This process is called “first dredge-up” and the implications on the chemical constitution of the star will be discussed in the next section. Eventually, the temperature in the contracting helium core is high enough to start fusion via the triple-alpha process, and the helium core ignites at the tip of the RGB. For stars with masses lower than approximately $1.8 M_{\odot}$ the core has become electron degenerate and the helium ignition happens along a so-called violent helium core flash, allowing helium to burn rapidly in a runaway process, producing large amounts of energy. More massive stars ignite in a less violent way.

After helium ignition, the star settles on the zero-age horizontal branch (ZAHB) to quietly burn helium in the core and hydrogen in a shell, shortly moving to higher temperatures but decreased luminosity. At some point, all helium in the core is transformed into an electron degenerate carbon and oxygen (C-O) core, leading to a decrease in temperature, the establishing of a helium burning shell around the core in addition to the persistent hydrogen burning shell, and yet another rise on the red giant branch. This time the evolutionary track only approaches the original RGB asymptotically, naming the following evolutionary phase asymptotic giant branch (AGB).

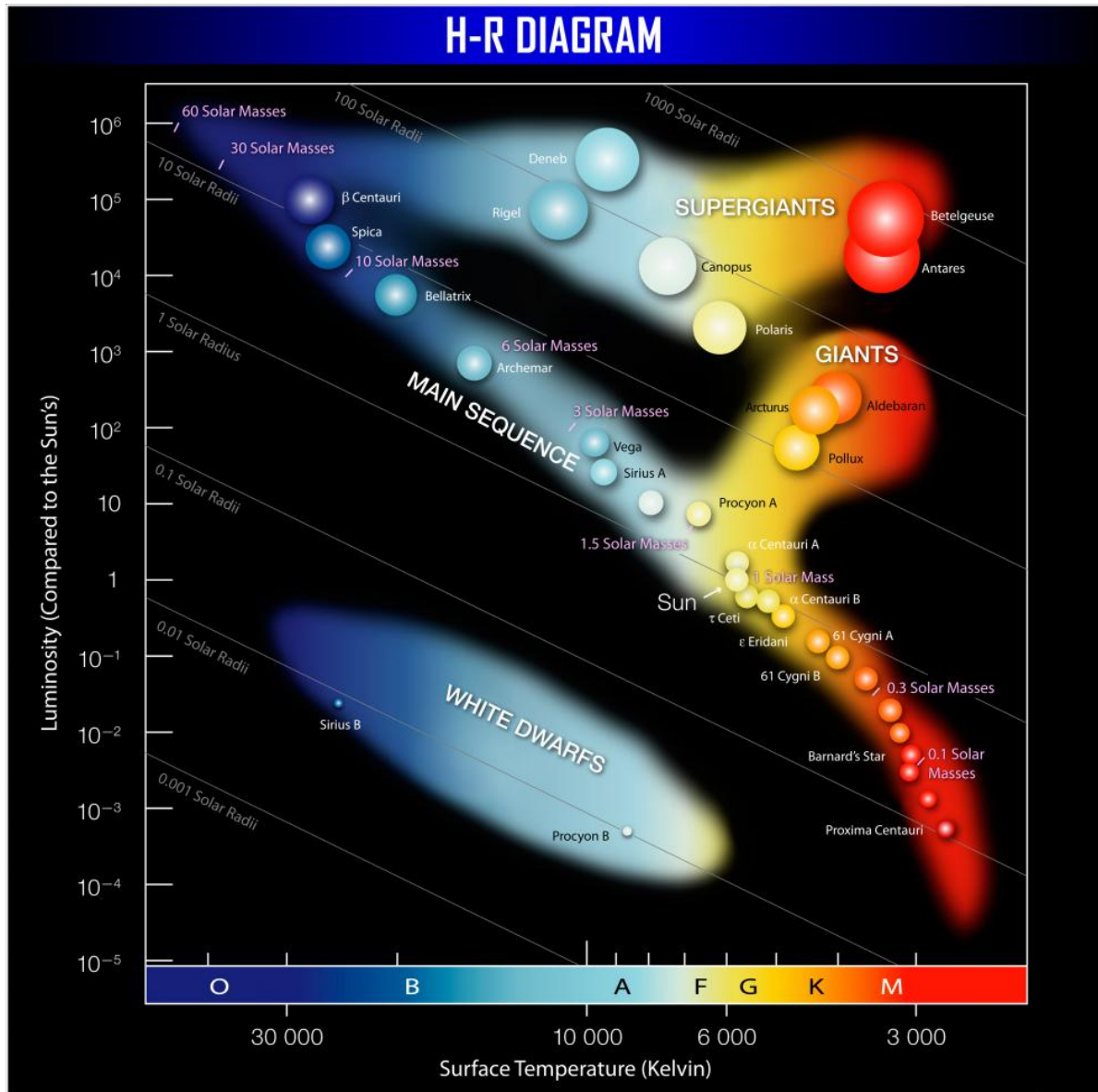


FIGURE 1.1: Hertzsprung-Russell diagram showing the main sequence, giant branch, supergiants and white dwarf regions in relation to luminosity and surface temperature, populated by examples of known stars of different masses. Spectral classifications are denoted in the colorbar of the temperature axis.

Image credit: ESO

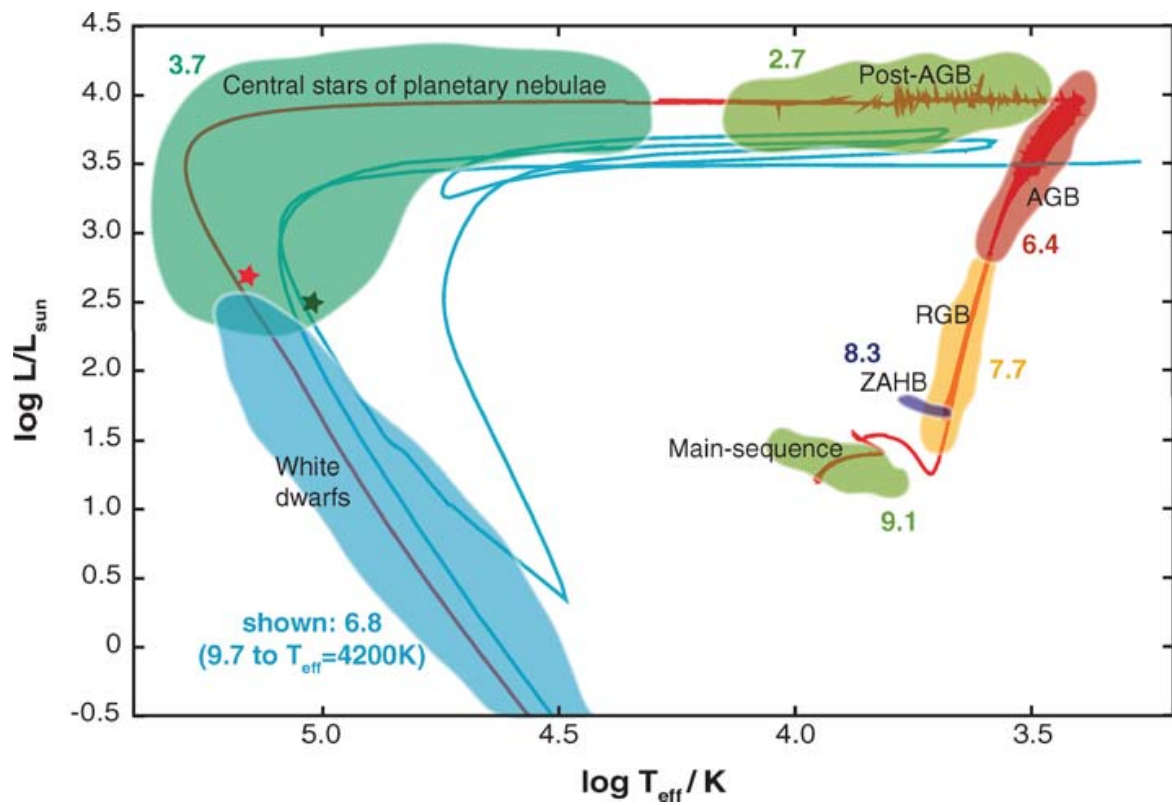


FIGURE 1.2: Hertzsprung-Russell diagram with the evolutionary track of a $2 M_{\odot}$ star with solar metallicity. The differently colored regions denote the different phases of stellar evolution, the blue track represents a “born-again” evolution. The numbers attributed to each evolutionary phase give the log of the approximate duration of this phase for a $2 M_{\odot}$ star in years (Herwig 2005).

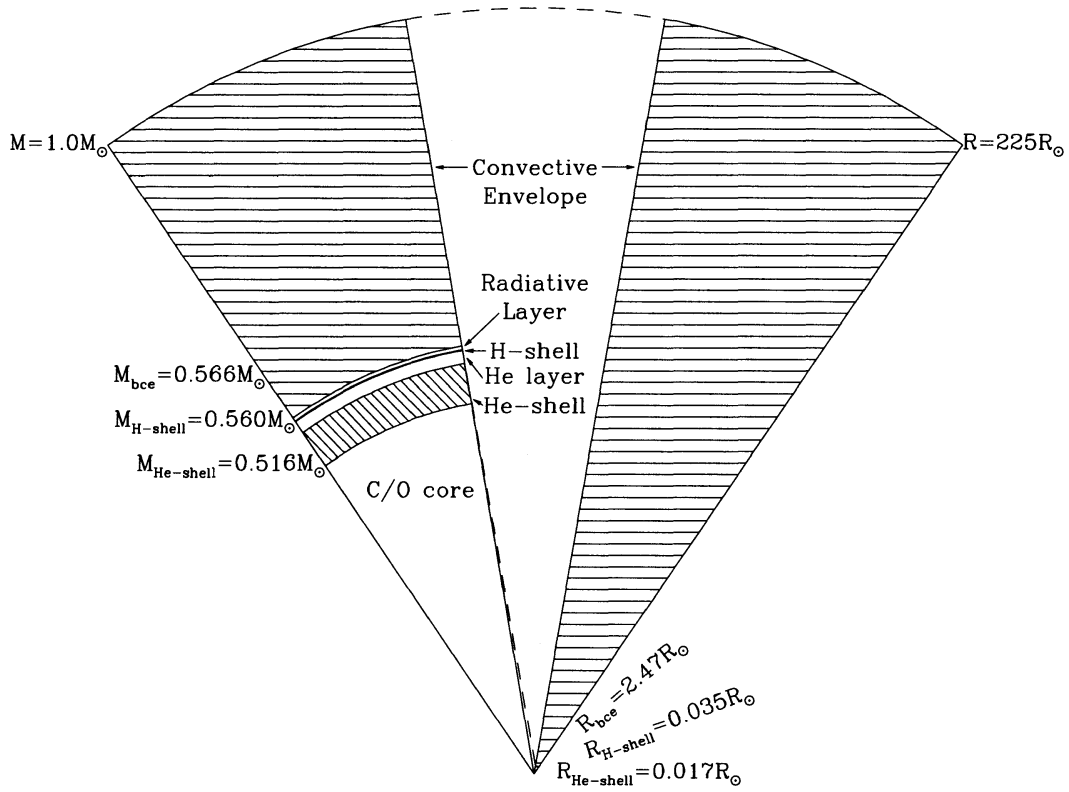


FIGURE 1.3: Schematic view of the stellar structure of an AGB star with initial mass of $1 M_{\odot}$, shown in mass coordinate (left) and radius (right). The abbreviation *bce* is marking the base of the convective envelope (Habing & Olofsson 2003).

1.1.2 Evolution on the AGB

At the beginning of the AGB phase, the stellar structure (as depicted in Figure 1.3) is more or less the same, regardless of the initial stellar mass: the massive but comparably small stellar core, consisting of electron degenerate carbon and oxygen, is surrounded by a thin helium-burning shell, a subsequent intershell layer of helium, a thin hydrogen burning shell with an adjacent radiative layer, and finally a huge convective envelope, which is taking up roughly half of the stellar mass but almost all of the volume. The core is supported by the pressure of degenerate electrons and the degeneracy prevents carbon burning due to cooling by neutrino emission. The condition of the core degeneracy limits the mass of AGB stars to about $8 M_{\odot}$. Since stellar evolution on the AGB strongly depends on the initial stellar mass, the differences are summarised in Fig. 1.4, and in the following I will focus on the description of AGB stars between $1 M_{\odot}$ and $4 M_{\odot}$, unless otherwise noted.

The helium- and hydrogen-burning shells do not smoothly burn and steadily produce energy, but instead they are subject to thermal instabilities and interaction processes that lead to reoccurring outbursts of luminosity, so-called thermal pulses. At first, the helium shell is the major source of energy, processing outwards through the helium layer generated by previous core hydrogen burning. As the helium burning shell is approaching the hydrogen burning shell, the intershell helium layer becomes smaller and smaller, slowing down the progression of the helium-burning shell, and at some point the hydrogen burning shell dominates the energy production. Small temperature perturbations in the helium burning shell can lead to a thermal runaway process, driven by the high temperature sensitivity of the helium burning

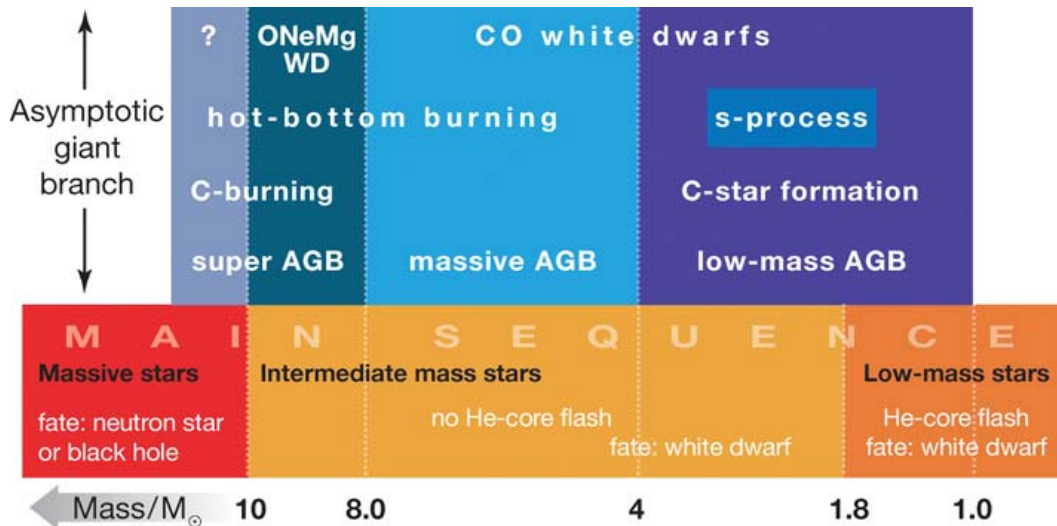


FIGURE 1.4: Schematic view of main-sequence and AGB evolution as a function of stellar mass. The initial main-sequence mass is shown at the bottom of the figure. The classical main-sequence mass-ranges are denoted in the lower part of the figure, while the AGB mass-ranges are marked in the upper part of the figure, according to the associated stellar processes (Herwig 2005).

process (triple-alpha process, see Section 1.2) and sustained by the thinness of the shell. This leads to an increase in the helium shell energy production, which in return decreases the hydrogen shell energy production due to the sudden energy outburst and restructuring of the layers. As soon as the helium in the intershell region is again mostly used up, the helium shell energy production ceases again, and the hydrogen shell takes over. This marks the thermally pulsing AGB phase, which has important implications on the chemical evolution and mass-loss evolution, as described in the sections below. Thermal pulses (or helium-shell flashes) occur periodically on timescales of roughly 10,000 years, lasting for a quite short time of roughly a few 100 years. Along with a thermal pulse (TP) the outer convective envelope is able to penetrate into the intershell zone, from where it dredges up material. This is called “third dredge-up”² and represents an important step in the chemical evolution of an AGB star.

During the whole AGB evolution and especially within the last few cycles of thermal pulsing, the star loses mass in the form of an intense stellar wind (the mass-loss evolution is described in detail in Section 1.3), which eventually terminates its life on the AGB, when it reaches its maximum as a “superwind”.

1.1.3 Post-AGB evolution

When the star reaches the tip of the AGB, the intense stellar wind reduces the hydrogen-rich stellar envelope severely, which means that the star cannot longer sustain its radius and starts to shrink. At the same time, the radiative layer between the hydrogen-burning shell and the convective envelope is still maintaining the luminosity of the star, and while the temperature increases due to the reduced radius, the luminosity stays roughly constant. The star now quickly moves horizontally through the post-AGB regime in the HRD and eventually the

²Note that a “second dredge-up” only occurs for stars with initial masses larger than roughly $4 M_{\odot}$, right after the star begins to ascend the AGB. At this point, the hydrogen-burning shell is extinguished by the sudden expansion for a short time in which the convective envelope penetrates into the intershell zone.

majority of the CSE is ejected from the star, slowly expanding and cooling. The expelled CSE is interacting with the persistent stellar wind and the hardening stellar radiation field, leading to the formation of a so-called planetary nebula (PN). At the point where there is not enough mass left in the hydrogen-rich envelope of the post-AGB star to maintain the temperature required for hydrogen burning, its luminosity drops and it moves downwards in the HRD. The stellar remainder is now called white dwarf (WD), and it essentially represents the leftover carbon-oxygen core of the progenitor AGB star, surrounded by the illuminated parts of the former CSE, which now is a PN. The timescales on which white dwarfs cool down are estimated to be as long as the current age of the Universe, meaning that they can belong to the oldest objects of the Universe.

1.2 Chemical evolution on the AGB

This section is mostly based on the reviews by Karakas & Lattanzio (2014), Herwig (2005), Busso et al. (1999) and chapter 2 of the book by Habing & Olofsson (2003), unless another citation is explicitly given.

The structural changes and internal stellar evolution processes to and on the AGB can lead to significant mixing of nucleosynthesis products within the stellar atmosphere and CSE. Since AGB stars are considered to be among the most important producers of molecules and dust within the Universe, it is fundamental to describe and ultimately quantify the nucleosynthesis processes and products for each evolutionary stage, in which substantial mass loss and therefore feedback to the surrounding ISM is present. In this section I describe the basic chemical evolution sequence of AGB stars and its consequence on observations as well as the enrichment of the ISM. I will comment shortly on current loose ends in the theoretical description of AGB nucleosynthesis and chemical evolution.

1.2.1 Initial composition, sites of nucleosynthesis, and mixing events

As described in Section 1.1 and schematically shown in Figure 1.3, an AGB star initially consists of a carbon-oxygen core, surrounded by a helium-burning shell, which is separated from the hydrogen-burning shell by a very thin intershell layer. Outside the hydrogen-burning shell a thin radiative buffer zone is located, followed by the huge convective envelope, which is taking up the majority of the stellar radius. The AGB chemical composition at the surface of the convective envelope represents the initial stellar composition with imprints of the first (and possibly second) dredge-up process.

Sites of nucleosynthesis

In the hydrogen-burning shell, hydrogen is transformed into helium (^4He) primarily through the CNO cycle, generating ^{13}C and ^{14}N as byproducts. At the same time, the chemical reactions associated with the CNO cycle reduce the abundances of ^{12}C , ^{16}O and ^{18}O . This means that regions where hydrogen-burning has taken place have different chemical abundances than before and any structural change that results in a mixing of these regions will influence the propagation of the abundance changes to outward stellar layers.

The helium-burning shell is powered by the triple-alpha process, which essentially fuses three alpha particles – that is ^4He – into ^{12}C . This is probably the most important element produced

by AGB stars. As a byproduct, ^{14}N is transformed into ^{22}Ne by capturing two alpha particles. Between the hydrogen- and helium-burning shell, the intershell region periodically becomes convective during thermal pulses. This is called intershell convective zone (ISCZ) and it transports helium-burning products to the hydrogen-burning shell, where proton capture can alter the composition of the injected elements. The chemical composition of the ISCZ is mostly ^4He (70-75%), a significant fraction of ^{12}C (20-25%), a few percent of ^{16}O , and a small fraction of ^{22}Ne . While these elements are mixed to the hydrogen-burning shell, the freshly produced helium is in return mixed downwards to the helium-burning shell. Overall, the ISCZ is mostly homogenised in its chemical abundance. For the scenario of convective overshooting at the edges of the ISCZ, the ^{16}O abundance can be increased significantly, when the material from the C-O core is mixed into the ISCZ.

A fundamental and very important nucleosynthesis process in AGB stars, which makes them significant contributors to the chemical evolution of galaxies and the Universe, is the slow neutron capture or so-called *s*-process. Due to the fact that hydrogen- and helium-burning products are frequently mixed in the intershell region and can be re-processed again and again, as well as be exposed to neutrons that can be captured, heavy elements can be formed in AGB stars. For example, AGB stars are strong contributors to the fluorine abundance in the Universe, and in general the *s*-process can be considered to be the origin of half of all elements heavier than iron. The neutron source for the *s*-process to be activated in the intershell region was and still is a topic of debate, since it was first suspected that the reaction from ^{22}Ne to ^{25}Mg by capture of an alpha particle is the main source of neutrons, but no sufficient ^{25}Mg excess could be detected spectroscopically. An alternative major neutron source is the reaction from ^{13}C to ^{16}O by capture of an alpha particle, but for this reaction a sufficient abundance of ^{13}C has to be available. Current theory predicts the formation of so-called ^{13}C pockets in the ISCZ, which are formed by the proton capture of the abundant ^{12}C . These pockets would for example have to be subsequently created through intershell downward mixing of hydrogen to the helium-burning product ^{12}C .

First dredge-up

The first dredge-up (FDU), already occurring during the first rise of the star on the RGB (see Section 1.1.1), reaches from the convective envelope down to deeper layers that have undergone partial hydrogen burning. Therefore, the outer stellar layers are enriched with CNO cycle products, and the abundances of ^{13}C and ^{14}N increase while the abundance of ^{12}C decreases. The C isotopic ratio can be used to track the stellar evolution and nucleosynthesis for star that undergo RGB (and subsequent AGB) evolution, and the $^{12}\text{C}/^{13}\text{C}$ ratio can be derived from stellar spectra. There is a general agreement between observations and models of the abundance change caused by the FDU in the RGB evolution, but for some cases like for example open metal-rich clusters, metal-poor field stars or giants in globular clusters, the theoretically derived $^{12}\text{C}/^{13}\text{C}$ ratio is a lot higher than the actually observed one. This is interpreted as indication for extra mixing, which should be accounted for in stellar evolution models. The physical origin of extra mixing is not yet completely clear and has to be investigated more thoroughly.

Second dredge-up

The second dredge-up (SDU) does only occur for stars with initial masses larger than roughly $4 M_{\odot}$, when they start to move up on the AGB. The convective envelope penetrates deep into

the region of complete hydrogen burning, contrary to the FDU, which only penetrates into partial hydrogen-burning regions. The increase in helium is significantly higher than for the FDU, while the other elemental abundances do not change a lot compared to the FDU. An exception is the $^{14}\text{N}/^{15}\text{N}$ ratio, which can increase significantly since the CNO cycle has transformed most CNO nuclei into ^{14}N .

Hot-bottom burning

Stars with masses above about $5 M_{\odot}$ can develop deep convective envelopes that allow temperatures high enough for nuclear burning at their bottom, next to the hydrogen burning shell. The surface abundances can be severely changes through hot-bottom burning (HBB), because if the temperatures get indeed high enough, the CNO cycle as well as Ne-Na and Mg-Al reactions can set in. Since all stars further discussed in this thesis are considered to be of lower masses than the limit for hot-bottom burning, I refer to the extensive reviews cited at the beginning of this chapter for a more complete description of hot-bottom burning and its consequences.

Third dredge-up

The third dredge-up (TDU) is a major mixing event that follows thermal pulses on the AGB, where the helium- and hydrogen-burning shells periodically extinguish and reignite themselves due to thermal instabilities and runaway helium-burning. It produces the largest change in surface abundances and subsequently influences the chemical composition of the whole CSE during the intense mass-loss phase (see Section 1.3). When a thermal pulse has happened and the hydrogen-burning shell is extinguished, the convective envelope can penetrate deeply into the region of previous hydrogen burning and in the ISCZ, where nuclear processed elements from helium burning as well as the *s*-process are present. These elements – most importantly ^{12}C – are mixed to the stellar surface and subsequently enrich the CSE.

1.2.2 Chemical evolution from M- to S- to C-type

All the above described nucleosynthesis processes together with the individual and partially reoccurring mixing events – and especially the TDU – can alter the surface abundance of AGB stars significantly, so that we classify them with three main spectral types, according to their carbon-to-oxygen (C/O) ratio:

Initially, the surface abundance of oxygen is greater than the abundance of carbon, meaning that early on the AGB the stars show a C/O ratio of < 1 (~ 0.5) and are of spectral type M. As stars evolve along the AGB, they periodically undergo thermal pulses and subsequent TDUs, which means that primarily ^{12}C but also other helium-burning products as well as *s*-process elements are dredged up to the stellar surface, leading to an increasing C/O ratio with passing TPs. Stars with a C/O ratio of > 1 are classified as C-type stars, and they reach their carbon over-abundance after a sufficient number of TPs, where mostly ^{12}C is dredged up to the stellar surface. Note that massive stars, which exhibit hot-bottom burning, are not able to become C-type stars, since the CNO cycle of HBB destroys most of the available carbon, before it can be dredged up.

While the spectra of M-type stars are dominated by TiO bands, C-type stars show spectral bands of CN and molecular carbon C_2 . In between those two spectral types lie the S-type stars, with C/O ratios close to 1, which are further divided into MS-, S- and SC-type, depending on

their exact C/O of ~ 1 , while the C/O ratio of MS- and S-type stars lies a bit below 1. MS-type stars show ZrO bands, enabled by the s -process, in addition to TiO bands, while SC-type stars show spectral features similar to C-type stars but are dominated by spectral features of s -process elements. One particularly useful spectral signature to trace the existence and recent dredge-up of s -process elements is the radioactive isotope ^{99}Tc , which is produced in the s -process and only has a half-life time of roughly 10^5 years. Its detection is direct observational evidence for the recent production of new elements inside the star and the efficient mixing to its surface, which indirectly indicates the chemical evolution to S- and C-type stars. The C/O abundance ratio has significant consequences for the chemical composition of the CSE and the mass-loss process, which will be discussed in the next section.

1.3 Mass-loss evolution and circumstellar envelopes

This section is mostly based on the review of Höfner & Olofsson (2018) as well as chapter 2 and 9 of the book by Habing & Olofsson (2003), unless another citation is explicitly given.

This section covers the mass-loss process and its temporal evolution, as well as the evolution and geometry of circumstellar envelopes (CSEs), which are created through mass loss and expand out to several thousand stellar radii. Since the chemical and dynamical processes within the stellar interior of AGB stars provide significant amounts of heavy elements, deposited on the stellar surface, and according to the initial mass function AGB stars are very common, they have to be considered important contributors to the cosmic cycle of matter and chemical enrichment of the Universe, provided they expel significant amounts of mass into the surrounding ISM.

Figure 1.5 shows a schematic overview on the circumstellar environment of AGB stars and its associated chemical as well as physical processes involved. The degenerate C-O core and the convective stellar envelope have been subject to the previous sections, while this section will focus on the dynamical atmosphere, where the stellar wind is launched, and the circumstellar envelope, where the mass-loss material is deposited. At the end of this section I will discuss the morphology of CSEs, briefly touching the subject of the ISM interaction region, where the stellar wind collides with the surrounding medium.

1.3.1 Mass-loss mechanism

AGB stars have high luminosities (from a few 1,000 to 10,000 solar luminosities) and low effective temperatures (around 3000 K or lower), while their radii typically are as large as several hundred solar radii. Together with their generally low masses, this generates a sufficiently low surface gravity to ease stellar wind ejection. According to well-established theory, the stellar wind is basically driven by radiation pressure, which is a reasonable assumption, since AGB stars exhibit high luminosities.

In the cool and extended dynamical atmosphere (see Fig. 1.5), the density is periodically increased by pulsation of the convective stellar envelope and subsequent shockwaves, running through the chemically enriched atmosphere. Firstly, this leads to molecule formation in dense enough regions. Secondly, if the temperatures are low and the densities high enough, also dust formation will set in. The dust condensation zone is typically at temperatures around 1000-1500 K, and the densities required for dust formation are most likely achieved through shocks running through the outer stellar atmosphere.

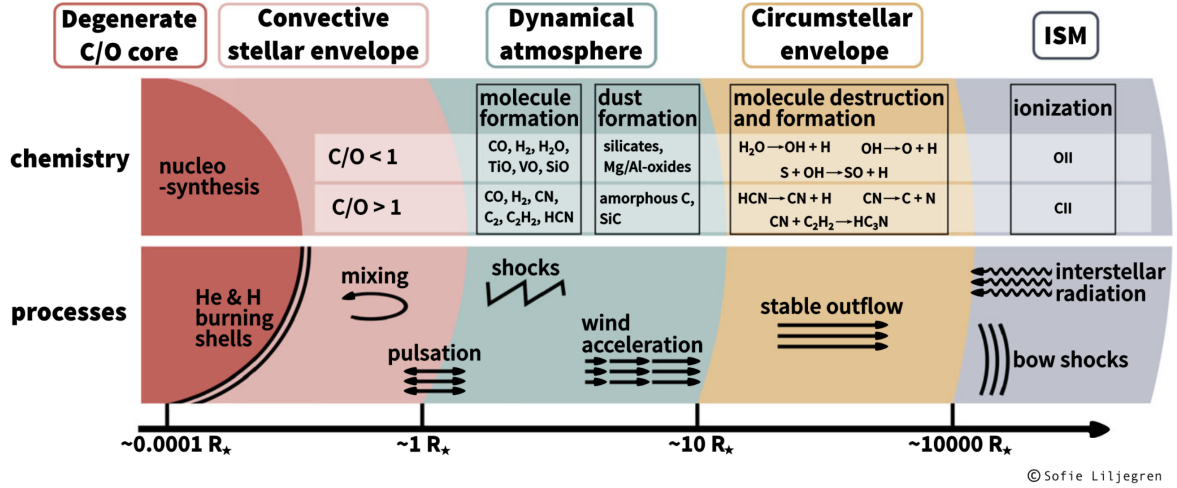


FIGURE 1.5: Schematic view of an AGB circumstellar environment from star to ISM interaction front. The figure is divided into 5 spatial domains, which are labelled at the top, and 2 separate descriptions of circumstellar chemistry (top half) and dynamical/interaction processes (bottom half). The radius for each spatial domain is indicated in the scale at the bottom of the figure (Höfner & Olofsson 2018).

Since the luminosities of AGB stars are very high, an obvious wind-driving mechanism is radiation pressure on particles, for which the scattering or absorption efficiency is very high near the spectral radiation maximum of the star, i.e. around the near infrared wavelength region. Although this is true for the rotational-vibrational spectra of molecules abundant in AGB CSEs, models predict that the molecular opacities are not big enough to completely drive the wind. On the other hand, sufficiently high opacities for efficient stellar winds can be reached for dust grains, such as amorphous carbon or Mg-Fe silicates, which can be found in AGB atmospheres. Current models and observations indicate that pulsation enhanced dust driven outflows are describing AGB winds best. In this scenario, stellar pulsation of the convective envelope sends shock waves through the molecular atmosphere and enables dust formation. Subsequently, radiation pressure on those dust grains creates a stellar outflow, where momentum is transferred to the molecular gas, and the stellar wind consisting of both dust and gas is driven outwards. Typical outflow velocities are in the range of 5 to 15 km/s, but can range up to 30 km/s as well. Typical mass-loss rates are in the range of 10^{-8} to $10^{-5} M_{\odot}/\text{yr}$, with exceptions of high mass-loss periods up to $10^{-4} M_{\odot}/\text{yr}$. The dust percentage of a typical CSE is about 1 percent or less, but it is still sufficient enough to drive the stellar wind.

1.3.2 Chemical composition of CSEs

The chemical composition of the CSE strongly depends on the atmospheric abundances of carbon and oxygen, and is particularly dominated by the C/O ratio, which depends on the efficiency of previous dredge-up events. The most stable and common molecule to be found in CSEs is H₂, followed by the observationally much easier to be observed carbon-monoxide CO molecule. This molecule is almost equally abundant in M-, S- and C-type stars, but the molecular chemistry strongly depends on the excess abundance of either O (for M-type stars) or C (for C-type stars), which consists of the respective elements not locked in CO. M-type (or also called: oxygen rich) stars will predominately form molecules associated with oxygen in their atmosphere, while C-type (or: carbon rich) stars will mostly form carbon rich molecules. S-type stars typically show a mixed molecular composition, depending on their closeness to

either M-type or C-type. In total, roughly 90 molecules (excluding isotopologues) have been observed in the CSEs of AGB stars, highlighting their importance when it comes to chemical diversity and the chemical enrichment of the Universe.

Although circumstellar dust only takes up a very small fraction of the total CSE mass, AGB stars are considered to be among the most important producers of dust in the Universe, next to supernovae. The abundant circumstellar molecules will form silicates or Mg/Al-oxides in the case of M-type, or amorphous carbon or SiC dust in the case of C-type stars, respectively. These different dust species can have quite different absorption and scattering properties, which additionally depend on the grain size and geometry.

1.3.3 Morphology and evolution of the CSE

Assuming a spherically symmetric star and constant, homogeneous stellar wind, CSEs should be spherically symmetric spheres with homogenous density, at some radius interacting with the surrounding ISM. Observationally, this is frequently not the case, and apart from clearly irregularly shaped CSEs, there are a couple of repeatedly observed geometries of CSEs, that can reveal a more complex mass-loss history than spherically symmetric constant-wind models would predict.

First of all, one has to distinguish between CSE morphologies driven by the stellar mass-loss itself, and those morphologies created through the interaction of the stellar wind with the surrounding medium. The latter are usually dominated by shock fronts or so-called bow shocks caused by the stellar motion through the ISM and the wind colliding with it. A good overview on the large scale geometry of CSEs and the CSE-ISM interface is presented in the *Herschel* infrared survey of 78 evolved stars by Cox et al. (2012), which was imaging the dusty component of CSEs. In this survey, 4 different morphologies were detected and classified: “fermata”, “eyes”, “rings”, and “irregular” CSEs. While “fermata” is used to describe bow-shock geometries with clear ISM interaction fronts, “eyes” and “rings” are considered to be associated with intrinsic properties of the AGB star, corresponding to suspected binarity and episodal mass loss, respectively (both scenarios are more detailedly described in the paragraphs below). Source intrinsic mass-loss variations, which can shape the CSE significantly, have to be observed at much higher spatial resolution, which is usually done in the sub-millimeter wavelength regime, where the very abundant CO molecule has strong emission lines. CSEs can be big enough to be observed with single-dish telescopes and reveal basic structures or large scale asymmetries, but for a detailed morphological analysis one has to observe at higher spatial resolutions with interferometers (see Chapter 2). Along with high spatial resolution, also high spectral resolution is essential to investigate the mass-loss evolution of AGB stars, since the kinematics of the stellar wind can be mapped through Doppler-shifting of the observed molecular emission lines.

If the wind velocities at a certain radius of the CSE can be measured, one can estimate the ejection timescales of the stellar wind. From the brightness distribution of the CSE and the distance to it, one can estimate mass-loss rates through radiative transfer modelling (see Chapter 3).

Detached shells

Detached shells are thin, spherically symmetric shells, clearly separated from the continuous mass loss, which are up to now found around a small sample of approximately a dozen carbon-rich AGB stars. They represent snapshots of significant changes in the AGB mass-loss

evolution during a thermal pulse, where the mass-loss rate increases drastically for a brief period of roughly a few hundred years and subsequently declines to pre-pulse mass-loss rates again. They can be observed both in dust and gas emission, but have not been observed around M-type or S-type AGB stars, where most likely the different dust composition prevents the formation of a detached shell during a thermal pulse.

Observing detached shells in molecular emission, such as CO, and measuring the gas velocities enables the estimate of the detached shell age or time since the last TP, if the distance to the object is sufficiently well constrained. Currently observed detached shells have ages of a few thousand years, and it is commonly believed that significantly older detached shells will be destroyed by the interstellar radiation field and therefore cannot be observed anymore. Prominent examples of detached shells, which are well studied in molecular and dusty emission, include U Antliae and R Sculptoris, which are part of the sample of observed stars in this thesis and are presented in the next section. The formation mechanism of detached shells is believed to be a combination of a sharp increase of the mass-loss rate and the interaction with a previous, usually slower stellar wind, creating a shock-like density enhancement. With high resolution observations, details and fine structure in the shell geometry can be resolved, showing dynamic instabilities and providing input for detailed hydrodynamical modelling.

Influence of binarity

Apart from significant changes in the primary star's stellar evolution (e.g. reviewed by De Marco & Izzard 2017), binary partners can strongly influence the shape and evolution of the primary stellar wind on the AGB, depending on the orbital separation and mass ratio between the two stars. Binarity is also one of the possible explanations for a multitude of complex non-spherically symmetric geometries, observed in the successors of AGB stars, namely PNe, and noticeably more and more studies come to the conclusion that the binary rate among stars in the local Universe is higher than expected.

Close binarity can lead to the formation of so-called common envelopes, where the two stars share an envelope of ejected mass, and also the formation of disks as well as bipolar jets or outflows is associated with binarity. A morphological signature of binary stars with intermediate separation is the formation of spiral- or arc-like structures, which are created through orbital interaction of the binary companion, moving through the outflow of the primary star. These spiral structures have been observed around a handful of AGB stars, the most prominent example of it being the carbon rich AGB star R Sculptoris, observed in high resolution with ALMA.

While binarity complicates the calculation of mass-loss rates and stellar wind parameters, it can also offer insights to the mass-loss evolution of the primary star, since for example the separation of the spiral windings can be used to trace the evolution of the wind velocity (as impressively shown by Maercker et al. 2012). The deformation of the CSE through a binary companion can also serve as additional detection criterion for binary systems, since other binary tracers such as UV excess fluxes are not always non-ambiguous.

1.4 The sample of AGB stars covered in this work

The core of this PhD thesis consists of four publications, all of which address the analysis of individual AGB stars in varying evolutionary stages, focusing on different stellar properties, observational techniques, and modelling approaches. Therefore, a total sample of four AGB

stars is covered in this work, and a scientific overview on each star is presented in the sections below.

The order in which the individual objects are presented here also corresponds to the order in which the publications are included in this thesis, and is chosen in such a way that it resembles an evolutionary sequence of the investigated AGB stars, based on their estimated C/O ratio. Three of the four stars are carbon rich and surrounded by detached shells of various degrees of fine structure and morphology. Additionally, three out of four publications are based on observations conducted with the Atacama Large sub-/Millimeter Array (ALMA). The various observational techniques and sources of data for the discussed publications are presented in Chapter 2, the modelling techniques used in the respective publications are summarised in Chapter 3.

1.4.1 W Aquilae

W Aquilae (W Aql) is classified as S-type AGB star, which has a spectral type of S6.6 (Keenan & Boeshaar 1980), and – supposing an AGB evolutionary sequence from M- to S- to C-type stars – it is in the intermediate stage between an oxygen-rich and carbon-rich chemistry. Its C/O ratio according to the classification scheme by Keenan & Boeshaar (1980) is 0.98. The star has a period of 490 days and belongs to the Mira variables (Feast & Whitelock 2000). From the period-magnitude relation (Whitelock et al. 2008) and the 2MASS *K* band magnitude (Cutri et al. 2003), a distance of 395 pc is derived. Ramstedt et al. (2011) present archival Hubble Space Telescope (HST) images, which show that W Aql belongs to a resolved binary system, locating the binary in the South-West direction at a distance of $0.46''$, which corresponds to projected binary separation of ~ 180 AU (see Fig. 1.6). Nevertheless, the inclination of this relatively wide binary system, and therefore the real orbit, is unknown. Mayer et al. (2013) and Danilovich et al. (2015) attempt to analyse the binary companion in more detail, and both come to the conclusion that it most likely is located behind or within the CSE of W Aql, possibly shaping the CSE due to wind-binary interaction into the form of a loose Archimedian spiral (as suggested by Mayer et al. (2013), and shown by resolved images of the thermal dust emission in Fig. 1.7). Additionally, the innermost region ($\sim 1'$) of the dust distribution around W Aql was mapped through polarimetric observations of dust scattered light by Ramstedt et al. (2011), and an asymmetric dust distribution peaking to the South-West direction – being consistent with the projected binary location – was found.

Several studies at a wavelength range from IR to sub-mm, based on single-dish observations and radiative transfer modelling, have investigated the molecular line emission, corresponding mass-loss rates and chemical abundances (e.g. Decin et al. 2008; Danilovich et al. 2014). A large number of carbon and oxygen bearing molecular gas species have been detected around W Aql, and from the CO radiative transfer analysis a mass-loss rate of $4.0 \times 10^{-6} M_{\odot} \text{ yr}^{-1}$ was derived (Danilovich et al. 2014). Its evolutionary status as a late S-type star together with the confirmed and resolved binary system makes W Aql a compelling target to study the circumstellar envelope and chemistry.

In **Paper V** (see Chapter 8) of this thesis, the circumstellar molecular CO emission around W Aql was for the first time resolved by sub-mm interferometric observations with ALMA, allowing a detailed analysis of the wind-binary interaction by 3D hydrodynamic modelling and the derivation of an updated mass-loss rate by 1D radiative transfer modelling. Apart from CO, an additional set of a total of eight molecular lines of four different molecular gas

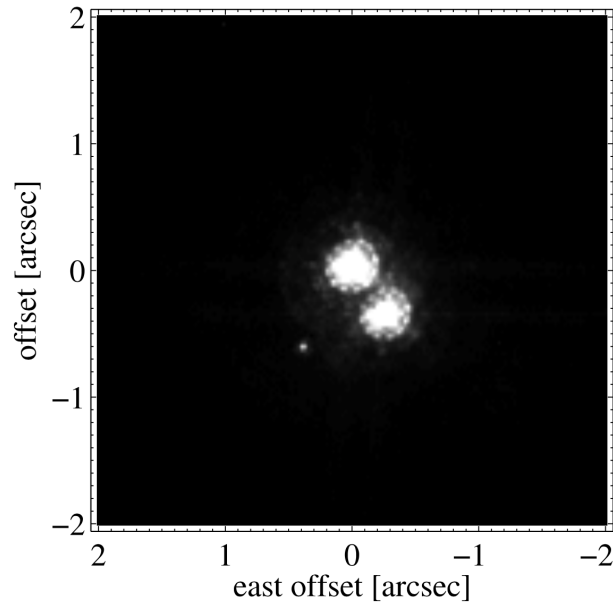


FIGURE 1.6: High resolution B band HST image of W Aql and the resolved binary. North is up and East is left; W Aql is centered at $0''$ offset, the binary companion is located in the South-West (Ramstedt et al. 2011).

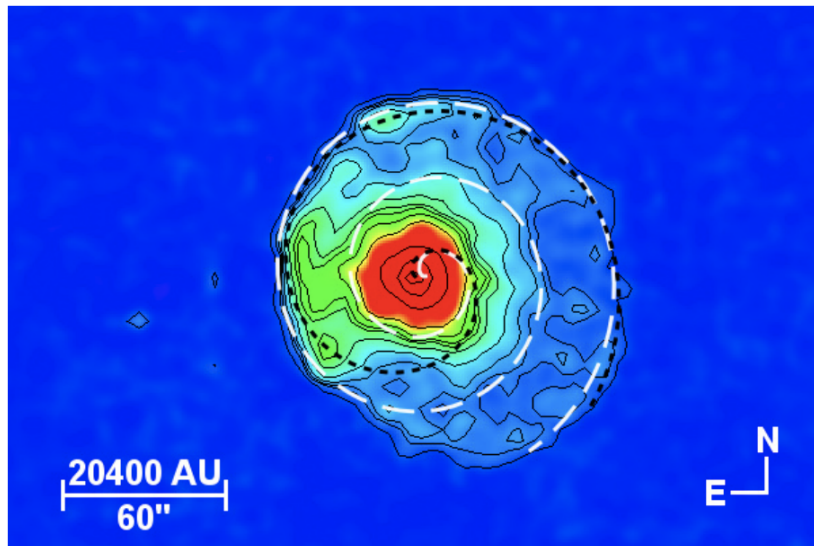


FIGURE 1.7: Deconvolved $70\mu\text{m}$ Herschel PACS image of W Aql overlaid with contours. Two Archimedian spirals, fitting the IR emission outline and resulting from two different wind-binary interaction scenarios, are plotted in black and white dashed lines (Mayer et al. 2013).

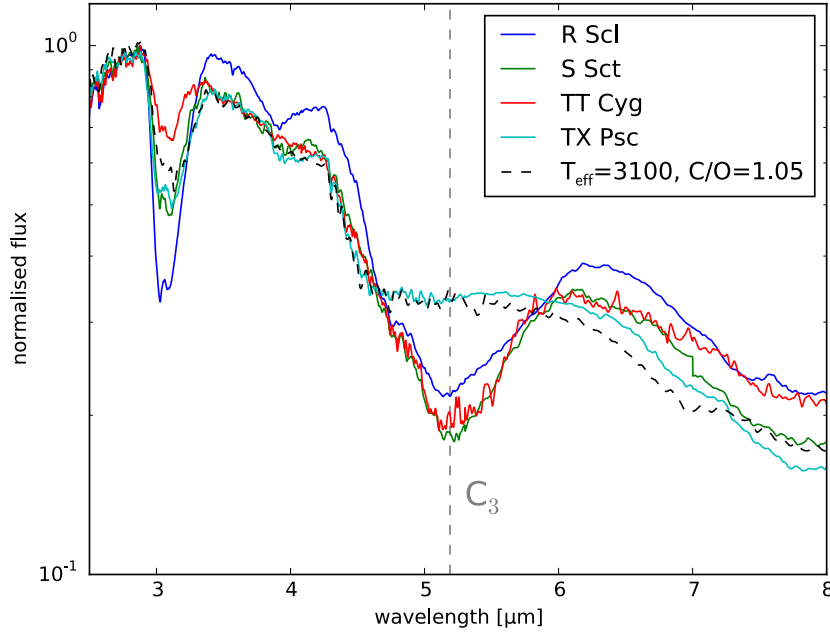


FIGURE 1.8: Comparison of the C_3 feature between TX Psc and known C-type AGB stars with detached shells (ISO spectra, solid colored lines). As comparison, an atmospheric model (COMARCS model, black dashed line) for an AGB star with a C/O ratio of 1.05 is plotted as well (Mecina private communication).

species was observed in the same ALMA dataset. In **Paper I** (see Chapter 4) of this thesis, the observations as well as radiative transfer modelling of the strongest of these molecular lines are presented and discussed.

1.4.2 TX Piscium

TX Piscium (TX Psc) is classified as semi-regular variable (SRa/b) star, has an average period of 224 d (Wasatonic 1997) and is located at a distance of 275 ± 30 pc (van Leeuwen 2008). Its spectral type is C7,2 (Yamashita 1972). As summarised by Jorissen et al. (2011) (and references therein), it shows large and regular variations in the radial velocity, which could either point to an undetected binary companion or so-called long-secondary periods, seen in some long-period variables. Since no further clear indication for a binary companion is reported for TX Psc, Jorissen et al. (2011) consider the radial velocity variation more likely to be of non-orbital origin.

The C/O ratio of TX Psc, as average derived from a summary of multiple studies discussed by Klotz et al. (2013), is 1.07, marking the star as C-type very close to S-type stars. A comparison of the C_3 molecular absorption feature around $5 \mu\text{m}$ between TX Psc and known carbon rich (detached shell) sources shows, that the feature is not visible for TX Psc. A COMARCS model with a low C/O ratio of 1.05 agrees with these observations, confirming that the object likely turned very recently into a carbon star (Fig. 1.8; ISO spectra, Sloan/Cornell database, Mecina priv. comm.). Additionally, the position of the star in the Hertzsprung-Russell diagram (HRD), compared to AGB evolutionary tracks, fits a 2 - 3 M_{\odot} “fresh” carbon star with a C/O ratio between 1 and 1.1 (Klotz et al. 2013). Technetium is found in TX Psc, meaning that it has recently undergone at least a couple of TPs to dredge up sufficient amounts of ^{99}Tc (Lebzelter & Hron 2003).

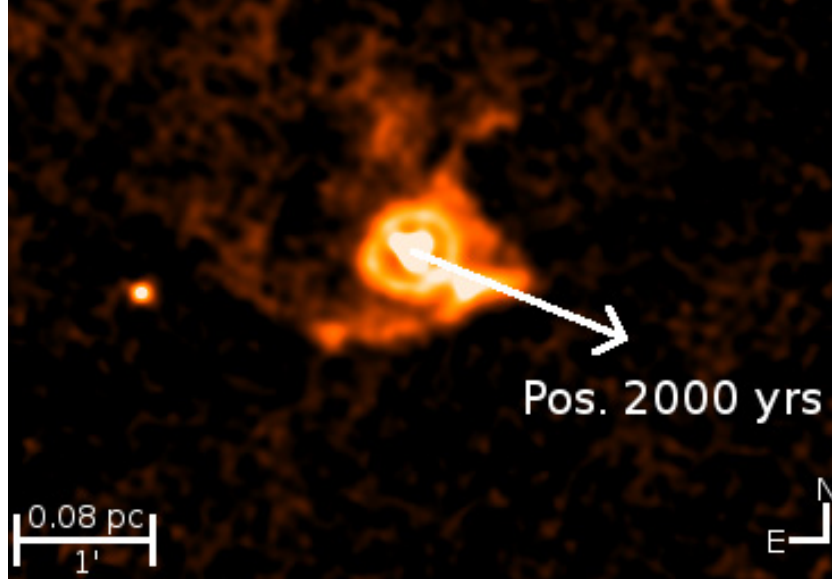


FIGURE 1.9: Herschel/PACS observations of the thermal dust emission of TX Psc at $70\,\mu\text{m}$. A spherical shell can be seen at a radius of $\sim 17''$, which is surrounded by the wind-ISM interaction region in direction of the space motion (shown with white arrow). The location of the star after 2000 yr of motion is indicated with the length of the arrow (Jorissen et al. 2011).

In the IRAS color-color diagram, TX Psc lies in the region of stars with detached dust shells, although the IRAS low-resolution spectrum has been classified as featureless (Jorissen et al. 2011). The most recent study of the IR dust emission of TX Psc has been made within the Herschel guaranteed time key observing programme MESS (Groenewegen et al. 2011) and is presented by Jorissen et al. (2011). Within this observing programme, Herschel PACS images at 70 and $160\,\mu\text{m}$ have been taken for TX Psc, and the interaction region of the dusty CSE with the ISM are analysed.

Figure 1.9 shows the deconvolved Herschel PACS $70\,\mu\text{m}$ image of the thermal dust emission around TX Psc, revealing an asymmetric interaction front with the ISM and – well behind that and separated from it – a shell-like structure with a size of $\sim 17''$ around the central peak emission of the star itself. This dusty shell can not be caused by interaction with the ISM and has to be originating from the stellar wind itself. On much smaller spatial scales, asymmetries towards the direction of space motion are detected through adaptive optics and lunar occultation observations in the K band, respectively (Cruzalebes et al. 1998; Bogdanov 1997, the latter interpreting the results as proof for binarity).

The molecular CSE of TX Psc has not yet been observed in much detail, since only single-dish observations of CO (1–0) and (2–1) have been carried out so far (Olofsson et al. 1993; Heske et al. 1989; Heske 1990). No detailed geometry of the molecular CSE could be measured, but Heske et al. (1989) report CO (2–1) and CO (1–0) emission at an offset of about $20''$ from the star in all four directions of the sky, as observed with the IRAM 30 m telescope (see Fig. 1.10). The CO (1–0) emission line is slightly asymmetric for some of the offset pointings, and higher spectral resolution observations reveal a two component spectral line profile with a narrow peak and broader underlying component (Heske 1990). The circumstellar CO gas around TX Psc is most likely clumpy and a bipolar shape of the emission can not be excluded. More recent CO (3–2) observations made with the SEST (Schöier & Olofsson 2001)

reveal a similar line profile as for the lower transitions, making detailed radiative transfer analysis impossible due to the line complexity and large uncertainty in estimated wind velocities (from 7.5 to 12.2 km/s).

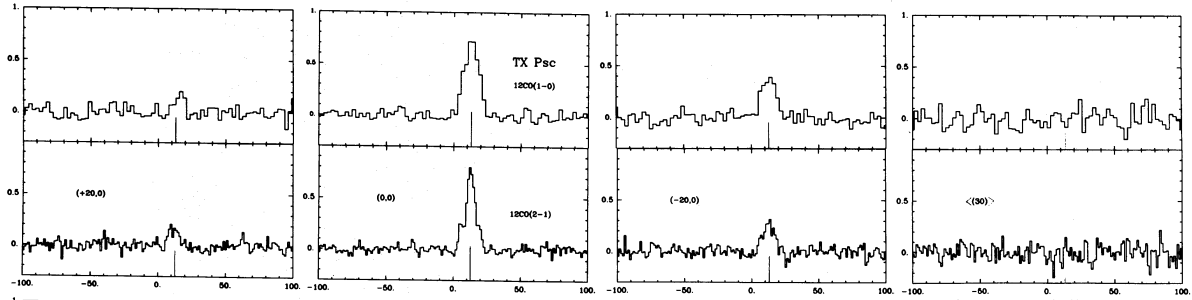


FIGURE 1.10: Molecular CO (1–0) (top row) and CO (2–1) (bottom row) emission of TX Psc observed with the IRAM 30 m telescope. The center-left panel shows the emission received from the central pointing on the stellar position, while the left and center-right panels show the emission at west and east offsets of $20''$, respectively. The right panel shows the direction averaged emission at offsets of $30''$.

In **Paper II** (see Chapter 5) I present high resolution ALMA observations of the CO(2–1) emission around TX Psc, focusing on the analysis of the molecular counterpart to the already detected dusty shell structure. A clearly elliptical and additionally filamentary detached molecular shell is detected around TX Psc, which adds it to the sample of known detached shell sources. From an evolutionary point of view, this detached shell is particularly interesting due to the fact that TX Psc has the lowest C/O ratio of all carbon stars hosting detached shells, which puts it very close to the transition stage between oxygen and carbon chemistry, which is represented by the S-type stars with C/O ratios close to 1. This, together with the unexpected and unprecedented ellipticity of the detached shell, deserves thorough investigation with respect to detached shell formation scenarios and the general mass-loss history of TX Psc.

1.4.3 R Sculptoris

R Sculptoris (R Scl) is a well studied, semi-regular carbon rich AGB star with a pulsation period of ~ 370 days (Knapp et al. 2003) and a C/O ratio of 1.34 (Bergeat & Chevallier 2005). The distance estimates to R Scl range from 266 pc (revised Hipparcos distance Knapp et al. 2003) to 370 pc (from Period-Luminosity relationships Knapp et al. 2003; Whitelock et al. 2008). R Scl is surrounded by a detached shell, which has been observed and addressed in multiple studies in molecular gas emission (e.g. Olofsson et al. 1990, 1996; Maercker et al. 2012) as well as dust emission through scattered light (e.g. González Delgado et al. 2001, 2003; Olofsson et al. 2010; Maercker et al. 2014) and thermal dust emission (Cox et al. 2012). R Scl was the first AGB star to be observed by ALMA in high resolution CO emission, and additionally to the first resolved mapping of the thin detached shell the observations revealed a very surprising spiral structure, extending from the star to the detached shell (see Fig. 1.11, Maercker et al. 2012). This spiral structure is a clear indication for wind-binary interaction, meaning that R Scl possesses a previously unknown binary companion, which is in a close enough orbit to interact heavily with the expelled stellar wind. The detached shell itself has a radius of $19.5''$, a width of roughly $2''$ and the distribution of gas and dust is highly correlated (see Fig. 1.12, Maercker et al. 2014). The expansion velocity of the gas in the shell is

14.5 km/s, leading to an approximate expansion age of the shell of 2300 yr for a distance of 370 pc.

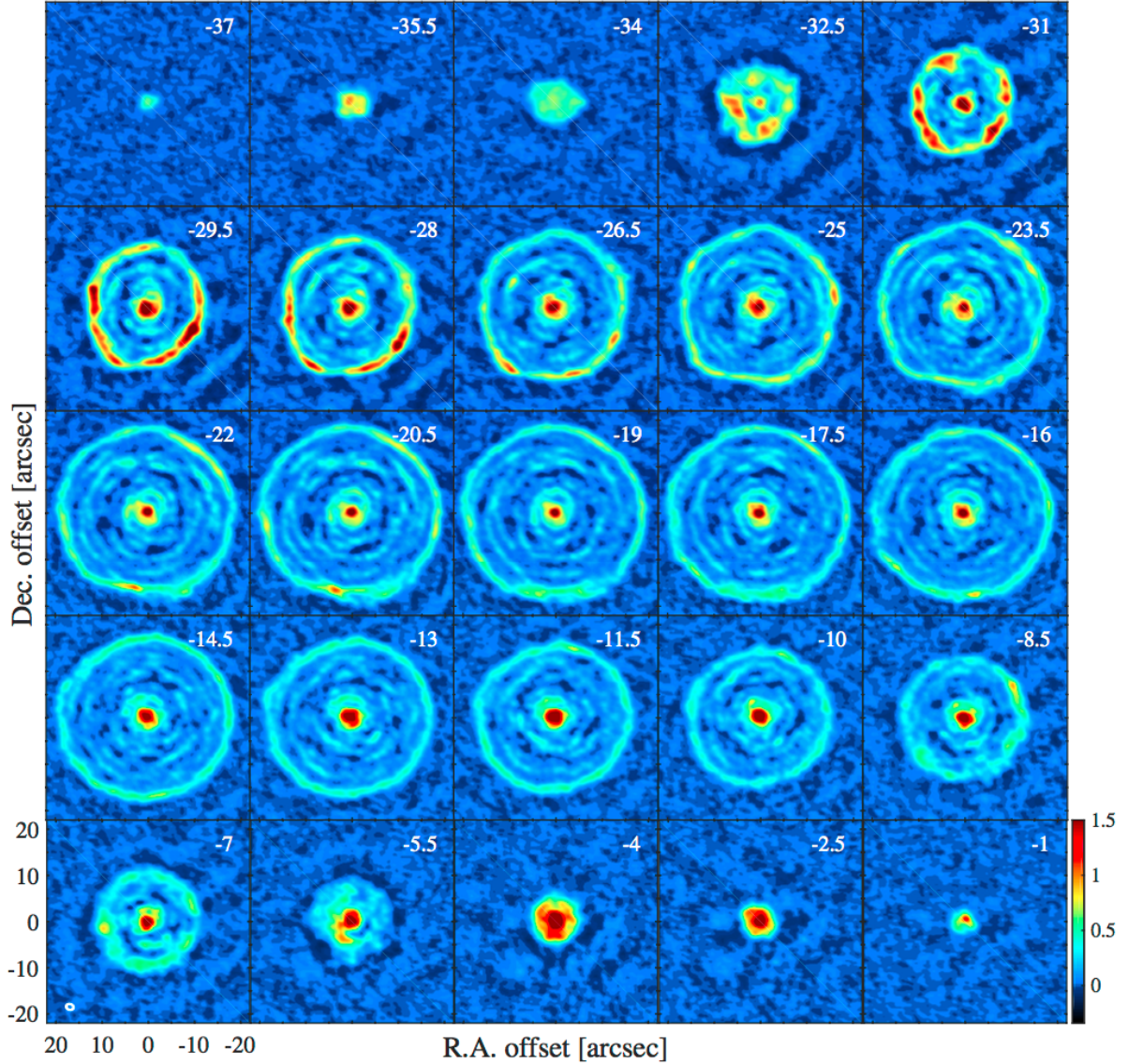


FIGURE 1.11: ALMA observations of the CO(3–2) line in the CSE of R Scl. The velocity binning is 0.5 km/s and the individual panel spacing is 1.5 km/s. The stellar velocity is ~ 19 km/s (middle panel) and the beam size is shown in the lower left panel as white ellipse. The colorscale is given in Jy/beam (Maercker et al. 2016).

Paper III (see Chapter 6) presents a study of dust radiative transfer modelling of the detached shell, examining the dust grain properties and respective dust shell masses needed to reproduce the SED of R Scl from the optical to sub-mm wavelengths. In this publication we tried to quantify which dust grain properties influence the SED and dust shell mass the most, in order to estimate the general uncertainties of derived dust masses. In **Paper VI** (see Chapter 9) all details of the ALMA molecular CO observations of the CSE of R Scl are summarised and radiative transfer models to determine the mass-loss rate and its evolution are presented. An additional study to determine the distance to R Scl independently by measuring the light echo of the stellar pulsation reflected in the detached shell is given in **Paper VII** (see Chapter 10).

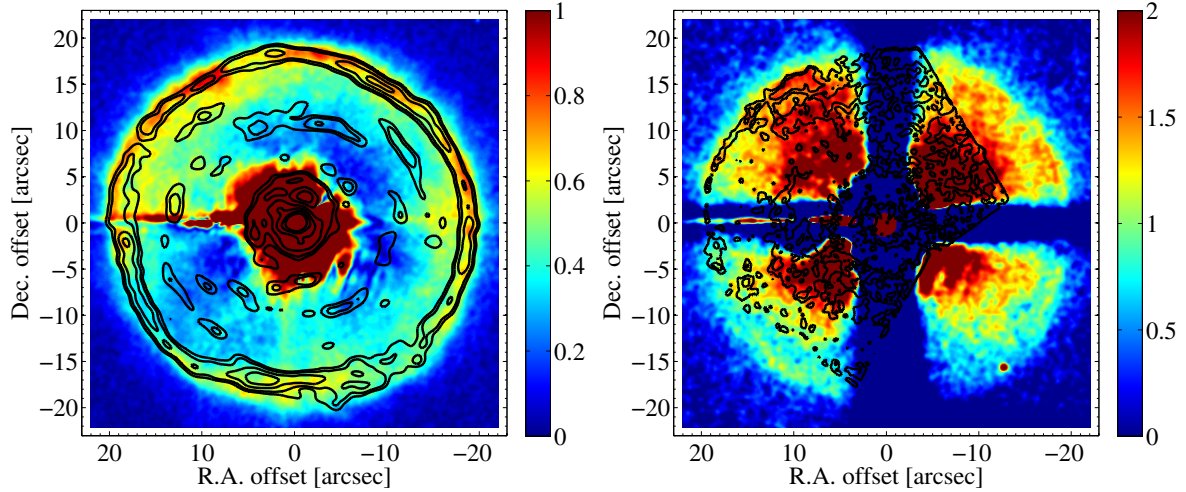


FIGURE 1.12: Left: Comparison between polarised light observations of the dust scattered light (PolCor polarised intensity in the R-band; colorscale) and molecular line observations at stellar velocity (ALMA CO(3–2); black contours) of the CSE around R Scl. Right: Polarised total intensity image (PolCor; colorscale) compared to optical scattered light observations (*Hubble* Space Telescope at $0.8\,\mu\text{m}$; black contours) (Maercker et al. 2014).

1.4.4 U Antliae

U Antliae (U Ant) is a carbon star with irregular variability, located at a distance of 260 pc (Knapp et al. 2003). It has a C/O ratio of 1.44 (Bergeat & Chevallier 2005) and is surrounded by a well studied CSE and detached shell, which has been observed multiple times over the last two decades. Previous studies cover low resolution single-dish observations of molecular gas (Olofsson et al. 1996; Maercker et al. 2010) followed by radiative transfer modelling (Schöier et al. 2005), intermediate resolution infrared observations of thermal dust emission (Kerschbaum et al. 2010; Cox et al. 2012), high resolution optical observations of scattered light on dust grains (González Delgado et al. 2001) and of polarised light (González Delgado et al. 2003; Maercker et al. 2010). The conclusions of the previous observations are that U Ant is surrounded by a molecular detached shell of gas at a radius of $43''$ (see Fig. 1.13), while there is at least one additional dust dominated shell located at a radius of $50''$. Furthermore, the dust-scattered light observations show a complicated mix of multiple shell-like or arc-like structures at different radii (see Fig. 1.14). The molecular gas shell expands with a velocity of $\sim 19.8\,\text{km s}^{-1}$, which results in an approximate age of the shell of 2700 yr.

New high resolution ALMA observations of the molecular CO(2–1) and CO(1–0) emission of the CSE around U Ant are presented in **Paper IV** (see Chapter 7) of this thesis. The detached shell is imaged in high detail, revealing the fine filamentary structure of the thin shell, resulting from possible hydrodynamical instabilities in the formation process. Although the shell around U Ant can be considered to be a “classical” detached shell, details like the seemingly double shell structure are interesting to explore and can lead to a better understanding of the interacting processes and physical phenomena during detached shell formation.

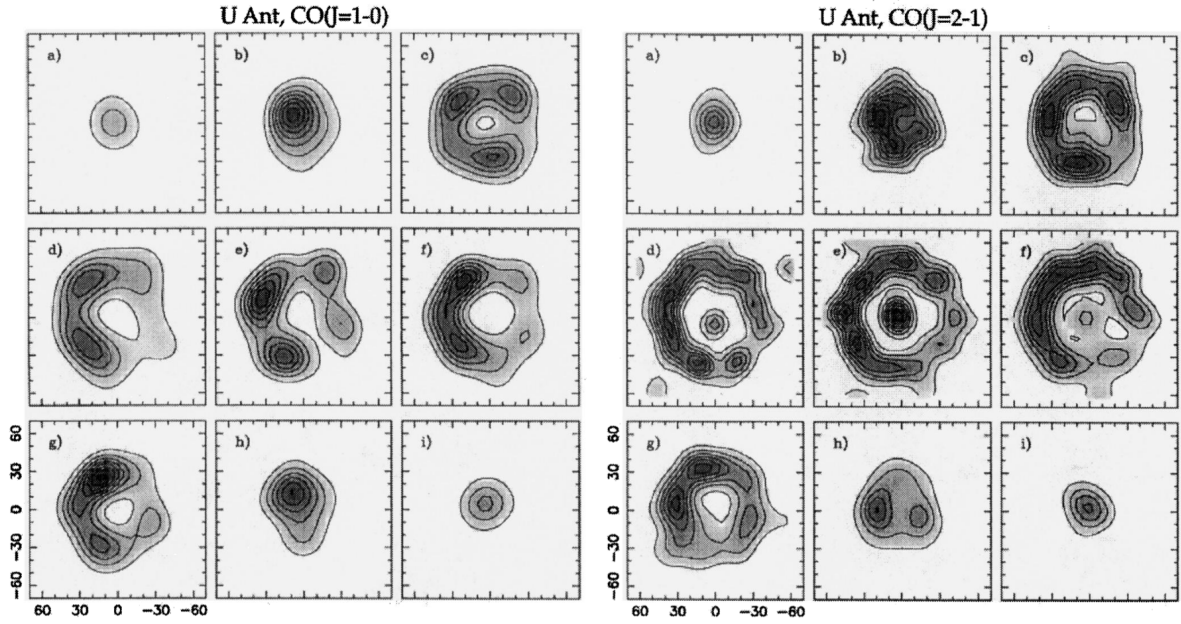


FIGURE 1.13: Single-dish SEST observations of the molecular CO(1–0) (left) and CO(2–1) (right) emission of the CSE and detached shell around the carbon star U Ant. The different panels correspond to different gas expansion velocities (i.e. a doppler shift of the molecular line); the central panel represents the local rest frame at stellar velocity (Olofsson et al. 1996).

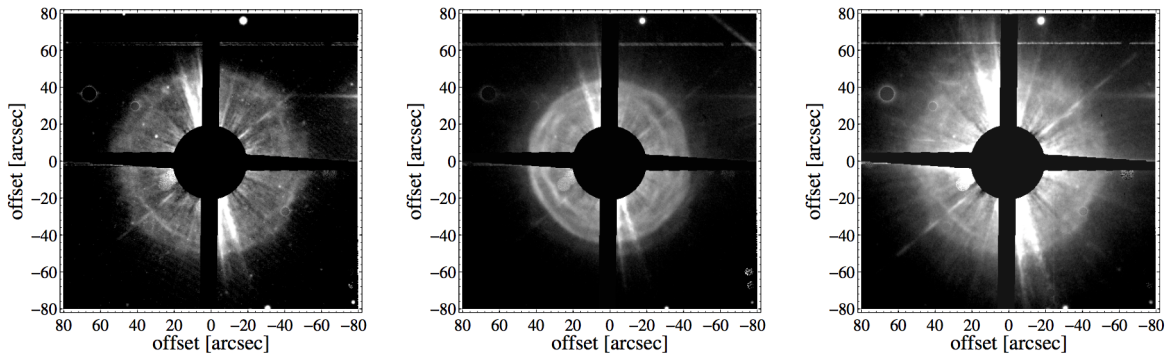


FIGURE 1.14: Dust scattered light observations of the CSE around U Ant, observed with EFOSC2 at the ESO 3-6 m telescope. The three panels show the total intensity images of the Str- γ , F59 and H α filters, respectively. The star is covered by a coronagraph to allow imaging of the faint CSE and the multiple shell- or arc-like structures within (Maercker et al. 2010).

Chapter 2

Equipped with his five senses, man
explores the universe around him and
calls the adventure Science.

Edwin Hubble

Observational methods

This dissertation is based on the observational investigation and subsequent analysis of circumstellar envelopes around AGB stars. The majority of observations discussed within this thesis have been carried out in the submillimeter wavelength regime with the Atacama Large Millimeter/submillimeter Array (ALMA), but additional complimentary observations have been carried out with other instruments as well. In this chapter I summarise the different observing techniques and instruments relevant for the core publications of this thesis.

2.1 Millimeter/submillimeter interferometry with ALMA

The millimeter and submillimeter wavelength range offers detailed insight in the molecular gas distribution of cool stellar environments, where rotational and vibrational molecular line transitions occur. One drawback of observations at long wavelengths is that the resolution of a telescope scales with the observed wavelength. The angular size of the resolution element, θ , scales as

$$\theta \propto \frac{\lambda}{D}. \quad (2.1)$$

This means that the longer the observed wavelength, the bigger the resolution element and therefore the lower the angular resolution of the observed brightness distribution. The angular resolution of a telescope is proportional to the telescope size, and while building bigger and bigger telescopes is the natural way to improve the resolution, this is not effective enough at long wavelengths, such as the in the submillimeter regime, to balance the decrease in resolution due to the wavelength dependency itself. As an example, the upcoming and highly ambitious Extremely Large Telescope (ELT)¹, operating in the optical wavelengths around 550 nm, will have a diameter of approximately 40 m, resulting in an angular resolution of roughly 0.0034". A submillimeter telescope, operating at a wavelength of 870 μm , would have to have a diameter of roughly 64 km to achieve the same resolution as the ELT, which is more than unrealistically large. Therefore, the advanced observing method of interferometry has to be invoked to achieve a similar angular resolution in the millimeter/submillimeter regime as in optical wavelengths.

The principle of interferometry is based on the wave-like optical properties of electromagnetic radiation and its capacity of creating interference patterns of two (or more) incoming waves. The interference patterns can be linked to the origin and shape of the incoming waves via the mathematical concept of Fourier transformation. In astronomically applied interferometry, multiple telescopes act together as large-scale interferometer, where each telescope

¹<https://www.eso.org/public/unitedkingdom/teles-instr/elt/>

pair is used to create an interference pattern between the incoming waves of the observed electromagnetic radiation from observed astronomical objects. Figure 2.1 shows two schematic telescopes detecting the wavefront of an incoming signal at a distance – or baseline – of b from each other and under an inclination angle of θ . Since the wavefront is arriving earlier at telescope 2, because of the geometric alignment of the two telescopes, there is a phase difference τ_g , or geometric delay, between the two detected signals. This phase difference contains the position information of the observed object. The two detected waves V_1 and V_2 are brought to interference at a mixer, and after time averaging at the complex correlator, the interference pattern R is created (only the real part of the signal is shown in Fig. 2.1). This interference pattern can be described by quantities of the so-called complex visibility, whose real and imaginary parts are measured by the complex correlator and can be used to derive the visibility amplitude and phase. The basic theorem of interferometry is that the visibility of an interference signal represents the Fourier transform of the sky-brightness distribution, which makes it possible to extract source brightness information from the correlated signals of an interferometer.

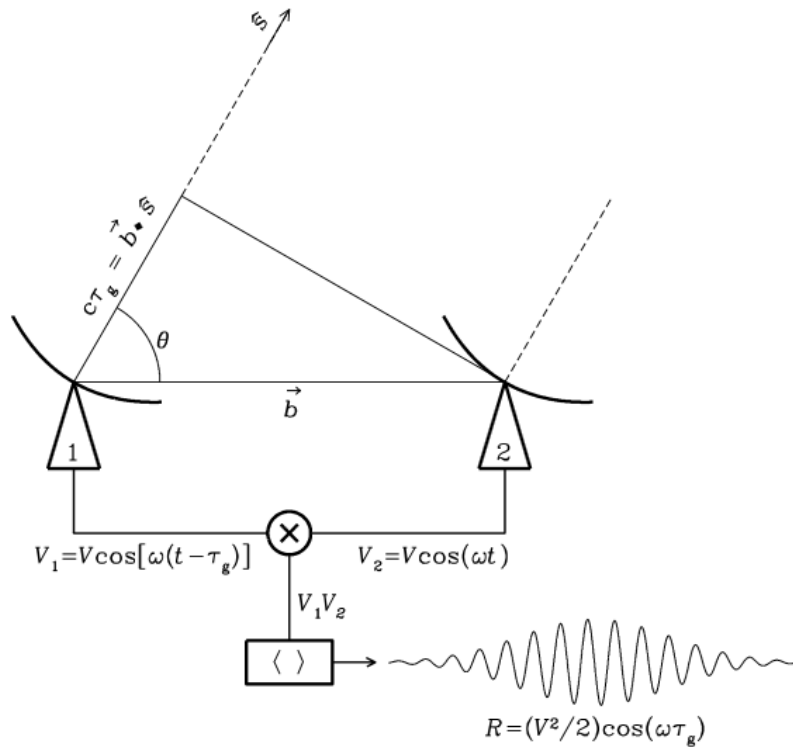


FIGURE 2.1: Schematic view of a simplified two-telescope interferometer. Image credit: J.J. Condon and S.M. Ransom, Essential Radio Astronomy course

For an interferometer array, not only consisting of two but significantly more telescopes, the two-dimensional visibility information can even be used to reconstruct images, at much higher resolution than possible with the individual telescopes of the interferometer array. The essential parameter for the determination of the effective spatial resolution is now not the diameter of an individual telescope of the interferometer, but the distance between the two individual telescopes, called baseline, b . The spatial resolution now scales as

$$\theta \propto \frac{\lambda}{b}, \quad (2.2)$$

which immediately shows the potential to increase the spatial resolution at long wavelengths significantly by increasing the baseline lengths between the telescopes of an interferometer. This technique is very efficient at long wavelengths, where the big advantage compared to short wavelengths (e.g. optical and near-infrared interferometry) is that the incoming signal can indeed be received as wave pattern, with amplitude and phase, which can be coherently recorded and manipulated with submillimeter/radio techniques. This is not possible for radiation at short wavelengths, i.e. high frequencies, where signals cannot coherently be recorded as wave and have to be manipulated in real time, posing bigger instrumental challenges.

In theory, a single telescope can be considered to be a perfect interferometer with an infinite number of highly redundant baselines, composed of the difference of all points on the telescope surface to each other. To achieve images with comparable quality from interferometers with a strictly limited number of baselines, initial assumptions about the observed brightness distribution have to be made in order to reconstruct the image from the visibilities, which introduces artefacts and uncertainties. Interferometers with a large number of baselines, which are distributed in a non-redundant way within the telescope array, are able to recover better images than interferometers with a sparse distribution of baselines. The attempt to recover preferably all possible baselines with all possible lengths is called aperture synthesis, and since the effective baselines are the projected baselines as seen from the observed source, the Earth's rotation helps to recover more and more baselines over the total observing time.

An important point to make is that an interferometer with an incomplete sample of baseline lengths is essentially filtering out emission with spatial sizes corresponding to the hypothetical resolution achieved with the missing baselines. This effect can be seen in Fig. 2.2, where simulations of interferometric observations of the same object with different interferometer array configurations, i.e. different baselines, are shown. Therefore it is not desirable to build an interferometer with just the longest possible baselines, but a balanced selection of baselines in unique configurations is to be preferred.

2.1.1 ALMA – Atacama Large Millimeter/submillimeter Array

The Atacama Large Millimeter/submillimeter Array (or short: ALMA) is an interferometer operating in the millimeter/submillimeter wavelength range, consisting of a total of 66 individual telescopes, which are also called antennas. ALMA is operated under the partnership of the European Southern Observatory (ESO; Europe), the National Radio Astronomy Observatory (NRAO; North America) and the National Astronomical Observatory of Japan (NAOJ; East Asia). It is located at the Chajnantor plateau in the Chilean Atacama desert, South America, at an altitude of approximately 5000 m, and is operated from the lower altitude Operations Support Facility (OSF) at around 2900 m. Since the Earth's atmosphere is the declared enemy of any astronomical observation, and the atmospheric transmission is especially bad in the submillimeter regime, this very high and extremely dry observation site improves the observation quality immensely. Nevertheless, the operation of a complex facility, such as ALMA, at such a remote location, is not an easy endeavour to undertake, further underlining the absolute requirement of international collaboration, funding and organisation.

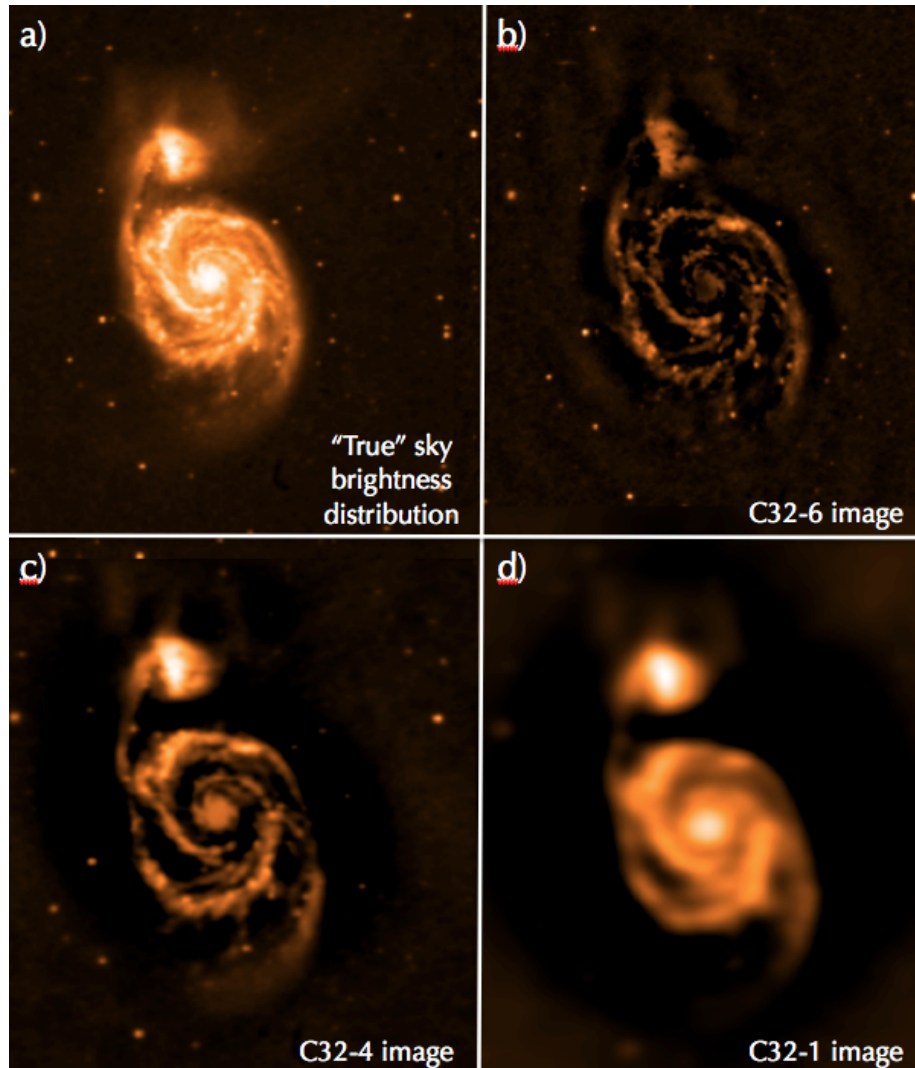


FIGURE 2.2: Simulated ALMA observations of M51 with different array configurations, consisting of different baseline lengths, to show the effect of “spatial filtering”. Panel a) shows an optical image of M51, panel b) simulated ALMA observations with long baseline configurations, panel c) simulated ALMA observations with intermediate baseline configurations, and panel d) simulated ALMA observations with short baseline configurations. Image credit: ALMA Cycle 3 Technical Handbook

To optimise the baseline coverage, ALMA is split into three different parts: the main array, consisting of up to 50 telescopes with a diameter of 12 m, distributed on baselines from 15 m up to 16 km, the Atacama Compact Array (ACA), consisting of 12 telescopes with a diameter of 7 m and baselines from 9 m up to 45 m, and the Total Power (TP) array, consisting of four telescopes with 12 m diameter, which are not observing as interferometer but provide complimentary data of the so-called zero spacings (i.e. “baselines” of 0 m). The ALMA main array telescope configuration is in regular rotation, providing different spatial resolutions depending on the observing time, and its telescopes are transported to fixed locations at the observing site. The ACA is permanently in its compact configuration, as well as the stationary TP telescopes. Figure 2.3 shows the ALMA operation site from above.



FIGURE 2.3: ALMA operation site from above. A collection of main array (12 m) telescopes is visible spread out over the image, while the ACA (7 m) telescopes are clustered in its compact configuration in the center of the image. The triangular structures on the ground mark alternative main array telescope locations for different baseline configurations. Image credit: Clem&Adri Bacri-Normier (wingsforscience.com)/ESO

The total number of available telescopes in the main array varies due to technical maintenance and adjustments, and the exact available number is announced for each observing cycle. The achieved spatial resolution of ALMA observations does not only depend on the array configuration and maximum baseline length, but also the observed frequency enters the equation again. ALMA currently offers 8 different receiver bands from 85 GHz (start of Band 3) to 950 GHz (end of Band 10), which are optimised for atmospheric transmission windows. The maximum achievable spectral resolution ranges from 20 milli-arcseconds (mas) to 43 mas for the longest possible baseline of 16 km and frequencies of 230 GHz and 110 GHz, respectively. Note that the spectral bands with higher frequencies currently cannot be used for the longest baseline configuration. The highest achievable spectral resolution, at an observing

frequency of 110 GHz, is 3.8 kHz (or $R = 30,000,000$) and translates to a velocity resolution of 0.01 km/s.

Since ALMA is currently the most powerful and best millimeter/submillimeter interferometer of the world, the competition to get access to observing time is very high. A call for proposals is publicly announced once a year, and the proposal process is handled via a specifically developed software tool, the ALMA Observing Tool (OT), with which proposals have to be generated and submitted. In addition to the scientific justification of the proposal, also the intricate technical observation details have to be specified precisely beforehand. Although ALMA aims to be accessible to the entire astronomical community, it still requires a basic level of experience with interferometry to be used efficiently. Hence, especially for non-expert users, an extensive support structure has been developed. In Europe, this structure consists of a network of ALMA Regional Centre (ARC) nodes, coordinated by the central ARC at ESO. The ARC nodes provide help from the submission of a proposal to the data reduction and analysis of ALMA datasets. All relevant and up-to-date information about the scientific use of ALMA can be found on the website: <https://almascience.eso.org>.

2.1.2 Observing techniques

Depending on the science case, different observing strategies and techniques can be chosen with ALMA. Its main advantages are the high spatial resolution and sensitivity, combined with high spectral resolution. This means that ALMA does not only deliver high resolution two-dimensional image data, but it can also operate at a whole range of frequencies at the same time. The data output therefore is a three-dimensional (3D) data cube, where each slice through the cube can translate to an image at a certain frequency. The field of view (FOV) of ALMA is limited by the size of the individual telescopes in the array, and for an observing frequency of 300 GHz, the FOV is roughly 21'' for the 12 m main array telescopes, and 35'' for the ACA 7 m telescopes, respectively. Based on these conditions, the below described observing strategies can be distinguished:

Array configuration and combination

The array configuration is determined through two parameters: the smallest source structure to be resolved, which results in the requested angular resolution, and the largest structure of the observed source. The requested angular resolution at the requested wavelength will define the maximum baseline lengths needed to achieve this resolution. If the required baselines are very short (<45 m), then the ACA is sufficient for the observations. Otherwise, the main array has to be used for the observations. Since the shortest baselines within the used array configuration will determine the maximum recoverable scale (MRS), it is important to check whether the (assumed) source brightness distribution to be observed exceeds this MRS or not. If the largest source structures are smaller than the MRS of the used main array baseline configuration, the main array alone is sufficient to recover the source brightness distribution. If the largest source structure exceeds the MRS, the interferometer filters out emission, and additional short baselines, provided by the ACA and TP array are needed to recover the full source brightness distribution. Therefore, the choice of used arrays and baselines has to be carefully checked and motivated by the source structure. Since AGB CSEs are very large structures, but at the same time exhibit intricate small-scale structures as well, the optimal observing strategy is to combine long baselines from a main array configuration with supplementing shorter ACA (and TP) baselines. This was already illustrated in Fig. 2.2. Within this thesis, this

combination of arrays was done for all ALMA observations, except for the observations of R Scl presented in Papers III and VI (Chapters 6 and 9), where the ACA was not yet available at the time of the observations.

Single pointing vs. mosaic

If the observed source size exceeds the FOV, a single pointing observation will not recover the whole source brightness distribution. As long as only the central parts of the source are subject to the scientific investigation, this can still be a viable observing technique. But since the primary beam sensitivity decreases from center to the edges, the source brightness distribution can only be reliably mapped at the center of the image. Therefore it makes sense to observe in mosaic mode, where a grid of overlapping pointings is used to create a larger map of the observed source with reliable brightness distribution over the mosaic (except the very edges of mosaics). Naturally, the observing time increases proportionally to the number of mosaic pointings, and technical overheads have to be included as well. Since the CSEs of the sample of AGB stars covered in this thesis are larger than the FOV of ALMA, all ALMA observations reported in this thesis are done in mosaic mode.

Spectral lines vs. continuum

Regarding the spectral setup, it is important to distinguish between observations of spectral lines and continuum emission. While continuum emission is the integrated emission over a relatively broad spectral range, requiring a large bandwidth of observation but low spectral resolution, the observation of spectral lines requires small bandwidths and high spectral resolution. The continuum emission of an astrophysical object in thermal equilibrium follows approximately a blackbody spectrum and represents mostly the dust within these objects at the ALMA wavelengths. On top of the continuum, atoms and molecules radiate at distinct and narrow wavelengths, excited due to interaction of the particle with photons or other particles. In the submillimeter wavelength regime, excitation through rotation and vibration is the source for spectral lines of molecules, which can be found in the CSEs of AGB stars. Each individual spectral line of a certain excitation state of a molecule has a fixed frequency, which is called frequency of rest. As soon as an object, which is emitting radiation or any kind of wave (e.g. light or also sound), is under motion, the emitted frequency of the wave changes. This is known as the Doppler-effect or Doppler-shift, and objects moving towards the observer will emit shorter waves and exhibit blue-shifted spectral lines, while objects moving away from the observer will emit longer waves and exhibit red-shifted spectral lines. This effect can be used to map the velocity of molecular gas distributions, if observations are done at multiple wavelengths with sufficient spectral resolution. All reported ALMA observations in this thesis have been carried out in spectral line mode to investigate the 3D velocity structure of different molecular species in AGB CSEs. Generally, if spectral line observations have been carried out, the line-free frequency channels of the observed datasets can still be used to create a continuum image by averaging over many spectral channels.

2.1.3 Data reduction

As an interferometer, ALMA does not deliver conventional images as direct data products, but instead the visibility phase and amplitude for every observed baseline, frequency, and timestamp are the measured quantities, which are tabulated and stored in an accessible table format, called measurement set. The general flow of data is the same for all observing techniques, and

is schematically shown in Fig. 2.4. Since the observed and correlated signals can be recorded coherently, all kinds of data manipulation and reduction can be carried out from archived data and do not have to be done in real time. Each ALMA dataset goes through the so-called ALMA data reduction pipeline, which is a semi-automated pipeline for all data reduction steps from raw data to science-ready images. In principle, the pipeline reduced datasets and images should be of good enough quality for scientific analysis, but many observing projects can profit from additional, careful data reduction, optimised for the individual science case.

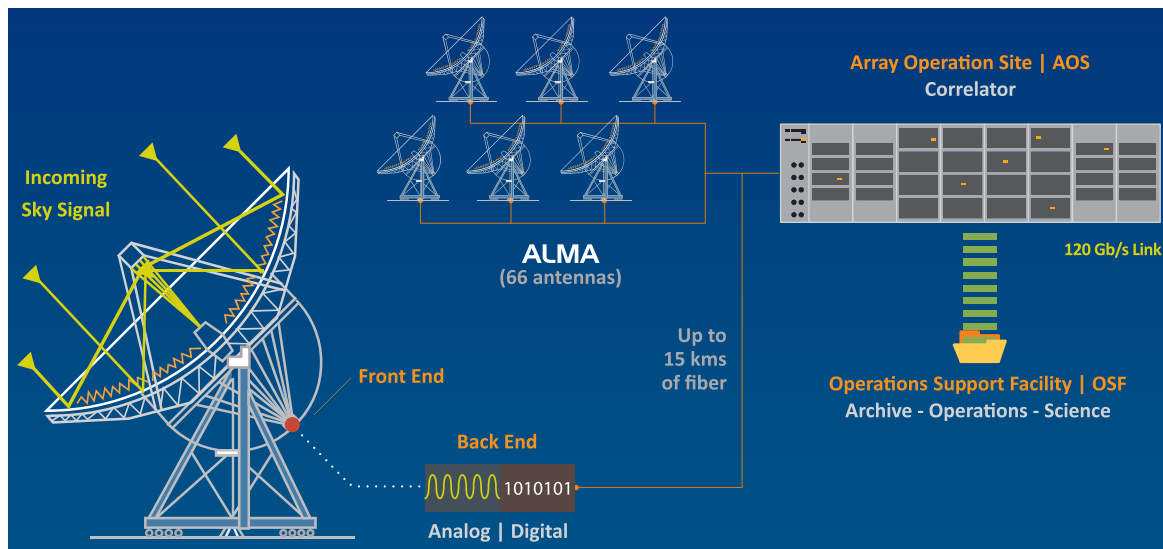


FIGURE 2.4: Schematic view of the data collection process with ALMA. Image credit: ESO

The official software developed for ALMA data reduction is called Common Astronomy Software Application (CASA)², and is capable of calibration, deconvolution³ and visualisation of interferometric data. It is operated by calling specified CASA tasks via the commandline, and allows data inspection in several different graphical user interfaces (GUIs) as well as data export to other file formats. The CASA terminal is an interactive python environment, which also allows the execution of scripts, which can either be user-defined or for example downloaded scripts from the ALMA pipeline, to re-do data reduction from scratch.

In principle, interferometric data reduction can be divided into two parts: data calibration and imaging, which are shortly discussed below.⁴

Calibration

Just as any other astronomical observation, ALMA observations are subject to a number of different contaminations and uncertainties, influencing the real source signal and reducing the signal-to-noise ratio as well as the general data reliability. Any instrument or medium, which is put between the light source and observer – or more accurately detector – is diverting the signal, and even the detector system itself introduces deviations from the real source signal. In order to calibrate the data, a set of calibration measurements has to be made, to be sure of the nature and variability of the effects to be calibrated for. To this end, either well known stars or

²<https://casa.nrao.edu>

³In interferometry, deconvolution is the term used to describe the attempt to disentangle the real source brightness distribution from artefacts and image effects introduced by the observing array itself.

⁴For a more detailed description of the data reduction process of ALMA data with CASA, I refer to my master's thesis, "ALMA observations of R Sculptoris", available on <http://othes.univie.ac.at/29335/>

comparable objects are regularly observed during an observing run, to create a reference frame for all observed data, or additional instruments, such as for example water vapour radiometers (WVRs), are used to measure certain observing conditions, in this case the real-time humidity and therefore transmission of the atmosphere. The most important calibrations to be done are bandpass calibration, amplitude and phase calibration, and absolute flux calibration:

Bandpass calibration is the correction for the frequency dependency of the receiver system, which has a slightly different transmission of incoming radiation for different frequencies. This is done by the observation of a calibrator object with a well known and well behaving spectral energy distribution at the observed wavelength as reference to correct for any sensitivity shifts of the receivers with frequency. Bandpass calibration has to be done for each baseline.

Amplitude and phase calibration has to be done to correct for the time-dependent amplitude and phase shift in the observing system, which are mostly introduced by fluctuations in the atmospheric transmission, which can change both amplitude and phase of the incoming signal. A well known, unresolved (i.e. point-like) calibrator source, with a relatively stable amplitude and phase over the whole observing run, is observed regularly in between the observations of the scientific object to determine the amplitude and phase shift of the signal. Additionally, also the observing system itself may be subject to time-dependent amplitude and phase gain shifts, which makes it necessary to carry out the amplitude and phase calibration for each baseline.

Absolute flux calibration is necessary to convert the arbitrary flux units of the receiver system to real flux densities, which then can be measured and interpreted correctly for the observed scientific object. The flux calibrator can be any object with a well known flux density, and apart from point-like sources like quasars, also objects from the solar system, such as planets, moons or asteroids, can be used. Flux calibration is usually not time dependent, so a flux calibrator has only to be observed at the start of the observing run. It is, however, very dependent on the receiver system, and therefore has to be carried out for each baseline.

Imaging

Once the interferometric data, that is the visibilities, are calibrated, they are ready for the imaging process, during which visibilities are converted into 2D brightness distributions of the source signal. For an ideal interferometer, covering all possible baselines, this process would resemble a pure Fourier transform, and recover the true source brightness distribution. In our less ideal case of a restricted number of telescopes and distinct array configurations, this process becomes a bit more complicated, and without initial assumptions of the source structure, the real brightness distribution cannot be recovered free from image artefacts. Similar to each individual telescope, also the whole interferometric array has a certain point-spread function (PSF), i.e. a certain 2D sensitivity to recover a point source, deviating from the real source structure. This array PSF is also called “dirty beam”, which can and has to be subtracted from the images by deconvolution to try to get as closely as possible to the real source brightness distribution. The CASA task to accomplish the Fourier transform from visibilities to image data, and then the subsequent deconvolution of the dirty beam (and individual telescope PSF), is called “clean”. It relies on the CLEAN algorithm, which was developed by Högbom (1974). CLEAN is usually executed in several iterations, reconstructing more and more of the original source brightness distribution with each iteration. At each step, a small number of point sources is fitted to the emission maxima in the dirty image, these point sources are convolved with the dirty beam, and they are subsequently subtracted from

the dirty image to be transferred to the clean image. The residuals undergo additional iterations of CLEANing, until a pre-defined residual flux threshold is reached. This technique has proven to be very reliable for simple and compact sources, but the more complex the original source brightness distribution gets, the more artefacts are introduced in the final deconvolved image. To improve the deconvolution of complex sources, a CLEAN mask can be introduced, specifying an area of the image where real source emission is expected to be located. The CLEAN algorithm will only subtract and deconvolve point sources from the masked region, avoiding the accidental CLEANing of noise and artefacts introduced by the dirty beam.

A special note has to be made about imaging datasets consisting of different array configurations, as well as on the combination of ACA and TP arrays with the main array: while the visibilities of arrays with a different configuration but the same telescope diameter can easily be combined to achieve images with a better baseline coverage and less artefacts, the combination of visibilities from different arrays with different telescope diameters adds additional problems regarding the sensitivity of different telescope-specific PSFs, especially towards the edges of the FOV, and creates the need for a consistent weighting scheme between the different arrays. The combination of TP data to interferometric data poses another challenge, which is based on the fact that either artificial visibilities have to be created from non-interferometric data, or already imaged interferometric data has to be combined with TP images in the image plane.

Generally, images created from interferometric observations have to be analysed with care, always being aware of the fact that image deconvolution has an impact on the exact outcome of the final image.

2.2 Other observational methods

In addition to interferometric observations with ALMA, the below introduced observing methods have been used to obtain data, related to this dissertation.

2.2.1 Submillimeter photometry with APEX

The Atacama Pathfinder EXperiment (APEX)⁵ is a single-dish telescope prototype of one of the ALMA 12 m telescopes, and has been taken into operation in 2005. It is a collaboration between the Max Planck Institut für Radioastronomie (MPIfR), the Onsala Space Observatory (OSO), and the European Southern Observatory (ESO), and is situated at a location close to ALMA. Since it is a prototype for ALMA, it has the same telescope specifics and sensitivity. There are currently two available stationed instruments at APEX, LABOCA and SABOCA, and a whole number of PI instruments can be mounted to the telescope with approval and collaboration with the respective PI groups. For the analysis of the spectral energy distribution (SED) of R Sculptoris, as discussed in **Paper III** (Chapter 6), I used continuum photometry data from LABOCA.

The Large APEX BOlometer CAmera (LABOCA, Siringo et al. 2009) is a bolometer array with 295 pixels, operating at 345 GHz (or $870\ \mu\text{m}$), and with a spectral bandwidth of 60 GHz (or $150\ \mu\text{m}$). It has a spatial resolution of $18.6''$ half-power beam width (HPBW) and a FOV of $11' \times 11'$. LABOCA is used for continuum observations and allows an optimised

⁵<http://www.apex-telescope.org>

raster mapping setup for the observation of extended sources with a homogeneous coverage of $15' \times 15'$.

2.2.2 Infrared photometry with *Herschel*

The *Herschel Space Observatory* (*Herschel*, Pilbratt et al. 2010)⁶ is a space-based telescope with a 3.5 m primary mirror, observing from the near-infrared (NIR) to the submillimeter wavelengths. It is located at the stable Lagrange point L2, i.e. on an orbit between the Earth and Sun at approximately 700,000 km distance, and is operated by the European Space Agency (ESA). It is named after the scientist Friedrich Wilhelm Herschel (1738 – 1822), who discovered the infrared radiation in 1800 together with his sister Caroline Herschel. The *Herschel* telescope was used to observe the cold Universe, as seen in dust emission, covering the wavelength range between $55 \mu\text{m}$ and $672 \mu\text{m}$, and was shut down from operation in 2013, shortly after the liquid helium supply for instrument cooling ran out. It had three instruments on board: the very high resolution heterodyne spectrometer HIFI, the imaging photometer and medium resolution grating spectrometer PACS, and the imaging photometer and an imaging Fourier transform spectrometer SPIRE. Again, for the analysis of the spectral energy distribution of R Sculptoris, as discussed in **Paper III** (Chapter 6), I used photometry data obtained both by PACS and SPIRE, and describe the two instruments shortly below.

PACS

The Photodetector Array Camera and Spectrometer (PACS, Poglitsch et al. 2010) is an instrument for integral-field spectroscopy and imaging photometry, covering the wavelength range between $60 \mu\text{m}$ and $210 \mu\text{m}$. In photometry mode, it delivers images in two spectral bands: $60 - 85 \mu\text{m}$ or $85 - 125 \mu\text{m}$, and $125 - 210 \mu\text{m}$. The image FOV is $1.75' \times 3.5'$. The pixel size is $3.2'' \times 3.2''$ for the short wavelength spectral bands and $6.4'' \times 6.4''$ for the long wavelength spectral band, respectively. In **Paper III** I use PACS photometry from the $60 - 85 \mu\text{m}$ and $125 - 210 \mu\text{m}$ spectral bands to constrain the SED of R Sculptoris. Additionally, PACS images for all of the objects presented in this thesis have been used to analyse and constrain the dusty component of the studied CSEs around those stars (based on the observing program by Groenewegen et al. 2011).

SPIRE

The Spectral and Photometric Imaging REceiver (SPIRE, Griffin et al. 2010) consists of an imaging photometer and an imaging Fourier-transform spectrometer (FTS), operating in the submillimeter wavelength range. The photometer operates in broad spectral bands centered at 250, 350, and $500 \mu\text{m}$, respectively, while the covers the whole range from $194 - 671 \mu\text{m}$ simultaneously. The photometer beams have full-width half maximum (FWHM) sizes of $18.1''$, $25.2''$, and $36.6''$, at 250, 350, and $500 \mu\text{m}$, respectively. The photometer has a FOV of $4' \times 8'$. In **Paper III** I use SPIRE photometry from all three spectral bands, taken in course of the observing program by Groenewegen et al. (2011), to constrain the SED of R Sculptoris.

⁶<http://sci.esa.int/herschel/>

Chapter 3

no whisper mars the utter silence of
the untranslated stars.

E.E. Cummings

Modelling methods

In this chapter I will describe the basic concept of radiative transfer (RT) modelling, which is used to model and calculate the propagation of light in a medium, including the interaction of the radiation with the medium, with respect to CSEs of AGB stars. Radiative transfer modelling is widely used throughout different fields of research in astrophysics and it is represented by many different approaches to solve the same underlying problem, namely the consistent and full solution of the radiative transfer equation (see Equation 3.1). Since there are probably countless variants of similar radiative transfer codes provided by various research groups, after a general introduction I will only focus on the codes that have been used in the analysis and modelling of data of the publications presented in **Paper I** (Chapter 4) and **Paper III** (Chapter 6).

3.1 Radiative transfer modelling

This basic introduction is mostly based on the lecture notes on “Radiative transfer in astrophysics”, held by C.P. Dullemond at the Ruprecht-Karls-University of Heidelberg¹, unless otherwise noted.

The only way to study distant astrophysical objects is to analyse the electromagnetic radiation, emitted by these objects, which has usually travelled a very long way to us as observers. Along this way, the radiation is interacting with circumstellar, interstellar or other media, resulting in different properties of the radiation, which we receive on Earth. The process of this interaction between radiation and matter is called radiative transfer. In the case of the study of CSEs around AGB stars, radiative transfer modelling links observations and theory of the circumstellar medium together, and allows us to derive basic properties of the medium, such as temperature or density, as well as parameters such as mass-loss rates or abundances of molecules. Radiative transfer can be considered to be the main cooling process of most astrophysical objects, and also a major heating process in many occasions. Additionally, it has a major influence on chemical processes and ionisation of astrophysical gas accumulations.

The propagation of electromagnetic radiation in circumstellar environments can mathematically be described by the radiative transfer equation (RTE)

$$\frac{dI_\nu}{ds} = j_\nu - \alpha_\nu I_\nu, \quad (3.1)$$

¹http://www.ita.uni-heidelberg.de/~dullemond/lectures/radtrans_2012/index.shtml

where I_ν is the spectral specific intensity, j_ν is the emission coefficient, and α_ν is the absorption coefficient, or also called opacity². The analytic solution of this equation is only possible for the most simple of cases, and generally it can only be attempted to be solved by numerical modelling, working with simplifications and approximations. The first important approximation to be made is that the wavelength of the radiation is much smaller than the size of the object, through which it travels, which enables us to treat the radiation not as waves but as individual photons, travelling on distinct paths or rays through the medium. The second approximation is that we only analyse radiative transfer through media that are of low enough density to have a refractive index of ~ 1 . This approximation holds fairly well for astrophysical environments such as stellar or planetary atmospheres, circumstellar environments, or interstellar clouds.

In principle, radiative transfer can be described as following a photon along a ray and observing where it is either absorbed, scattered, or re-emitted. This sounds not too complicated, but one fundamental problem of consistent radiative transfer is the fact that the radiation field depends on the absorption and emission coefficient, but those coefficients in return depend on the radiation field. This feedback loop, together with the issue that photons can switch to other rays by scattering events, is the main reason for the need of powerful numerical modelling techniques to solve radiation transfer consistently. When multiple scattering events can occur for a photon, the origin of the photon cannot reliably be determined analytically, and either approximations such as the single-scattering approximation are used, or numerical methods to simulate the path of a multiply scattered photon through the medium are developed. A very common type of numerical modelling approach for radiative transfer is the so-called Monte-Carlo (MC) method, which essentially does send photon packages through the modelled medium and calculates randomised paths through the medium for each package of photons. This is done for sufficiently large numbers of photons to achieve statistically relevant samples, and determine the total radiation field.

Below I give an overview on the two different regimes of radiative transfer modelling that were used in the publications presented in this thesis, and present the numerical codes used to model radiative transfer in the observed CSEs of this thesis.

3.1.1 Molecular line modelling

In the submillimeter regime, the spectrum of AGB stars is dominated by spectral lines originating from molecular gas, which is excited through rotation and vibration of the molecules. The observation of these spectral lines – especially those of very abundant molecules such as CO – give us information about the circumstellar distribution of gas, and by analysing the Doppler-shift of the lines we can draw conclusions on the velocity field of the gas. By using molecular line radiative transfer modelling, we can derive the temperature, density and abundance of molecular gas in CSEs, as well as mass-loss rates, total gas masses, and isotopic ratios of molecular species. To this end, we need tabulated values of the emission and absorption coefficients – or short: of the opacities – for the modelled molecular species and specific line transitions, which can usually be found in online databases like the Leiden Atomic and Molecular Database (LAMDA)³.

²Note that more generally the mass-weighted opacity κ_ν , which is given by the absorption coefficient per density, α_ν/ρ , is used to describe the absorption of materials or media.

³<http://home.strw.leidenuniv.nl/~moldata/>

For the modelling procedure of the data presented in **Paper I** (Chapter 4) a combination of two different radiative transfer modelling codes is used to accurately model the molecular line emission of four different molecular species and respective isotopologues. Most of the molecular line modelling, especially for the CO line, was done with the Monte-Carlo Program (MCP), for example described by Schöier & Olofsson (2001) and Ramstedt et al. (2008). For the modelling of the H₂O line, the Accelerated Lambda Iteration Program (ALI), described by Rybicki & Hummer (1991), was used, since MCP does not sufficiently deal with high optical depths such as associated with H₂O in the CSEs of AGB stars.

3.1.2 Dust modelling

Interstellar and circumstellar dust can be considered to be of very high importance regarding the galactic cycle of matter, although the fraction of dust compared to gas in the galaxy is approximately as low as 1%. Dust particles provide solid surfaces, on which chemical reactions can take place, and they also shield gas from interstellar radiation and therefore prevent destruction through photodissociation and enable molecule formation. In CSEs of AGB stars, dust grains are considered to be the main wind-driving agents through radiation pressure on the dust grains and drag forces between gas and dust. Ultimately, dust grains can coagulate to larger and larger structures, eventually creating solid bodies and enabling rock and planet formation. Unlike molecular line opacities, dust opacities cover a much larger spectral range and do not result in spectral line emission but continuum emission, influencing the spectral energy distribution of AGB stars from the NIR- to mm-wavelengths. Apart from that, certain dust species also are reflected in dust emission features at smaller spectral ranges. The most commonly known dust species in AGB CSEs are silicates and amorphous carbon. For dust radiative transfer modelling, the opacities for the modelled dust species can be retrieved from online databases such as the Jena database⁴, and the tabulated opacities come from various laboratory measurements.

For the modelling procedure of the dusty CSE of R Scl, presented in **Paper III** (Chapter 6), I used the Monte-Carlo radiative transfer code MCMax (Min et al. 2009) to derive the dust temperature, present-day mass-loss rate, and shell mass, for different model setups with different dust grains. The input parameters for MCMax include the tabulated dust opacities, the density profile of the modelled medium, the parameters of the input radiation field, and the wavelength grid to be used. The complete modelling strategy is described in detail in the respective publication.

⁴<http://www.astro.uni-jena.de/Laboratory/Database/jpdoc/f-dbase.html>

Part II

Main publications

Chapter 4

The molecule-rich envelope around W Aquilae (Paper I, accepted)

Title: *Molecular line study of the S-type AGB star W Aquilae*

Authors: M. Brunner, T. Danilovich, S. Ramstedt, W.H.T. Vlemmings, M. Lindqvist, and F. Kerschbaum

Year: 2018

Journal: Astronomy and Astrophysics, accepted May 29th 2018

DOI: <https://doi.org/10.1051/0004-6361/201832724>

Credit: Brunner et al. 2018, A&A, in press, reproduced with permission © ESO

In this publication we investigate a total of eight molecular lines in the close CSE of the S-type AGB star W Aql, which is associated to be in a transition state between an oxygen- and carbon-rich circumstellar chemistry. The observations are done with ALMA and are complemented with single-dish observations. Additionally, W Aql is a binary star and binary interaction holds the potential to influence the molecular wind, especially in the inner regions that are studied here. To investigate the chemical state of W Aql, we employ radiative transfer modelling on the spectral lines – CS, H¹³CN, SiO and SiS and isotopologues – and extract radial abundance profiles, that can be compared to previous studies as well as other objects. We also extract isotopic ratios, which help us analyse the chemical processes in the CSE.

Personal contribution: As first author of this paper, I was responsible for the complete data reduction of all available ALMA datasets, the majority of the data analysis and creation of the manuscript. The radiative transfer modelling was carried out in close collaboration with the co-author T. Danilovich, who additionally provided important insights to the interpretation of the results. The uv-fitting was carried out with extensive support by I. Marti-Vidal, who contributed his technical expertise in this field.

Molecular line study of the S-type AGB star W Aquilae

ALMA observations of CS, SiS, SiO and HCN

M. Brunner¹, T. Danilovich^{2,3}, S. Ramstedt⁴, I. Marti-Vidal², E. De Beck², W.H.T. Vlemmings², M. Lindqvist², and F. Kerschbaum¹

¹ Department for Astrophysics, University of Vienna, Türkenschanzstrasse 17, A-1180 Vienna
e-mail: magdalena.brunner@univie.ac.at

² Department of Space, Earth and Environment, Chalmers University of Technology, Onsala Space Observatory, 439 92 Onsala, Sweden

³ Department of Physics and Astronomy, Institute of Astronomy, KU Leuven, Celestijnenlaan 200D, 3001 Leuven, Belgium

⁴ Department of Physics and Astronomy, Uppsala University, 75120 Uppsala, Sweden

Received Month nr, YYYY; accepted Month nr, YYYY

ABSTRACT

Context. With the outstanding spatial resolution and sensitivity of the Atacama Large Millimeter/sub-millimeter Array (ALMA), molecular gas other than the abundant CO can be observed and resolved in circumstellar envelopes (CSEs) around evolved stars, such as the binary S-type Asymptotic Giant Branch (AGB) star W Aquilae.

Aims. We aim to constrain the chemical composition of the CSE and determine the radial abundance distribution, the photospheric peak abundance, and isotopic ratios of a selection of chemically important molecular species in the innermost CSE of W Aql. The derived parameters are put into the context of the chemical evolution of AGB stars and are compared with theoretical models.

Methods. We employ one-dimensional radiative transfer modeling – with the accelerated lambda iteration (ALI) radiative transfer code – of the radial abundance distribution of a total of five molecular species (CS, SiS, ³⁰SiS, ²⁹SiO and H¹³CN) and determine the best fitting model parameters based on high-resolution ALMA observations as well as archival single-dish observations. The additional advantage of the spatially resolved ALMA observations is that we can directly constrain the radial profile of the observed line transitions from the observations.

Results. We derive abundances and *e*-folding radii for CS, SiS, ³⁰SiS, ²⁹SiO and H¹³CN and compare them to previous studies, which are based only on unresolved single-dish spectra. Our results are in line with previous results and are more accurate due to resolution of the emission regions.

Key words. Stars: abundances – Stars: AGB and post-AGB – Stars: circumstellar matter – Stars: mass-loss – Stars: winds, outflows – Submillimeter: stars

1. Introduction

W Aquilae (W Aql) is a cool, intermediate-mass S-type star located on the Asymptotic Giant Branch (AGB). In this phase of stellar evolution, a star suffers from substantial mass loss, and, as a consequence, a circumstellar envelope (CSE) is created. In this circumstellar environment, molecules and dust grains are formed, making AGB stars important contributors to the chemical evolution of the interstellar medium and ultimately the universe (e.g. Habing & Olofsson 2003). On the AGB, different molecular bands in near-infrared (NIR) spectra (e.g., TiO, ZrO, CN) are used to discriminate between three different spectral types of AGB stars. These are also thought to reflect their carbon-to-oxygen (C/O) ratios, measured in the stellar atmosphere: M-type (oxygen-rich, C/O < 1), S-type (C/O ≈ 1) and C-type (carbon-rich, C/O > 1). Owing to the varying circumstellar chemical composition, certain molecular and dust species will be formed preferentially to others, depending on the chemical type of an AGB star.

In AGB stars, carbon is produced from helium through the triple-alpha process. A deep convective envelope and dredge-up events mix the freshly created carbon up into the stellar atmosphere, where the C/O ratio can be measured. The dredged-up

carbon increases the C/O ratio, leading to a change in the circumstellar chemistry and the evolution from M-type to C-type stars. This implies that S-type stars represent transition objects in the chemical stellar evolution on the AGB, connecting two very distinct chemical types of stars and stellar atmospheres. As reviewed in Höfner (2015), the stellar wind is most likely driven by radiation pressure on dust grains, meaning that the differing chemical composition of M- and C-type stars will require different wind-driving dust species. Up to now, the wind acceleration process and the respective wind-driving dust species are well studied for C-type stars and recently solutions have been suggested for M-type stars as well (e.g. Höfner 2008; Bladh & Höfner 2012; Bladh et al. 2015). Comparable studies for S-type stars are difficult, however, given the uncertain circumstellar chemistry. This makes the detailed chemical analysis of different types of AGB stars crucial for our understanding of this evolutionary stage.

For the determination of properties such as mass-loss rates or circumstellar morphology, the observation and analysis of the abundant and stable CO molecule is most commonly used, which is present in the CSEs of all three chemical types (e.g. Knapp et al. 1998; Schöier et al. 2002; Olofsson et al. 2002; Ramstedt et al. 2009; De Beck et al. 2010; Danilovich et al.

2015). Otherwise, it is commonly observed that the CSEs of oxygen-rich stars are dominated by oxygen-bearing molecules, while the CSEs of carbon-rich stars are dominated by carbon-bearing molecules. Apart from that simplified picture, it was predicted by Cherchneff (2006) and confirmed by Decin et al. (2008) that under non-LTE conditions a small selection of so-called “parent” molecules is present for all three chemical types, concentrated to the inner stellar wind. These “parent” molecules – CO, SiO, HCN, CS – can be formed in shock waves propagating through the outer layers of the stellar photosphere, and these molecules will influence the CSE chemistry and abundances. Recent observations suggest that the parent molecule inventory is supplemented with the species H₂O (Maercker et al. 2016; Danilovich et al. 2014; Neufeld et al. 2014) and NH₃ (Menten et al. 2010; Danilovich et al. 2014; Schmidt et al. 2016). For S-type stars, the chemical composition is highly sensitive to the exact C/O ratio and temperature, leading to the splitting into MS-, S-, and SC-type stars for different molecular features seen in the spectra, with the C/O ratio of S-type stars ranging from 0.75 to 0.99 (Zijlstra et al. 2004; Van Eck et al. 2017). The types MS and SC show similar molecular species to M- and C-type stars, while “pure” S-type stars show a mixed or intermediate molecular composition (e.g. Schöier et al. 2013). Nevertheless, Ramstedt et al. (2009) derive that the mass-loss rate distributions of M-, S- and C-type AGB stars are indistinguishable, which makes it even more important to investigate how the different chemical compositions can lead to a similar outcome.

Observations, in combination with detailed radiative transfer modelling, are indispensable in the investigation of the chemical composition of AGB CSEs. Their study yields chemical abundance distributions and isotopolog ratios. One prominent example for an in-depth study of the molecular CSE is the carbon AGB star IRC+10216, which is probably the best analyzed AGB star so far, and has for example been observed within an interferometric spectral line survey with the Submillimeter Array (SMA) executed by Patel et al. (2011). With this survey of unprecedented sensitivity, a total of 442 spectral lines, including more than 200 new ones, were detected. Although the emission has been mapped interferometrically, only a few of the strongest lines have been resolved. As discussed by, for example, Saberi et al. (2017), resolving the emitting region of molecules studied in this way strongly influences the derived abundance and radial size of the molecular envelopes, increasing the need for high-resolution observations of AGB CSEs and in particular their inner regions. This has now become possible with the Atacama Large Millimeter/sub-millimeter Array (ALMA), which provides the necessary spatial and spectral resolution as well as the sensitivity to observe even weak molecular emission close to AGB stars.

In this paper, we present ALMA observations of the molecules CS, SiS, ²⁹SiO and H¹³CN, as well as four different isotopologs and vibrational states of SiO and SiS around the S-type AGB star W Aql. The star and previous studies of it are introduced in Sect. 2. The observations are described and presented in Sect. 3, while detailed maps of all molecular lines are shown in Appendix A. The observational results are discussed in Sect. 4. Additionally, the sizes of the emitting regions are fitted in the uv-plane to further analyze the morphology of the molecular gas and partially unravel the three-dimensional (3D) structure of the CSE. Section 5 describes the radiative transfer modeling based on the work of Danilovich et al. (2014), which is improved by the incorporation of the new ALMA data. The main

uncertainty in circumstellar abundance estimates is the size of the emitting region. By measuring it directly with ALMA, this uncertainty is removed. The results of this whole study are summarized and discussed in Sect. 6, and the main conclusions are given in Sect. 7.

2. W Aql

W Aql is an S-type AGB star with a spectral type of S6.6, which is very close to the SC-type classification, and has an estimated C/O ratio of 0.98 according to the classification scheme by Keenan & Boeshaar (1980). It has a period of 490 days and is classified as a Mira variable (Feast & Whitelock 2000). Its distance is 395 pc, derived from the period-magnitude relation (Whitelock et al. 2008) and 2MASS *K* band magnitude (Cutri et al. 2003). As reported by Decin et al. (2008), the “parent” molecules CO, HCN, CS, SiO and SiS, expected to be formed close to the stellar photosphere, have all been detected for W Aql, but have not yet been resolved. The earlier study by Bieging et al. (1998) also suggests that SiO and HCN detected around W Aql could be of photospheric origin, under certain non-LTE conditions.

The chemical constitution of the CSE around W Aql has been investigated in several studies with observations and subsequent radiative transfer modeling (e.g., Decin et al. 2008; De Beck et al. 2010; Ramstedt et al. 2009; Ramstedt & Olofsson 2014; Schöier et al. 2013; Danilovich et al. 2014), but until now the observations of the molecular line emission have always been unresolved. According to Uttenthaler (2013), the star is Tc rich, confirming its evolutionary stage between M-type and carbon-rich AGB stars. Based on Danilovich et al. (2014), the stellar effective temperature, T_{eff} of W Aql is assumed to be 2300 K, the stellar luminosity L is $3000 L_{\odot}$ and the gas mass-loss rate is $4 \times 10^{-6} M_{\odot} \text{yr}^{-1}$.

Ramstedt et al. (2011) have shown W Aql to be a binary star, where they present an HST B-band image of the resolved binary system, with the binary located to the South-West. The angular separation of 0.46'' corresponds to a minimum projected binary separation of 190 AU (for the derived distance of 395 pc), making it a wide binary system. An optical spectroscopic classification of the binary companion was done by Danilovich et al. (2015) and lead to the spectral type F8 or F9, where the binary companion most likely lies behind or within the CSE of W Aql. Additionally, this analysis constrained the mass of the AGB star to $1.04 - 3 M_{\odot}$, leading to a total system mass of $2.1 - 4.1 M_{\odot}$. Newer mass estimates, based on observations of the ¹⁷O/¹⁸O ratio and comparison with stellar evolution models by De Nutte et al. (2017) give values of between 1.5 and 1.8 M_{\odot} for the initial mass of the primary star.

Asymmetries in the CSE of W Aql have been detected at several different spatial scales and at different wavelengths. Interferometric observations of the dusty CSE of W Aql with the UC Berkeley Infrared Spatial Interferometer (ISI) at 11.15 μm were reported by Tatebe et al. (2006), revealing an asymmetry of the dust distribution within a radius of 500 milli-arcseconds. A dust excess was detected to the east of the star, appearing to continuously extend from the star to the outer regions of dust emission probed by the observations. This leads the authors to the conclusion that the asymmetry has been stable over the last 35 years, which they estimate is the period since the ejection of the asymmetrically distributed material, using a typical wind velocity of 20 km s⁻¹. The authors argue that a close binary would disturb the stability of the asymmetry.

At larger spatial scales, observations with the Polarimeter and Coronagraph (PolCor) at the Nordic Optical Telescope (NOT) have been carried out by Ramstedt et al. (2011), revealing the dust CSE morphology of W Aql on scales from about $1''$ to $20''$. They report a clear asymmetry to the south-west of the star, extending out to almost $10''$, which is seen both in the total intensity image in the R band as well as in the polarised images, showing polarisation degree and angle. The direction of the asymmetry aligns with the binary position.

W Aql was observed with the PACS photometer of the Herschel space telescope as part of the MESS (Mass loss of Evolved StarS; Groenewegen et al. 2011) program to analyze the large scale morphology of the dusty CSE and wind-ISM interaction (Mayer et al. 2013) on spatial scales from approximately $10''$ to $120''$. The authors conclude that a strong feature in the $70\mu\text{m}$ IR image of the CSE to the east of the star can be explained by the interaction of the stellar wind with an ISM flow. They further report the shaping of the IR emission by wind-binary interaction, which can be tentatively traced with an Archimedean spiral and could be responsible for additional brightening of the ISM interaction zone to the east of the star and the overall elliptical shape of the CSE. The high-resolution CO gas emission around W Aql is presented and discussed in Ramstedt et al. (2017), where arc-like structures at separations of approximately $10''$ are found. While these structures can be linked to the binary nature of the object, small-scale arc structures at separations of $2-3''$ remain unexplained by the known orbital parameters of the binary system. The small-scale structures are confined to the south-west region of emission, which is also consistent with the previously detected asymmetry found in dust emission.

3. Observations and data reduction

W Aql was observed as part of a sample of binary stars with ALMA in Cycle 1 (observed in March and April 2014, PI: Sofia Ramstedt), combining ALMA main array observations (12 m diameter, long baselines), Atacama Compact Array (ACA) observations (7 m diameter, short baselines) and total power (TP) observations (12 m diameter, single-dish). An area of $25'' \times 25''$ is covered with both arrays, observing a mosaic of 10 and 3 pointings, respectively. Four spectral windows, with a bandwidth of 1875 MHz (main array) and 1992.187 MHz (ACA) each, were observed, centered at 331, 333, 343 and 345 GHz, respectively. The resulting spectral resolution is 488.281 kHz. Standard calibration was performed with the Common Astronomy Software Application (CASA), using Ceres as flux calibrator and the quasars J1924-2914 and J1911-2006 as bandpass calibrator and phase calibrator, respectively. In addition to the main goal of the proposal, focussing on the analysis of the binary interaction on the CO gas distribution (Ramstedt et al. 2017), eight additional molecular lines were detected with this configuration. The molecular lines, rest frequencies and final velocity resolution after calibration and imaging are listed in Table 1. The combination of the main array and ACA data is conducted in the visibility plane with antenna-specific weighting, whereas the TP data is combined with the rest of the data via feathering in the image plane. Imaging of all spectral lines was carried out with CASA using the CLEAN algorithm with natural weighting, resulting in a beam of $0.55'' \times 0.48''$ (PA 86.35°). Iterative masking for each spectral channel and molecular line was used to optimize the imaging process with CLEAN. The spectral channels were binned to a velocity resolution of 1 km s^{-1} and 2 km s^{-1} for

strong and weak spectral lines, respectively.

4. Observational results

Four of the eight detected spectral lines are considerably weaker than the others, making analysis and especially modeling of these lines very uncertain or even impossible. Therefore, we concentrate our efforts on the strong spectral lines and present the analysis and modeling process for the strong lines in the following sections. Additionally, we refer to Appendix B for a graphical representation of basic results on the weak lines. Channel maps of all strong spectral lines can be found in Appendix A. Figures 1 and B.1 show the integrated intensity (moment 0) maps for all observed spectral lines. A comparison between the spectra of the four strongest lines in this study is presented in Fig. 3.

4.1. Morphology of spectral line emission

For the strong spectral line emission – shown in moment-zero maps in Fig. 1 and channel maps in Appendix A – the peak emission seems to be roughly spherical, concentrated at the stellar position, and is spatially resolved. Additionally, we see a fainter and slightly elongated circumstellar emission component extending out to roughly $2-3''$. The elongation is oriented in the north-east and south-west (NE/SW) directions, which is also the direction of the binary orbit. We compare the molecular emission of the four strong spectral lines with the CO (3–2) emission reported by (Ramstedt et al. 2017) in Fig. 2 and find that the emission features along the NE/SW elongation are equally represented in the CO emission as well, with emission peaks in the molecular lines coinciding with CO emission peaks or clumps.

4.2. Spectral features

The four strongest emission lines (Fig. 3) all show a slight but noticeable excess in blue-shifted emission between approximately -35 and -40 km/s . This cannot be seen in the channel maps (Appendix A). Additionally, the SiS line shows a strong asymmetry with an excess in red shifted emission relative to the stellar rest frame at around -21 km s^{-1} . This feature can possibly be seen also in the channel maps (Fig. A.3), where between roughly -20 and -14 km s^{-1} an elongation of the bright peak emission to the east can be seen. It is most prominent at about -16 km s^{-1} , which coincides with the peak of the asymmetry in the spectrum. Furthermore, the ^{29}SiO profile shows two secondary features at about -32 km s^{-1} and -11 km s^{-1} .

Previous models on multiple spectral lines by Danilovich et al. (2014) report a stellar velocity (extracted from the line center velocity), v_{lsr} , of -23 km/s , which is backed up by and consistent with several other studies, reporting a very similar velocity (e.g., Bieging et al. 1998; Ramstedt et al. 2009; De Beck et al. 2010; Mayer et al. 2013; De Nutte et al. 2017). We note that, investigated separately from previously detected lines, the reported lines observed with ALMA seem to be generally red-shifted to this stellar velocity, and a v_{lsr} of -21 km/s (such as that calculated by Mayer et al. 2013) is more fitting. Taking the ALMA line peak velocities of all observed lines and calculating an average line peak velocity, we also arrive at a v_{lsr} of -21 km/s , but the asymmetry of the lines and deviation from parabolic line profiles is very line-specific (as seen in Fig. 3).

A&A proofs: manuscript no. WAql-v6-revision_02_final

Table 1. Observed quantities of the molecular line emission around W Aql.

Molecular line	Restfreq. (GHz)	Δv (km s ⁻¹)	$I_{v,peak}$ (Jy)	$v_{lsr,peak}$ (km s ⁻¹)	$\int I_v dv$ (Jy km s ⁻¹)	θ (")
CS (7–6)	342.8829	1	7.29	-13	167.77	4
H ¹³ CN (4–3)	345.3398	1	3.90	-21	96.73	4
SiS (19–18)	344.7795	1	3.51	-15	70.51	4
²⁹ SiO (8–7)	342.9808	1	2.91	-22	54.36	4
SiO v=1 (8–7)	344.9162	2	0.74	-23	11.33	4
SiS v=1 (19–18)	343.1010	2	0.34	-23	3.68	4
³⁰ SiS (19–18)	332.5503	2	0.29	-27	3.25	2
SiO v=2 (8–7)	342.5044	2	0.18	-25	0.34	2

Notes. Rest frequencies, velocity resolution (Δv), peak flux ($I_{v,peak}$), peak flux velocity ($v_{lsr,peak}$), integrated flux ($\int I_v dv$) and used aperture diameter (θ) for all eight detected molecular lines around W Aql. The rms noise measured from line-free channels is 10 mJy/beam.

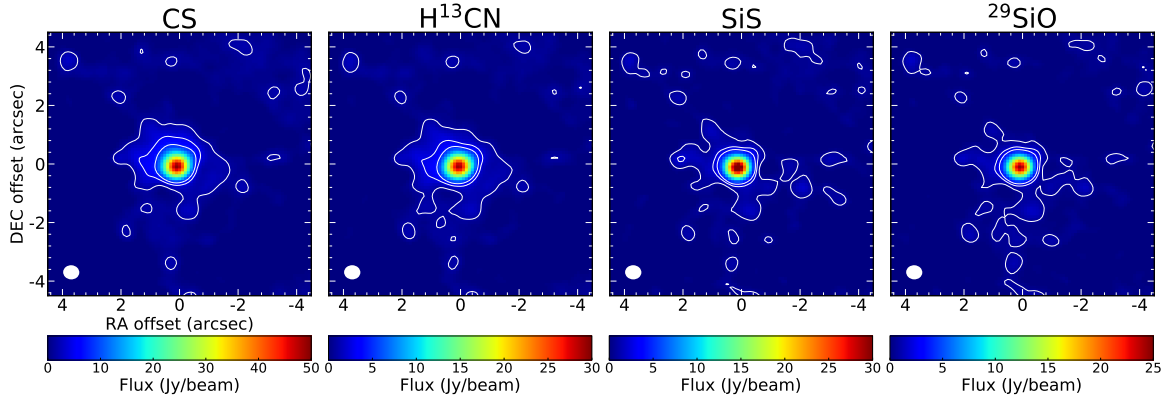


Fig. 1. ALMA integrated intensity (moment 0) maps of CS (7–6), H¹³CN (4–3), SiS (19–18), and ²⁹SiO (8–7) emission lines around W Aql. The ALMA beam (0.55'' × 0.48'', PA 86.35°) is given in the lower-left corner. Contours are marked in white for 1, 3 and 5 σ rms. North is up and east is left.

4.3. uv fitting

Since the imaging process of interferometric data involves initial knowledge of the source geometry and image artefacts are inevitably introduced during deconvolution, it is reasonable to analyze the observations already in the uv plane, directly working with the calibrated visibility data. For this reason, we use the CASA tool *uvmultifit* (Martí-Vidal et al. 2014), to fit geometric flux models to the bright emission regions of all spectral lines. Since the TP data combination for this project is done in the image plane and not in the uv plane, we can only fit to the combined 12 m main array and ACA data. This is a reasonable approach, since the maximum recoverable scale for the used 12 m main array and ACA configuration is 19'', and we concentrate our analysis on the central few arcseconds.

Therefore we conclude that for the analysis of the compact, bright emission it is sufficient to use only the main array and ACA data. As a first step, we fit a compact, circular Gaussian component to the data, which is described by its position (relative to the current stellar position of RA 19:15:23.379 and DEC -07:02:50.38 J2000.0 (Ramstedt et al. 2017)), flux density, and FWHM size. After subtracting the model visibilities from the observed ones, we imaged the residuals to verify the goodness of the Gaussian fit. The resulting residual images

for the four strong spectral lines are shown in the top row of Fig. 4. Apart from relatively faint, extended emission surrounding the subtracted compact Gaussian, which can be seen for all four spectral lines, a very compact emission peak remains at the stellar position, which can best be seen in the residual CS and H¹³CN emission. We succeed in fitting the compact, central emission by adding a delta function to the circular Gaussian, and arrive at significantly better residual images (see Fig. 4, bottom). Figure 5 shows the uv-fitting parameter results for the Gaussian position offset, the Gaussian flux density, and Gaussian FWHM fit parameters, as well as the flux ratio between the added delta component and the Gaussian, for the four strong spectral lines.

We note, however, that the true intensity distribution of a uniformly expanding envelope is not strictly Gaussian. When the emission is optically thin, the intensity distribution $\propto r^{-1}$, which cannot be straightforwardly implemented for use in a uv analysis. When the emission becomes optically thick, the inner part of the distribution flattens, improving a Gaussian approximation. The distribution in the outer envelope can be adequately described using a Gaussian distribution and the deviation mainly becomes apparent in the inner region, close to the resolution limit of our observations. The deviations in this part explain

M. Brunner et al.: Molecular line study of the S-type AGB star W Aquilae

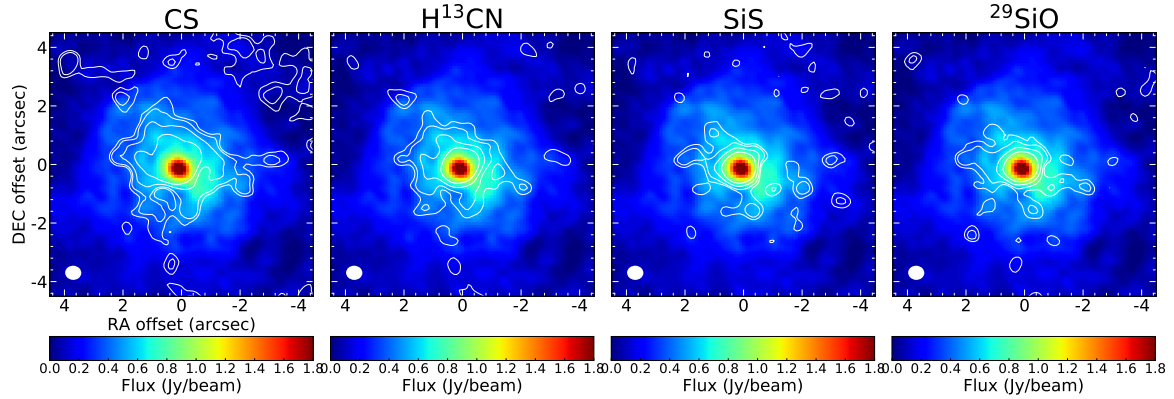


Fig. 2. ALMA CO image (color) overlaid with contours (white) of the CS (7–6), H^{13}CN (4–3), SiS (19–18), and ^{29}SiO (8–7) emission, shown at stellar velocity (about -21 km s^{-1}). The ALMA beam for the CS, H^{13}CN , ^{29}SiO and SiS lines ($0.55'' \times 0.48''$, PA 86.35°) is given in the lower-left corner. Contours are plotted for 3, 5, 10 and 20σ rms. North is up and east is left.

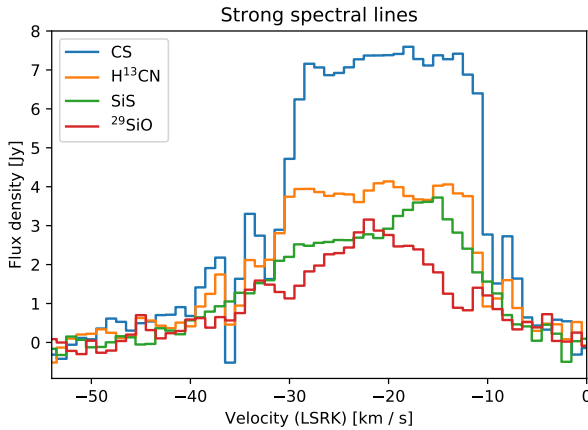


Fig. 3. Spectra of the four strongest spectral lines – CS, H^{13}CN , SiS and ^{29}SiO – measured within a circular $5''$ aperture centered on the star. The stellar velocity is at about -21 km s^{-1} .

the better fits obtained when including a delta-function, and the strength of the delta function depends on the line optical depth.

The offset of the fitted Gaussian position to the stellar position is well below the spatial resolution of the images and a clear general trend of the offsets for all four lines is barely visible. We note, however, that the photocenter seems to shift with increasing flux density towards slightly larger RA and DEC.

For all four lines, the FWHM size for channels with velocities larger than 0 km s^{-1} shows very large error bars, meaning that the fit does not converge in those channels and the estimated size of the emission region is very uncertain. The flux density fits show very similar line profiles to the observed ones (a direct comparison is given in Sect. 4.4), with the exception of the ^{29}SiO line profile, which does not show the additional peaks at blue- and red-shifted velocities in the Gaussian fit. The CS, H^{13}CN and ^{29}SiO lines each show a peak in the emission size at blue velocities, which cannot be directly associated with any features in the flux density profile. The only similarity to note here is that the size of the emission region changes at the velocities that belong to the slightly asymmetric and weaker part of the flux den-

sity profile. On the other hand, the asymmetric feature in the SiS line profile is associated with a slight increase in emission size. A very similar asymmetry in the SiS line has been observed for the carbon star RW LMi (Lindqvist et al. 2000).

We note that the fitted FWHM of the SiS line lies very close to the imaging resolution at some velocities, meaning that the uv fit is close to over-resolving the emission. We refer to Appendix C for a discussion about super-resolution in uv fitting, as well as the uncertainties attached to the fits.

As expected, the uv-fitting of the four weaker spectral lines is more uncertain and especially for the extreme velocity channels the emission size cannot be constrained confidently. The $\text{SiO } v=1$ and ^{30}SiS lines seem to be slightly resolved, while the $\text{SiO } v=2$ and SiS $v=1$ lines are unresolved in the image plane, and the signal-to-noise ratio (S/N) for all weak lines is too low for confident fitting. Therefore we refrain from presenting inaccurate uv-fitting results for the weak spectral lines.

4.4. Comparison between uv-fitted and observed spectral shape

We compare the uv-fitted spectra with the observed spectra extracted from the beam convolved images with an aperture of $5''$ diameter to compare the spectral contribution of the compact Gaussian and delta function emission components with the fainter, extended asymmetric emission component seen in the residual images (Fig. 4). Figure 6 shows the compared spectra for the strong lines. To illustrate the flux contribution of the compact delta component, we separately show the spectrum of a uv fit with just a circular Gaussian and a spectrum of the uv fit with a circular Gaussian and added delta function component.

For all four lines, we see that the fraction of recovered flux is significantly lower when no delta component is added to the uv fit. The model including a Gaussian and a delta component recovers almost the total flux for the CS and H^{13}CN lines, and the majority of flux for the SiS and ^{29}SiO lines. While for CS and H^{13}CN the contribution of the delta component seems to be roughly of the same strength for all velocities, the contribution of the delta component compared to the Gaussian is slightly higher at blue shifted velocities for SiS and ^{29}SiO .

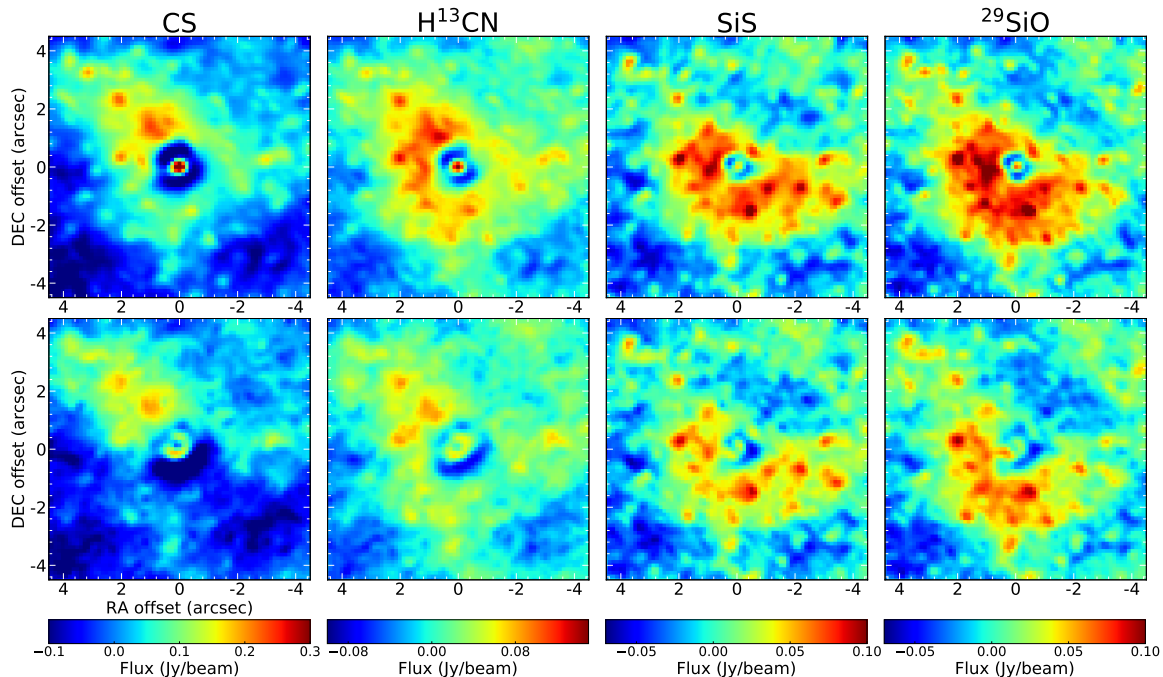


Fig. 4. Imaged residuals of the four strong emission lines after subtraction of the model visibilities of a uv fit. Only the central channel at -21 km/s is shown. Top row: Residuals after the subtraction of the uv fit of a circular Gaussian; Bottom row: Residuals after the subtraction of the uv fit of a circular Gaussian and a delta function.

We conclude that the overall emission line profile can be recovered well by uv models of a Gaussian and a delta component, while the remaining small deviations can be attributed to the residual extended and asymmetric emission.

5. Radiative transfer modeling

5.1. Modeling procedure

To model the molecular emission, we used ALI, an accelerated lambda iteration code (first introduced, and later applied and improved by Rybicki & Hummer 1991; Maercker et al. 2008, respectively), following the same procedure as described in Danilovich et al. (2014). The stellar parameters used for the models are given in Table 2. To constrain our models, we used the azimuthally averaged radial profile from the ALMA observations (convolved with a $0.6''$ beam) and the ALMA line profiles convolved with a $4''$ beam, and additional archival single-dish data listed in Table D.1. We note that the models are primarily fitted to the ALMA data, with the integrated flux of the archival single-dish data being used – in most cases – to discriminate between two equally good fits to the ALMA data. Our model uses the CO modeling results obtained by Danilovich et al. (2014) and refined by Ramstedt et al. (2017). For a distance of 395 pc, $1''$ corresponds to 5.91×10^{15} cm or 1×10^{15} cm corresponds to $0.17''$.

In all cases, we assumed a Gaussian profile for the molecular fractional abundance distribution, centred on the star, following

$$f(r) = f_0 \exp\left(-\left(\frac{r}{R_e}\right)^2\right), \quad (1)$$

where f_0 is the abundance relative to H_2 at the inner radius of the molecular CSE and R_e is the e -folding radius, the radius at which the abundance has dropped off by $1/e$.

The Gaussian models have two free parameters per molecular species: f_0 , the central fractional abundance, and R_e , the e -folding radius. When considering the ALMA radial profiles, we constrain our models using the central position and offset positions with spacings of $0.1''$ starting at $0.05''$ and extending to $0.75''$, although we include plots showing the models and ALMA profiles out to $2.55''$. The error bars on the ALMA observations are derived from an azimuthal average over the observed radial profile. Regarding optical depth, we note that ^{30}SiS and ^{29}SiO are optically thin, CS and ^{28}SiS are mostly optically thin, with the exception of the very innermost regions of CSEs, ^{28}SiO is mostly optically thick, H^{12}CN is very optically thick, and H^{13}CN is optically thick in the shell, but optically thin elsewhere.

5.2. Modeling results

When modeling the ALMA radial profiles, we found that for most molecules there was a “tail” in the radial profile, from around $1''$ outwards, which could not be fit with a Gaussian abundance profile in a smoothly accelerating CSE model. We first attempted to find a good fit with a non-Gaussian abundance profile, but such models that fit the observations well were not physically realistic, with increasing abundances with radius. Instead, we found that adjusting the wind density over a small region, as could be caused by a binary induced, spiral-like overdensity, for example, greatly improved our model fits to the en-

M. Brunner et al.: Molecular line study of the S-type AGB star W Aquilae

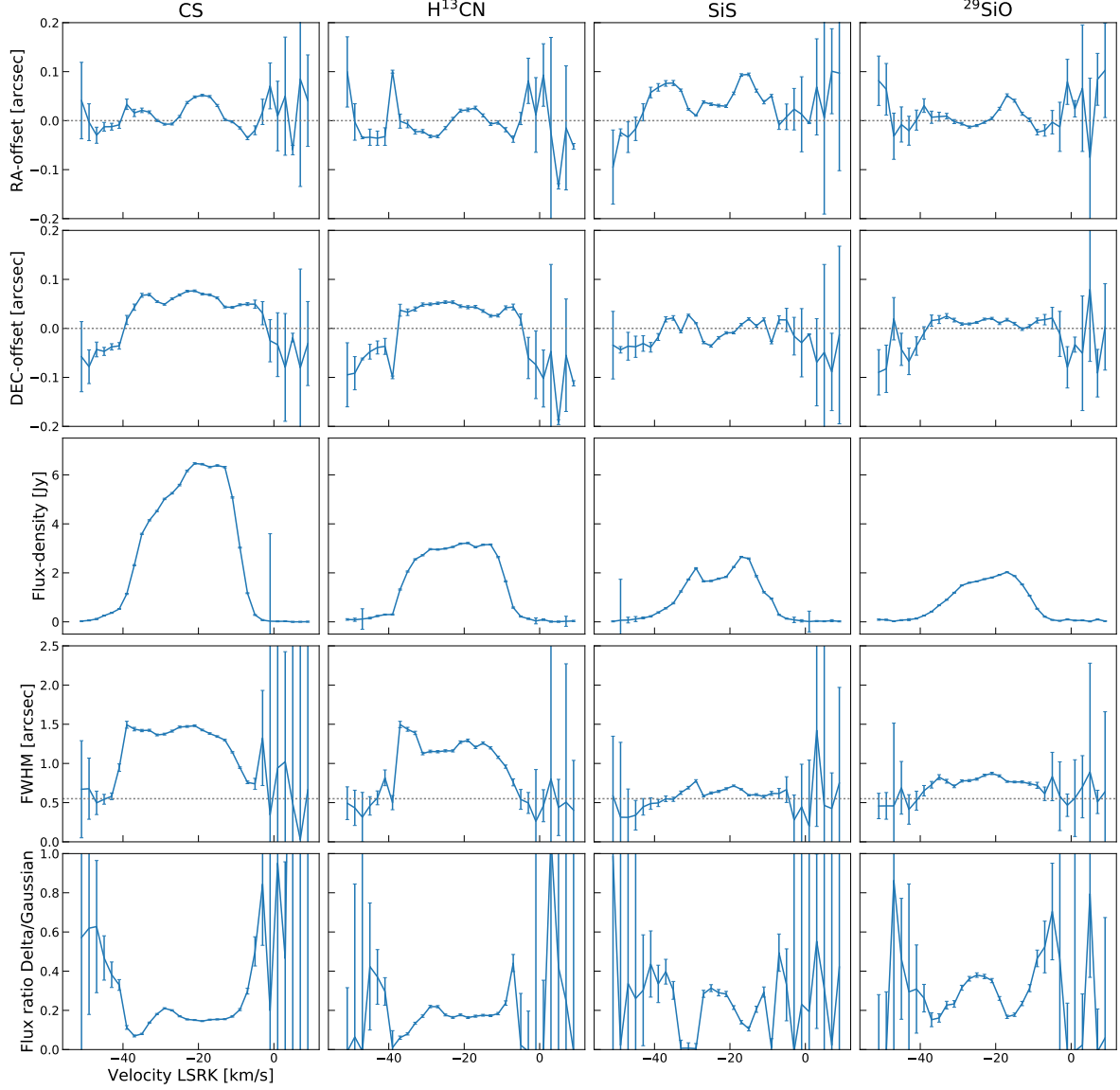


Fig. 5. uv-fitting of the four strong spectral lines detected in the inner CSE of W Aql. First row: RA offset position of the fitted Gaussian. Second row: DEC offset position. Third row: Fitted flux-density of circular Gaussian for each velocity bin of 2 km/s. Fourth row: Size of best-fitting circular Gaussian (FWHM). Fifth row: Flux ratio of fitted delta function to Gaussian. For reference, the effective beam size in the observed images of $0.55'' \times 0.48''$ is indicated by a gray dashed line in the fourth row. The gray dashed lines in the two top rows denote the zero point of position offset in RA and DEC, respectively.

tire profile. For a smoothly accelerating wind with no overdensities, the H_2 number density at radius r is given by

$$n_{\text{H}_2}(r) = \frac{\dot{M}}{4\pi r^2 m_{\text{H}_2} v(r)}, \quad (2)$$

where \dot{M} is the mass-loss rate, m_{H_2} is the mass of H_2 and $v(r)$ is the radial velocity profile. To adjust the H_2 number density, we multiplied a section of the smooth-wind radial profile (given by the mass-loss rate determined by Ramstedt et al. (2017), listed in Table 2, and the velocity profile defined by Danilovich et al.

(2014)) by integer factors up to 10. The result that did not over-predict the “tail” for any molecule was chosen as the best model. We found that the inner regions of the radial intensity profiles were not significantly affected by the inclusion of this overdensity and the central abundances and e -folding radii did not need to be adjusted when adding the overdensity.

The best fit for all molecules was found for an overdensity of a factor of five between 8×10^{15} cm and 1.5×10^{16} cm. This reproduces the observed radial profiles for H^{13}CN and ^{29}SiO well, without adjustments to the abundance profiles determined from

A&A proofs: manuscript no. WAql-v6-revision_02_final

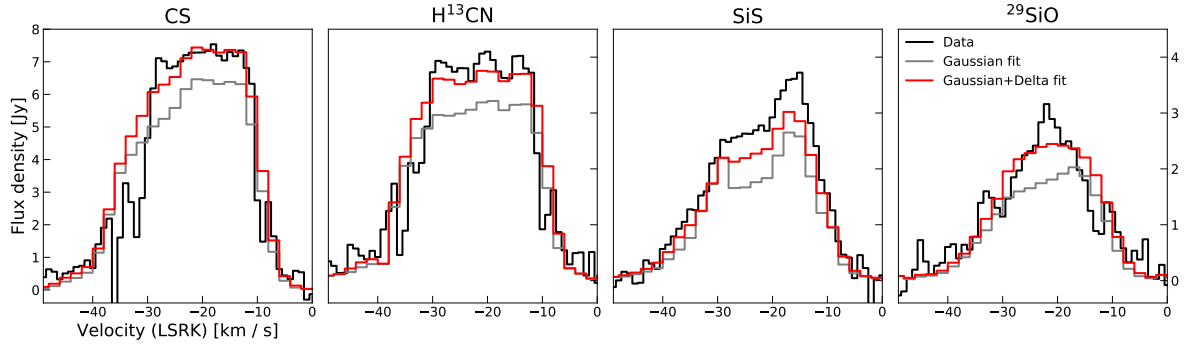


Fig. 6. Comparison of the observed spectra (black) with the uv-fitted spectra of the Gaussian fit (gray) and the fit including a Gaussian plus a delta function (red). The observed spectra were extracted from the images with an aperture of $5''$ diameter. The effective beam size in the observed images is $0.55'' \times 0.48''$. We note that the y-axis scales differently for the first spectral line, which is the strongest. The respective scales are given on the left-hand side for the first line, and on the right-hand side for the remaining lines.

Table 2. Stellar parameters used for radiative transfer modeling.

Model parameters W Aquilae	
Distance	395 pc ^a
Effective temperature	2300 K
Gas mass-loss rate	$3 \times 10^{-6} \text{ M}_{\odot}/\text{yr}^b$
Dust/gas mass ratio	2×10^{-3}
Luminosity	$7500 L_{\odot}^c$
Stellar mass	$1 M_{\odot}$
Gas expansion velocity	16.5 km/s ^d
Stellar velocity (LSRK)	-21 km/s ^d

Notes. All parameters are adopted from Danilovich et al. (2014).

^(a) Derived from period-magnitude relation (Whitelock et al. 2008) and 2MASS K band magnitude (Cutri et al. 2003). ^(b) Ramstedt et al. (2017)

^(c) Derived from period-luminosity relation (Glass & Evans 1981).

^(d) Measured from CO line data (Danilovich et al. 2014).

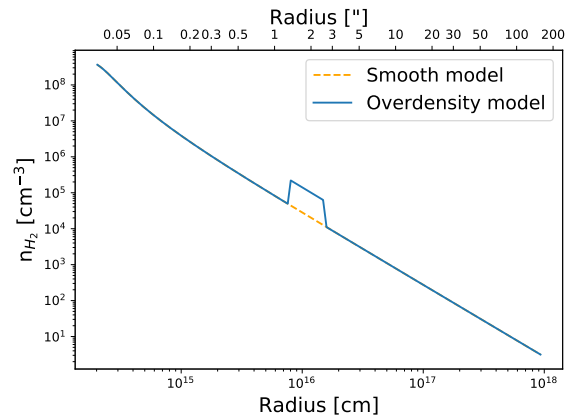


Fig. 7. Radial H_2 number density for both the smooth wind model and the overdensity model.

Table 3. Results of radiative transfer modeling.

Molecule	f_0	R_e (cm)	Overdensity abundance
CS	$(1.20 \pm 0.05) \times 10^{-6}$	7.0×10^{15}	$\times 2$
SiS	$(1.50 \pm 0.05) \times 10^{-6}$	6.0×10^{15}	$\times 3$
³⁰ SiS	$(1.15 \pm 0.05) \times 10^{-7}$	3.5×10^{15}	$\times 1$
²⁹ SiO	$(2.50 \pm 0.10) \times 10^{-7}$	1.4×10^{16}	$\times 1$
H ¹³ CN	$(1.75 \pm 0.05) \times 10^{-7}$	4.7×10^{16}	$\times 1$

Notes. f_0 is the central abundance relative to H_2 and R_e is the e -folding radius. The last column indicates if and with what factor the abundance in the overdensity region has to be increased by multiplication for achieving the best fit.

the smooth-wind models. For SiS and CS, we find that the overdensity model improves the fit to the tail, but not sufficiently to reproduce it entirely. The H_2 number densities for both the smooth wind and overdensity models are plotted in Fig. 7. While testing our models, we found that an overdensity factor of ten for

SiS or eight for CS were better fits, but these overdensity models strongly over-predicted the H¹³CN and ²⁹SiO “tails”. Instead, to find the best fits for SiS and CS, we additionally altered their abundances in the overdensity region. The scaling factors of the altered abundances are listed in the last column of Table 3. We find this approach justified because the same wind overdensity must be applied to all modeled molecules.

In Table 3, we list the best fit models for both the smooth wind model and the overdensity model, based on the vibrational ground state observations of the respective molecules. The presence of the tail and our overdensity model solution complicates the error analysis of the envelope size. However, if we exclude the overdensity model and discuss only the smooth model, we find that the constraints on the envelope size are tighter for the molecules with less prominent tails and less so for the molecules with the most pronounced tails, such as H¹³CN. In fact, we found that it was not possible to fit the tail of H¹³CN simply by increasing the Gaussian e -folding radius, while also providing a good fit to the inner radial points. A Gaussian with a comparable size to the CO envelope (unrealistic in the case of H¹³CN) would still not fit the tail. Hence the need for the overdensity model.

M. Brunner et al.: Molecular line study of the S-type AGB star W Aquilae

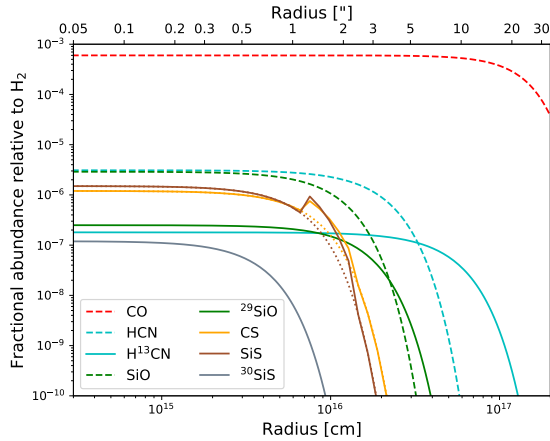


Fig. 8. Radial abundance profile. *Full lines*: molecules observed and modeled in this study, using the overdensity model. Where the abundances differ from the best fitting smooth model, the smooth model is indicated by a dotted line of the same color. *Dashed lines*: molecules modeled by Danilovich et al. (2014).

A comparison of the radial abundance distributions between all modeled molecules as well as some from the earlier study by Danilovich et al. (2014) is presented in Fig. 8. Similarly, in Fig. 9 we plot the best fitting smooth wind and overdensity models against the observed azimuthally averaged radial profiles. There, it is clearly seen that the addition of the overdensity has the most significant impact on the radial profiles of CS and H¹³CN, giving much better fits to the observations from $\sim 1''$ outwards. Below, we discuss the modeling results for the individual spectral lines. In general, the ALMA observations are reasonably well described by the models when looking at the radial intensity profiles, as are the single-dish observations.

5.2.1. CS

For the radiative transfer analysis of CS, we used a molecular data file including the ground- and first excited vibrational state with rotational energy levels from $J = 0$ up to $J = 40$, and their corresponding radiative transitions. Our models include the $8\mu\text{m}$ CS vibrational band. The energy levels, transition frequencies, and Einstein A coefficients were taken from CDMS (Müller et al. 2001, 2005) and the collisional rates were adapted from the Yang et al. (2010) rates for CO with H₂, assuming an H₂ ortho-to-para ratio of three and scaled to represent collisions between CS and H₂.

For the smooth wind model, we found a fractional abundance for CS of $f_0 = 1.20 \times 10^{-6}$ and an e -folding radius $R_e = 7.0 \times 10^{15}$ cm. While this model fits the inner radial profile and the single dish data well, the outer tail was not well-described by this model. For the overdensity model, using the same Gaussian abundance parameters, we found a much-improved fit, which was improved further by increasing the molecular abundance in the overdense region by a factor of two relative to the Gaussian abundance. The line profile and spectra predicted by the best-fitting (overdensity) model are plotted in Figs. 9 and 10, respectively.

5.2.2. SiS

For the radiative transfer analysis of ²⁸SiS, we used a molecular data file including the rotational levels from $J = 0$ up to $J = 40$ for the ground- and first excited vibrational states, and their corresponding radiative transitions. Our models include the $13\mu\text{m}$ SiS vibrational band. The energy levels, transition frequencies and Einstein A coefficients were taken from CDMS (Müller et al. 2001, 2005) and the collisional rates were taken from the Dayou & Balança (2006) rates for SiO with He, scaled to represent collisions between SiS and H₂.

For the smooth wind model, we found a fractional abundance for ²⁸SiS of $f_0 = 1.50 \times 10^{-6}$ and an e -folding radius $R_e = 6.0 \times 10^{15}$ cm. This model agreed with the single-dish observations well, but did not fully agree with the “tail” in the azimuthally averaged radial profile from the ALMA observations. We found the model improved with the inclusion of the overdensity and, as with CS, an increase of abundance in the overdense region. However, we found that the overdensity and especially the increase of abundance in the overdense region, had a significant effect on the low- J SiS lines, in a way that was not seen for the low- J CS lines at similar (or lower) energies. This provided an additional constraint on the extent of the overdense region, which we were unable to constrain based solely on the ALMA data, and on the abundance increase in the overdense region. An increase in abundance by a factor of seven in the overdense region provides the best fit when considering only the ALMA observations, but strongly over-predicts the single dish ($5 \rightarrow 4$) and ($12 \rightarrow 11$) SiS lines. Reducing the overdensity abundance down to a factor of three above the smooth wind Gaussian abundance provides the best possible fit when taking both the ALMA radial profile and the single dish observations into account. The line profile and spectra predicted by the best-fit model are plotted in Figs. 9 and 10, respectively.

For the radiative transfer analysis of ³⁰SiS, we constructed the molecular data file to contain the equivalent energy levels and transitions as the ²⁸SiS file.

The energy levels, transition frequencies and Einstein A coefficients were taken from the JPL molecular spectroscopy database (Pickett et al. 1998) and the same collisional rates as for ²⁸SiS were used, based on rates calculated in Dayou & Balança (2006).

We found a fractional abundance for ³⁰SiS of $f_0 = 1.15 \times 10^{-7}$ and an e -folding radius $R_e = 3.5 \times 10^{15}$ cm, which is in general agreement with the R_e found for ²⁸SiS. The inclusion of the overdensity did not have a significant impact on the ³⁰SiS model fit to the observations, most likely because the ³⁰SiS flux is much weaker, especially in the region where the brighter molecules exhibit a “tail”. As such, we also had no need to increase the ³⁰SiS abundance in the overdense region. In fact, since the ³⁰SiS flux is weak compared to the ²⁸SiS emission at the location of the employed overdensity, testing the ²⁸SiS overdensity and increased overdensity abundance does not produce a visible change in the ³⁰SiS model.

The line profile and spectra predicted by the ³⁰SiS best-fit model are plotted in Figs. 9 and 10. We include a plot of the spectrum at the center of the source convolved with a $0.6''$ beam, in addition to the $4''$ beam (used for the other molecules), since the $0.6''$ beam spectrum has a significantly higher S/N.

5.2.3. ²⁹SiO

We used the same molecular data file as that used for ²⁹SiO radiative transfer modeling in Danilovich et al. (2014). This in-

A&A proofs: manuscript no. WAql-v6-revision_02_final

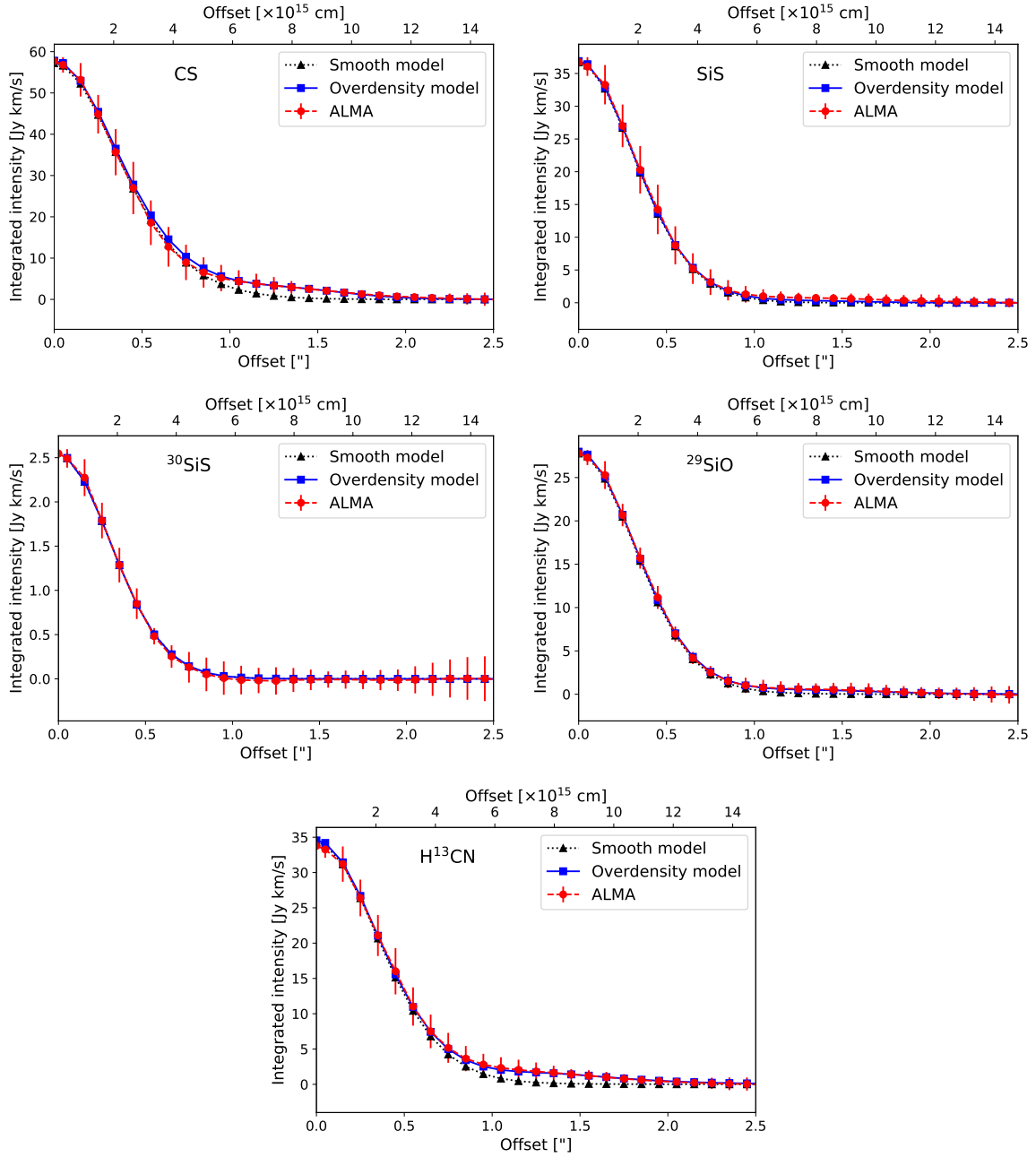


Fig. 9. Radial intensity profiles for the ALMA observations of CS, SiS, ³⁰SiS, ²⁹SiO and H¹³CN (red circles and dashed lines) compared to the best fitting radiative transfer model with an overdensity (blue squares and solid lines), and the best fitting smooth-wind radiative transfer model (black triangles and dotted lines).

cludes the rotational energy levels from $J = 0$ up to $J = 40$ for the ground and first excited vibrational states. Our models include the $8\mu\text{m}$ SiO vibrational band. The collisional rates were also taken from Dayou & Balança (2006).

For the smooth wind model, we found a fractional abundance of ²⁹SiO of $f_0 = 2.50 \times 10^{-7}$ and an e -folding radius

$R_e = 1.4 \times 10^{16}$ cm. The overdensity model provided a better fit to the azimuthally averaged ALMA radial profile, and did not require an additional adjustment to the abundance profile to reproduce the observations. The line profile and spectra predicted by the best-fit model are plotted in Figs. 9 and 10, respectively.

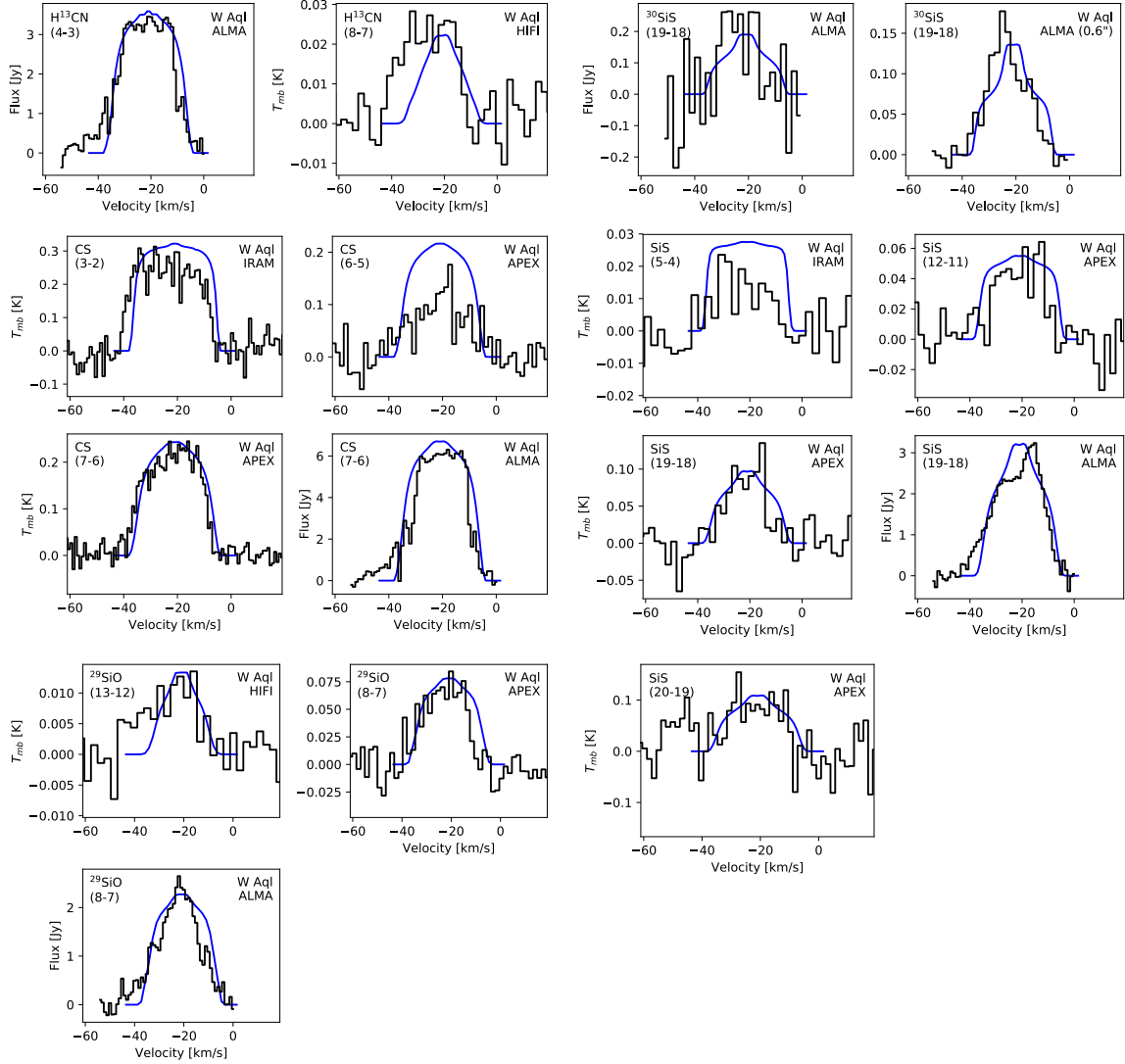
M. Brunner et al.: Molecular line study of the S-type AGB star *W* Aquilae

Fig. 10. Spectra of different molecular transitions of CS, SiS, ^{30}SiS , ^{29}SiO and H^{13}CN (black histograms) compared to the best fitting radiative transfer model (blue solid lines).

Our derived ^{29}SiO e -folding radius is in reasonable agreement with the R_e for the ^{28}SiO model by Danilovich et al. (2014), indicating that ^{28}SiO and ^{29}SiO are co-spatially distributed in the CSE. As an additional test, we re-ran the ^{28}SiO model using the R_e found for ^{29}SiO (and the original $f_0 = 2.9 \times 10^{-6}$ from Danilovich et al. 2014) and found that the smooth wind model was still in good agreement with the single dish ^{28}SiO data, albeit that the low- J single dish data was somewhat over-predicted by the overdensity model.

5.2.4. H^{13}CN

We used the same molecular data file as used for H^{13}CN radiative transfer modeling in Danilovich et al. (2014). This included the rotational energy levels from $J = 0$ up to $J = 29$ for the

ground vibrational state, the CH stretching mode at $3 \mu\text{m}$, and the bending mode at $14 \mu\text{m}$. The bending mode is further divided into the two l -type doubling states. The collisional rates were taken from Dumouchel et al. (2010).

For the smooth wind model, we found a fractional abundance for H^{13}CN of $f_0 = 1.75 \times 10^{-7}$ and an e -folding radius $R_e = 4.7 \times 10^{15}$ cm. H^{13}CN was one of the molecules for which the overdensity model made the most significant improvement to the fit of the model. No additional increase in abundance was required in the overdense region to reproduce the ALMA data. We also re-ran the H^{12}CN model from Danilovich et al. (2014) with our H^{13}CN R_e and the original abundance, $f_0 = 3.1 \times 10^{-6}$, and found that the overdense model still reproduced the $(1 \rightarrow 0)$ line well. The H^{13}CN line profile and spectra are plotted against the model in Figs. 9 and 10, respectively.

6. Discussion

6.1. Comparison with previous studies

With the ALMA observations at hand, the radial emission size for each measured molecular transition can be extracted directly from the observations and provides an important constraint on the radiative transfer models, which usually use empirical scaling relations to approximate the e -folding radii of individual molecules. Additionally, the sensitivity of interferometric observations is superior to single-dish observations, improving the detection threshold and S/N of the observed spectral lines significantly. This also allowed us to determine a model with an overdense region to better represent the ALMA observations — a feature which cannot be discerned from spatially unresolved observations.

Danilovich et al. (2014) modeled several molecules observed in the CSE of W Aql with multiple lines available. For ^{29}SiO and H^{13}CN , they only have one available line each and assume the same e -folding radii as for the respective main isotopologs. We compare the e -folding radius R_e for ^{29}SiO and H^{13}CN measured by this study to the calculated R_e by Danilovich et al. (2014), who use the scaling relations by González Delgado et al. (2003) (for ^{29}SiO , assuming the same radial distribution as for ^{28}SiO) and Schöier et al. (2013) (for H^{13}CN , assuming the same radial distribution as for H^{12}CN) to estimate the e -folding radius. For ^{29}SiO , the results roughly agree with each other, where we get a radius of 1.4×10^{16} cm and Danilovich et al. (2014) derive a radius of 1.0×10^{16} cm. The same is true for the ^{29}SiO abundance, which Danilovich et al. (2014) find to be $(2.3 \pm 0.6) \times 10^{-7}$, which is in agreement within the errors to our derived abundance of $(2.50 \pm 0.1) \times 10^{-7}$. For H^{13}CN , we get a radius of 4.7×10^{16} cm, while Danilovich et al. (2014) base their model on a radius of 1.8×10^{16} cm. Our H^{13}CN radius is a factor of approximately three larger than their calculated one. Additionally, we tested the H^{12}CN model from Danilovich et al. (2014) (using an abundance of $f_0 = 3.1 \times 10^{-6}$) with the R_e for H^{13}CN extracted from this study. We found that that model remained in good agreement with both the higher- J lines, such as $(13 \rightarrow 12)$, and the low- J lines, including $(1 \rightarrow 0)$. The H^{13}CN abundance derived by Danilovich et al. (2014) is $(2.8 \pm 0.8) \times 10^{-7}$, which is slightly higher than our result of $(1.75 \pm 0.05) \times 10^{-7}$. Since the model from Danilovich et al. (2014) was based only on one single line that showed a particularly pronounced blue wing excess and the fit was based on the integrated intensity, we expect that this discrepancy is caused by the uncertainty of the single-dish observations.

Schöier et al. (2007) present observations and detailed radiative transfer modeling of SiS for a sample of M-type and carbon AGB stars with varying C/O ratios (no S-type stars included), and assume that the SiS radius would be the same as for SiO, and therefore using the scaling relation of González Delgado et al. (2003) to calculate the e -folding radius. With this in mind, we compare the calculated SiO radius of 1.0×10^{16} cm by Danilovich et al. (2014) with our derived SiS radius of 6.0×10^{15} cm, which is a factor of 1.7 smaller. Additionally, Schöier et al. (2007) needed to add a compact, highly abundant SiS component close to the star to better fit their models, which we do not require. Indeed our Gaussian abundance distribution fits both the ALMA and single-dish data well, with the overdensity model only required to fit the outer regions of the ALMA radial profile.

Decin et al. (2008) perform a critical density analysis for SiO, HCN, and CS, which they detect through single-dish observations of a sample of AGB stars — including W Aql — to determine the formation region of the molecular lines. They use

two different methods to derive the maximum radius of the emission region (in contrast to the e -folding radius): radiative transfer modeling with the GASTRONoM code (Decin et al. 2006) for collisional excitation, and calculations for radiative excitation only. For CS, they derive 1.68×10^{15} cm and 2.64×10^{14} cm, respectively, using a distance of 230 pc (with a luminosity of $6800 L_{\odot}$ and an effective temperature of 2800 K). We derive 7.0×10^{15} cm, which is a factor of 4 and 27 larger than their reported values. The different stellar parameters and model setup make it difficult to compare the resulting radii of the emission regions, extracted from different models. As a rough estimate, we scale the reported sizes linearly with the distance and arrive at the conclusion that our CS radius is still bigger than the radii reported by Decin et al. (2008). Comparing their HCN radii — 9.6×10^{14} cm and 2.4×10^{14} cm — to our measured H^{13}CN radius of 4.7×10^{16} cm, we get a substantially larger radius, which also holds for the linear distance scaling. The same is true for the comparison of their SiO radii — 9.6×10^{14} cm and 2.16×10^{14} cm — to our measured ^{29}SiO radius of 1.4×10^{16} cm.

6.2. Limitations of radiative transfer models

The most obvious limitation of the radiative transfer models is that they assume spherical symmetry, which, as we can see from the extended emission in the channel maps, is clearly not a precise description of the more complex emission. This issue becomes more important for the strongest spectral lines, those of CS and H^{13}CN , where the asymmetric features are more pronounced in the observations. For those lines, we see a clear difference between the smooth wind models and the observed radial intensity profiles at distances greater than $1''$ from the star (Fig. 9). This is also visible in a much weaker form for the SiS and ^{29}SiO lines (also Fig. 9). Nevertheless, Ramstedt et al. (2017) show that the clearly visible and pronounced arc structures in the CO density distribution are not very pronounced in the overall radial density profile, but are simply represented by rather weak features on top of a smooth extended component. Here, in our overdensity model, we add a higher-density component to the smooth wind model (see Fig. 7) in a region that matches the ALMA radial profiles. Although the actual overdense region is unlikely to be spherically symmetric in reality (as the arcs seen in the CO emission by Ramstedt et al. 2017, are not), we find it to be well fit by our spherically symmetric model.

Another limitation is the direct comparison of often noisy and low-resolution single-dish spectra (often subject to uncertain calibration) with high S/N and high-resolution ALMA spectra as model input. The CS single-dish data in particular generally has a low S/N, and two of the single-dish spectra are not well fitted (Fig. 10). Since the single-dish data were taken at many different epochs, the stellar variability might have an influence on the extracted spectra as well (e.g., Teyssier et al. 2015; Cernicharo et al. 2014). Additionally, since we are probing high-spatial-resolution asymmetric and clumpy emission with the ALMA observations, the line profiles from the symmetric radiative transfer models are unlikely to be completely representative of the real complexity of the CSE around W Aql and therefore do not fit the observations perfectly. Nevertheless, the general agreement of the models with observations is good.

6.3. Comparison with chemical models

From the theoretical models of Cherchneff (2006) and a sample of observations by Bujarrabal & Cernicharo (1994) and Schöier

et al. (2007), it is evident that the SiS abundance is sensitive to the chemical type of AGB stars, with carbon stars showing generally higher abundances than M-type stars. The mean fractional SiS abundances of carbon and M-type stars reported by Schöier et al. (2007) are 3.1×10^{-6} and 2.7×10^{-7} , respectively. Our derived SiS abundance of 1.5×10^{-6} for W Aql as an S-type star falls close to the lower boundary of the expected region of carbon AGB stars (compared with Fig. 2 of Schöier et al. 2007). Predicted by the non-LTE chemical models of Cherchneff (2006), CS should be found in high abundance for all types of AGB stars in the inner wind, with a generally higher abundance of CS for carbon stars than M-type stars. The formation of CS is linked to HCN, which is predicted to be present in comparable abundances. As discussed by Cherchneff (2006), in their models, the maximum abundance of HCN – and therefore CS – is reached for S-type AGB stars. In Fig. 8, one can see that, for W Aql, the radial abundance profile of HCN (as derived by Danilovich et al. 2014) is indeed comparable to the profile of CS (excluding the overdensity enhancement), which is generally of slightly lower abundance and extends out to a slightly smaller radius. The abundance ratio of those molecules is $\text{HCN}/\text{CS} = 3.1 \times 10^{-6} / 1.3 \times 10^{-6} \approx 2.4$. In the theoretical models of Cherchneff (2006), the HCN/CS ratio for a “typical” AGB with a C/O ratio between 0.75 and 1 lies between 5.34 and 0.28, at radii larger than $5 R_*$. The best fitting theoretical HCN/CS ratio to our modeled ratio of 2.4 would be reached for a C/O ratio somewhere between 0.90 and 0.98. The theoretical HCN/CS ratio of 0.28 for a C/O ratio of 1 does not fit our models. A very similar value can be derived from thermodynamic equilibrium calculations (Gobrecht, priv. comm.), which yield a HCN abundance of 4.31×10^{-8} and a CS abundance of 1.38×10^{-7} , resulting in a HCN/CS ratio of 0.31. It must be noted, however, that the chemical models are focused on the innermost winds and our observations detect molecular emission as far away from the star as $\sim 4''$. Additionally, the stellar temperature can affect the chemical equilibrium and therefore the chemical abundances.

On a general note on sulphur bearing molecules in CSEs of AGB stars, Danilovich et al. (2016) found a very different S chemistry between low mass-loss rate and high mass-loss rate M-type stars when examining SO and SO₂, which was not predicted by chemical models.

6.4. Isotopic ratios

6.4.1. Silicon

Previous models by Danilovich et al. (2014) estimate a ^{28}SiO abundance of 2.9×10^{-6} , which we can use to derive the $^{28}\text{SiO}/^{29}\text{SiO}$ ratio, resulting in a value of 11.6. From our model estimates, we find the abundance ratio of $^{28}\text{SiS}/^{30}\text{SiS} = 13.0$, roughly corresponding to half of the $^{28}\text{Si}/^{30}\text{Si}$ ratio predicted by AGB stellar evolution models (Cristallo et al. 2015; Karakas 2010) and half of the value given by the solar abundances (Asplund et al. 2009). By assuming that both SiO and SiS ratios are good tracers for the Si ratios, we can approximate the $^{29}\text{Si}/^{30}\text{Si}$ ratio for W Aql, which results in a value of 1.1. For comparison, the solar $^{29}\text{Si}/^{30}\text{Si}$ ratio, as derived by Asplund et al. (2009) is 1.52, which is also consistent with the ratio derived for the ISM (Wolff 1980; Penzias 1981). Peng et al. (2013) investigate the $^{29}\text{Si}/^{30}\text{Si}$ ratio for 15 evolved stars and come to the conclusion that the older low-mass oxygen-rich stars in their sample have lower $^{29}\text{Si}/^{30}\text{Si}$ ratios, but the ratios are not influenced strongly by AGB evolution and merely reflect the interstellar environment in which the star has been born. The only S-type star in their sam-

ple, χ Cyg, shows a $^{29}\text{Si}/^{30}\text{Si}$ ratio of 1.1, which is incidentally identical to our derived value for W Aql. A bigger sample of Si isotopic ratios derived for S-type stars would be needed to draw any conclusions on the possible AGB evolutionary effects.

6.4.2. Carbon

As described by Saberi et al. (2017) for the carbon AGB star R Scl, the $\text{H}^{12}\text{CN}/\text{H}^{13}\text{CN}$ ratio is a very good tracer for the $^{12}\text{C}/^{13}\text{C}$ ratio, giving even more plausible results than estimates from the CO isotopic ratio in some cases. Using modeling results by Danilovich et al. (2014) for H^{12}CN , which has an abundance of $(3.1 \pm 0.1) \times 10^{-6}$, and the H^{13}CN abundance presented in this paper, we derive a $\text{H}^{12}\text{CN}/\text{H}^{13}\text{CN}$ ratio of 17 ± 6 (with the error mainly dominated by the H^{12}CN model), which can be used to estimate the $^{12}\text{C}/^{13}\text{C}$ ratio. This result differs by a factor of 1.7 to 1.5 from the $^{12}\text{C}/^{13}\text{C}$ ratio estimated from the CO isotopolog ratio by Danilovich et al. (2014) and Ramstedt & Olofsson (2014), who report a ratio of 29 and 26, respectively. Ramstedt & Olofsson (2014) also present C isotopic ratios for 16 other S-type AGB stars (in addition to 19 C- and 19 M-type AGB stars) and the resulting median carbon isotopic ratio for S-type stars is reported to be 26, which is also their derived value for W Aql. In general, the $^{12}\text{C}/^{13}\text{C}$ ratio increases following the evolution from M- to S- to C-type stars, since ^{12}C is primarily produced in the He burning shell of the star and will be dredged up to the surface through subsequent thermal pulses. Therefore, the $^{12}\text{C}/^{13}\text{C}$ ratio can be used as an indicator for the AGB evolutionary stage of a star.

7. Conclusions

We present ALMA observations of a total of eight molecular lines of the species CS, SiS, SiO and H^{13}CN , which are found in the close CSE of the S-type binary AGB star W Aql. The emission is resolved for almost all lines and a compact Gaussian emission component is surrounded by weak asymmetric emission, showing an elongation in the direction of the binary orbit. Adding an additional delta function emission component to the models at the same position as the Gaussian significantly improves the fits, carried out in the uv plane. Emission peaks in molecular emission out to approximately $2\text{--}3''$ coincide with the CO distribution. The spectral lines – especially the strongest four – are partly very asymmetric, with SiS standing out of the sample with a very distinct peak at the red-shifted velocities. We successfully model the circumstellar abundance and radial emission size of CS, SiS, ^{30}SiS , ^{29}SiO and H^{13}CN – mainly based on high-resolution sub-millimeter observations by ALMA and supplemented by archival single-dish observations – in the innermost few arcseconds of the CSE around the S-type AGB star W Aql. We produce two models, one assuming a smooth outflow, and one which approximates the asymmetries seen in the outflow by the inclusion of an overdense component, and which better fits the ALMA data. We compare the resultant radial abundance distributions to previous modeling and theoretical predictions, and find that our results are in agreement with previous studies. For some isotopologs, such as ^{29}SiO and H^{13}CN , previous studies worked with the assumption of a radial distribution identical to their main isotopologs, ^{28}SiO and H^{12}CN . We find that our modeled radial distribution of the ^{29}SiO and H^{13}CN isotopologs, which is constrained by the resolved ALMA observations, is different to the main isotopologs, with both rarer isotopologs having a larger radius than previously found for the most common isotopolog counterparts.

A&A proofs: manuscript no. WAql-v6-revision_02_final

By using the spatially resolved ALMA data, we can constrain the radial emission profile directly, which improves the independence of our models by reducing the number of input assumptions. Additionally, we need to develop improved models, which can take asymmetries into account. This and future high-resolution high sensitivity spectral scans of CSEs around AGB stars will provide more accurate input to chemical modeling and help us understand the chemical network of elements in these environments.

Acknowledgements. This paper makes use of the following ALMA data: ADS/JAO.ALMA#2012.1.00524.S. ALMA is a partnership of ESO (representing its member states), NSF (USA) and NINS (Japan), together with NRC (Canada), NSC and ASIAA (Taiwan), and KASI (Republic of Korea), in co-operation with the Republic of Chile. The Joint ALMA Observatory is operated by ESO, AUI/NRAO and NAOJ. We want to thank the Nordic ARC Node for valuable support concerning ALMA data reduction and uv-fitting, and David Gobrecht for his input to the chemical discussion. MB acknowledges the support by the uni:docs fellowship and the dissertation completion fellowship of the University of Vienna. EDB is supported by the Swedish National Space Board. TD acknowledges support from the Fund of Scientific Research Flanders (FWO).

References

- Asplund, M., Grevesse, N., Sauval, A. J., & Scott, P. 2009, *ARA&A*, 47, 481
- Bieging, J. H., Kneec, L. B. G., Latter, W. B., & Olofsson, H. 1998, *A&A*, 339, 811
- Bladh, S. & Höfner, S. 2012, *A&A*, 546, A76
- Bladh, S., Höfner, S., Aringer, B., & Eriksson, K. 2015, in *Astronomical Society of the Pacific Conference Series*, Vol. 497, *Why Galaxies Care about AGB Stars III: A Closer Look in Space and Time*, ed. F. Kerschbaum, R. F. Wing, & J. Hron, 345
- Bujarrabal, V. & Cernicharo, J. 1994, *A&A*, 288, 551
- Cernicharo, J., Teyssier, D., Quintana-Lacaci, G., et al. 2014, *ApJ*, 796, L21
- Cherchneff, I. 2006, *A&A*, 456, 1001
- Cristallo, S., Straniero, O., Piersanti, L., & Gobrecht, D. 2015, *ApJS*, 219, 40
- Cutri, R. M., Skrutskie, M. F., van Dyk, S., et al. 2003, *VizieR Online Data Catalog*, 2246, 0
- Danilovich, T., Bergman, P., Justanont, K., et al. 2014, *A&A*, 569, A76
- Danilovich, T., De Beck, E., Black, J. H., Olofsson, H., & Justanont, K. 2016, *A&A*, 588, A119
- Danilovich, T., Ramstedt, S., Gobrecht, D., et al. 2018, *A&A*, submitted
- Danilovich, T., Teyssier, D., Justanont, K., et al. 2015, *A&A*, 581, A60
- Dayou, F. & Balança, C. 2006, *A&A*, 459, 297
- De Beck, E., Decin, L., de Koter, A., et al. 2010, *A&A*, 523, A18
- De Nutte, R., Decin, L., Olofsson, H., et al. 2017, *A&A*, 600, A71
- Decin, L., Cherchneff, I., Hony, S., et al. 2008, *A&A*, 480, 431
- Decin, L., Hony, S., de Koter, A., et al. 2006, *A&A*, 456, 549
- Dumouchel, F., Faure, A., & Lique, F. 2010, *MNRAS*, 406, 2488
- Feast, M. W. & Whitelock, P. A. 2000, *MNRAS*, 317, 460
- Glass, I. S. & Evans, T. L. 1981, *Nature*, 291, 303
- González Delgado, D., Olofsson, H., Kerschbaum, F., et al. 2003, *A&A*, 411, 123
- Groenewegen, M. A. T., Waelkens, C., Barlow, M. J., et al. 2011, *A&A*, 526, A162
- Habing, H. J. & Olofsson, H., eds. 2003, *Asymptotic giant branch stars*
- Höfner, S. 2008, *A&A*, 491, L1
- Höfner, S. 2015, in *Astronomical Society of the Pacific Conference Series*, Vol. 497, *Why Galaxies Care about AGB Stars III: A Closer Look in Space and Time*, ed. F. Kerschbaum, R. F. Wing, & J. Hron, 333
- Karakas, A. I. 2010, *MNRAS*, 403, 1413
- Keenan, P. C. & Boeshaar, P. C. 1980, *ApJS*, 43, 379
- Knapp, G. R., Young, K., Lee, E., & Jorissen, A. 1998, *ApJS*, 117, 209
- Lindqvist, M., Schöier, F. L., Lucas, R., & Olofsson, H. 2000, *A&A*, 361, 1036
- Maercker, M., Schöier, F. L., Olofsson, H., Bergman, P., & Ramstedt, S. 2008, *A&A*, 479, 779
- Maercker, M., Vlemmings, W. H. T., Brunner, M., et al. 2016, *A&A*, 586, A5
- Martí-Vidal, I., Pérez-Torres, M. A., & Lobanov, A. P. 2012, *A&A*, 541, A135
- Martí-Vidal, I., Vlemmings, W. H. T., Muller, S., & Casey, S. 2014, *A&A*, 563, A136
- Mayer, A., Jorissen, A., Kerschbaum, F., et al. 2013, *A&A*, 549, A69
- Menten, K. M., Wyrowski, F., Alcolea, J., et al. 2010, *A&A*, 521, L7
- Müller, H. S. P., Schlöder, F., Stutzki, J., & Winnewisser, G. 2005, *Journal of Molecular Structure*, 742, 215
- Müller, H. S. P., Thorwirth, S., Roth, D. A., & Winnewisser, G. 2001, *A&A*, 370, L49
- Neufeld, D. A., Gusdorf, A., Güsten, R., et al. 2014, *ApJ*, 781, 102
- Olofsson, H., González Delgado, D., Kerschbaum, F., & Schöier, F. L. 2002, *A&A*, 391, 1053
- Patel, N. A., Young, K. H., Gottlieb, C. A., et al. 2011, *ApJS*, 193, 17
- Peng, T.-C., Humphreys, E. M. L., Testi, L., et al. 2013, *A&A*, 559, L8
- Penzias, A. A. 1981, *ApJ*, 249, 513
- Pickett, H. M., Poynter, R. L., Cohen, E. A., et al. 1998, *J. Quant. Spectr. Rad. Transf.*, 60, 883
- Ramstedt, S., Maercker, M., Olofsson, H., & Schöier, F. L. 2011, *A&A*, 531, A148
- Ramstedt, S., Mohamed, S., Vlemmings, W. H. T., et al. 2017, *A&A*, 605, A126
- Ramstedt, S. & Olofsson, H. 2014, *A&A*, 566, A145
- Ramstedt, S., Schöier, F. L., & Olofsson, H. 2009, *A&A*, 499, 515
- Rybicki, G. B. & Hummer, D. G. 1991, *A&A*, 245, 171
- Saberi, M., Maercker, M., De Beck, E., et al. 2017, *A&A*, 599, A63
- Schmidt, M. R., He, J. H., Szczerba, R., et al. 2016, *A&A*, 592, A131
- Schöier, F. L., Bast, J., Olofsson, H., & Lindqvist, M. 2007, *A&A*, 473, 871
- Schöier, F. L., Ramstedt, S., Olofsson, H., et al. 2013, *A&A*, 550, A78
- Schöier, F. L., Ryde, N., & Olofsson, H. 2002, *A&A*, 391, 577
- Tatebe, K., Chandler, A. A., Hale, D. D. S., & Townes, C. H. 2006, *ApJ*, 652, 666
- Teyssier, D., Cernicharo, J., Quintana-Lacaci, G., et al. 2015, in *Astronomical Society of the Pacific Conference Series*, Vol. 497, *Why Galaxies Care about AGB Stars III: A Closer Look in Space and Time*, ed. F. Kerschbaum, R. F. Wing, & J. Hron, 43
- Uttenhaler, S. 2013, *A&A*, 556, A38
- Van Eck, S., Neyskens, P., Jorissen, A., et al. 2017, *A&A*, 601, A10
- Whitelock, P. A., Feast, M. W., & van Leeuwen, F. 2008, *MNRAS*, 386, 313
- Wolff, R. S. 1980, *ApJ*, 242, 1005
- Yang, B., Stancil, P. C., Balakrishnan, N., & Forrey, R. C. 2010, *ApJ*, 718, 1062
- Zijlstra, A. A., Bedding, T. R., Markwick, A. J., et al. 2004, *MNRAS*, 352, 325

M. Brunner et al.: Molecular line study of the S-type AGB star W Aquilae

Appendix A: Channel maps for strong spectral lines

Appendix B: Results for weak spectral lines

Appendix C: uv-fitting: super-resolution and uncertainties

Appendix D: List of archival spectral line observations

As has been discussed in Martí-Vidal et al. (2012), high S/N interferometric observations may encode information about source substructures (much) smaller than the diffraction limit of the interferometer. Extracting such information, though, implies the use of *a priori* assumptions related to the source brightness distribution (e.g., the assumption of a Gaussian intensity distribution that we are using in our modeling). As long as the true source structure obeys these *a priori* assumptions (at least to the extent of the structure sizes being probed in the visibility analysis), it is possible to retrieve structure information that roughly scales as the diffraction limit divided by the square root of the S/N (see, e.g., Eq. 7 of Martí-Vidal et al. 2012). We notice, though, that this is an approximate rule of thumb that may be corrected by a factor of several, since the actual over-resolution power may depend on the baseline distribution of the array (i.e., the factor β in Eq. 7 of Martí-Vidal et al. 2012).

The modeling performed by *uvmultifit* (Martí-Vidal et al. 2014) estimates the uncertainties of the fitted parameters from the curvature of the χ^2 distribution at its minimum via the diagonal elements of the post-fit covariance matrix. The uncertainties provided in this way assume that the model used in the fit is *correct and able to describe the bulk of the visibility signal*, meaning that the reduced χ^2 can be assumed to be similar to its expected value of unity.

This assumption may result in underestimates of the parameter uncertainties *if* the model used in the fitting is incorrect. One way to test whether our fitting model is able to describe the bulk of the visibility function is to assess the post-fit residuals in the image plane. We show these residuals for a selection of two channels in the SiS line in Fig. C.1 (left). The intensity distribution of the residuals can be well characterized by Gaussian noise (Fig. C.1, right), which is indicative of a successful fit.

In order to further assess our size estimates and uncertainties, we have performed a Monte Carlo analysis of our Gaussian source model plus additional delta component across the full parameter space (i.e., varying the peak position, flux density, and size with a random exploration), to test how the χ^2 (and hence the probability density) varies in the neighborhood of the best-fit parameter values. We show the resulting *probability density functions* (PDF) for channels 13 and 20 in Fig. C.2. We notice that the standard assumptions of *uvmultifit* are applied here (i.e., a reduced χ^2 of 1 is assumed, which is justified by the post-fit residuals; see Fig. C.1). The crossing points between the 3σ deviations of the source size (vertical dashed lines) and the 3σ probability cutoff for a Gaussian PDF (horizontal dashed line) roughly coincide with the crossing points between the 3σ source-size deviation and the PDF retrieved with *uvmultifit*.

We can therefore conclude that, as long as the Gaussian plus delta component brightness distribution is a good approximation of the source structure, the source sizes (and their uncertainties) obtained with *uvmultifit* are correct. If the source shape were to not resemble a Gaussian brightness distribution, but were closer to, say, a disk or a filled sphere, there would be a *global systematic bias* in all source sizes reported here, even though the relative values among frequency channels (i.e., the frequency dependence of the source sizes) would still be correct.

A&A proofs: manuscript no. WAql-v6-revision_02_final

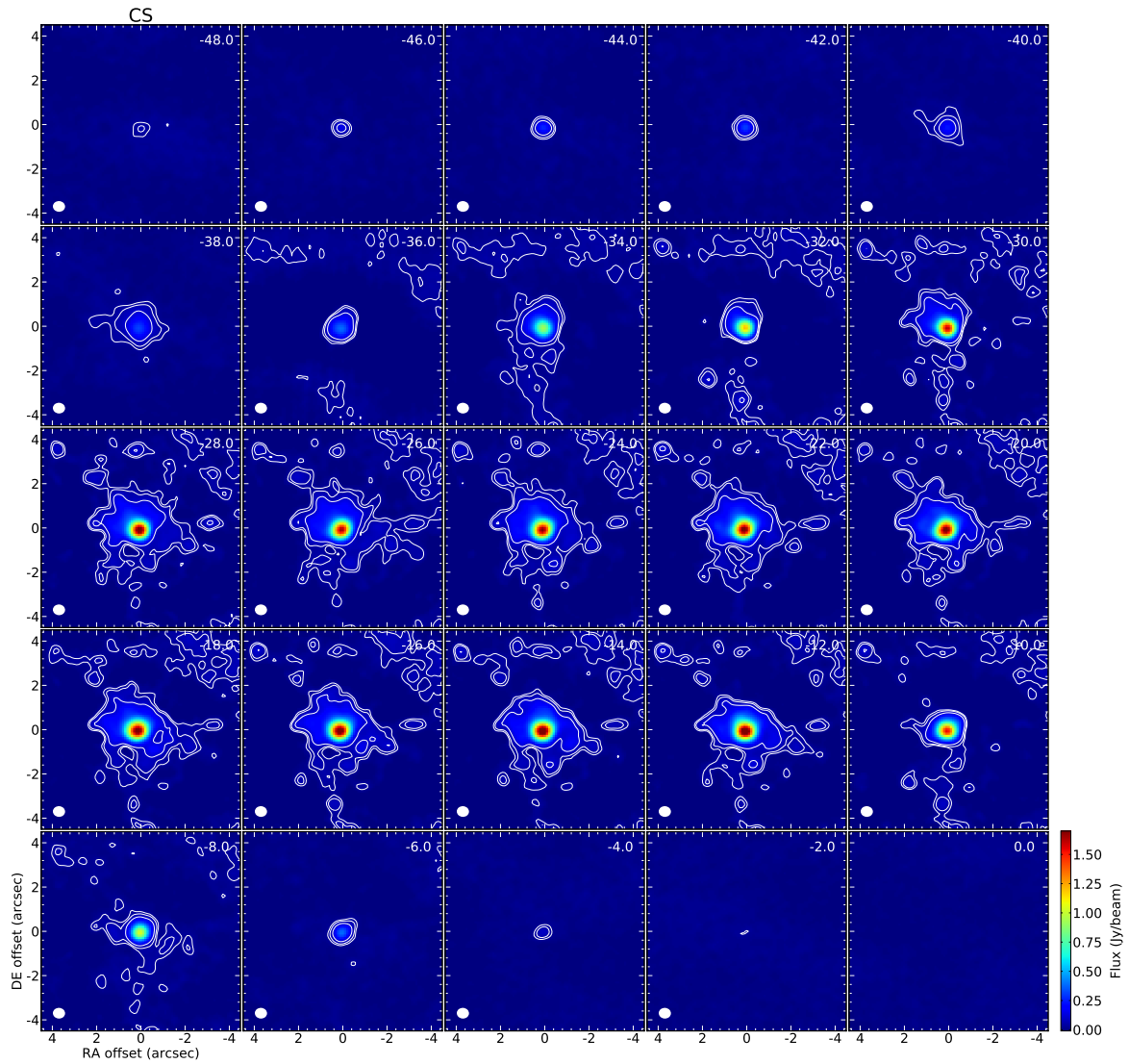


Fig. A.1. Channel map for the CS spectral line. The velocity resolution is 1 km s^{-1} , only every second channel is plotted. The stellar velocity is at about -21 km s^{-1} . The beam size is given in the lower left and the white contours are plotted for 3, 5, and 10σ rms (measured from line free channels). North is up and east is left.

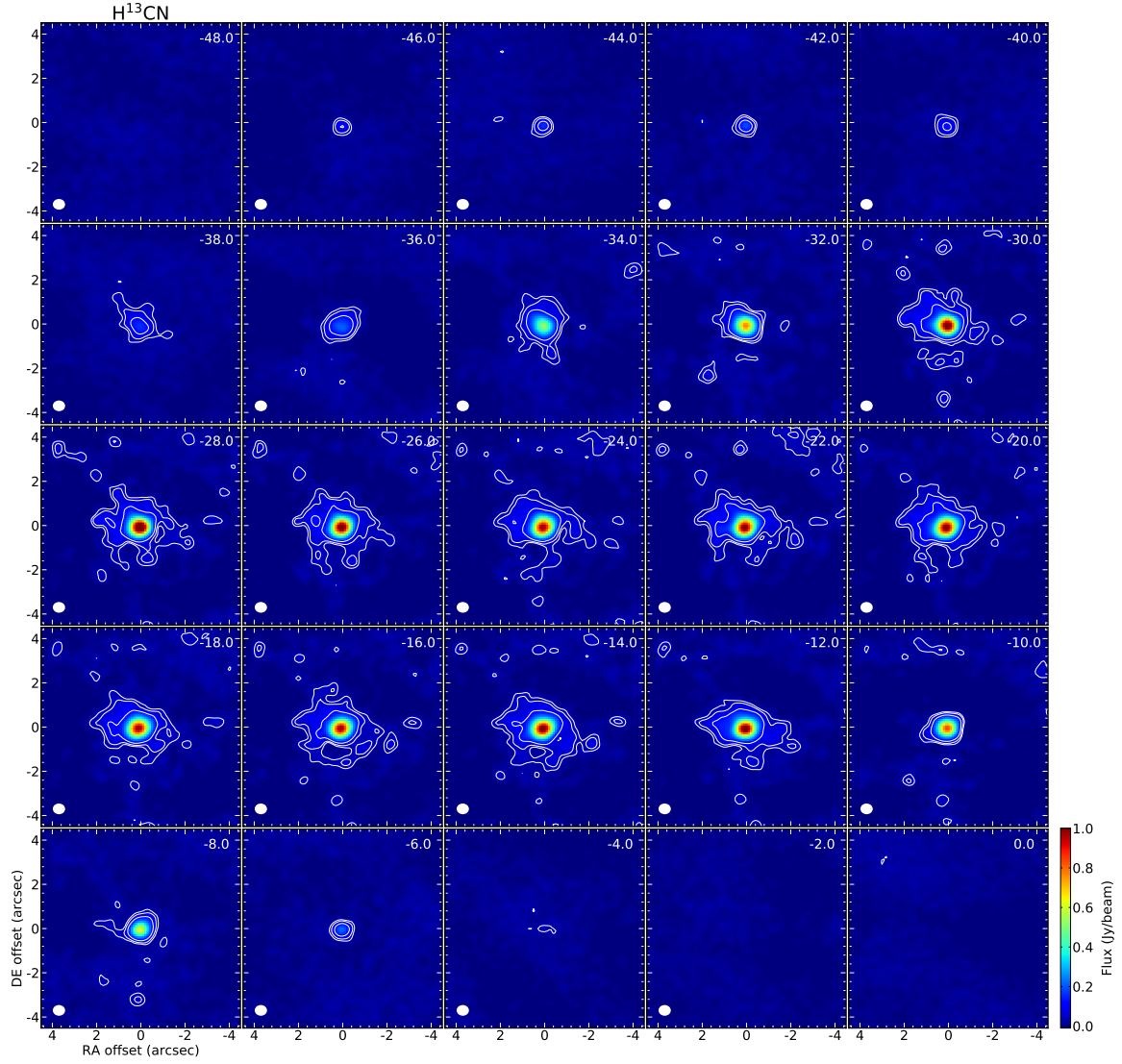
M. Brunner et al.: Molecular line study of the S-type AGB star *W* Aquilae

Fig. A.2. Channel map for the H^{13}CN spectral line. The velocity resolution is 1 km s^{-1} , only every second channel is plotted. The stellar velocity is at about -21 km s^{-1} . The beam size is given in the lower left and the white contours are plotted for 3, 5, and 10σ rms (measured from line free channels). North is up and east is left.

A&A proofs: manuscript no. WAql-v6-revision_02_final

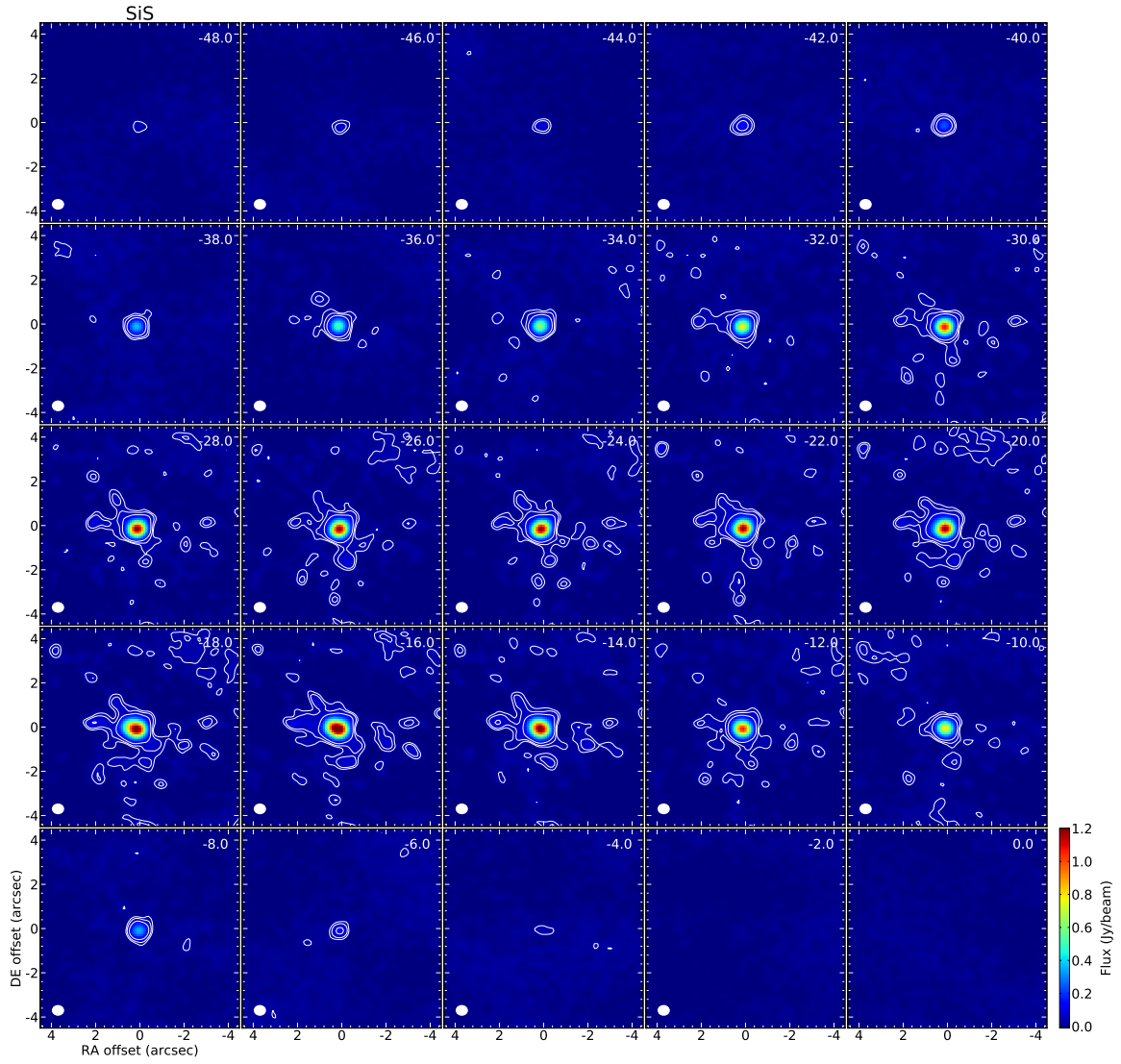


Fig. A.3. Channel map for the SiS spectral line. The velocity resolution is 1 km s^{-1} , only every second channel is plotted. The stellar velocity is at about -21 km s^{-1} . The beam size is given in the lower left and the white contours are plotted for 3, 5, and 10σ rms (measured from line free channels). North is up and east is left.

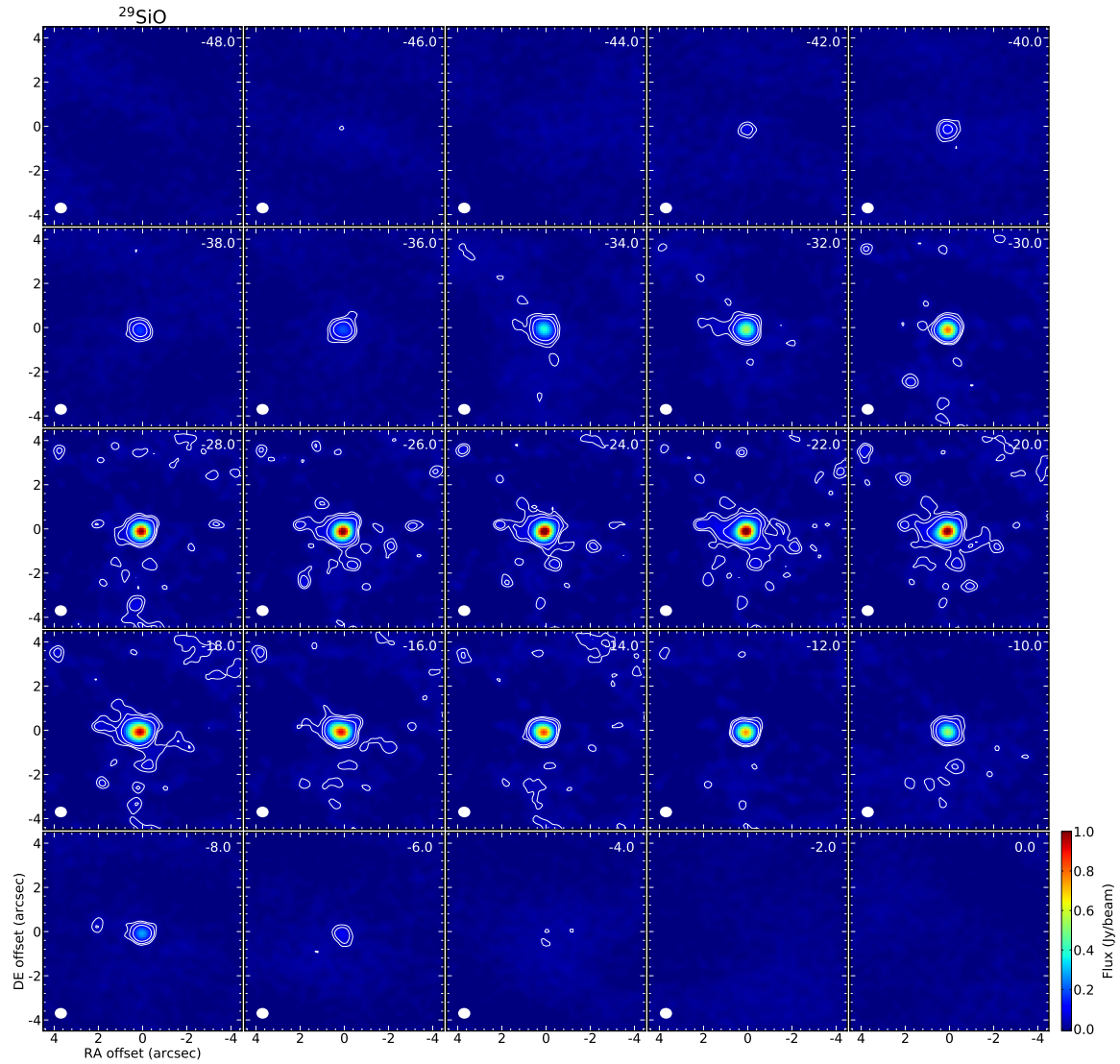
M. Brunner et al.: Molecular line study of the S-type AGB star *W* Aquilae

Fig. A.4. Channel map for the ^{29}SiO spectral line. The velocity resolution is 1 km s^{-1} , only every second channel is plotted. The stellar velocity is at about -21 km s^{-1} . The beam size is given in the lower left and the white contours are plotted for 3, 5, and 10σ rms (measured from line free channels). North is up and east is left.

A&A proofs: manuscript no. WAql-v6-revision_02_final

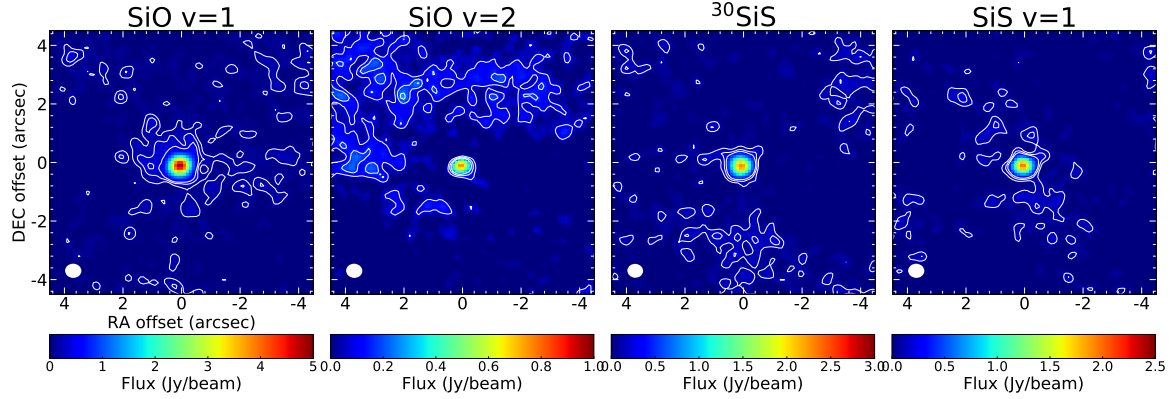


Fig. B.1. ALMA integrated intensity (moment 0) maps of SiO $v=1$ (8–7), SiO $v=2$ (8–7), ^{30}SiS (19–18) and SiS $v=1$ (19–18) emission around W Aql. The ALMA beam is given in the lower-left corner. Contours are given in white for 1, 2, and 3σ rms. North is up and east is left.

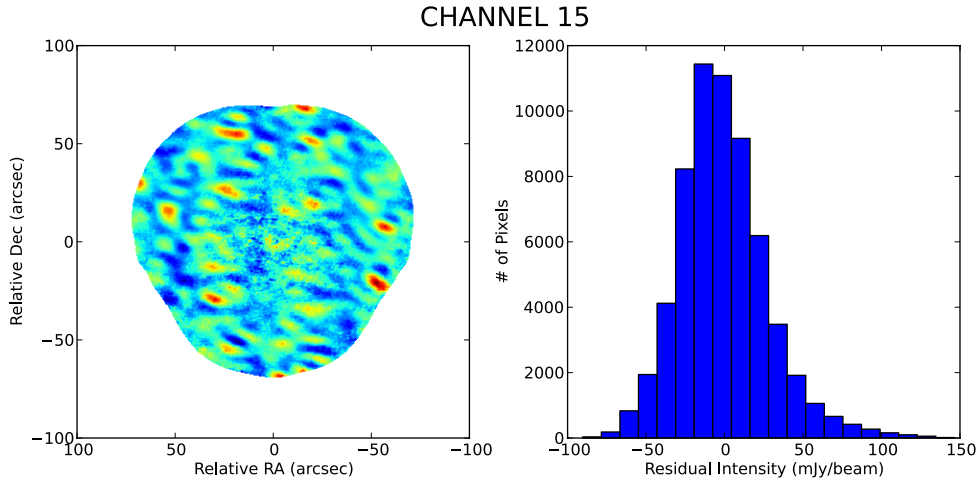


Fig. C.1. Left: Post-fit residual image for channel 15 (stellar velocity), using natural weighting (i.e., to maximise the detection sensitivity for any flux-density contribution left in the fitting). Right: Histogram of the post-fit image residuals.

Table D.1. Archival observations.

Molecule	Transition	Frequency [GHz]	Telescope	θ [$''$]	I_{mb} [K km s $^{-1}$]	Reference
CS	3 \rightarrow 2	146.969	IRAM	17	6.96	Danilovich et al. (2018, submitted)
	6 \rightarrow 5	293.912	APEX	21	2.73	APEX Archive
	7 \rightarrow 6	342.883	APEX	18	5.69	APEX Archive
SiS	5 \rightarrow 4	90.772	IRAM	27	0.35	Danilovich et al. (2018, submitted)
	12 \rightarrow 11	217.818	APEX	29	3.37	Danilovich et al. (2018, submitted)
	19 \rightarrow 18	344.779	APEX	18	1.58	Danilovich et al. (2018, submitted)
	20 \rightarrow 19	362.907	APEX	17	2.5	APEX Archive
^{29}SiO	13 \rightarrow 12	557.179	HIFI	38	0.25	Danilovich et al. (2014)
	8 \rightarrow 7	344.226	APEX	18	1.35	APEX Archive
H^{13}CN	8 \rightarrow 7	1151.452	HIFI	18.4	0.63	Danilovich et al. (2014)

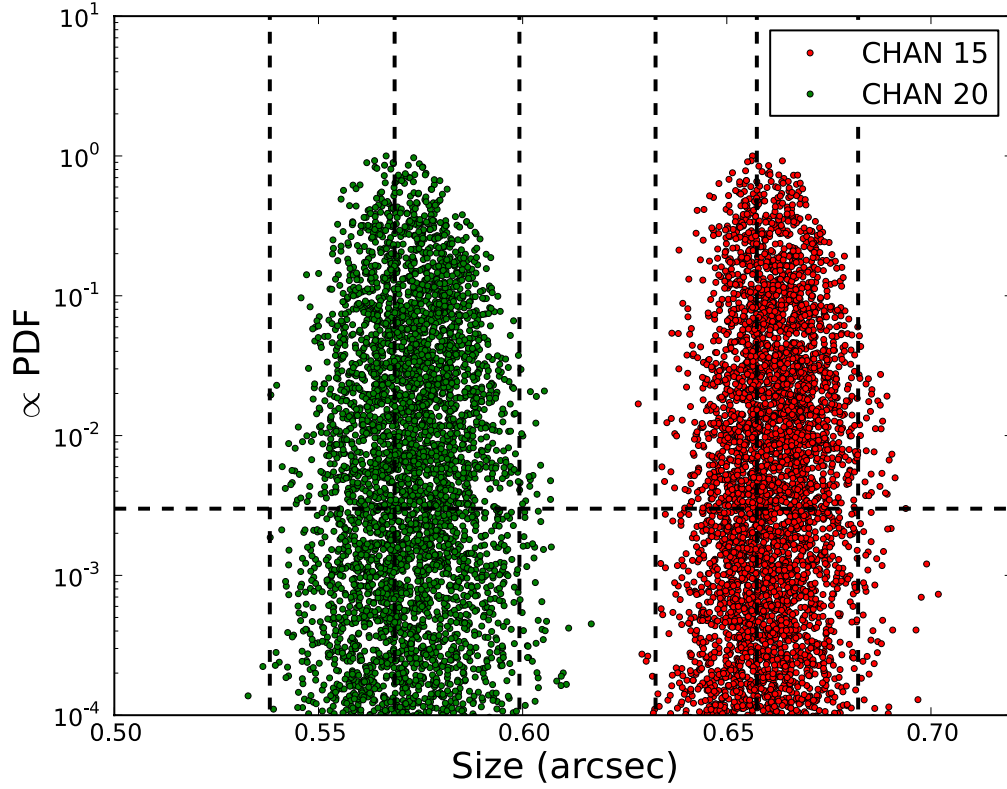
M. Brunner et al.: Molecular line study of the S-type AGB star *W* Aquilae

Fig. C.2. Probability density distributions from our model-fitting for the SiS line of channels 15 and 20, using a Gaussian source model with addition of a delta function model. The vertical dashed lines indicate the estimated best-fit values and their $\pm 3\sigma$ deviations. The horizontal dashed line is set to 3×10^{-3} (i.e., the probability density corresponding to the 3σ cutoff of a Gaussian probability distribution). The peaks of the PDFs have been further scaled to 1, for clarity.

Chapter 5

The elliptical detached shell around TX Piscium (Paper II, submitted)

Title: *ALMA observations of the “fresh” carbon AGB star TX Piscium: The discovery of an elliptical detached shell*

Authors: M. Brunner, M. Mecina, M. Maercker and F. Kerschbaum

Year: 2018

Journal: Astronomy and Astrophysics, submitted on June 18th 2018

The CSE of TX Psc was observed with ALMA to investigate the molecular counterpart to a ring-like dust structure around the star, which was observed with *Herschel/PACS* in the thermal infrared. This ring-like structure is spatially separated from the ISM interaction region and has a radius of roughly $17''$. For this publication, we mapped the CO(2–1) emission of the CSE in a mosaic field of $45'' \times 45''$ with a spatial resolution of $1''$ and discovered an elliptical detached shell at the same position as the dust structure has been detected with lower resolution. Not only was TX Psc not known to belong to the detached shell sources, but there are no reports of an elliptical detached shell up to now, whatsoever. We discuss the possible formation scenarios of an elliptical detached shell with respect to stellar properties, evolutionary status and wind interaction processes such as binarity.

Personal contribution: As principal investigator of the observing program, I was responsible for the generation and submission of the observing proposal, including technical and scientific justification, as well as the interaction with the observing facility to ensure the correct observation and later access to the finished datasets. Furthermore, I reduced the data in cooperation with the Nordic ARC Node to optimise the data products to the science case. As first author of the publication, I was responsible for the data presentation, analysis and discussion, as well as the coordination with the co-authors to add their insights to the discussion. The models for stellar rotation were provided by E.A. Dorfi.

ALMA observations of the “fresh” carbon-rich AGB star TX Piscium:

The discovery of an elliptical detached shell

M. Brunner¹, M. Mecina¹, M. Maercker², E.A. Dorfi¹, F. Kerschbaum¹, H. Olofsson², and G. Rau^{3,4}

¹ Department for Astrophysics, University of Vienna, Türkenschanzstrasse 17, A-1180 Vienna
e-mail: magdalena.brunner@univie.ac.at

² Department of Space, Earth and Environment, Chalmers University of Technology, 43992 Onsala, Sweden

³ NASA Goddard Space Flight Center, Code 667, Greenbelt, MD 20771, USA

⁴ Department of Physics, The Catholic University of America, Washington, DC 20064, USA

Received Month nr, YYYY; accepted Month nr, YYYY

ABSTRACT

Aims. The carbon-rich asymptotic giant branch (AGB) star TX Piscium (TX Psc) has been observed multiple times during multiple epochs and within different wavelengths and resolutions, showing a complex molecular CO line profile and a ring-like structure in thermal dust emission. We investigate the molecular counterpart in high resolution, aiming to resolve the ring-like structure and identify its origin.

Methods. Atacama Large submillimeter/Millimeter Array (ALMA) observations have been carried out to map the circumstellar envelope (CSE) of TX Psc in CO(2–1) emission and investigate the counterpart to the ring-like dust structure.

Results. We report the detection of a thin, irregular and elliptical detached molecular shell around TX Psc, which coincides with the dust emission. This is the first discovery of a non-spherically symmetric detached shell, raising questions about the shaping of detached shells.

Conclusions. We investigate possible shaping mechanisms for elliptical detached shells and find that in the case of TX Psc, stellar rotation of ~ 2 km/s can lead to a non-uniform mass-loss rate and velocity distribution from stellar pole to equator, recreating the elliptical CSE. We discuss the possible scenarios for increased stellar momentum, enabling the rotation rates needed to reproduce the ellipticity of our observations, and come to the conclusion that momentum transfer of an orbiting object with the mass of a Brown Dwarf would be sufficient.

Key words. stars: AGB and post-AGB – stars: carbon – stars: evolution – stars: mass-loss – stars: late-type

1. Introduction

At the low- to intermediate-mass end of the final stages of stellar evolution, Sun-like stars evolve into asymptotic giant branch (AGB) stars, exhibiting a rapid increase in size and luminosity. This leads to the formation of a pulsating stellar atmosphere, where dust grains are formed and strong stellar winds originate (Habing 1996, e.g.). A complex interplay between multiple physical processes is involved in this stage of stellar evolution, challenging our current attempts to reconstruct these processes in consistent models (Höfner & Olofsson 2018). As a consequence of the significant amount of mass lost through stellar winds, huge circumstellar envelopes (CSEs) of molecular gas and dust are formed. Those CSEs can be analysed observationally to achieve insights into the mass-loss history of AGB stars, and therefore to entangle some parts of the interplay of processes at work during the creation of these CSEs. In theory, the stellar wind is spherically symmetric and homogeneous, but due to variations in the mass-loss rate and possible irregularities imposed by intrinsic stellar properties, interaction with the surrounding (interstellar or previously ejected) medium, interaction with binaries, or possibly also the interaction with magnetic fields, this is in most cases not true. Therefore, the morphology and dynam-

ics of CSEs rather represent snapshots of the recent mass-loss history of their host stars.

An example of the manifestation of the stellar mass-loss history in CSEs is the existence of so-called detached shells, currently found around about a dozen carbon AGB stars. These detached shells are believed to be linked to thermal pulses (TPs), which are short events (a few hundred years) of significantly increased mass-loss, produced by alternating extinction and re-ignition of the hydrogen- and helium-burning shells in the stellar interior (e.g. Steffen & Schönberner 2000; Mattsson et al. 2007; Olofsson et al. 1988, 1990).

Observations of extended CSEs can be conducted in three different wavelength regimes: for the analysis of the dusty component, optical observations of scattered light on dust grains (e.g. González Delgado et al. 2001; Olofsson et al. 2010; Maercker et al. 2014) or infrared observations of the thermal dust emission (e.g. Cox et al. 2012; Jorissen et al. 2011) can be used. The second component, the molecular gas, can be observed in the millimeter and sub-millimeter wavelength range, and mostly the very stable and abundant CO molecule is used as a tracer of molecular CSEs (e.g. Olofsson et al. 1993). Especially within the last decade, observatories such as the *Herschel* Space Observatory, operating in the infrared, and the At-

acama Large Millimeter/sub-millimeter Array (ALMA)¹, operating in the millimeter/sub-millimeter range, have enabled high-resolution observations of previously unresolved or barely resolved CSEs and structures within them.

The target of this publication, TX Piscium (TX Psc), is a relatively well studied carbon-rich AGB star of spectral type C7,2 (Yamashita 1972), which was originally classified as a variable star of type Lb in the General Catalogue of Variable Stars (GCVS) but Wasatonic (1997) found an average period of 224 days, changing the classification to a semi-regular variable (SRa/b). For a detailed overview on the derived and modelled stellar parameters we refer to Table 3 in Klotz et al. (2013), and in the current work we adopt that the effective temperature T_{eff} of TX Psc is 3000 K (average of values from multiple references in the literature), the luminosity L is $7700 L_{\odot}$ (Claussen et al. 1987), and the most recent distance estimate to the star is 275^{+34}_{-26} pc (van Leeuwen 2007). Regarding its evolutionary status, the average C/O ratio derived from multiple observations and models, as summarised by Klotz et al. (2013), is 1.07, which indicates a recent transition from an oxygen-rich atmosphere to a carbon-rich one and makes TX Psc a relatively "fresh" carbon star. Mass-loss rates reported in literature range from $9.8 \times 10^{-7} M_{\odot}/\text{yr}$ (average value of Olofsson et al. 1993) to $5.6 \times 10^{-7} M_{\odot}/\text{yr}$ (Loup et al. 1993). We summarise the most important stellar parameters that we use in the course of this publication in Table 1.

The CSE of TX Psc has been observed in multiple wavelengths with different methods of observations, ranging from UV to sub-millimeter/radio wavelengths, including both low- and high-resolution observations. Asymmetries and clumps in the close vicinity of the star have been detected at small spatial scales in the optical and infrared (e.g. Cruzalebes et al. 1998; Ragland et al. 2006; Hron et al. 2015), focusing on the dusty component of the CSE. The molecular counterpart has also been investigated with multiple instruments in the millimeter/sub-millimeter range (e.g. Heske et al. 1989; Olofsson et al. 1993; Schöier & Olofsson 2000, 2001), but the spatial resolution of these single-dish observations has not been sufficient to map the CSE in detail. Heske et al. (1989) put limits on the spatial extent of the molecular CSE and report CO(1–0) and CO(2–1) emission at offsets of $20''$ from the star. Because of the multi-component line profile of the CO lines, up to now no radiative transfer modelling has been attempted by any of the investigators, and suggestions about a bipolar or binary-shaped nature of the molecular emission have been raised in the literature. The first large-scale image of the CSE around TX Psc with sufficient resolution to analyse the CSE structure was delivered by the *Herschel*/PACS instrument (Poglitsch et al. 2010) through the Mass loss of Evolved StarS (MESS) program (Groenewegen et al. 2011). Jorissen et al. (2011) report the detection of a circular ring-like structure around the star with a radius of $\sim 17''$ as well as clear indication for a separate ISM interaction front.

In this paper, we present high resolution ALMA Cycle 3 observations of the CO(2–1) emission around TX Psc, for the first time resolving the molecular CSE in detail and revealing an elliptical detached shell at the location of the dusty ring-like structure. We discuss the implications of this discovery on the mass-loss evolution of the star as well as on the evolution and properties of AGB stars in general.

In Sect. 2 we describe the observations, followed by their subsequent analysis in Sect. 3. Our results are discussed with respect to previous observations, stellar parameters and evolution-

Table 1. Stellar parameters of TX Psc.

Stellar parameters TX Psc	
Distance	275^{+34}_{-26} pc ^a
Effective Temperature	3000 K ^b
Gas mass-loss rate	$3.2 \times 10^{-7} M_{\odot}/\text{yr}$ ^c
Dust/gas mass ratio	0.72×10^{-3} ^c
Luminosity	$7700 L_{\odot}$ ^d
Stellar mass	$2 M_{\odot}$ ^b
Gas expansion velocity	$\sim 10 \text{ km/s}$ ^e
Stellar velocity (LSRK)	$\sim 13 \text{ km/s}$ ^e

Notes. Stellar parameters extracted from following references:

(^a) van Leeuwen (2007) (^b) Klotz et al. (2013) (^c) Bergeat & Chevallier (2005) (^d) Claussen et al. (1987) (^e) this study

ary status of TX Psc in Sect. 4, and we summarise and conclude our findings in Sect. 5.

2. Observations

The ALMA observations have been carried out in Cycle 3 (October 2015 – September 2016) and consist of main array (MA), Atacama Compact Array (ACA) and total power (TP) data, to recover all spatial scales larger than $\sim 1''$. We requested an angular resolution of $1''$ to observe the CO($J = 2-1$) spectral line in a mosaic of $45'' \times 45''$ around the star. This covers the ring structure seen in the IR dust emission, but not the close-by ISM interaction region. The spectral setup was optimised for the CO(2–1) line emission at 230.538 GHz with a spectral resolution of 499.84 kHz (0.65 km s^{-1}). Two additional spectral windows were set up at 244.936 and 231.221 GHz to cover the frequencies of the CS(5–4) and $^{13}\text{CS}(5-4)$ lines, respectively, with the same spectral resolution as for the CO line. Additionally, one continuum spectral windows was set up at 248.000 GHz with a spectral resolution of 0.977 MHz and a bandwidth of 1875 MHz.

Standard calibration of the interferometric data was performed with the Common Astronomy Software Application (CASA)², using Uranus and Neptune as flux calibrators, the quasars J2253+1608, J0006-0623 and J2232+1143 as band-pass calibrators, and J0006-0623 as phase calibrator. The TP data were calibrated according to standard procedure using the quasars J2327+0940, J0010+1058, and J2323-0317 as calibrators. Imaging of the interferometric data was carried out and improved in collaboration with the Nordic ARC Node³ using CLEAN. The requested angular resolution for this project was $1''$, calculated for the requested signal-to-noise ratio (S/N) in the extended CSE. The MA baselines at the date of the observations allowed a higher angular resolution and we used uv-tapering to reduce the angular resolution and gain S/N in the faint regions of the CSE. Nevertheless, we also imaged the MA data with the full available spatial resolution (without uv-tapering) for the analysis of the brighter regions of the CSE.

Since the primary beams of the MA and ACA are different, due to the different antenna size, a previously not foreseen and undocumented problem prevented us from doing any useful array combination in the visibility plane: if the imaged area contains emission at the edges of the mosaic, which is the case for

¹ <https://almascience.nrao.edu>

² <https://casa.nrao.edu>

³ <https://www.oso.nordic-alma.se>

M. Brunner et al.: ALMA observations of the “fresh” carbon-rich AGB star TX Piscium:

Table 2. Beam sizes and image properties of the ALMA observations.

Data	θ_b (arcsec)	PA ($^\circ$)	θ_{\max} (arcsec)	rms (mJy)
MA	1.06×0.98	-80.09	5.6	3
ACA	7.60×4.44	-89.26	18.6	9
TP	28.15	-55.35	–	44

Notes. Given are the beam size θ_b , beam position angle PA, the maximal recoverable scale θ_{\max} , and the average rms noise of line-free channels.

a multitude of large scale structures to be observed with ALMA, and especially true for TX Psc with its close-by ISM interaction region, the different primary beams of the MA and ACA pick up different fractions of the signal from the edges of the mosaic. Therefore, they do not contain the same amount and spatial distribution of emission. Hence, not only is flux lost, but also artefacts, that decrease the image quality of a combined image, are introduced. For this reason, we refrained from combining the MA and ACA data and in the following always analyse the data separately, focusing on the small-scale emission and fine structure of the observed CSE when looking at the MA, and on the large-scale emission and general shape of the emission when looking at the ACA. The slightly resolved TP data are analysed as standalone as well, to confirm the general shape of the CSE. The beam sizes and image properties for all datasets are given in Table 2.

3. Analysis

3.1. Detached shell

We report the detection of a thin detached shell around TX Psc, which is seen both in the high resolution MA and low resolution ACA data, as presented in the respective CO(2–1) channel maps in Figs. A.1 and A.2. The shell is inhomogeneous and clumpy, and not spherically symmetric but of elliptical shape in the plane of the sky. We measure an extent in the North-West/South-East direction of $\sim 22''$ (semi-major axis), while the extent in North-East/South-West direction is only $\sim 17''$ (semi-minor axis), which results in an axis ratio of 1.3. The shell thickness seems to be roughly at the same size as the resolving beam, but since it appears to be very inhomogeneous, we cannot constrain it efficiently. For the course of the subsequent analysis, we estimate a shell thickness of $1''$. From the spectrum extracted from the image cube (Fig. 1) we determine an expansion velocity of roughly 10 km/s, attributed to the shell. We assume that this velocity corresponds to the expansion along the semi-major axis, which is based on the assumption that the extent of the ellipsoidal shell along the line of sight is similar to the semi-major axis, i.e. the ellipsoid is axisymmetric to the semi-minor axis and not significantly tilted with respect to the line of sight. With an expansion velocity of 10 km/s along the semi-major axis along the shell, the upper limit of the age of the detached shell is ~ 2600 years.

To analyse the geometry using the projected ellipticity of the detached shell, we constructed a 3D geometrical model with *Shape* (Steffen et al. 2011) and compared rendered model channel maps with the observations to extract geometric parameters. The *Shape* channel maps are created from a geometric model of homogeneous density with attached velocity field. As measured from the observations under the assumption of either no or very

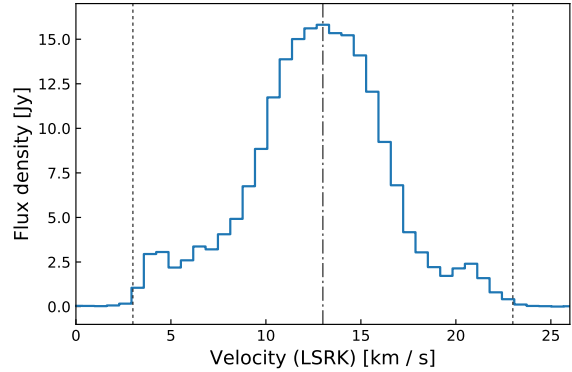


Fig. 1. CO(2–1) spectral line observed with the ALMA main array. The spectrum is extracted from a circular aperture of $25''$ radius. The black dotted-dashed line marks the stellar velocity of 13 km/s (LSRK) and the dotted lines mark the stellar velocity ± 10 km/s.

small inclination of the axisymmetric ellipsoid with respect to the line of sight, the model ellipsoidal shell has a semi-major axis of $22''$, a semi-minor axis of $17''$, and a thickness of $1''$. With the assumption that the elliptical shell was generated during a thermal pulse (or any other single event happening at a specific time), the expansion velocity along the semi-minor axis has to be lower than along the semi-major axis, to generate an ellipsoidal shape. We describe the ellipsoidal velocity profile by an elliptical function, assigning 10 km/s as the velocity along the semi-major axis, the extracted maximal expansion velocity from the spectrum. The corresponding expansion velocity along the semi-minor (polar) axis then equals 7.7 km/s. *Shape* allows the rendering of channel maps, which we can directly compare to our observations.

Since the maximum projected ellipticity of an axisymmetric ellipsoid is encountered when the line of sight is perpendicular to the symmetry axis, we first rendered the 3D model in this configuration with an inclination angle of 90° and a position angle (PA) of 0° , and subsequently changed first the PA and later the inclination, to find a best fitting interval of both parameters to the observations. We arrived at a good fitting PA interval of roughly $15^\circ - 45^\circ$, with the best fit at a PA of approximately 30° , and a good fitting inclination interval of $90^\circ - 110^\circ$, with the best fit at an inclination of approximately 100° . Note that in this model the PA is counted counter-clockwise from North and an inclination angle $> 90^\circ$ means that the bottom (or southern) half of the semi-minor axis is tilted towards the observer. Figure 2 shows the MA channel maps overlaid with the rendered geometric model from *Shape* with the best fitting PA and inclination.

The geometric projection effect of a rotational ellipsoid with corresponding velocity field viewed under an inclination of 100° can best be seen in the extreme velocity channels, where the projected ellipse is located off-center, shifted to North-East in the blue shifted channels, and shifted to South-West in the red shifted channels. Additionally, in those extreme channels the ellipse is thicker than in the channels around the systemic velocity (13 km/s). The 3D model ellipsoid fits the observations very well in the velocity channels from around 7.8 km/s to 18.2 km/s and gradually deviates more from the observations when going to the more extreme velocities, where the observed shell looks more irregular and particularly clumpy. Fig. 3 shows the ACA channel map overlaid with the best *Shape* model. For this lower

resolution data, the agreement of the geometric model with the observations also holds for the more extreme velocities, where the MA data appears too patchy to constrain the geometry well.

3.2. Present-day wind

Figure 2 shows that the present-day wind is well resolved and the S/N is higher than in the shell. To analyse the present-day wind in detail, we use the images created without uv-tapering (as described in Sect. 2), using the full resolution of the main array with a beam of $0.61'' \times 0.57''$ and zoom in on the central $7.5''$ of emission (Fig. 4). The brightest and compact part of the emission is roughly contained within the innermost $2''$ (in diameter), but the extended part of the present-day emission also appears to be of elliptical shape with a size of roughly $3.25''$ along the semi-major axis (North-West/South-East direction) and roughly $2.5''$ along the semi-minor axis (North-East/South-West direction). Thus, the axis ratio of the present-day extended emission of 1.3 is the same as for the elliptical shell. It should be noted that the measurement uncertainty is quite high, since the exact extent of the present-day wind is hard to extract from the images due to its inhomogeneities and small size, compared to the image resolution. The extended present-day emission, as seen in the spectrum, roughly ranges from 7.2 km/s to 18.9 km/s, corresponding to an expansion velocity of about 5.9 km/s along the line of sight. With these measurements, we model the geometric 3D structure and velocity profile of the present-day wind and confirm a good fit of the models to the observations (Fig. 4). The expansion velocity along the semi-major axis is assumed to be the line of sight velocity, 5.9 km/s, as a first approximation, and the expansion velocity along the semi-minor axis is 4.5 km/s.

Within the extended and elliptical present-day emission there seems to be a small cavity or at least an emission minimum to the North-West of the star, which is best visible at the velocity channel of 11.05 km/s. In general, the extended present-day emission shows substructure at the resolution limit.

3.3. Comparison of gas and dust

We compare the molecular CO(2–1) gas emission, as observed with the lower resolution ACA, with the thermal dust emission at $70\mu\text{m}$ observed by *Herschel*/PACS in the infrared. In Fig. 5 we show an integrated intensity (moment 0) map of the ACA observations overlaid with contours of the *Herschel* observations. The gaseous and dusty emission seem to coincide very well with each other, especially the shell structure is very similar in the two components. The emission blob, picked up with *Herschel* just outside the South-West of the shell, is not particularly visible in the ACA observations. In this region we already expect to observe the ISM interaction front (Jorissen et al. 2011). In general, it is expected that the interstellar radiation field is destroying CO molecules through photo-dissociation at the ISM interaction front, which is consistent with the lack of clear CO detection on these spatial scales.

4. Discussion

Only a small sample of detached shells is known until now, and while some show a clumpy or irregular fine structure similar to that of TX Psc (e.g. Kerschbaum et al. 2017), all of them show spherical symmetry when it comes to the general shape of the detached shell. The detached shell around TX Psc is the first with an elliptical shape. In the subsections below we discuss

processes that might significantly influence the shaping of the detached shell, and potentially explain the ellipticity.

4.1. Stellar motion and ISM interaction

Although the minor axis of the elliptical detached shell is aligned with the stellar proper motion through space, we can confidently claim that the ellipticity is not caused by ISM interaction, because the ISM interaction front can clearly be seen in the *Herschel* dust image (Jorissen et al. 2011), and it lies beyond the detached shell. Furthermore, the shell is also elliptical in the direction opposite to the space motion, and furthermore the present-day wind shows an ellipticity with the same orientation as the shell. Therefore we conclude that the ellipticity of the detached shell around TX Psc is not caused by external interaction with a different medium, but has to originate from internal stellar properties or processes much closer to the star itself.

4.2. Binary companion

Optical radial velocity measurements by Barnbaum (1992a,b) indicate only minor radial velocity variations smaller than 5 km/s, and they even use TX Psc as a standard star for the optical radial velocity analysis of their sample. On the other hand, Jorissen et al. (2011) report new observations from 2009–2010 with the HERMES/MERCATOR spectrograph that show slightly larger variations between 8 and 15 km/s. These variations take place on a timescale much longer than the semi-regular pulsation period of 224 days, wherefore Jorissen et al. (2011) interpreted these variations as either an influence by an unidentified binary companion, or an example of so-called long-secondary periods (Nicholls et al. 2009). High resolution studies of TX Psc achieved from multiple lunar occultations show that the star can not be described by a simple stellar disk, but more likely high-temperature circumstellar dust in a possibly clumpy state or large cold spots on the stellar photosphere are responsible for the observed signatures (Richichi et al. 1995). Another interpretation of the lunar occultation data has been published by Bogdanov (1997), who used a different analysis method to derive the brightness profile, and arrived at the conclusion that TX Psc has a close binary companion at a separation of $0.052''$ and a position angle of 241° . GALEX observations in the ultra-violet (UV) wavelength range by Ortiz & Guerrero (2016) also put TX Psc in the category of possible binary stars since far-UV radiation is detected, which is usually mostly attributed to a secondary star. Nevertheless, the ratio of the predicted-to-observed near-UV excess does not reach the proposed threshold for a binary indication.

A potential binary companion can significantly shape the stellar wind, but up to now the wind-binary interaction in AGB stars is mainly observed as spiral structure extending from the star outwards (e.g. Maercker et al. 2012; Ramstedt et al. 2017; Kim 2017). On the other hand, in the study of planetary nebulae (PNe), the successors of AGB stars, a multitude of shapes and structures of the nebulae has been observed, and a long-standing debate is ongoing about the importance of binaries as sources for most of the observed shapes (e.g. review by De Marco 2009). Overall, there is no clear consensus on the binary state of TX Psc in the literature, and we cannot confidently claim binarity from our observations of the CSE alone.

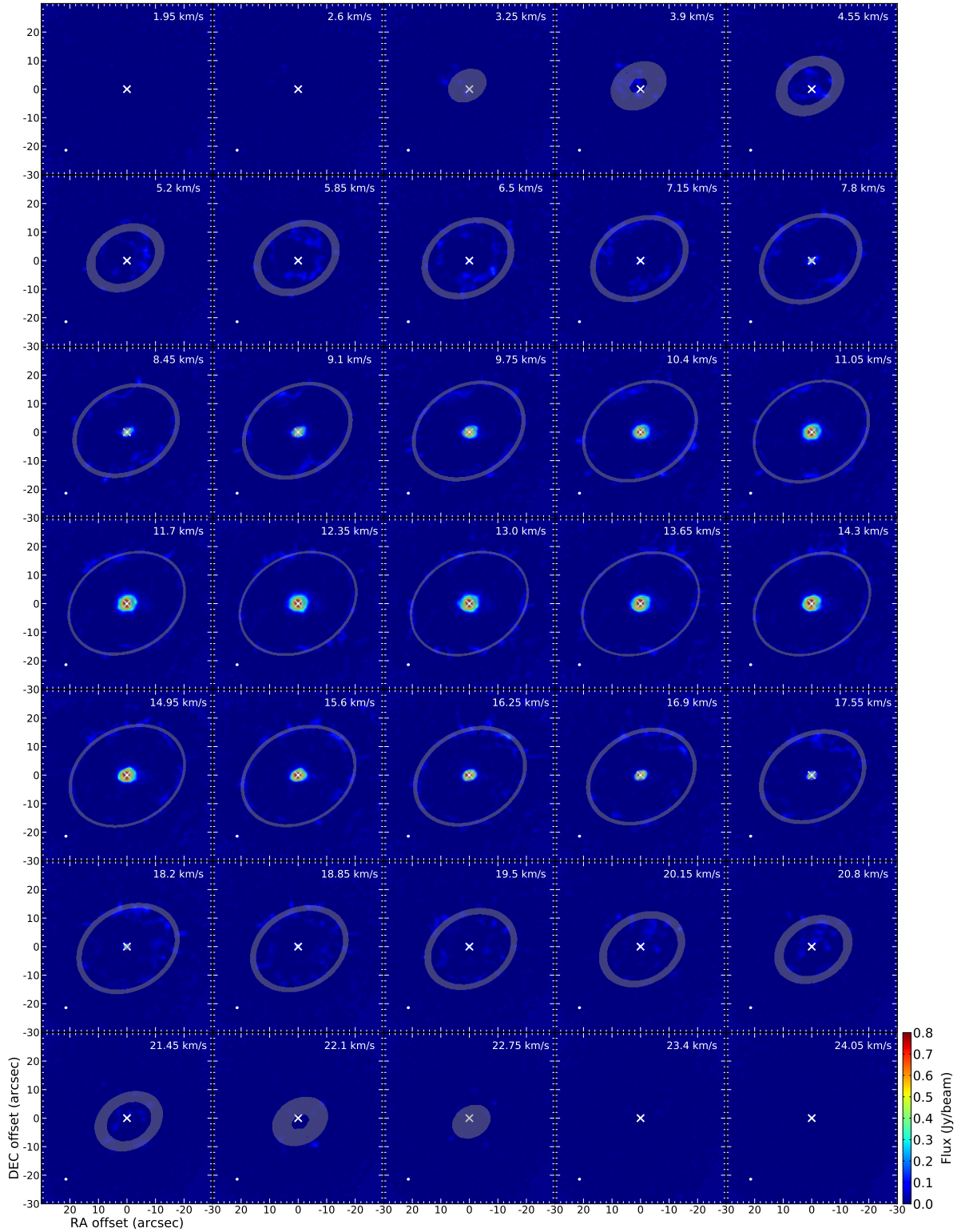


Fig. 2. Channel map of the CO(2–1) emission observed with the ALMA main array (colorscale) overlaid with the best fitting *Shape* geometric model with an inclination of 100° and a PA of 30° (grey). North is up, East is left. The stellar position is marked as white cross for reference. The beam is given as white ellipse in the lower left of the images.

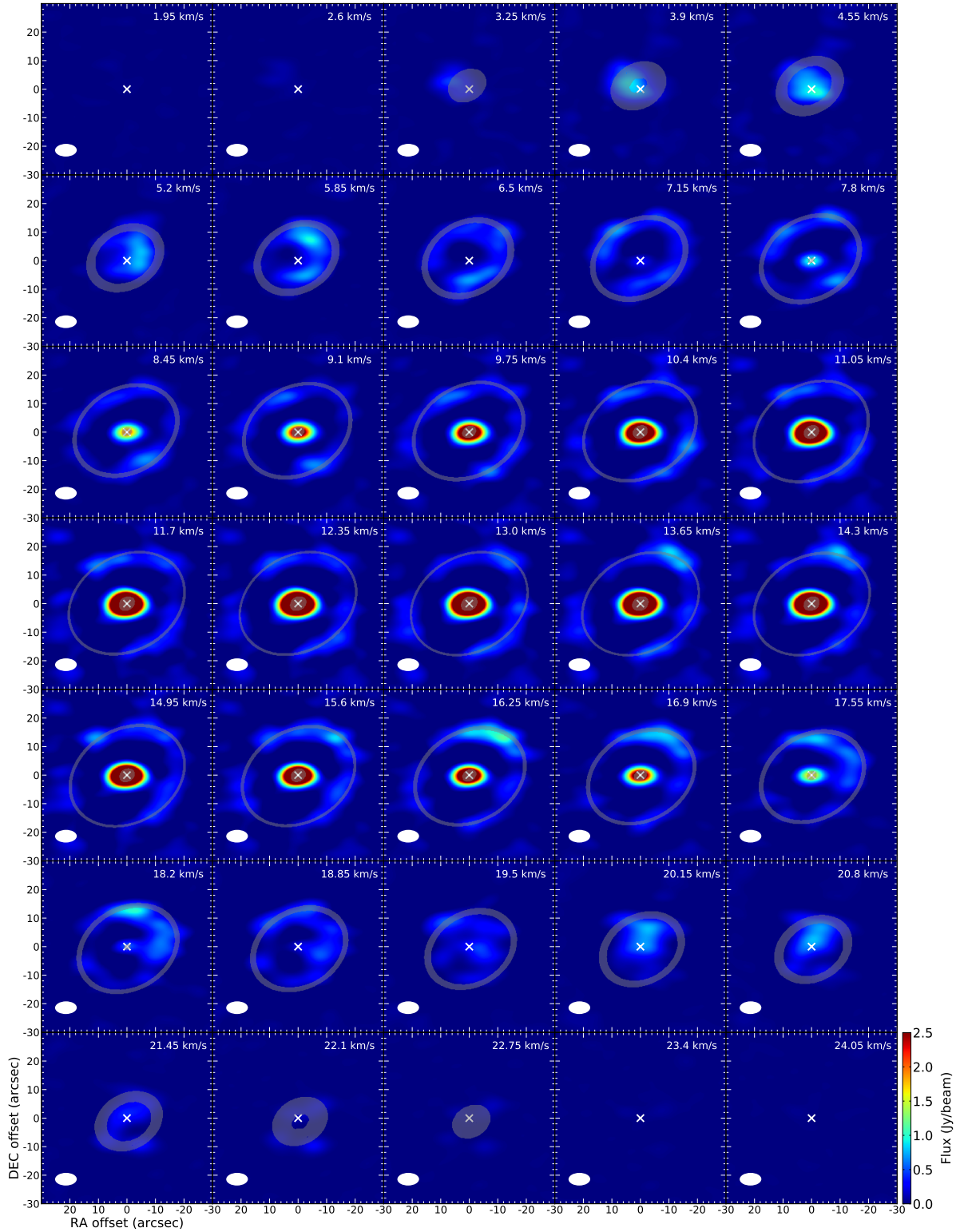


Fig. 3. Channel map of the CO(2–1) emission observed with the ACA (colorscale) overlaid with the best fitting *Shape* geometric model with an inclination of 100° and a PA of 30° (grey). North is up, East is left. The stellar position is marked as white cross for reference. The beam is given as white ellipse in the lower left of the images.

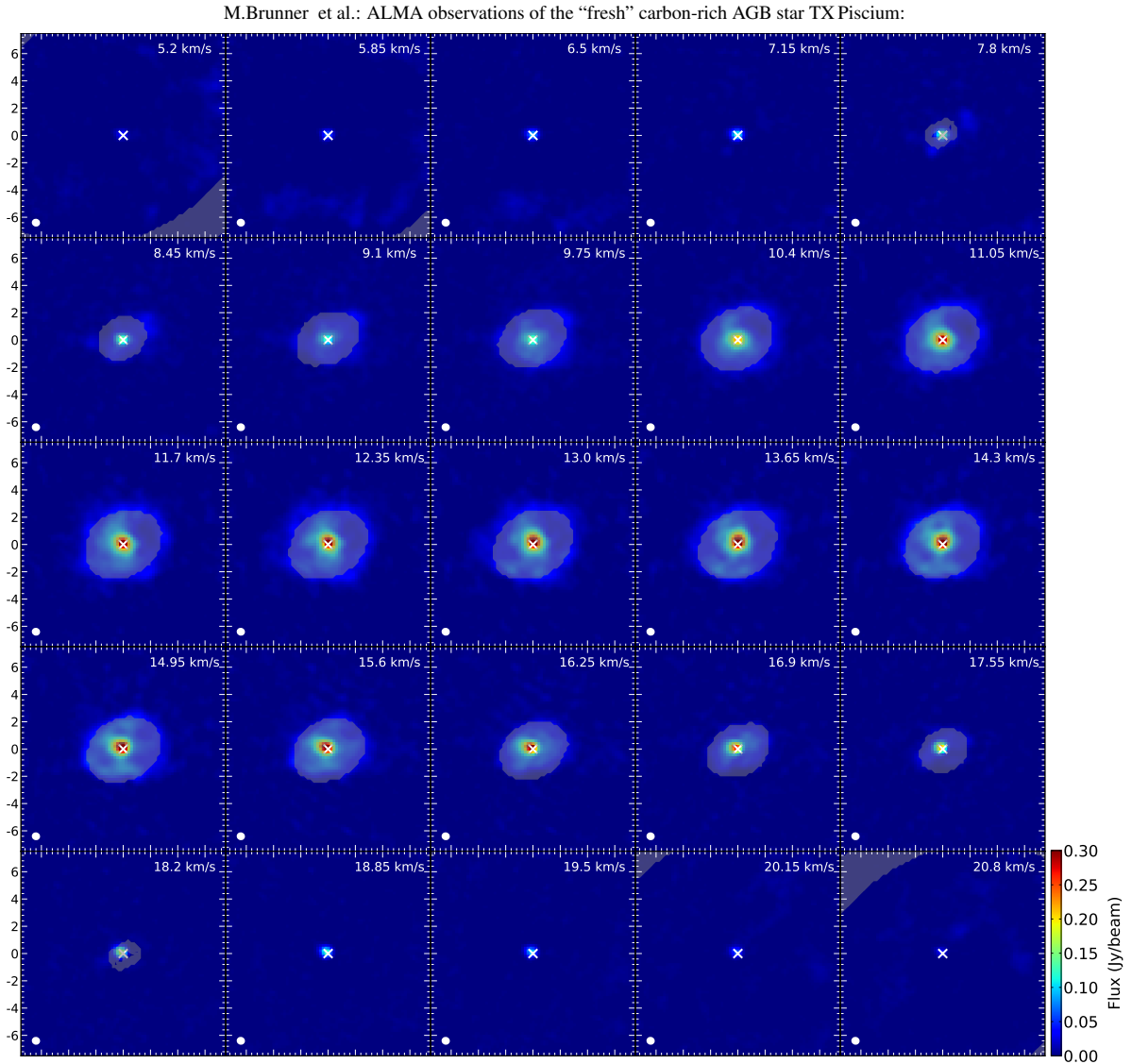


Fig. 4. Channel map of the CO(2–1) present-day wind emission observed with the ALMA main array (colorscale), overlaid with the *Shape* model (grey). North is up, East is left. The stellar position is marked as white cross. The beam has a size of $0.61'' \times 0.57''$ and is given as white ellipse in the lower left of the images.

4.3. Asymmetries in the close CSE

On small spatial scales, below the resolution limit of the presented ALMA observations, asymmetries in the close CSE were detected in multiple studies at multiple wavelengths. [Richichi et al. \(1995\)](#) presented lunar occultation observations in the near infrared and reported that observations in the K-band indicate that the circumstellar emission is more extended along the East-West direction than in the North-South direction. Their average uniform disk diameter is 8.38 ± 0.05 mas, but there are substantial variations between the measurements. Adaptive optics observations by [Cruzalebes et al. \(1998\)](#) at the same wavelengths reveal a roughly circular geometry around the star, but an additional clump with a size of $0.25''$ and an intensity of 2% of the total flux in the South-West direction at a distance of $\sim 0.35''$ from the star. Interestingly, this clump is located at the same position angle as

the potential binary position, reported by [Bogdanov \(1997\)](#), but significantly farther away from the star. Other observations indicate variable asymmetries on timescales of months ([Ragland et al. 2006](#)) or even days ([Sacuto et al. 2011](#)). An indication for a bright spot 70–210 mas South of the star was detected in the near infrared by [Hron et al. \(2015\)](#).

All of the above listed findings of asymmetry in the close CSE underline the inhomogeneity of the stellar wind. We also see these reflected in the clumpiness of the detached shell, but none of the reported results presents a valid explanation for the ellipticity of the detached shell.

4.4. Stellar rotation

According to theory, AGB stars are believed to be very slow rotators. Despite that, recent observations by [Vlemmings et al.](#)

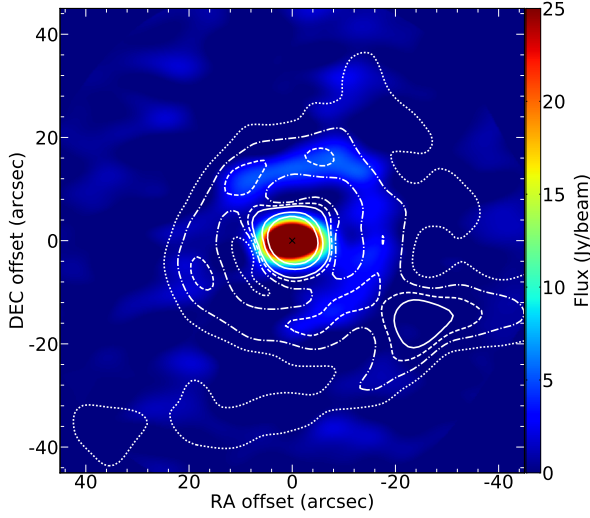


Fig. 5. Integrated intensity (moment 0) map of the CO(2–1) present-day wind emission observed with the ACA (colorscale) overlaid with contours of the *Herschel*/PACS dust emission. North is up, East is left. The stellar position is marked as black cross. The contours are plotted in white at 1.1σ (dotted lines), 1.2σ (dash-dotted lines), 1.3σ (dashed lines), 1.4σ , 2σ and 3σ (solid lines).

(2018) show a directly measured apparent rotation velocity, $v \sin i$, of ~ 1 km/s for the AGB star R Dor. This is still in the regime of low rotation velocities, but two orders of magnitude higher than what is expected from theory. The only exception of a fast rotating AGB star is V Hya, where the rotation has been deduced from spectroscopic observations and is most likely explained by angular momentum transfer from a binary companion in a common envelope system (Barnbaum et al. 1995). For V Hya, the authors derive a $v \sin i$ of 11 km/s. Even smaller rotational velocities can lead to a noticeable difference in mass-loss rate and wind velocity between the equatorial plane and the poles, as shown and discussed by Dorfi & Hoefner (1996). This could lead to an asymmetric and elliptical CSE, such as we observe around TX Psc. We use the models and estimates of Dorfi & Hoefner (1996) to calculate the effect of stellar rotation in the case of TX Psc. Even though modelling of mass loss of AGB stars has improved considerably over the years, this modelling approach still captures the basic processes that determine the magnitudes of the mass-loss rate and gas expansion velocity to warrant its application in this context. Small rotational velocities will generate lateral asymmetries in density, temperature and luminosity. Launching a dust driven wind at different polar angles can increase these variations, since all dust forming processes depend critically on physical parameters like density and temperature, and the centrifugal force lowers the effective gravity. In order to keep the analysis as simple as possible, we approximate these variations along the polar angle by adopting models for slowly rotating polytropes with polytropic index of $n = 3/2$, which corresponds to a fully convective envelope. Such models are constructed along a structural parameter

$$\eta = \frac{\omega^2}{2\pi G \rho_c}, \quad (1)$$

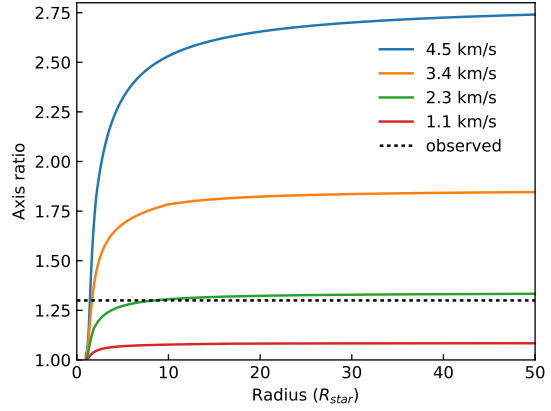


Fig. 6. Axis ratio of modelled elliptical density surfaces as a function of radius, shown for different rotational velocities $v \sin i$ (solid lines) and with a stellar radius of $325 R_\odot$. The observed axis ratio of 1.3 of the elliptical detached shell and present-day wind is plotted as dashed line.

where ρ_c denotes the central density and ω the angular velocity. $\eta = 0$ corresponds to a non-rotating envelope (see e.g. Tasoul (1978) for all details of rotating polytropes). We emphasise, that already very small deviations from spherical symmetry (cf. Table 3, last column) are sufficient to generate non-spherical density shells. Adopting these (small) deviations from sphericity, we construct stationary dust driven winds within a so-called quasi-spherical approximation, and due to the expanding flow we do not expect any significant lateral interactions. A more detailed description of the models can be found in Dorfi & Hoefner (1996).

The observed CO-lines are excited by collisions within the outflowing gas, and therefore we can assume that the observed structures are good indications of the gas density structure. Since the wind models are stationary, we have no temporal information on the expanding shell, but we can look for surfaces of constant density as the material is moving outward. The main shaping of non-spherical density shells occurs during the initial acceleration zone within a few stellar radii, as plotted for different rotational velocities in Fig. 6. Further out, the axial ratio of such density structures becomes constant in case of a constant outflow velocity. This fact is also confirmed by the observational data, which shows that both elliptical structures seen in the detached shell as well as in the present-day wind exhibit the same axis ratio. For the assumed distance of 275 pc, the present-day wind has an extent of $\sim 1000 R_*$, which is clearly outside the initial acceleration zone. Using the observed stellar parameters of TX Psc (see Table 2) we obtain a mean stellar radius of $R_* = 325 R_\odot$, which was used throughout all our models and calculations.

We note, that a thermal pulse can synchronise the outflow at different polar angles, but in our stationary models we do not have such a temporal synchronisation which would set a zero point for the flow time.

The properties of our calculated rotational models are summarised in Table 3, and the derived axis ratios vs. radius of the density surfaces created by the models are plotted in Fig. 6. We use the angular velocity ω as our basic parameter, which corresponds to an observable rotational velocity of $v \sin i = R_* \cdot \omega$. Comparing the different models of Fig. 6, we see that Model

M. Brunner et al.: ALMA observations of the “fresh” carbon-rich AGB star TX Piscium:

Table 3. Rotational quantities of the TX Psc models. $v \sin i$ is the rotational velocity, ω is the angular velocity, r_e/r_p is the ratio of the equatorial axis to the polar axis, v_e/v_p is the ratio of the equatorial to polar outflow velocity, $v_{e,\infty}$ is the final outflow velocity along the equatorial plane, and the last column gives the polytropic parameter η , as defined in Eq. (1), multiplied by a factor of 10^2 .

ID	$v \sin i$ (km/s)	ω (s ⁻¹)	r_e/r_p	v_e/v_p	$v_{e,\infty}$ (km/s)	$10^2 \eta$
A	4.51	$2.0 \cdot 10^{-8}$	2.74	3.38	14.3	0.1934
B	3.39	$1.5 \cdot 10^{-8}$	1.84	2.04	12.2	0.1088
C	2.26	$1.0 \cdot 10^{-8}$	1.33	1.42	10.1	0.0484
D	1.13	$5.0 \cdot 10^{-9}$	1.08	1.10	8.5	0.0121

C, with a rotational velocity of ~ 2 km/s, can explain the observed shell and present-day axis ratio fairly well. We find that already an increase of the best fitting rotational velocity by 50% to 3.4 km/s would increase the axis ratio of the shell to a value of 1.84, which is far beyond the observational values. Lowering the rotation by 50% reduces the aspect ratio to an almost spherical shell, since we get an axis ratio of 1.08.

Although a rotational velocity of ~ 2 km/s seems small, typical AGB rotation velocities are assumed to be much lower, and a rotation velocity of ~ 2 km/s cannot be achieved without transferring additional angular momentum into the stellar envelope. If we take e.g. a mean solar rotational period of $P = 24.5$ days and assume conservation of angular momentum, we calculate a rotational velocity of only 5 m/s when the star expands from $1 R_\odot$ to $325 R_\odot$.

In Fig. 7 we show the orbital angular momentum a body of certain mass, circling around a star with a mass of $2 M_\odot$, as a function of distance in AU. We show three different objects: a Jupiter-like object with M_{jup} , an object with $10 M_{\text{jup}}$, and a brown dwarf (BD) with $0.08 M_\odot$ (M_{BD} , solid line). The vertical dashed line corresponds to the inferred radius of TX Psc, $R_{\text{TX Psc}} = 325 R_\odot$. If we assume that the rotational velocity of TX Psc is generated by an engulfed body, this vertical line will define the outer boundary of such an orbital interaction. The filled triangles are computed for our rotating polytropic models, presented in Table 3, and we see that only the body with a BD mass (full line) can meet our requirements for an induced rotational velocity of about $v \sin i \simeq 2$ km/s, necessary to explain the ellipticity of the observed CO shell.

The total moment of inertia of TX Psc, $I_{\text{TX Psc}}$, is difficult to estimate. However, adopting the same model of a slowly rotating polytrope with a polytropic index of $n = 3/2$ as used in the above calculations and models, the corresponding moment of inertia I can be calculated analytically (see Tassoul (1978), p. 246). We emphasize that due to the small rotation rates, the difference between the equatorial and polar moments of inertia is less than 1%. At this level of approximations, all quantities describing a fully convective stellar envelope are consistent with the computed polar variations of luminosity, temperature and density. The plotted values of the angular momentum (filled triangles) are then simply given by

$$J = I_{\text{TX Psc}} \cdot \omega, \quad (2)$$

with the values of ω taken from Table 3. The process of adding angular momentum of a circulating object to the stellar envelope will be rather complicated, and without detailed numerical simulations it remains unclear which amount of the stellar envelope is being forced into rotation. Hence, we can conclude that our esti-

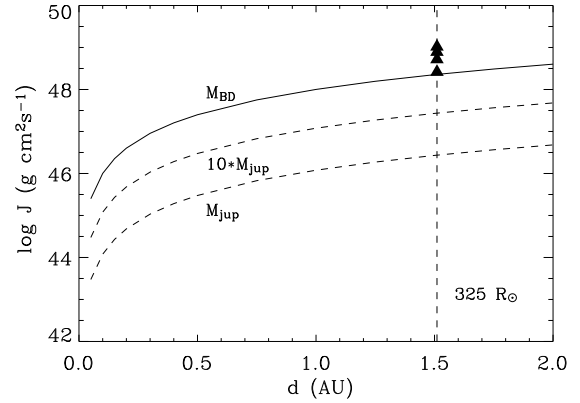


Fig. 7. Orbital angular momentum for objects of different masses circling around TX Psc at distances d from the stellar position. The stellar radius of TX Psc is indicated as vertical dashed line. The angular momenta of the four rotational models are depicted as black triangles.

mates can be used as upper limits to the total angular momentum, therefore reducing the required mass of an orbiting body.

Based on this simple modelling of stationary dust-driven winds of rotating AGB stars, equatorial rotation velocities around $v \sin i \simeq 2$ km/s are found to be sufficient to explain the observed axis ratio of the elliptical detached shell and present-day wind around TX Psc. It seems plausible, that an engulfed BD could add enough angular momentum to the stellar atmosphere to produce the observed asymmetries in the expanding CO shells.

4.5. Stellar evolution

The low C/O ratio of TX Psc stands to reason that the star only recently turned into a carbon-rich AGB star, changing from oxygen rich to carbon rich during one or more recent thermal pulses. We cannot confidently pinpoint this transition to a single event, such as the thermal pulse that created the observed detached shell, but we can speculate about the likeliness and consequences of this thermal pulse being either the very first or one of the first thermal pulses to have altered the photospheric chemistry of TX Psc. As described in detail in Mattsson et al. (2007), a detached shell can be formed through the combination of an eruptive mass-loss event and the interaction of a slow and fast stellar wind. If we assume that the wind-wind interaction acts like a “snow-plow effect” shaping the thin detached shell, one can further presume that a detached shell will be shaped more precisely if the pre-TP, interacting wind is more dense. As thermally pulsing AGB stars will undergo multiple thermal pulses until they reach the end of the TP-AGB phase, subsequent detached shells might run into an increasingly denser and also smoother outer CSE, and therefore later TPs might generate more precisely structured detached shells. One possible upper limit for this effect might be the increase of the inter-pulse mass-loss rate to values so high, that the density contrast between detached shell and wind becomes almost indistinguishable. This mass-loss rate increase is expected to happen for stars that become more regular pulsators (i.e. Miras), which could explain the reason for the observation that so-far only irregular or semi-regular variables are found to host detached shells.

Reversely to the above described "snow-plow effect", the first few TPs might generate less well structured detached shells, because they run into a CSE that has not yet been "swept up" by multiple preceding detached shells. These assumptions could be an explanation for the irregular and patchy fine structure of the detached shell around TX Psc, which could be produced through one of the very first TPs of this star. In comparison, the well resolved detached shells of R Scl (Maercker et al. 2012, 2016), TT Cyg (Olofsson et al. 2000), and U Ant (Kerschbaum et al. 2017) are significantly smoother with a continuous structure. R Scl has a C/O ratio of 1.34 (Bergeat & Chevallier 2005) and can therefore be considered to be of later evolutionary stage than TX Psc. While the detached shell of R Scl also shows intensity peaks within the thin shell, it is a clearly continuous and connected shell, unlike what we observe for TX Psc. U Ant has a C/O ratio of 1.44 (Bergeat & Chevallier 2005) and the detached shell is similarly continuous and thin as the one of R Scl. There is a general weakness of its shell emission in the South-West quadrant, which is anti-correlated with the intensity of the dust emission, seen with Herschel (Kerschbaum et al. 2010). The scattered light observations by Maercker et al. (2010) show a distinct separation between different shells seen in gas and dust emission. For TX Psc, however, the gas and dust distribution seem to be co-spatial (see Sect. 3.3, which is also true for R Scl (Maercker et al. 2014). This could imply and further strengthen the idea that gas and dust are initially well coupled and only later in stellar evolution effects like photodissociation and interaction with the interstellar radiation field could destroy or influence the molecular gas distribution in CSEs.

5. Conclusions

We have discovered the first elliptical detached shell around an AGB star that, most likely, only recently turned carbon rich through one or a few thermal pulses. The molecular gas distribution aligns well with the dust distribution observed in the thermal infrared. The detached shell is clearly separated from the ISM interaction front, and the ellipticity is seen also at smaller spatial scales in the present-day wind. Therefore we conclude that the shaping of the elliptical detached shell has its origin at the stellar level.

Assuming a rotational ellipsoidal structure of the 3D CSE geometry together with an elliptical velocity distribution, we can constrain the inclination of the rotational axis to roughly 100° , through comparison of observations with geometric models and generated projected-velocity maps. The small-scale structure of the detached shell is very filamentary and patchy compared to other observed detached shells, which raises the question whether this could be an effect of the evolutionary status of TX Psc. Its very low C/O ratio suggests that it is a young carbon star.

We have investigated possible mechanisms behind the ellipticity of the shell and come to the conclusion that a stellar rotation of ~ 2 km/s of TX Psc could lead to a circumstellar elliptical structure, as a consequence of higher mass-loss rate and expansion velocity in the equatorial plane, which resembles the observed one. This would be the first indirect observation of significant AGB rotation, which is influencing the large scale geometry of CSEs (while slower AGB rotation has been shown recently by Vlemmings et al. (2018)). A likely requirement for the conservation and increase of angular momentum, needed to drive such significant stellar rotation, is the existence of a companion object of considerable mass up to the mass of a BD, either in a close orbit or being engulfed by the primary star.

Acknowledgements. M.B. acknowledges funding through the Abschlussstipendium fellowship of the University of Vienna. F.K. and M.B. acknowledge funding by the Austrian Science Fund FWF under project number P23586. M.Maercker acknowledges support from the Swedish Research Council.

References

- Barnbaum, C. 1992a, *AJ*, 104, 1585
 Barnbaum, C. 1992b, *ApJ*, 385, 694
 Barnbaum, C., Morris, M., & Kahane, C. 1995, *ApJ*, 450, 862
 Bergeat, J. & Chevallier, L. 2005, *A&A*, 429, 235
 Bogdanov, M. B. 1997, *Astronomy Letters*, 23, 784
 Claussen, M. J., Kleinmann, S. G., Joyce, R. R., & Jura, M. 1987, *ApJS*, 65, 385
 Cox, N. L. J., Kerschbaum, F., van Marle, A.-J., et al. 2012, *A&A*, 537, A35
 Cruzalebes, P., Lopez, B., Bester, M., Gendron, E., & Sams, B. 1998, *A&A*, 338, 132
 De Marco, O. 2009, *PASP*, 121, 316
 Dorfi, E. A. & Hoefner, S. 1996, *A&A*, 313, 605
 González Delgado, D., Olofsson, H., Schwarz, H. E., Eriksson, K., & Gustafsson, B. 2001, *A&A*, 372, 885
 Groenewegen, M. A. T., Waelkens, C., Barlow, M. J., et al. 2011, *A&A*, 526, A162
 Habing, H. J. 1996, *A&A Rev.*, 7, 97
 Heske, A., te Lintel Hekkert, P., & Maloney, P. R. 1989, *A&A*, 218, L5
 Höfner, S. & Olofsson, H. 2018, *A&A Rev.*, 26, 1
 Hron, J., Uttenthaler, S., Aringer, B., et al. 2015, *A&A*, 584, A27
 Jorissen, A., Mayer, A., van Eck, S., et al. 2011, *A&A*, 532, A135
 Kerschbaum, F., Ladjal, D., Ottensamer, R., et al. 2010, *A&A*, 518, L140
 Kerschbaum, F., Maercker, M., Brunner, M., et al. 2017, *A&A*, 605, A116
 Kim, H. 2017, in *IAU Symposium*, Vol. 323, *Planetary Nebulae: Multi-Wavelength Probes of Stellar and Galactic Evolution*, ed. X. Liu, L. Stanghellini, & A. Karakas, 199–206
 Klotz, D., Paladini, C., Hron, J., et al. 2013, *A&A*, 550, A86
 Loup, C., Forveille, T., Omont, A., & Paul, J. F. 1993, *A&AS*, 99, 291
 Maercker, M., Mohamed, S., Vlemmings, W. H. T., et al. 2012, *Nature*, 490, 232
 Maercker, M., Olofsson, H., Eriksson, K., Gustafsson, B., & Schöier, F. L. 2010, *A&A*, 511, A37
 Maercker, M., Ramstedt, S., Leal-Ferreira, M. L., Olofsson, G., & Floren, H. G. 2014, *A&A*, 570, A101
 Maercker, M., Vlemmings, W. H. T., Brunner, M., et al. 2016, *A&A*, 586, A5
 Mattsson, L., Höfner, S., & Herwig, F. 2007, *A&A*, 470, 339
 Nicholls, C. P., Wood, P. R., Cioni, M.-R. L., & Soszyński, I. 2009, *MNRAS*, 399, 2063
 Olofsson, H., Bergman, P., Lucas, R., et al. 2000, *A&A*, 353, 583
 Olofsson, H., Carlstrom, U., Eriksson, K., Gustafsson, B., & Willson, L. A. 1990, *A&A*, 230, L13
 Olofsson, H., Eriksson, K., & Gustafsson, B. 1988, *A&A*, 196, L1
 Olofsson, H., Eriksson, K., Gustafsson, B., & Carlstrom, U. 1993, *ApJS*, 87, 305
 Olofsson, H., Maercker, M., Eriksson, K., Gustafsson, B., & Schöier, F. 2010, *A&A*, 515, A27
 Ortiz, R. & Guerrero, M. A. 2016, *MNRAS*, 461, 3036
 Poglitsch, A., Waelkens, C., Geis, N., et al. 2010, *A&A*, 518, L2
 Ragland, S., Traub, W. A., Berger, J.-P., et al. 2006, *ApJ*, 652, 650
 Ramstedt, S., Mohamed, S., Vlemmings, W. H. T., et al. 2017, *A&A*, 605, A126
 Richichi, A., Chandrasekhar, T., Lisi, F., et al. 1995, *A&A*, 301, 439
 Sacuto, S., Jorissen, A., Cruzalbes, P., et al. 2011, in *Astronomical Society of the Pacific Conference Series*, Vol. 445, *Why Galaxies Care about AGB Stars II: Shining Examples and Common Inhabitants*, ed. F. Kerschbaum, T. Lebzelter, & R. F. Wing, 171
 Schöier, F. L. & Olofsson, H. 2000, *A&A*, 359, 586
 Schöier, F. L. & Olofsson, H. 2001, *A&A*, 368, 969
 Steffen, M. & Schönberner, D. 2000, *A&A*, 357, 180
 Steffen, W., Koning, N., Wenger, S., Morisset, C., & Magnor, M. 2011, *IEEE Transactions on Visualization and Computer Graphics*, Volume 17, Issue 4, p.454–465, 17, 454
 Tassoul, J.-L. 1978, *Theory of rotating stars* (Princeton Series in Astrophysics, Princeton: University Press, 1978)
 van Leeuwen, F. 2007, *A&A*, 474, 653
 Vlemmings, W. H. T., Khouri, T., Beck, E. D., et al. 2018, *A&A*, 613, L4
 Wasatonic, R. P. 1997, *Journal of the American Association of Variable Star Observers (JAAVSO)*, 26, 1
 Yamashita, Y. 1972, *Annals of the Tokyo Astronomical Observatory*, 13, 169

M.Brunner et al.: ALMA observations of the “fresh” carbon-rich AGB star TX Piscium:

Appendix A: Channel maps of ALMA observations

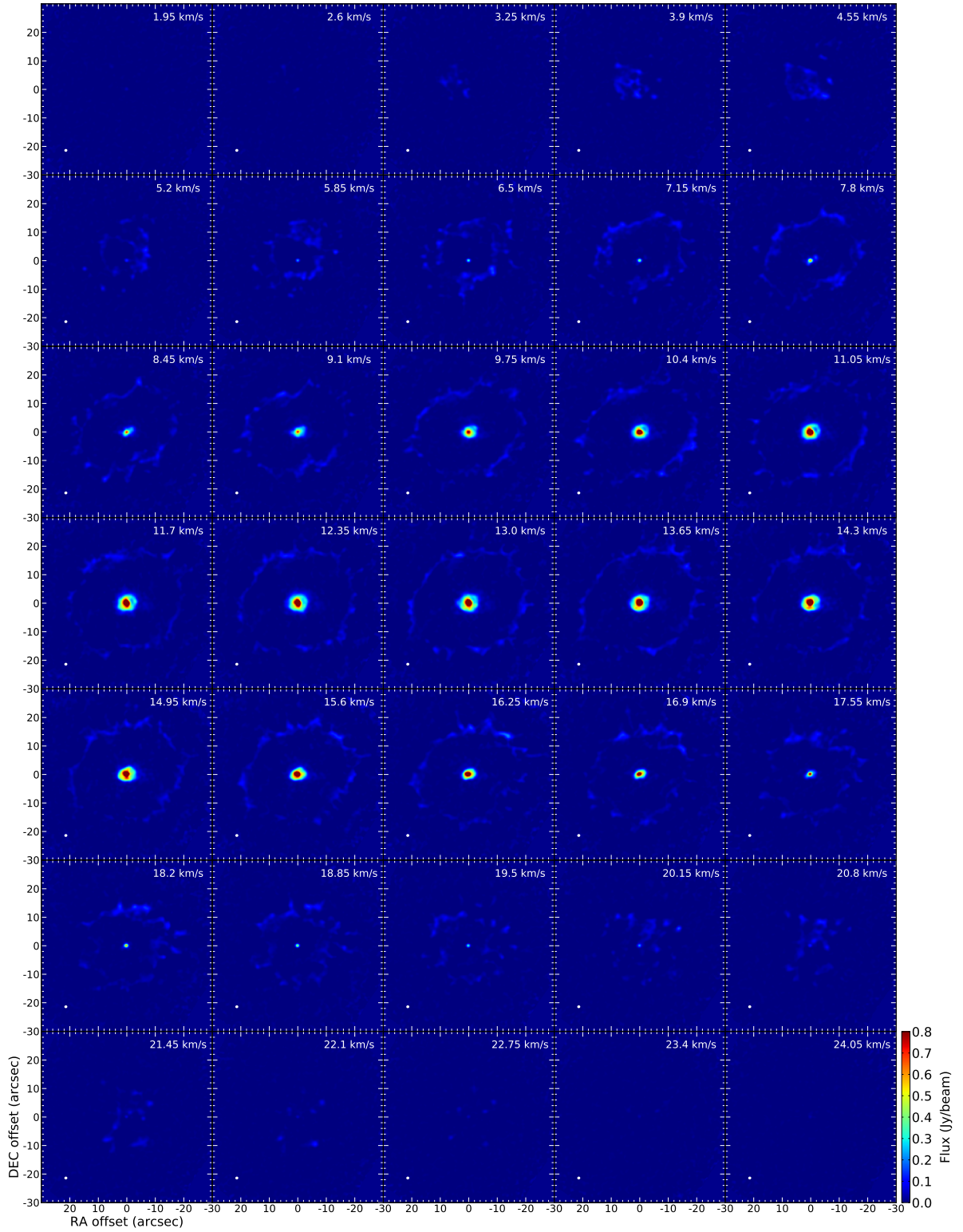


Fig. A.1. Channel map of the CO(2-1) emission observed with the ALMA main array. North is up, East is left. The beam is given as white ellipse in the lower left of the images.

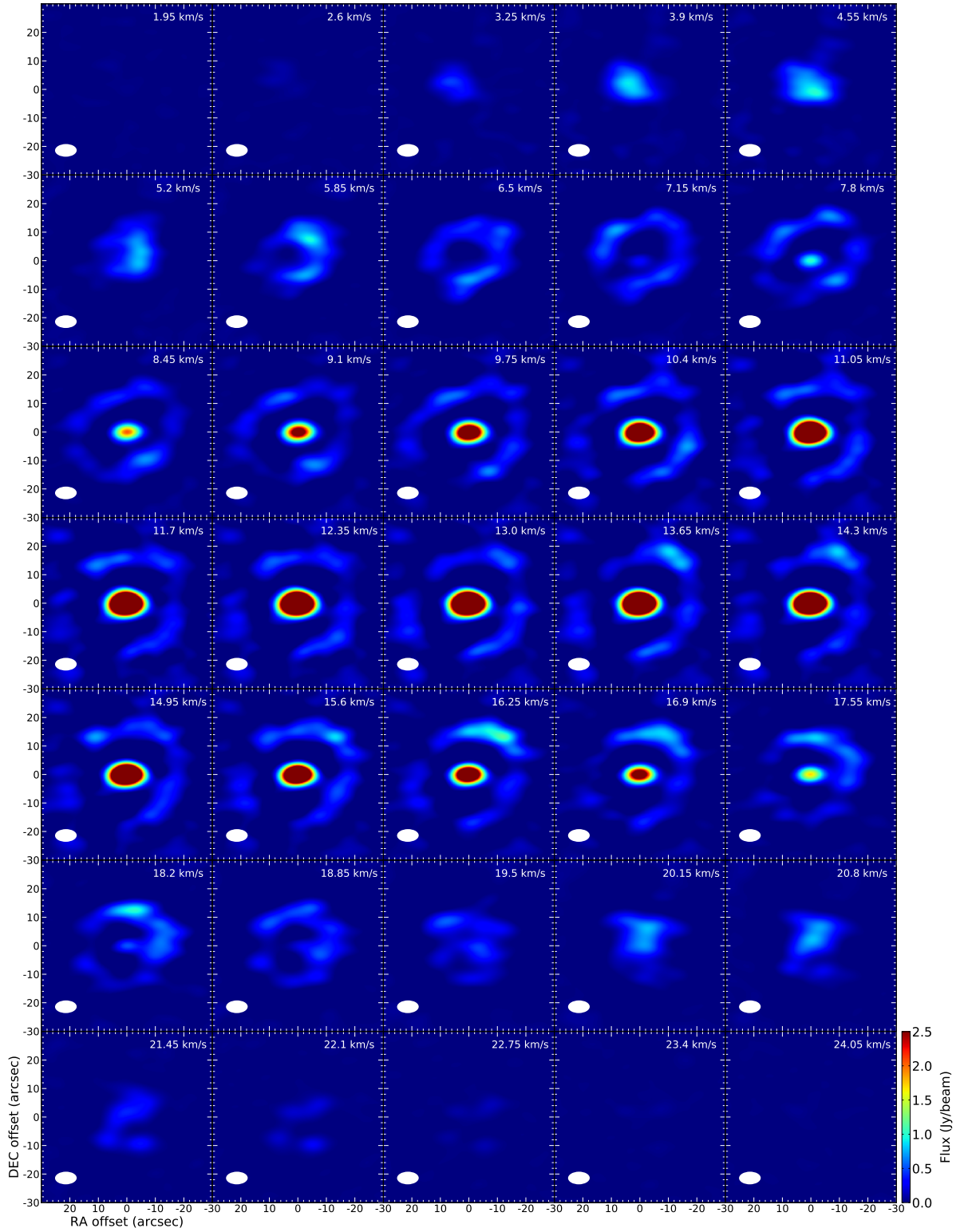


Fig. A.2. Channel map of the CO(2-1) emission observed with the ACA. North is up, East is left. The beam is given as white ellipse in the lower left of the images.

Chapter 6

The dusty detached shell around R Sculptoris (Paper III)

Title: *The carbon AGB star R Sculptoris: Constraining the dust properties in the detached shell based on FIR and sub-mm observations*

Authors: M. Brunner, M. Maercker, M. Mecina, T. Khouri, and F. Kerschbaum

Year: 2017

Journal: Astronomy and Astrophysics

DOI: <https://doi.org/10.1051/0004-6361/201732065>

Credit: Brunner et al. 2018, A&A, 614, A17, reproduced with permission © ESO

This publication is focused on the analysis of dust properties in the detached shell of R Scl, based on radiative transfer modelling and spectral energy distribution (SED) fitting to observations. We improve existing models of this object by adding observations in the infrared by Herschel PACS and SPIRE as well as sub-mm observations by LABOCA on the APEX telescope. We derive the present-day mass-loss rate and detached shell mass for a variety of models, exploring the parameters space of different dust properties such as the dust opacities, chemical composition, geometry and grain size. Additionally we report a sub-mm excess, which can not sufficiently be explained by our models and is most likely not of thermal origin. We find that the derived dust shell mass is most strongly affected by the geometric model of used dust grains, while the other dust grain properties are not influencing the derived detached shell mass significantly.

Personal contribution: As first author of this paper, I was responsible for the main bulk of work on this whole project. All models were run by myself, and the model analysis as well as the textual presentation of the work was also done by myself. The co-authors were contributing to the project by intensive discussion about the modelling procedure and input parameters, as well as the final analysis of the results.

A&A 614, A17 (2018)
<https://doi.org/10.1051/0004-6361/201732065>
 © ESO 2018

**Astronomy
&
Astrophysics**

Modelling the carbon AGB star R Sculptoris

Constraining the dust properties in the detached shell based on far-infrared and sub-millimeter observations[★]

M. Brunner¹, M. Maercker², M. Mecina¹, T. Khouri², and F. Kerschbaum¹

¹ Department for Astrophysics, University of Vienna, Türkenschanzstrasse 17, 1180 Vienna, Austria
 e-mail: magdalena.brunner@univie.ac.at

² Department of Space, Earth and Environment, Chalmers University of Technology, 43992 Onsala, Sweden

Received 9 October 2017 / Accepted 25 January 2018

ABSTRACT

Context. On the asymptotic giant branch (AGB), Sun-like stars lose a large portion of their mass in an intensive wind and enrich the surrounding interstellar medium with nuclear processed stellar material in the form of molecular gas and dust. For a number of carbon-rich AGB stars, thin detached shells of gas and dust have been observed. These shells are formed during brief periods of increased mass loss and expansion velocity during a thermal pulse, and open up the possibility to study the mass-loss history of thermally pulsing AGB stars.

Aims. We study the properties of dust grains in the detached shell around the carbon AGB star R Scl and aim to quantify the influence of the dust grain properties on the shape of the spectral energy distribution (SED) and the derived dust shell mass.

Methods. We modelled the SED of the circumstellar dust emission and compared the models to observations, including new observations of *Herschel*/PACS and SPIRE (infrared) and APEX/LABOCA (sub-millimeter). We derived present-day mass-loss rates and detached shell masses for a variation of dust grain properties (opacities, chemical composition, grain size, and grain geometry) to quantify the influence of changing dust properties to the derived shell mass.

Results. The best-fitting mass-loss parameters are a present-day dust mass-loss rate of $2 \times 10^{-10} M_{\odot} \text{ yr}^{-1}$ and a detached shell dust mass of $(2.9 \pm 0.3) \times 10^{-5} M_{\odot}$. Compared to similar studies, the uncertainty on the dust mass is reduced by a factor of 4. We find that the size of the grains dominates the shape of the SED, while the estimated dust shell mass is most strongly affected by the geometry of the dust grains. Additionally, we find a significant sub-millimeter excess that cannot be reproduced by any of the models, but is most likely not of thermal origin.

Key words. stars: AGB and post-AGB – stars: evolution – stars: carbon – stars: mass-loss – stars: late-type

1. Introduction

During the late stages of stellar evolution, stars with low to intermediate mass (~ 0.8 to $8 M_{\odot}$) develop strong stellar winds as they evolve along the asymptotic giant branch (AGB). On the AGB they consist of a carbon-oxygen core surrounded by hydrogen- and helium-burning shells and a deep convective envelope. The average mass-loss rates range roughly from 10^{-7} to $10^{-5} M_{\odot} \text{ yr}^{-1}$, but large variations in the mass-loss rates and a non-linear mass-loss evolution are seen throughout different evolutionary stages on the AGB (e.g. review by [Habing 1996](#)).

The chemistry in the outer layers of AGB stars changes during its evolution due to nuclear burning in shells around the stellar core and dredge-up events of nuclear processed elements to the stellar surface during thermal pulses (TPs). This alters the chemical composition of the stellar atmosphere, and consequently also of the molecular gas and dust species found in the circumstellar envelopes (CSEs). These molecules and dust grains can be formed in regions of low temperatures and high densities in the outer CSE.

[★] *Herschel* is an ESA space observatory with science instruments provided by European-led Principal Investigator consortia and with important participation from NASA.

Through their mass loss, AGB stars provide up to 80% of dust in the Milky Way and contribute to the chemical evolution of local galaxies ([Forestini & Charbonnel 1997](#); [Herwig & Austin 2004](#); [Schneider et al. 2014](#)), while their contribution to the total dust budget is less certain in the early Universe ([Mancini et al. 2015](#)). The origin of dust grains and the associated dust grain properties are important for understanding their chemical composition, the lifetime of dust grains in the interstellar radiation field, and their role in star and planet formation. In particular, the grain size and geometry strongly affect the survival of dust grains in the interstellar medium (ISM) and star formation processes, and the possibility for the grains to carry organic molecules into proto-planetary disks.

During a TP the luminosity and radius of the star increase for a few hundred years. This leads to an increase in the mass-loss rate and expansion velocity of the stellar wind, before subsequently declining to pre-pulse values (e.g. [Steffen & Schönberner 2000](#); [Mattsson et al. 2007](#)). A consequence of this change in mass-loss properties is the formation of detached shells – geometrically thin shells of dust and gas that expand away from the star (e.g. [Olofsson et al. 1988, 1990](#)). Detached shells offer a direct opportunity to study the evolution of the star and stellar mass-loss throughout the TP-cycle, and hence provide

A&A 614, A17 (2018)

the possibility to constrain one of the fundamental processes in late stellar evolution.

The target of this publication is R Scl, a well-studied carbon-rich AGB star with a semi-regular pulsation period of ~ 370 days (Knapp et al. 2003). Models by Sacuto et al. (2011) and Wittkowski et al. (2017) require a luminosity of $7000 L_{\odot}$ and effective temperatures of 2700 and 2640 ± 80 K for distances of 350 and 370 pc, respectively. We adopt a distance of 370 pc, which is derived from the P – L relationship for semi-regular variables (with an uncertainty of 370_{-70}^{+100} pc, Knapp et al. 2003), which is in agreement with a recent study on an independent, more accurate distance estimate of Maercker et al. (2018).

R Scl is known to be surrounded by a detached shell, believed to have been formed during a TP event, and is seen in molecular gas (e.g. Olofsson et al. 1990, 1996; Maercker et al. 2012) as well as co-spatial dust emission (e.g. González Delgado et al. 2001, 2003; Olofsson et al. 2010; Maercker et al. 2014). Additionally, a spiral structure, which is associated with wind-binary interaction, connects the present-day wind with the detached shell (Maercker et al. 2012). These high-resolution observations of the molecular CO gas, carried out with the Atacama Large sub-Millimeter Array (ALMA)¹, have given good constraints on the spatial density distribution of the gas, and constrained the evolution of the gas mass-loss rate during and after the most recent thermal pulse (Maercker et al. 2012, 2016). Based on the expansion velocity of the CO shell and the distance of 370 pc, the detached shell was created 2300 years ago (Maercker et al. 2016). Observations of the polarised dust-scattered stellar light at optical wavelengths have provided detailed information on the distribution of dust in the shell and give an average radius of $19.5'' \pm 0.5''$ and (FWHM) width of $2'' \pm 1''$ (González Delgado et al. 2003; Maercker et al. 2014). Nonetheless, the scattered-light observations do not provide information on the velocity and temperature of the dust, and only with difficulty allow determining the total dust mass or the grain properties. To date, modelling of the thermal dust emission from the detached shell around R Scl is limited to models of the spectral energy distribution (SED) from optical to far-infrared (FIR) wavelengths (Schöier et al. 2005). However, this previous study did not consider the spatial constraints on the dust shell provided by the scattered-light observations, and was not aimed at constraining the dust properties in detail.

In this paper we present new radiative transfer models of the thermal dust emission towards R Scl. The primary goals of this study are to derive the dust mass in the detached shell around R Scl and to determine the dust properties. We attempt to describe the dependency of the derived dust-shell parameters on implemented opacities, chemical grain composition, grain sizes and grain geometries. We model the SED and include FIR observations with *Herschel* PACS (Poglitsch et al. 2010) and SPIRE (Griffin et al. 2010). In addition, we present a map of the dust emission at sub-millimeter wavelengths ($870 \mu\text{m}$) observed with LABOCA (Siringo et al. 2009) on APEX². The spatial resolution of the LABOCA observations resolves the shell around R Scl. The new observations and models allow us to study the dust properties in the circumstellar environment around R Scl across the entire wavelength range from optical to sub-millimeter, and

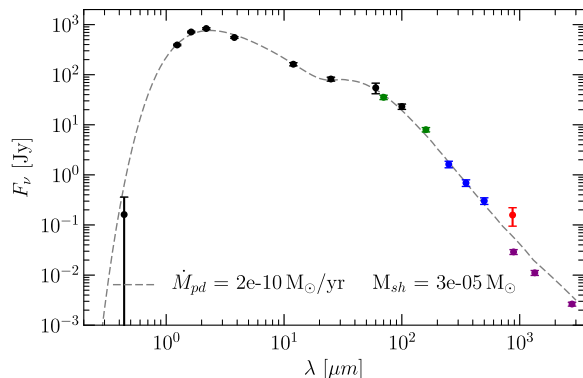


Fig. 1. SED of R Scl. Black: points used in Schöier et al. (2005); green: *Herschel*/PACS; blue: *Herschel*/SPIRE; red: LABOCA; purple: ALMA. Plotted with the grey dashed line is the overall best-fit model of the star, present-day wind, and detached shell (see Sect. 4.1).

in particular allow us to constrain the properties of the dust in the cold shell around the star.

In Sect. 2 we present a summary of new and archive observations as well as previous modelling results. Our approach of the dust radiative transfer modelling is described in Sect. 3, and our results are summarised and discussed in Sect. 4. A conclusion of our findings is given in Sect. 5.

2. Observations of R Scl

2.1. Spectral energy distribution towards R Scl

Following the work done previously by Schöier et al. (2005), we used archival photometric observations to create the SED from 0.44 to $100 \mu\text{m}$. We additionally included *Herschel*/PACS photometry at 70 and $160 \mu\text{m}$, and *Herschel*/SPIRE photometry at 250 , 350 and $500 \mu\text{m}$ (Obs. IDs 1342213264, 1342213265 and 1342188657) observed in the Mass-loss of Evolved StarS (MESS) program (Groenewegen et al. 2011; Cox et al. 2012). We added new observations of the continuum emission towards R Scl at sub-millimeter wavelengths at $870 \mu\text{m}$ with APEX/LABOCA (see Sect. 2.3). Additionally, ALMA continuum observations between 887 and $2779 \mu\text{m}$ were included (see next section). A list of the used SED data points is given in Table 1, and the full SED is plotted in Fig. 1.

2.2. Continuum observations from ALMA

The ALMA observations were taken during ALMA Early Science in Cycle 0 (ADS/JAO.ALMA#2011.0.00131.S), with 16 antennas in the main array in ALMA Bands 3, 6, and 7 (for more details on the observations, we refer to Maercker et al. 2012, 2016). The aim of the observations was to observe the CO emission from the detached shell and CSE. In the continuum, the ALMA observations only allow detecting the stellar emission (possibly with a small contribution from the very recent mass loss) – the detached shell is not visible with the achieved sensitivity and resolution. This is confirmed by the models of the stellar contribution to the SED (see Sect. 3.3). The ALMA observations are hence not used for constraining our radiative transfer models of the star, shell, or present-day mass loss, but are merely used to verify the spatial origin of the LABOCA observations (see next section).

¹ <https://almascience.nrao.edu>

² This publication is based on data acquired with the Atacama Pathfinder Experiment (APEX). APEX is a collaboration between the Max-Planck-Institut für Radioastronomie, the European Southern Observatory, and the Onsala Space Observatory.

M. Brunner et al.: Modelling the carbon AGB star R Sculptoris

Table 1. Observations of the spectral energy distribution.

Wavelength (μm)	Flux (Jy)	Flux error (Jy)	Reference
0.44	0.16	0.20	Kerschbaum & Hron (1994)
1.24	392.65	14.47	Kerschbaum & Hron (1994)
1.63	713.38	26.28	Kerschbaum & Hron (1994)
2.19	835.75	30.79	Kerschbaum & Hron (1994)
3.79	553.50	20.39	Kerschbaum & Hron (1994)
12.00	162.10	11.83	IRAS
25.00	82.07	7.39	IRAS
60.00	54.80	13.15	IRAS
100.00	23.18	2.85	IRAS
70.00	35.44	0.35	Herschel/PACS
160.00	8.00	0.80	Herschel/PACS
250.00	1.63	0.24	Herschel/SPIRE
350.00	0.69	0.10	Herschel/SPIRE
500.00	0.30	0.05	Herschel/SPIRE
870.00	0.16	0.06	APEX LABOCA
886.91	0.0290	0.0032	ALMA Band 7
1341.80	0.0111	0.0012	ALMA Band 6
2778.63	0.0026	0.0002	ALMA Band 3

2.3. APEX/LABOCA observations

The Large Bolometer Camera (LABOCA) on APEX is a 295-channel bolometer array that observes the sky at $870\mu\text{m}$ with a bandwidth of $150\mu\text{m}$ (Siringo et al. 2009). The beam size of APEX at this wavelength is $18.6''$.

We retrieved archival data of R Scl observed with LABOCA in August, October, and November 2007 (Program ID: O-079, F-9309A). The total observing time (on- and off-source) was 10.8 h. The data were re-reduced using CRUSH (Kovács 2008). The final map has an rms noise of 4.5 mJy, and the peak flux corresponds to 0.1 Jy beam^{-1} (Fig. 2, top). The extended emission is detected at a signal-to-noise ratio of approximately 10.

Since the ALMA observations only show the stellar emission, we used them to separate the stellar from the circumstellar flux observed in the LABOCA data. We convolved the ALMA Band 7 observations with the LABOCA beam, and subtracted the emission from the LABOCA map. The resulting map shows the remaining circumstellar emission (Fig. 2, middle), which no longer includes any stellar emission. The bottom panel of Fig. 2 shows the circumstellar emission subtracted by a thin shell corresponding to the detached shell around R Scl, showing that the circumstellar emission indeed is consistent with a shell with a radius of $\sim 19''$ and a width of $\sim 2''$ around R Scl. The residual emission seen in the bottom panel of Fig. 2 can be attributed to asymmetries compared to the spherically symmetric shell that was subtracted.

3. Dust radiative transfer modelling

3.1. SED models with MCMax

We used the Monte Carlo dust radiative transfer code MCMax (Min et al. 2009) to model the circumstellar dust emission of R Scl. The Monte Carlo method of radiative transfer calculates the absorption, re-emission, and scattering processes for a

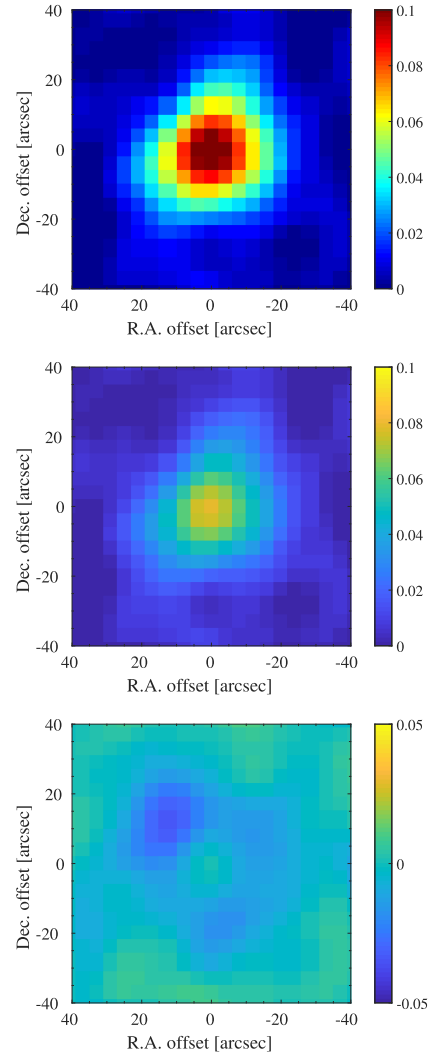


Fig. 2. Top: LABOCA observations towards R Scl. The colour scale is given in Jy beam^{-1} . Middle: LABOCA map with the stellar SED (retrieved from the ALMA continuum observations convolved by the LABOCA beam) subtracted. Bottom: residual map after subtracting the stellar SED and a spherical detached shell with a radius of $18''.5$ and width of $2''$. The structures in the residual map are due to asymmetric emission from the shell, consistent with scattered-light observations.

large number of individual photon packages, which are moving through the modelled medium described by a specific density and opacity at each grid cell. After all photon packages have escaped the grid, the temperature and frequency structure at each grid cell is the output of the model. The resulting observables are the SED, images of the emission, polarisation maps, and visibilities. The required input for such models are the properties of the illuminating source, the density profile, and the opacity of the surrounding medium.

Although MCMax is capable of 3D (axisymmetric) radiative transfer modelling, we employed only a 1D radial density profile to describe the spherically symmetric detached shell and present-day mass loss of R Scl. This creates a homogeneous

A&A 614, A17 (2018)

envelope and shell around the star. Although small-scale structure and clumpiness is observed around R Scl (in the form of a spiral imprinted on the CSE and clumpy structure in the shell; Maercker et al. 2012, 2016), in the case of optically thin dust emission, the dominating parameter affecting the dust emission is the radial distance to the star and the intrinsic properties of the individual dust grains.

3.2. General assumptions and modelling strategy

We modelled and discuss the circumstellar environment of R Scl with respect to three thermal components that contribute to the observed SED: the star itself as dominating radiation source, surrounded by the present-day wind or CSE (starting at the dust condensation radius), and the thin, spherical dust shell located at $\approx 19''$ from the star. We assumed that the dust emission is optically thin. This allowed us to model the three different contributions to the SED separately, adding the flux from the star, the present-day wind, and the shell to obtain the full SED to be compared to observations. We limited the outer radius of the dust density distribution to 10 000 AU (at 370 pc the shell has a physical radius of ≈ 7200 AU), while the inner radius was automatically calculated by MCMax through dust destruction of all particles with a temperature above the given dust condensation temperature (which is considered to be equivalent to the dust destruction temperature).

The focus of this modelling strategy is the analysis of the properties of the shell, and in particular, exploring the constraints set by the FIR and sub-millimeter observations. We therefore did not model the stellar SED and present-day wind in (much) detail, other than reproducing the effective flux created inside the shell.

3.3. Stellar parameters and contribution

We treated the star as a black body with an effective temperature $T_{\text{eff},\star}$ and luminosity L_\star , located at a distance D . The emitted flux thus follows the Planck law for black-body radiation, and for AGB stars with low effective temperatures, the emission will peak around a few μm – dominating the SED in that wavelength range. The stellar parameters of R Scl have been derived with several different approaches and have been extracted from various modelling attempts (as described in the introduction). To be consistent within our modelling approach, we calculated a small grid of black bodies with varying $T_{\text{eff},\star}$ and L_\star to determine the best-fitting parameters to our observational data, shorter than $4\mu\text{m}$ (main stellar contribution). The best-fitting parameters are $T_{\text{eff},\star} = 2250$ K and $L_\star = 7000 L_\odot$ for a distance of $D = 370$ pc. As presented in the introduction, these values are in general agreement with earlier publications (e.g. Schöier et al. 2005; Sacuto et al. 2011; Wittkowski et al. 2017), although our best-fitting effective temperature is lower than in all previous models. We emphasise that this is most likely because we included optical data in our SED fit. In general, the difference in temperature is not significant for our further analysis, since we did not attempt to separate the stellar and present-day wind contribution perfectly, but concentrated on modelling the shell emission. These parameters were used as input in all following models of the present-day wind and shell, and were not changed. Figure 3 shows the model grid of calculated black bodies for determining the best-fitting stellar parameters. It is evident that the ALMA observations do not represent any detached-shell contribution but are reproduced by the stellar contribution alone.

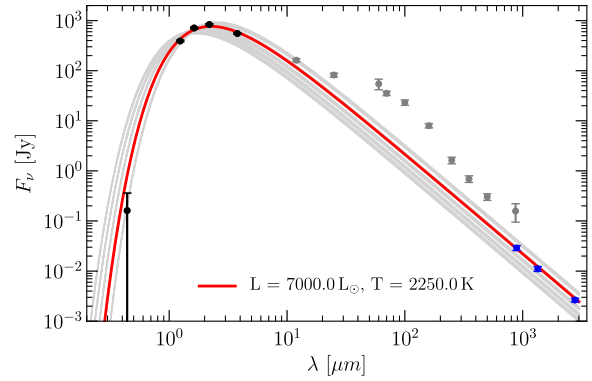


Fig. 3. Model grid of black bodies with different luminosities and effective temperatures (grey lines). The best-fitting model is shown as a red line. All SED data points below $4\mu\text{m}$ are used for χ -square fitting (black dots); data points with wavelengths longer than that are plotted in grey; the ALMA data points are shown in blue for reference.

3.4. Present-day wind description

The present-day wind is described as the “most recent” mass-loss process, usually attributed to a smooth, spherical stellar wind, expanding outwards from the dust-condensation radius at a few stellar radii, with a constant and low to intermediate mass-loss rate $\dot{M}_{\text{pd,dust}}$ and expansion velocity $v_{\text{pd,dust}}$. The associated 1D radial density profile of the present-day wind, $\rho_{\text{pd}}(r)$, can be described by a power law:

$$\rho_{\text{pd}}(r) = \frac{\dot{M}_{\text{pd,dust}}}{4\pi v_{\text{pd,dust}} r^2}. \quad (1)$$

The dust expansion velocity, $v_{\text{pd,dust}}$, cannot be directly measured by observations. Gas expansion velocities can be measured with high accuracy, however, and assuming full coupling between the dust and gas (i.e. zero drift velocity), we can obtain a first-order estimate of the dust velocity. A non-zero drift velocity will change our model output by scaling the calculated dust mass-loss rates. The presented dust mass-loss rates are therefore lower limits, concerning a possibly higher dust velocity than currently used.

We note that for the shell, the dust and gas seem to coincide almost perfectly (Maercker et al. 2014), indicating that the drift-velocity is indeed close to zero. However, this does not have to be true throughout the evolution of the shell and wind, or for all components of the circumstellar dust distribution.

Observations of the molecular gas indicate that the mass-loss rate has not been constant since the last thermal pulse, but rather has been continuously declining in both rate and expansion velocity (Maercker et al. 2012, 2016). The density distribution of the CSE created in that case would not follow the r^{-2} dependence of Eq. (1). However, we are primarily interested in the properties of the dust in the shell, which are constrained by observations at wavelengths $>20\mu\text{m}$, and the details of the dust distribution at radii smaller than the shell radius are not critical, as long as they provide the correct radiation field. More importantly, the spatial resolution of the current observations are not sufficient to constrain the distribution of the dust inside the shell. The determined value for the present-day mass-loss rate should therefore be interpreted with some care.

M. Brunner et al.: Modelling the carbon AGB star R Sculptoris

3.5. Detached-shell description

The spatial extent of the detached shell of dust around R Scl (in angular scale) is well defined through the observations in dust scattered stellar light (Maercker et al. 2014, and references therein), and appears to be the same as for the shell of gas in high-resolution observations with ALMA (Maercker et al. 2012, 2016). Assuming that the distance to R Scl is known, a linear radius and thickness of the shell can be derived. We assumed a smooth, Gaussian density distribution for the shell with the following radial density profile:

$$\rho_{\text{shell}}(r) = \rho_0 \cdot \exp\left(\frac{-(r - r_{\text{shell}})^2}{2\sigma_{\text{shell}}^2}\right), \quad (2)$$

where σ_{shell} is the standard deviation of the Gaussian shell, related to the FWHM of the shell. ρ_0 is the peak density in the detached shell, which we derived by dividing $M_{\text{shell, dust}}$, the mass contained within $\pm 5\sigma$ of the Gaussian shell, by the corresponding volume, V_{shell} , of the Gaussian shell:

$$\rho_0 = \frac{M_{\text{shell, dust}}}{V_{\text{shell}}} \quad (3)$$

$$V_{\text{shell}} = 4\pi \cdot \int_{r_{\text{shell}} - 5\sigma_{\text{shell}}}^{r_{\text{shell}} + 5\sigma_{\text{shell}}} r^2 \cdot \exp\left(\frac{-(r - r_{\text{shell}})^2}{2\sigma_{\text{shell}}^2}\right) dr. \quad (4)$$

Therefore, the radial density profile of the shell can be directly defined by the input of a specific dust shell mass, $M_{\text{shell, dust}}$, which is the only variable to define.

3.6. Dust properties

The emission from the dust grains is determined by the properties of the individual dust grains. The dust parameters such as grain size, grain density, grain geometry (e.g. solid spheres, distribution of hollow spheres), chemical composition, and condensation temperature determine the absorption and scattering efficiency of the material, and are reflected in the form of the individual opacity tables. These are necessary input for the modelling code. Such opacity tables are based on laboratory measurements of the real and imaginary part of the complex refractive index, which are provided in various databases (e.g. the Jena database³), and were used to calculate the frequency dependent absorption opacity κ_v^{abs} and the scattering opacity κ_v^{scat} based on the assumed grain model. With the dust properties and frequency-dependent opacity tables, the radiative transfer equations were solved for each absorption, scattering or emission event for each photon package, sent through the CSE.

Since R Scl is a carbon star, the expected main component of the circumstellar dust will be composed of amorphous carbon (amC) grains. We started with the assumption that the dust grains are spherical and solid, and of a single grain size. We adopted a grain size of $0.1 \mu\text{m}$ and a grain density of 1.8 g cm^{-3} , typical for the dust around carbon AGB stars (Schöier et al. 2005). We assumed a dust condensation temperature of 1500 K and used the optical constants derived by Suh (2000), unless otherwise mentioned.

3.7. SED fitting

To find the best-fitting dust model to our SED, we minimised the χ^2 value

$$\chi^2 = \sum_{i=1}^N \left[\frac{(F_{\text{mod}, \lambda} - F_{\text{obs}, \lambda})^2}{\sigma_{\lambda}^2} \right] \quad (5)$$

for each model, where N is the number of individual data points, $F_{\text{mod}, \lambda}$ is the modelled flux, $F_{\text{obs}, \lambda}$ is the observed flux, and σ_{λ} is the uncertainty of the observed flux at a specific wavelength λ . In the following analysis, we always present the reduced χ^2 value, χ_{red}^2 , which is the χ^2 value per number of degrees of freedom (which is equal to the number of observations subtracted by the number of fitted parameters).

3.8. Model grid and refinement

The general modelling procedure we employed for our analysis is a two-step process. First, we calculated MCMAX radiative transfer model grids with typical sizes of 50–150 models and varying step sizes, depending on the individual input parameters of the model grids. From these relatively coarse model grids, we selected the best-fitting model and the associated mass-loss parameters through SED fitting.

As a second step, we further constrained the shell mass by calculating a much finer grid of (scaled) models and derived associated errors on the best-fitting shell mass. For this strategy, we separated the spectral contribution of the shell to the rest of the SED (consisting of stellar and present-day wind contribution) and multiplied the shell spectrum by a scaling factor, ranging from 0.05 to 2 in 1000 steps. We thus created a fine model grid of 1000 scaled models close to the best-fitting radiative transfer model to extract a refined best-fitting shell mass. Additionally, we used this fine model grid to calculate the error on the extracted best-fitting shell mass by calculating the 1σ confidence interval on the lowest χ^2 value, and extracting the associated scaled models and their respective shell masses. We note that for this method we only varied the shell mass and kept the (best fitting MCMAX model) present-day wind mass-loss rate constant. Therefore we fit the scaled SED only to the observational data points between $20 \mu\text{m}$ and $350 \mu\text{m}$, where the SED is influenced by the shell. Furthermore, to justify this approach, we assumed that the emission is optically thin.

4. Modelling results and discussion

Unless explicitly mentioned otherwise, the dust properties for our models were chosen as described in Sect. 3.6.

4.1. Best-fitting standard model for present-day wind and detached shell

We initially determined a best-fit present-day mass-loss rate and shell mass using the standard dust parameters described in Sect. 3.6. We ran a grid of models containing the stellar black body as radiation source (using the best-fitting stellar parameters as described in Sect. 3.3), the dust density distribution of a present-day wind around the star (as described in Sect. 3.4), and the dust density distribution of a detached shell (with a radial density profile as defined in Sect. 3.5 and a radius of $19.7''$ with a width of $3.2''$, as measured directly in polarised,

³ <http://www.astro.uni-jena.de/Laboratory/Database/databases.html>

A&A 614, A17 (2018)

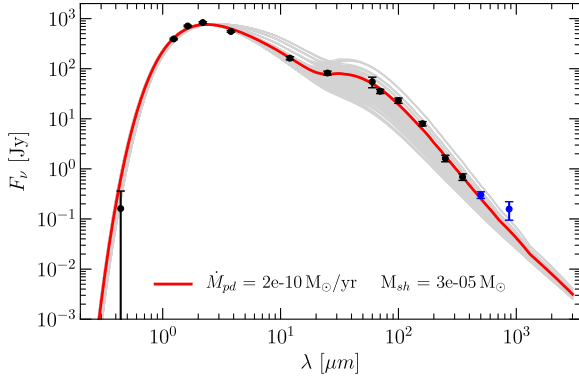


Fig. 4. Model grid for $0.1\,\mu\text{m}$ solid, spherical amC dust grains in a present-day wind and detached shell. The best-fitting model is plotted as the red line; the other models, showing present-day mass-loss rates from 5×10^{-12} to $1 \times 10^{-9}\,M_{\odot}\,\text{yr}^{-1}$ and detached-shell masses from 5×10^{-6} to $7 \times 10^{-5}\,M_{\odot}$, are shown with grey lines.

dust-scattered light by Maercker et al. (2014), i.e., not the average radius and width). The values of the present-day mass-loss rate in the grid vary between 5×10^{-12} and $1 \times 10^{-9}\,M_{\odot}\,\text{yr}^{-1}$, while the detached-shell mass ranges between 5×10^{-6} and $7 \times 10^{-5}\,M_{\odot}$. The best-fit model is given by a present-day mass-loss rate of $2 \times 10^{-10}\,M_{\odot}\,\text{yr}^{-1}$ and a detached-shell mass of $(3.1 \pm 0.5) \times 10^{-5}\,M_{\odot}$ (Fig. 4), with a χ^2_{red} of 3.7.

Comparing this best-fitting model with modelling results from Schöier et al. (2005), our best-fitting shell mass is consistent with their published $(3.2 \pm 2.0) \times 10^{-5}\,M_{\odot}$, and constrains the shell mass with much higher accuracy (reducing the error on the shell mass by a factor of 4). Additionally, the distance used by Schöier et al. (2005) (290 pc) results in an angular size of their shell of $\sim 28''$, while the observations of dust-scattered stellar light clearly indicate a shell of dust at roughly $19''$. Our results are hence consistent with observations. For the present-day wind, they reported a gas mass-loss rate of $< 3.8 \times 10^{-7}\,M_{\odot}\,\text{yr}^{-1}$ and a dust-to-gas ratio of 1.7×10^{-3} , resulting in a present-day dust mass-loss rate of $< 6.5 \times 10^{-10}\,M_{\odot}\,\text{yr}^{-1}$. This is consistent with our best-fitting present-day dust mass-loss rate of $2 \times 10^{-10}\,M_{\odot}\,\text{yr}^{-1}$ (which is not well constrained).

For the assumed dust parameters, the present-day mass-loss mainly affects the near-infrared part of the SED at wavelengths around $10\,\mu\text{m}$, while the shell has a greater impact at wavelengths longer than $\sim 20\,\mu\text{m}$. This is a natural consequence of the temperature of the shell, given by the distance of the shell to the star. In the models, the shell has a temperature of $\sim 77\,\text{K}$, corresponding to emission that peaks at $\sim 37\,\mu\text{m}$. Dust in the present-day wind will be closer to the star and hence at warmer temperatures, and therefore will radiate at shorter wavelengths.

The best-fit model reproduces the entire SED at wavelengths $\leq 350\,\mu\text{m}$ well. However, there is a significant discrepancy between observed and modelled dust emission at $870\,\mu\text{m}$, where the best-fitting model fails to reproduce a clear excess in the observation. We discuss this discrepancy in more detail in Sect. 4.3. As explained in Sect. 4.3, the nature of this emission is probably not due to thermal dust emission, and therefore we did not include data points at wavelengths $> 350\,\mu\text{m}$ in the fitting of SED models. The *Herschel*/SPIRE point at $500\,\mu\text{m}$ was excluded to avoid a possible transition region between regions dominated by thermal and non-thermal emission.

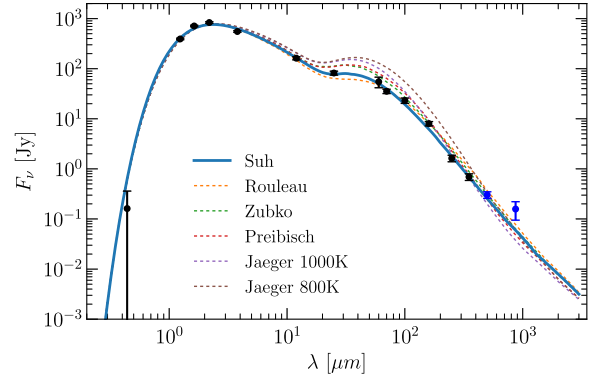


Fig. 5. Effect of the different opacities on the SED (detailed model setup described in Sect. 4.2.1). The best-fitting model is drawn with a solid line, while the other models, corresponding to different opacities, are plotted as dotted lines.

4.2. Changing the dust grain properties

In the following, we explore the parameter space of different dust properties and study how they influence the estimate of the detached-shell dust mass. We explore the effect on the model SED of the assumed optical constants, grain composition, grain size, and geometrical grain model.

4.2.1. Optical constants

The basis of dust radiative transfer modelling lies in the description of the radiative dust grain properties, which are defined by optical constants (n and k) that are used to derive the frequency-dependent absorption and scattering opacities. However, since the optical constants are measured in laboratory experiments by different researchers under different conditions, the choice of optical constants can influence the modelling results – even for theoretically identical dust particles. We show this effect by plotting the best-fitting model for $0.1\,\mu\text{m}$ sized solid amC grains in the present-day wind and detached shell using the results from Sect. 4.1 for different sets of opacities (Fig. 5), derived by Preibisch et al. (1993); Rouleau & Martin (1991); Suh (2000); Zubko et al. (1996); and Jager et al. (1998). The greatest change between the different opacities can be seen in the infrared region of the SED at $\lambda > 20\,\mu\text{m}$. The opacities might therefore influence the best-fitting shell mass.

We ran a grid of models varying the present-day mass-loss rate and shell mass for each of the optical constants shown in Fig. 5. The best-fitting models for the different optical constant were then compared to the one when using optical constants by Suh (2000). The best-fitting mass-loss parameters for all tested opacities are presented in Table 2. The χ^2_{red} of the opacities by Suh (2000); Preibisch et al. (1993); and Zubko et al. (1996) are equally good, while the derived shell masses for these three opacities are slightly different.

The model grids for the Zubko et al. (1996) and Preibisch et al. (1993) opacities are presented in Fig. A.1. For the Zubko et al. (1996) opacities, a best-fitting present-day wind mass-loss rate of $1 \times 10^{-10}\,M_{\odot}\,\text{yr}^{-1}$ and a best-fitting detached-shell mass of $(2.1 \pm 0.3) \times 10^{-5}\,M_{\odot}$ are found. For the Preibisch et al. (1993) opacities, a best-fitting present-day wind mass-loss rate of $1 \times 10^{-10}\,M_{\odot}\,\text{yr}^{-1}$ and a best-fitting detached-shell mass of $(1.9 \pm 0.3) \times 10^{-5}\,M_{\odot}$ are found.

M. Brunner et al.: Modelling the carbon AGB star R Sculptoris

Table 2. Best-fitting mass-loss parameters for the tested opacities.

Opacity	$\dot{M}_{\text{pd, dust}}$ ($M_{\odot} \text{ yr}^{-1}$)	$M_{\text{shell, dust}}$ (M_{\odot})	χ^2_{red}
Suh	2×10^{-10}	$(3.1 \pm 0.5) \times 10^{-5}$	3.7
Zubko	1×10^{-10}	$(2.1 \pm 0.3) \times 10^{-5}$	3.7
Preibisch	1×10^{-10}	$(1.9 \pm 0.3) \times 10^{-5}$	3.7
Jäger 800 K	5×10^{-11}	$(1.1 \pm 0.2) \times 10^{-5}$	4.4
Rouleau	3×10^{-10}	$(2.4 \pm 0.4) \times 10^{-5}$	4.8
Jäger 1000 K	5×10^{-11}	$(1.6 \pm 0.3) \times 10^{-5}$	5.7

Notes. The number of degrees of freedom is 6.

In comparison to the best-fitting mass-loss parameters found with Suh (2000) opacities, the present-day mass-loss rate decreased by a factor of two, while the best-fitting shell mass decreased by a factor of about 1.5 for both opacities. The change in shell mass is above the 1σ level of the best-fitting model calculated with Suh (2000) opacities.

For the further investigation (unless otherwise mentioned), we always used the opacities by Suh (2000) and assumed the present-day wind to consist of $0.1 \mu\text{m}$ sized grains with a mass-loss rate of $2 \times 10^{-10} M_{\odot} \text{ yr}^{-1}$. The Suh (2000) opacities are the most recent measurements, and allow for a direct comparison to previous models by Schöier et al. (2005).

4.2.2. Grain composition

All previous models were calculated with the dusty wind consisting of pure amorphous carbon, which is a valid first assumption but in general not what is expected in circumstellar environments. Typical dust species that are found in CSEs of carbon-rich AGB star are magnesium sulfide (MgS) and silicon carbide (SiC). For R Scl, we adopted literature abundances of 4% for MgS (Hony & Bouwman 2004, detailed modelling of R Scl) and 10% for SiC (Sacuto et al. 2011, fitting procedure for R Scl), respectively. To test the influence of these two dust species on the modelled SED and derive the best-fitting shell mass, we computed models with the standard parameters ($2 \times 10^{-10} M_{\odot} \text{ yr}^{-1}$ and $3 \times 10^{-5} M_{\odot}$) for a set of models with 4% MgS and 10% SiC and a set of more extreme abundances (20% MgS; 20% SiC) in both the present-day wind and the shell. For these models, the grains are not in thermal contact. In the more extreme case, thermal contact decreases the shell temperature by approximately 10%, but does not change the estimated dust shell mass significantly.

The results are shown in Fig. 6. It is evident that the general influence on the shape of the SED is almost negligible for the realistic abundances. The effect is very weak even for the more extreme abundances. This is expected, since the introduction of these dust species will mainly lead to the introduction of material specific emission features at distinct wavelengths ($\sim 30 \mu\text{m}$ for MgS and $\sim 11 \mu\text{m}$ for SiC). The MgS feature is slightly visible for the models with high MgS content (right panel of Fig. 6), while the SiC feature is not seen in the modelled SED at all.

In addition to the qualitative analysis of the shape of the SED, we also derived the best-fitting shell masses for all calculated mixtures of dust species. The results are presented in Table 3. As expected, adding a significantly large amount of dust grains with different optical properties will increase the total shell mass needed to reproduce the SED well. This effect is still within the

Table 3. Best-fitting mass-loss parameters for the tested mixtures of dust species (amC, MgS, SiC).

Abundances			pd-wind ($M_{\odot} \text{ yr}^{-1}$)	Shell mass (M_{\odot})
amC (%)	MgS (%)	SiC (%)		
100	0	0	2×10^{-10}	$(3.1 \pm 0.5) \times 10^{-5}$
96	4	0	2×10^{-10}	$(3.2 \pm 0.6) \times 10^{-5}$
90	0	10	2×10^{-10}	$(3.5 \pm 0.6) \times 10^{-5}$
86	4	10	2×10^{-10}	$(3.6 \pm 0.6) \times 10^{-5}$
80	20	0	2×10^{-10}	$(3.7 \pm 0.6) \times 10^{-5}$
80	0	20	2×10^{-10}	$(4.0 \pm 0.7) \times 10^{-5}$
60	20	20	2×10^{-10}	$(4.9 \pm 0.8) \times 10^{-5}$

errors of realistic abundances, but for unrealistically high abundances of MgS and SiC, the shell mass increases significantly up to a factor of 1.5 for the case where 20% MgS and SiC and only 60% amC are present. We conclude that the shell mass is not influenced significantly for realistic MgS and SiC abundances.

4.2.3. Grain sizes

The size of the dust grains will determine the temperature, and hence the black-body emission, of the grains. In particular, large grains at the same distance from the star as small grains will have a lower temperature, contributing more to the long-wavelength part of the shell. We probed the influence of larger dust grains, contributing to a cooler dust component in the SED, on the derived dust shell mass. For the sake of simplicity, we assumed a single grain size ($0.1 \mu\text{m}$) in the present-day wind and a two-component population of grains in the shell, with $0.1 \mu\text{m}$ grains and a population of larger grains. The radii of the large grains were 0.25, 0.5, 0.75, 1, 2, and $5 \mu\text{m}$. For this analysis, we did not run a whole grid of MCMAX models, but assumed optically thin emission to derive scaled models for the mix of large and small grains in the shell (as explained in Sect. 3.8). For each model we varied the mass in the small and large grains to determine the best-fit to the SED. Since we only changed the properties of the dust in the shell, we now only fit the SED to points between $20 \mu\text{m} < \lambda \leq 350 \mu\text{m}$. The results of this grid of models can be found in Table 4.

From the χ^2_{red} values it is obvious that adding large grains to the shell deteriorates the model fit compared to the model with only small grains in the shell. For all large grain sizes except $0.75 \mu\text{m}$, the majority of the mass is located in small grains, while only a very small fraction of mass is located in large grains. For $0.75 \mu\text{m}$ sized grains in the shell, the mass distribution is the opposite, which emphasises the high degeneracy of the models (as described in more detail below). The total mass of the shell increases slightly with increasingly larger grain size. Overall, the χ^2_{red} value decreases slightly with larger grain sizes (for the models including large grains).

Figures 7–9 show the best-fitting SED as well as the corresponding χ^2 map for the smallest ($0.25 \mu\text{m}$), one intermediate ($0.75 \mu\text{m}$), and for the largest ($5 \mu\text{m}$) grain sizes we modelled. From the χ^2 maps of 0.25 and $0.75 \mu\text{m}$ large grains, it is obvious that the mass ratio between $0.1 \mu\text{m}$ and larger grains is highly degenerate, and similarly good results can be achieved with a reverse mass ratio between small and large grains. The larger the large grains, the more the degeneracy dissolves, and for $5 \mu\text{m}$

A&A 614, A17 (2018)

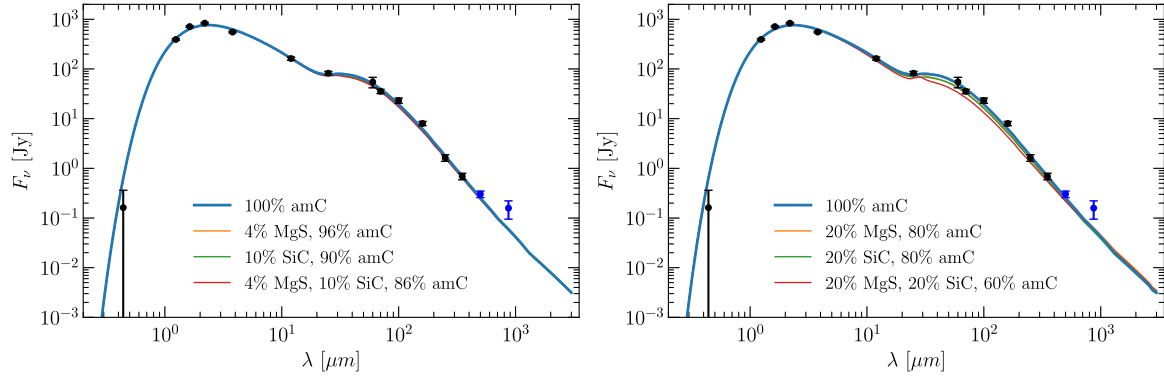


Fig. 6. Model grid for a set of different abundances of MgS and SiC. *Left:* set of abundances based on literature values. *Right:* set of high abundances. The present-day mass-loss is $2 \times 10^{-10} M_{\odot} \text{ yr}^{-1}$, and the detached-shell mass is $3 \times 10^{-5} M_{\odot}$.

Table 4. Best-fitting mass-loss parameters for the addition of large grains to the shell.

Size large grain (μm)	Large grain (M_{\odot})	Shell mass 0.1 μm (M_{\odot})	Total (M_{\odot})	χ^2_{red}
–	–	2.9×10^{-5}	3.1×10^{-5}	1.46
0.25	1.1×10^{-6}	3.0×10^{-5}	3.1×10^{-5}	1.76
0.5	1.1×10^{-6}	3.0×10^{-5}	3.1×10^{-5}	1.76
0.75	3.0×10^{-5}	2.0×10^{-6}	3.2×10^{-5}	1.75
1	5.6×10^{-6}	2.6×10^{-5}	3.2×10^{-5}	1.75
2	5.2×10^{-6}	2.8×10^{-5}	3.3×10^{-5}	1.74
5	3.7×10^{-6}	3.0×10^{-5}	3.4×10^{-5}	1.73

Notes. For reference, the first row gives the shell mass and reduced χ^2 value for the model containing only 0.1 μm grains.

sized large grains, the small grains dominate the shell mass, i.e. large grains do not significantly contribute to the total mass in the detached shell. Additionally, the long-wavelength part of the SED where the LABOCA excess emission is visible is not influenced by grains smaller than and equal to 5 μm .

4.2.4. Grain geometry: hollow spheres and fluffy grains

Our standard dust parameters assume spherical and solid dust grains. However, the dust coagulation process in reality likely favours more complex geometries than that (e.g. Mathis & Whiffen 1989). This is taken into account by alternative geometrical descriptions of astrophysical dust. Two widely used descriptions of geometry in dust radiative transfer modelling are the distribution of hollow spheres (DHS) and continuous distribution of ellipsoids (CDE). The DHS describes spherical dust grains with a specific radius and a varying amount of vacuum included in the grain interior, leading to different masses for each grain of same size. In the CDE approach, the shape of the grains follows a distribution of ellipsoids with different axis ratios, while the grains are solid. Min et al. (2003) concluded that the general absorption properties of CDE and DHS grain geometries are very similar and on average not really distinguishable from each other in an SED analysis. We therefore only tested the influence of the DHS geometry on the SED with respect to

the changing shell mass. In this case, we changed the dust properties in both the present-day wind and in the shell. The left panel of Fig. 10 shows the results of a model grid for DHS grains with a maximum vacuum volume fraction of 0.7 (Min et al. 2007). The best-fitting present-day mass-loss rate is $7.5 \times 10^{-11} M_{\odot} \text{ yr}^{-1}$ and the best-fitting detached-shell mass is $(1.3 \pm 0.2) \times 10^{-5} M_{\odot}$. As expected, less mass is needed to achieve the same emission from hollow grains that have the same surface area as the solid grains. Compared to the best-fitting model with solid grains, only 40% of the shell mass is needed for the best fit with DHS grains.

Another approach that most likely represents the most accurate description in terms of dynamic grain growth is the introduction of fluffy grains (e.g. Ossenkopf 1993, and references therein). Such fluffy grains are aggregates of individual small particles that stick together and form a larger, mostly irregular structure. A simple approach to mimic such particles is the method of ballistic agglomeration (BA; e.g. Shen et al. 2008). A library of sample aggregates can be found on the web for different aggregate properties and sizes⁴. The aggregate dust grain optical properties can be exactly computed by the discrete dipole approximation (DDA). Describing grains in this way is computationally very time-consuming, and the calculation of a single aggregate can take up to several days of computation time, even on advanced computing systems. For an overview on the computation of fluffy grains and their opacities, we refer to Min et al. (2016), who studied the characteristics of aggregate dust grains in the context of protoplanetary disks. They concluded that approximating opacities for aggregate grains by simpler approaches works relatively well in their modelling cases when using DHS-shaped grains in combination with effective medium theory and porosity. One of the main effects of using aggregate grains on the opacity is seen in the sub-millimeter wavelength range, where DHS as well as aggregate grains have a flatter slope than solid spheres. While a full study of the effects of fluffy aggregate dust grains in the CSE of AGB stars on the sub-millimeter SED is beyond the scope of this paper, we still present a simple radiative transfer model made for an example fluffy aggregate grain (see Fig. 11 for more details) to show the effect at sub-millimeter wavelengths. The results of a model grid for this fluffy grain species are shown in the right panel of Fig. 10. We note that by introducing fluffy grains in the detached shell, the overall shell mass required to reproduce the observed SED decreases, since the effective surface

⁴ <http://www.astro.princeton.edu/~draine/agglom.html>

M. Brunner et al.: Modelling the carbon AGB star R Sculptoris

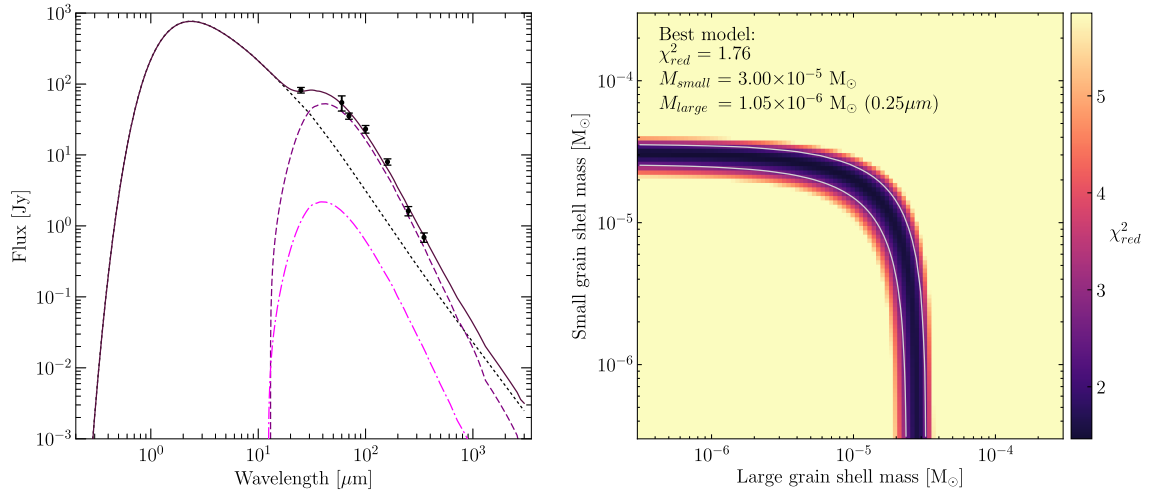


Fig. 7. *Left:* best-fitting model SED (purple solid line) consisting of the stellar and present-day wind contribution (grey dotted line), a detached-shell contribution of $0.1 \mu\text{m}$ grains (purple dashed line), and an additional shell contribution of $0.25 \mu\text{m}$ grains (magenta dot-dashed line). The wind parameters are $2 \times 10^{-10} M_{\odot} \text{ yr}^{-1}$ in $0.1 \mu\text{m}$ sized grains for the present-day wind, $3.00 \times 10^{-5} M_{\odot}$ in the $0.1 \mu\text{m}$ grain shell, and $1.05 \times 10^{-6} M_{\odot}$ in the $0.25 \mu\text{m}$ grain shell, derived for solid sphere amC grains. *Right:* χ -square map for the grid of different shell masses for small ($0.1 \mu\text{m}$) and large ($0.25 \mu\text{m}$) sized grains. The grey contour shows the 1σ level on the best-fitting χ -square value.

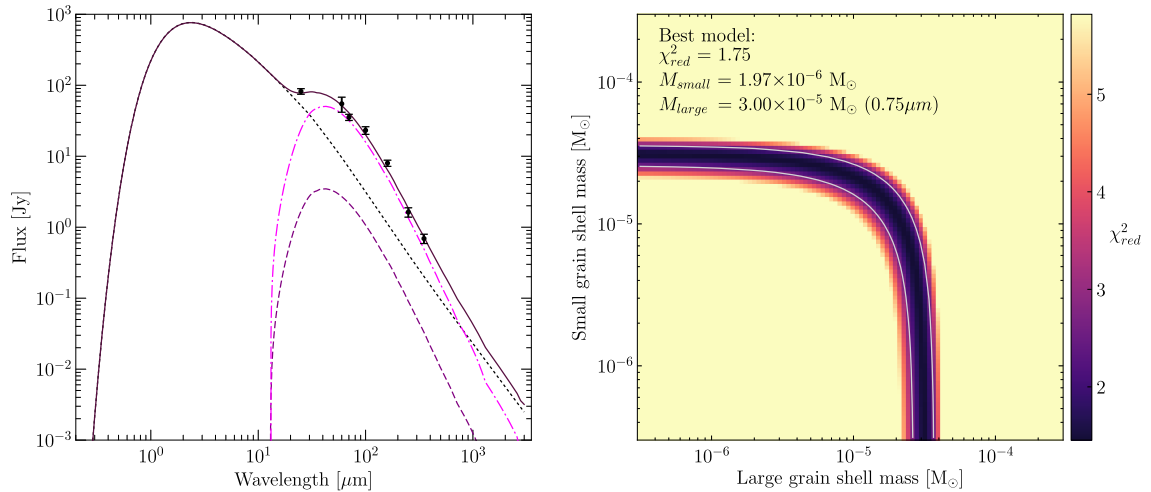


Fig. 8. *Left:* best-fitting model SED (purple solid line) consisting of the stellar and present-day wind contribution (grey dotted line), a detached-shell contribution of $0.1 \mu\text{m}$ grains (purple dashed line), and an additional shell contribution of $0.75 \mu\text{m}$ grains (magenta dot-dashed line). The wind parameters are $2 \times 10^{-10} M_{\odot} \text{ yr}^{-1}$ in $0.1 \mu\text{m}$ sized grains for the present-day wind, $1.97 \times 10^{-6} M_{\odot}$ in the $0.1 \mu\text{m}$ grain shell, and $3.00 \times 10^{-5} M_{\odot}$ in the $0.75 \mu\text{m}$ grain shell, derived for solid sphere amC grains. *Right:* χ -square map for the grid of different shell masses for small ($0.1 \mu\text{m}$) and large ($0.75 \mu\text{m}$) sized grains. The grey contour shows the 1σ level on the best-fitting χ -square value.

area of fluffy grains is much larger than for spherical grains. The best-fitting model for fluffy grains is given by a present-day mass-loss rate of $1 \times 10^{-10} M_{\odot} \text{ yr}^{-1}$ and a detached-shell mass of $(2.3 \pm 0.4) \times 10^{-5} M_{\odot}$, which is about three quarters of the shell mass obtained when using solid spherical grains.

4.3. Sub-millimeter excess

While a variation of the dust properties may change the estimated dust mass in the shell, it does not lead to great changes in the shape of the best-fitting SED. In particular, none of

the models presented here can satisfactorily explain both the emission observed with LABOCA and the data at shorter wavelengths. This excess emission is consistent with emission from the detached shell of dust observed around R Scl, as shown in Sect. 2.3. Independent observations of R Scl with LABOCA (Program ID: O-079.F-9300A) have a significantly lower signal-to-noise ratio. However, the measured continuum flux is consistent with the measurements given here, hence we judge that the excess emission is real and not due to a calibration error.

It is not straightforward to find an explanation for the flux observed with LABOCA. Dehaes et al. (2007) detected excess

A&A 614, A17 (2018)

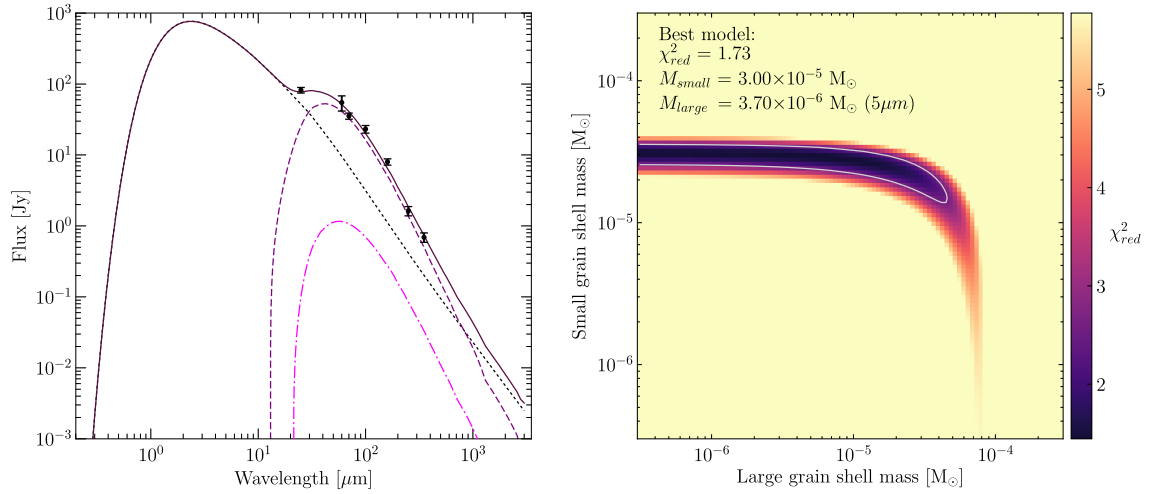


Fig. 9. *Left:* best-fitting model SED (purple solid line) consisting of the stellar and present-day wind contribution (grey dotted line), a detached-shell contribution of $0.1 \mu\text{m}$ grains (purple dashed line), and an additional shell contribution of $5 \mu\text{m}$ grains (magenta dot-dashed line). The wind parameters are $2 \times 10^{-10} M_{\odot} \text{ yr}^{-1}$ in $0.1 \mu\text{m}$ sized grains for the present-day wind, $3.00 \times 10^{-5} M_{\odot}$ in the $0.1 \mu\text{m}$ grain shell, and $3.7 \times 10^{-6} M_{\odot}$ in the $5 \mu\text{m}$ grain shell, derived for solid sphere amC grains. *Right:* χ -square map for the grid of different shell masses for small ($0.1 \mu\text{m}$) and large ($5 \mu\text{m}$) sized grains. The grey contour shows the 1σ level on the best-fitting χ -square value.

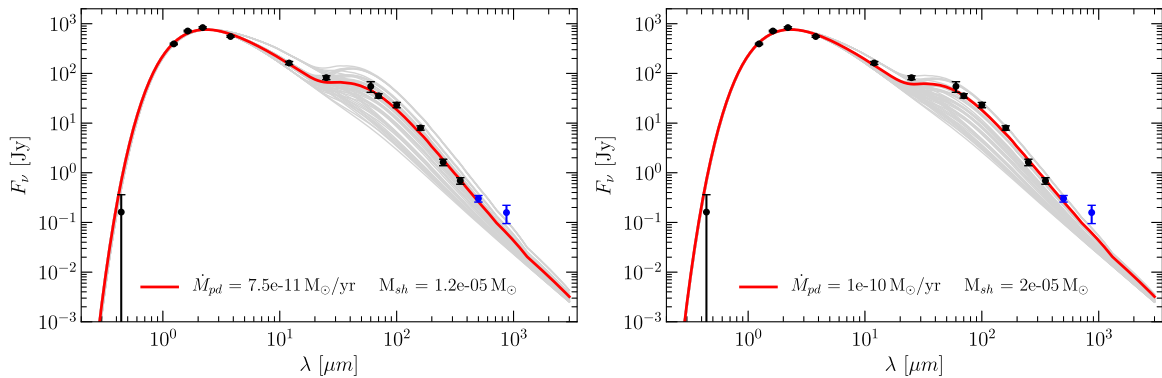


Fig. 10. *Left:* model grid for $0.1 \mu\text{m}$ sized amC grains described by a DHS model with a maximum volume fraction for vacuum of 0.70; opacities based on Suh (2000). *Right:* model grid for small, fluffy amC grains (as presented in Fig. 11) with a volume corresponding to the volume of $0.1 \mu\text{m}$ solid spheres.

emission at 1.2 mm in a small sub-sample of AGB stars, including R Scl (with a flux of 61.2 mJy at 1.2 mm). They offered a number of possible explanations for the excess flux: (1) contribution from molecular lines, (2) a change in emissivity of the dust grains at the relevant wavelengths, (3) the presence of cold dust, and (4) emission from the photosphere/chromosphere.

We calculated the effects of photometric bandpass correction and molecular line contamination in the LABOCA band and come to the conclusion that both are negligible with respect to the strength of the excess, in line with the conclusions by Dehaes et al. (2007) for regular AGB CSEs. In particular in the case of detached-shell sources, the contribution from molecular lines is likely to be very low because of the photodissociation of molecules in the shell by the interstellar radiation field. In principle, a population of very cold dust grains would add emission at long wavelengths. However, fitting the entire SED for R Scl, including the LABOCA observations, requires adding

a black body with a peak at $\lambda \lesssim 500 \mu\text{m}$. This corresponds to temperatures lower than 5 K (Fig. 12). Not only would this require a population of very large grains, but also for this population to be completely distinct from the population of small grains, since a continuous grain size distribution would lead to a smoother SED shape in the FIR and sub-millimeter, and hence no turn-off to fit both the LABOCA data and the shorter wavelength data. The excess emission is therefore likely not due to thermal emission from dust grains. Finally, the spatial information from the LABOCA and ALMA high-angular observations excludes a photospheric or chromospheric origin of the emission (see Sect. 2.3).

A change in the emission properties from the standard grains generally assumed to be present around AGB stars hence seems to be the most likely explanation for the observed sub-millimeter excess. In the case of R Scl (a carbon AGB star), one possible mechanism may be the presence of polycyclic aromatic

M. Brunner et al.: Modelling the carbon AGB star R Sculptoris

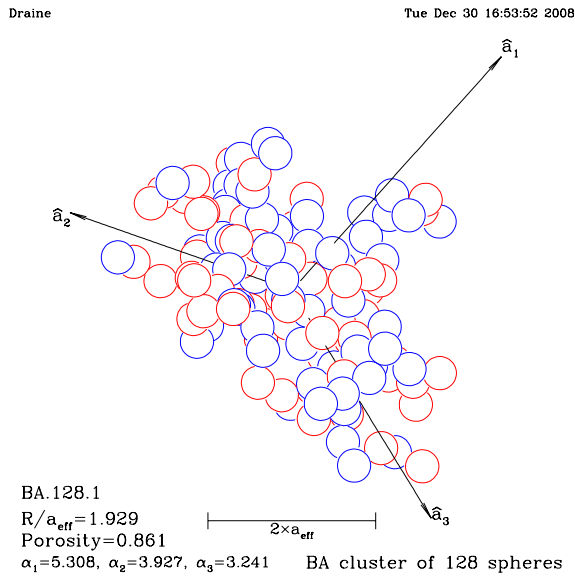


Fig. 11. Example fluffy grain model (<http://www.astro.princeton.edu/~draine/agglom.html>) used for calculating opacities with DDSCAT (Draine & Flatau 1994). This particular grain with an effective size of $0.1 \mu\text{m}$ is composed of 128 smaller particles. No particle migration is assumed.

hydrocarbons (PAHs; Dehaes et al. 2007). In addition to R Scl and the sources in Dehaes et al. (2007), the same excess is observed in the sub-millimeter in the detached-shell sources U Ant, DR Ser, and V644 Sco (Maercker et al., in prep.), possibly indicating that the grain properties causing the excess may be a general phenomenon in the dust from (carbon) AGB stars.

In observations of the ISM in the Magellanic clouds (Gordon et al. 2014), a similar problem arises where a sub-millimeter excess is detected with *Herschel* SPIRE that cannot be reproduced by standard dust models. Previous studies by Bot et al. (2010) and Israel et al. (2010) explain the sub-millimeter excess by the introduction of cold dust grains, while a similar excess at longer wavelengths (millimeter to centimeter) is explained by emission due to spinning dust grains. Subsequently, Gordon et al. (2014) tested two scenarios: a change in dust emissivity by introducing a “broken emissivity law” by changing the optical properties of the dust at the relevant wavelengths, and the introduction of a cold temperature dust population. This has a significant effect on the estimated total dust mass in these galaxies; a very cold dust component would potentially contain a hitherto undetected large reservoir of dust mass. However, the authors concluded that a broken emissivity law fits the observations best and that a colder dust component is less likely the origin of the sub-millimeter excess in the Magellanic clouds, in line with the results obtained here. The fact that a very similar excess is observed in the LMC and SMC raises the question of how significant the contribution from AGB stars to the total dust budget is also in low-metallicity galaxies.

We note that without a combination of the SPIRE and LABOCA data, the turn-off in the sub-millimeter would not have been detected. The conclusion without the data at the SPIRE wavelengths would rather have been a continuous grain size population growing to comparatively large grains – a scenario that seems to be excluded now. Observations in the FIR and

sub-millimeter are hence essential to properly establish a turn-off in the emissivity in the sub-millimeter, while spatially resolved observations at longer wavelengths (sub-millimeter to millimeter) are needed to constrain the grain properties and determine the origin of the sub-millimeter excess in the detached shell around R Scl and other detached-shell sources.

5. Discussion and conclusions

We modelled the dusty present-day wind and detached shell around R Scl and derived values for the present-day dust mass-loss rate and detached-shell dust mass. We investigated the effect of different dust properties (chemical composition, grain sizes, and geometry) and optical constants on the estimated best-fitting shell mass. We conclude the following:

- The observed SED below $350 \mu\text{m}$ is reproduced equally well, regardless of the dust properties.
- A change in the implemented optical constants only mildly affects the estimated shell mass.
- An introduction of realistic amounts of MgS and SiC dust does not have any significant influence on the derived shell mass.
- Including large grains up to $5 \mu\text{m}$ in the detached shell does not influence the determined total shell mass and does not improve the fit to the SED.
- The estimated shell mass is most strongly affected by the geometry of the dust grains. Hollow spheres or fluffy grains require a lower dust mass in order to fit the observed SED. Based on this study, the largest uncertainty in determining the return of dust from AGB stars hence lies in the geometrical description of the grains.
- We observe a significant sub-millimeter excess that cannot be reproduced by any of the models. The origin of this excess is not clear and requires additional observations to determine the spectral index of the dust at sub-millimeter and centimeter wavelengths. A possible explanation is that the opacity of the dust in R Scl (and other carbon stars) has a more complex spectral profile than that considered by us, which could be caused by the presence of PAHs.

We provided a new estimate of the dust mass in the detached shell around R Scl and investigated the dependence of the determined mass on critical grain properties. Based on our models, the upper limit for the shell mass is $3 \times 10^{-5} M_{\odot}$, assuming solid $0.1 \mu\text{m}$ sized grains. The estimated gas mass in the shell is $4.5 \times 10^{-3} M_{\odot}$ (Maercker et al. 2016), resulting in a dust-to-gas ratio of 0.007. This value is relatively high compared to results for other carbon-rich AGB stars (Ramstedt et al. 2008). However, if we instead assume DHS grains, the total dust mass decreases by a factor of 2.4 – affecting our estimate of the total dust-masses produced by stars. In that sense, the structure of the dust grains is important when determining the total amount of dust produced from stars and present in galaxies, independent of stellar mass, and when comparing different sources of dust.

In addition to estimating the dust mass in the shell, we also find a significant excess emission in the sub-millimeter. We were unable to constrain the origin of this excess emission. In order to properly constrain the properties of grains around AGB stars, observations at long wavelengths (sub-millimeter to millimeter and possibly centimeter) are also needed.

Acknowledgements. We wish to thank Robin Lombaert for his valuable support and intensive help concerning radiative transfer modelling. M.B. acknowledges funding through the uni:docs fellowship of the University of Vienna. F.K. and M.B. acknowledge funding by the Austrian Science Fund FWF under project

A&A 614, A17 (2018)

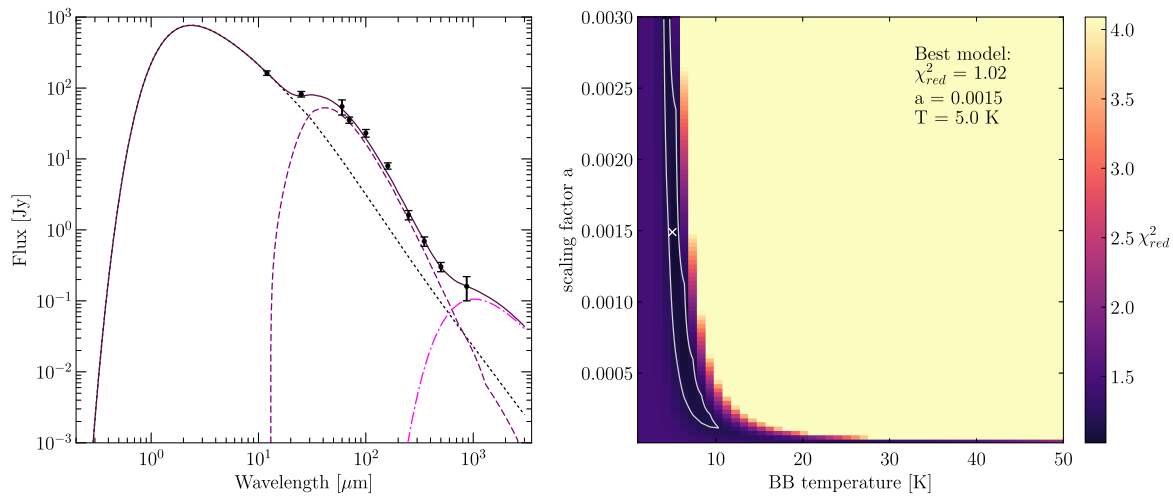


Fig. 12. *Left:* best-fitting model SED (solid line) consisting of the stellar and present-day wind contribution (dotted line), a detached-shell contribution (dashed line), and an additional black body (dot-dashed line). The wind parameters are the best-fitting parameters of $1 \times 10^{-10} M_{\odot} \text{ yr}^{-1}$ for the present-day wind and $3 \times 10^{-5} M_{\odot}$ for the shell mass, derived for $0.1 \mu\text{m}$ solid sphere amC grains. The best-fitting cool black-body temperature is 5 K. *Right:* χ -square map for the grid of cool black bodies used to find the best fit. The scaling factor a scales the flux of the black body.

number P23586. M. Maercker acknowledges support from the Swedish Research Council under grant number 2016-03402.

References

- Bot, C., Ysard, N., Paradis, D., et al. 2010, *A&A*, **523**, A20
- Cox, N. L. J., Kerschbaum, F., van Marle, A.-J., et al. 2012, *A&A*, **537**, A35
- Dehaes, S., Groenewegen, M. A. T., Decin, L., et al. 2007, *MNRAS*, **377**, 931
- Draine, B. T., & Flatau, P. J. 1994, *J. Opt. Soc. Am. A*, **11**, 1491
- Forestini, M., & Charbonnel, C. 1997, *A&AS*, **123**, 241
- González Delgado, D., Olofsson, H., Schwarz, H. E., Eriksson, K., & Gustafsson, B. 2001, *A&A*, **372**, 885
- González Delgado, D., Olofsson, H., Schwarz, H. E., et al. 2003, *A&A*, **399**, 1021
- Gordon, K. D., Roman-Duval, J., Bot, C., et al. 2014, *ApJ*, **797**, 85
- Griffin, M. J., Abergel, A., Abreu, A., et al. 2010, *A&A*, **518**, L3
- Groenewegen, M. A. T., Waelkens, C., Barlow, M. J., et al. 2011, *A&A*, **526**, A162
- Habing, H. J. 1996, *A&ARv*, **7**, 97
- Herwig, F., & Austin, S. M. 2004, *ApJ*, **613**, L73
- Hony, S., & Bouwman, J. 2004, *A&A*, **413**, 981
- Israel, F. P., Wall, W. F., Raban, D., et al. 2010, *A&A*, **519**, A67
- Jager, C., Mutschke, H., & Henning, T. 1998, *A&A*, **332**, 291
- Kerschbaum, F., & Hron, J. 1994, *A&AS*, **106**, 397
- Knapp, G. R., Pourbaix, D., Platais, I., & Jorissen, A. 2003, *A&A*, **403**, 993
- Kovács, A. 2008, in *Millimeter and Submillimeter Detectors and Instrumentation for Astronomy IV*, *Proc. SPIE*, **7020**, 70201S
- Maercker, M., Mohamed, S., Vlemmings, W. H. T., et al. 2012, *Nature*, **490**, 232
- Maercker, M., Ramstedt, S., Leal-Ferreira, M. L., Olofsson, G., & Floren, H. G. 2014, *A&A*, **570**, A101
- Maercker, M., Vlemmings, W. H. T., Brunner, M., et al. 2016, *A&A*, **586**, A5
- Maercker, M., Brunner, M., Mecina, M., & De Beck, E. 2018, *A&A*, **611**, A102
- Mancini, M., Schneider, R., Graziani, L., et al. 2015, *MNRAS*, **451**, L70
- Mathis, J. S., & Whiffen, G. 1989, *ApJ*, **341**, 808
- Mattsson, L., Höfner, S., Wahlin, R., & Herwig, F. 2007, in *Why Galaxies Care About AGB Stars: Their Importance as Actors and Probes*, eds. F. Kerschbaum, C. Charbonnel, & R. F. Wing, *ASP Conf. Ser.*, **378**, 239
- Min, M., Hovenier, J. W., & de Koter, A. 2003, *A&A*, **404**, 35
- Min, M., Waters, L. B. F. M., de Koter, A., et al. 2007, *A&A*, **462**, 667
- Min, M., Dullemond, C. P., Dominik, C., de Koter, A., & Hovenier, J. W. 2009, *A&A*, **497**, 155
- Min, M., Rab, C., Woitke, P., Dominik, C., & Ménard, F. 2016, *A&A*, **585**, A13
- Olofsson, H., Eriksson, K., & Gustafsson, B. 1988, *A&A*, **196**, L1
- Olofsson, H., Carlstrom, U., Eriksson, K., Gustafsson, B., & Willson, L. A. 1990, *A&A*, **230**, L13
- Olofsson, H., Bergman, P., Eriksson, K., & Gustafsson, B. 1996, *A&A*, **311**, 587
- Olofsson, H., Maercker, M., Eriksson, K., Gustafsson, B., & Schöier, F. 2010, *A&A*, **515**, A27
- Ossenkopf, V. 1993, *A&A*, **280**, 617
- Poglitsch, A., Waelkens, C., Geis, N., et al. 2010, *A&A*, **518**, L2
- Preibisch, T., Ossenkopf, V., Yorke, H. W., & Henning, T. 1993, *A&A*, **279**, 577
- Ramstedt, S., Schöier, F. L., Olofsson, H., & Lundgren, A. A. 2008, *A&A*, **487**, 645
- Rouleau, F., & Martin, P. G. 1991, *ApJ*, **377**, 526
- Sacuto, S., Aringer, B., Hron, J., et al. 2011, *A&A*, **525**, A42
- Schneider, R., Valiante, R., Ventura, P., et al. 2014, *MNRAS*, **442**, 1440
- Schöier, F. L., Lindqvist, M., & Olofsson, H. 2005, *A&A*, **436**, 633
- Shen, Y., Draine, B. T., & Johnson, E. T. 2008, *ApJ*, **689**, 260
- Siringo, G., Kreysa, E., Kovács, A., et al. 2009, *A&A*, **497**, 945
- Steffen, M., & Schönberner, D. 2000, *A&A*, **357**, 180
- Suh, K.-W. 2000, *MNRAS*, **315**, 740
- Wittkowski, M., Hofmann, K.-H., Höfner, S., et al. 2017, *A&A*, **601**, A3
- Zubko, V. G., Mennella, V., Colangeli, L., & Bussoletti, E. 1996, *MNRAS*, **282**, 1321

M. Brunner et al.: Modelling the carbon AGB star R Sculptoris

Appendix A: Additional opacity models

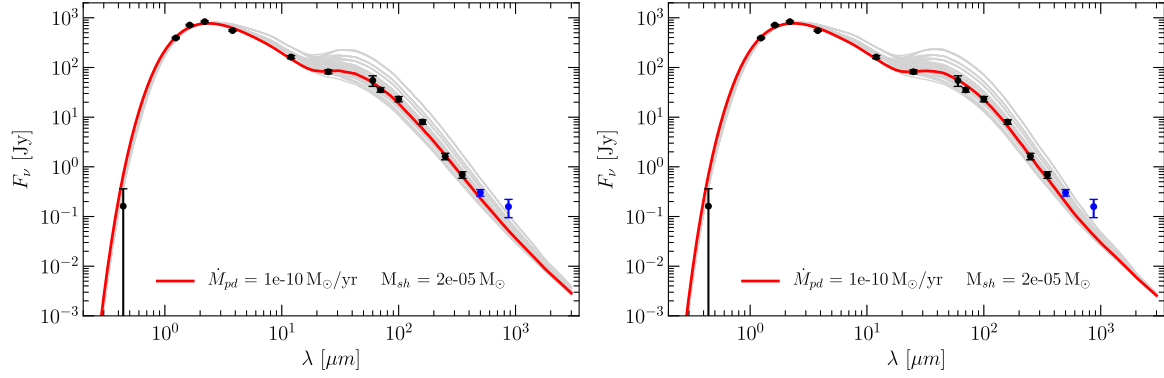


Fig. A.1. Model grids calculated with opacities by Zubko et al. (1996) (left) and Preibisch et al. (1993) (right) for $0.1 \mu\text{m}$ solid, spherical amC dust grains in a present-day wind and detached shell. The best-fitting model is represented with a solid red line, and the respective best-fitting model parameters are given in the legend. The grey lines represent the other models in the grid.

Chapter 7

The filamentary detached shell around U Antliae (Paper IV)

Title: *Rings and filaments: The remarkable detached CO shell of U Antliae*

Authors: F. Kerschbaum, M. Maercker, **M. Brunner**, M. Lindqvist, H. Olofsson, M. Mecina, E. De Beck, M.A.T. Groenewegen, E. Lagadec, S. Mohamed, C. Paladini, S. Ramstedt, W.H.T. Vlemmings, and M. Wittkowski

Year: 2017

Journal: Astronomy and Astrophysics

DOI: <https://doi.org/10.1051/0004-6361/201730665>

Credit: Kerschbaum et al. 2017, A&A, 605, A116, reproduced with permission © ESO

In this publication we present new high resolution sub-mm ALMA observations of the detached shell around the carbon AGB star U Ant. We analyse the morphology and possible formation history of the very thin shell with respect to its remarkable filamentary structure, which has not been imaged in such detail in any other detached shell before. By simple radiative transfer modelling of the two available spectral lines, a present-day wind mass-loss rate and detached shell mass can be derived, through which the mass-loss evolution can be estimated.

Personal contribution: The fundamental part of this work, namely the data reduction from raw ALMA interferometric data to calibrated image cubes, has been performed by myself. Additionally, I performed the extraction of spectra and radial profiles and prepared the necessary input data to the radiative transfer models. Furthermore, I was actively contributing to the scientific discussion of the results and will continue to work on a more detailed analysis of the data including hydrodynamical modelling of the circumstellar outflow.

A&A 605, A116 (2017)
 DOI: [10.1051/0004-6361/201730665](https://doi.org/10.1051/0004-6361/201730665)
 © ESO 2017

**Astronomy
&
Astrophysics**

Rings and filaments: The remarkable detached CO shell of U Antliae ★,★,★,★

F. Kerschbaum¹, M. Maercker², M. Brunner¹, M. Lindqvist², H. Olofsson², M. Mecina¹, E. De Beck²,
 M. A. T. Groenewegen³, E. Lagadec⁴, S. Mohamed^{5,6,10}, C. Paladini⁷, S. Ramstedt⁸,
 W. H. T. Vlemmings², and M. Wittkowski⁹

¹ Department of Astrophysics, University of Vienna, Türkenschanzstr. 17, 1180 Vienna, Austria
 e-mail: franz.kerschbaum@univie.ac.at

² Department of Earth and Space Sciences, Chalmers University of Technology, Onsala Space Observatory, 43992 Onsala, Sweden

³ Koninklijke Sterrenwacht van België, Ringlaan 3, 1180 Brussels, Belgium

⁴ Laboratoire Lagrange, Université Côte d'Azur, Observatoire de la Côte d'Azur, CNRS, Bd de l'Observatoire, CS 34229, 06304 Nice Cedex 4, France

⁵ South African Astronomical Observatory, PO Box 9, 7935 Observatory, South Africa

⁶ Astronomy Department, University of Cape Town, 7701, Rondebosch, South Africa

⁷ Institut d'Astronomie et d'Astrophysique, Université Libre de Bruxelles, Campus Plaine C.P. 226, Boulevard du Triomphe, 1050 Brussels, Belgium

⁸ Department of Physics and Astronomy, Uppsala University, Box 516, 75120 Uppsala, Sweden

⁹ European Southern Observatory, Karl-Schwarzschild-Straße 2, 85748 Garching, Germany

¹⁰ National Institute for Theoretical Physics, Private Bag X1, 7602 Matieland, South Africa

Received 20 February 2017 / Accepted 3 August 2017

ABSTRACT

Aims. Our goal is to characterize the intermediate age, detached shell carbon star U Antliae morphologically and physically in order to study the mass-loss evolution after a possible thermal pulse.

Methods. High spatial resolution ALMA observations of unprecedented quality in thermal CO lines allow us to derive first critical spatial and temporal scales and constrain modeling efforts to estimate mass-loss rates for both the present day as well as the ejection period of the detached shell.

Results. The detached shell is remarkably thin, overall spherically symmetric, and shows a barely resolved filamentary substructure possibly caused by instabilities in the interaction zone of winds with different outflow velocities. The expansion age of the detached shell is of the order of 2700 yr and its overall width indicates a high expansion-velocity and high mass-loss period of only a few hundred years at an average mass-loss rate of $\approx 10^{-5} M_{\odot} \text{ yr}^{-1}$. The post-high-mass-loss-rate-epoch evolution of U Ant shows a significant decline to a substantially lower gas expansion velocity and a mass-loss rate amounting to $4 \times 10^{-8} M_{\odot} \text{ yr}^{-1}$, at present being consistent with evolutionary changes as predicted for the period between thermal pulses.

Key words. stars: AGB and post-AGB – stars: carbon – stars: evolution – stars: mass-loss

1. Introduction

Mass loss on and shortly after the asymptotic giant branch (AGB) is a major factor in the post-main-sequence evolution of low- and intermediate-mass stars. The photospheres and expanding outflows show a rich molecular chemistry, and are the formation sites for microscopic dust particles. Mass loss plays a crucial role within the cosmic cycle of matter, providing up to 70% of the interstellar dust (e.g. [Schneider et al. 2014](#)). Understanding the chemistry in the atmospheres and circumstellar

envelopes (CSEs) of AGB stars, the mass loss, and the mixing of material into the interstellar medium (ISM) is therefore crucial to understanding early star formation and the evolution of galaxies. Studies of AGB stars are also important for understanding the future of our solar system.

Mass loss of AGB stars takes the form of slow (typically $5\text{--}25 \text{ km s}^{-1}$) winds with high mass-loss rates (of up to $10^{-4} M_{\odot}/\text{yr}$). Although mass loss has been studied since the 1960s, many basic questions on its temporal evolution, geometry, and dynamics remain unanswered.

There is growing evidence that mass loss on the AGB is not a continuous process. One cause for variations are He shell flashes (thermal pulses), which occur typically every 10^4 to 10^5 yr ([Vassiliadis & Wood 1993](#)). They are thought to be responsible for the formation of detached shells observed around carbon AGB stars ([Olofsson et al. 1996](#)). High spatial resolution observations of these objects have shown thin, clumpy, detached shells, indicative of short phases of intense mass loss, colliding with a previous, slower AGB wind ([Lindqvist et al. 1999](#); [Olofsson et al. 2000](#); [Schöier et al. 2005](#); [Maercker et al. 2012](#)).

* This paper makes use of the following ALMA data: ADS/JAO.ALMA2015.1.00007.S. ALMA is a partnership of ESO (representing its member states), NSF (USA) and NINS (Japan), together with NRC (Canada), NSC and ASIAA (Taiwan), and KASI (Republic of Korea), in cooperation with the Republic of Chile. The Joint ALMA Observatory is operated by ESO, AUI/NRAO and NAOJ.

** The reduced ALMA FITS data cubes are available at the CDS via anonymous ftp to cdsarc.u-strasbg.fr (130.79.128.5) or via <http://cdsarc.u-strasbg.fr/viz-bin/qcat?J/A+A/605/A116>

*** The movie is available at <http://www.aanda.org>

A&A 605, A116 (2017)

The presence of a binary companion can further complicate outflows from AGB stars (e.g. Mayer et al. 2011; Maercker et al. 2012; Ramstedt et al. 2014, and references therein), and high spatial resolution observations of gas and dust (in mm-CO, far-IR and visual scattered light) are needed to determine morphology and mass-loss-rate evolution. The same holds for the clumpiness of the detached shells and the relative location of dust and gas (Kerschbaum et al. 2010; Olofsson et al. 2010; Maercker et al. 2010, 2016), since they potentially hold crucial information on the mass-loss mechanism and the physical processes predominating in the wind.

The carbon star U Antliae provides a special opportunity to study these questions in detail. Known already for its far-IR excess in the late 1980s and imaged using the Infrared Astronomical Satellite (IRAS; Waters et al. 1994; Izumiura et al. 1995), it was evident that this object (260 pc from HIPPARCOS) had a spatially extended detached dust shell with a radius of about 50". Single-dish mapping in the $^{12}\text{CO}(1-0)$ and $(2-1)$ lines revealed a detached shell of radius $\sim 43''$ (Olofsson et al. 1996). Observations of scattered stellar light around U Ant (González Delgado et al. 2001) revealed a complex shell structure. The authors identified four shells at $\sim 25''$, $37''$, $43''$, and $46''$, referred to as shell 1, 2, 3, and 4 below. This structure was confirmed by studying scattered polarized light (González Delgado et al. 2003; Maercker et al. 2010). The mass of the outermost shell 4 (after Maercker et al. (2010) more at 50") is dominated by dust, while shell 3 at $43''$ mainly consists of gas. Radiative transfer models of single-dish CO data are consistent with a thin CO shell at $43''$ (Schöier et al. 2005).

The peak intensity of the thin ($<3''$) dust shell seen using *Herschel*-PACS at $70\mu\text{m}$ (Kerschbaum et al. 2010) coincides with shell 3, which is attributed to material expelled ~ 3000 yr ago. This age places U Ant just between other detached-shell objects that were observed by mm-interferometers in the last decade: U Cam (~ 800 yr, observed with the Institut de radioastronomie millimétrique Plateau de Bure interferometer (IRAM PdB; Lindqvist et al. 1999), R Scl (~ 2300 yr, observed with Atacama Large Millimeter/submillimeter Array (ALMA); Maercker et al. 2012, 2016), and the more evolved shell of TT Cyg (~ 7000 yr, observed with IRAM PdB; Olofsson et al. 2000).

Observations by Maercker et al. (2010) also provide information on light scattered by Na and K atoms in the shell. Such data sets provided the highest spatial resolutions so far. Nevertheless, a complete picture is hampered by the low spatial resolution of the single dish mm-CO data, and the lack of velocity information in the optical and IR observations.

2. Observations and data reduction

ALMA observations hold the potential to change this situation dramatically, delivering high sensitivity observations of the circumstellar environment of U Ant at high angular and spectral resolution. We observed U Ant in ALMA Cycle 3 using an intermediate and a compact 12 m-array (MA) configuration in band 3 (B3) and band 6 (B6), targeting the $^{12}\text{CO}(J = 1-0)$ and $^{12}\text{CO}(J = 2-1)$ lines. The CSE of U Ant was covered by a mosaic of 23 and 85 individual pointings in B3 and B6, respectively, resulting in a map of $110'' \times 110''$. Additionally, short-baseline observations with the 7 m-array (ACA) and single-dish measurements with the total power (TP) array to recover all spatial scales were carried out. The beam sizes in the reduced maps are $1.82'' \times 1.63''$ (PA = 80.5°) for CO(1-0) and $1.37'' \times 1.00''$ (PA = 86.6°) for CO(2-1). In B3 the main target

of the spectral setup was the CO(1-0) line at 115.271 GHz, using a spectral resolution of 244.019 kHz, which corresponds to a velocity resolution of 0.635 km s^{-1} . In B6 the main target was the CO(2-1) line at 230.538 GHz, observed with a resolution of 488.037 MHz to achieve the same velocity resolution as in B3.

In order to optimize the final data product quality, we re-calibrated and re-imaged the data. The calibration was done with the Common Astronomy Software Application (CASA) pipeline scripts as delivered to the principal investigator and no major adjustments needed to be done. Flux calibrators for the individual data sets were Mars and Ganymede; phase calibrators were the quasars J1042-4143 and J1107-4449. The calibrated data sets of the MA and ACA were combined in the uv-plane with appropriate weighting.

The imaging process, which is critical for the final data quality, was carried out with extended and custom python imaging scripts by our team; these scripts were executed in CASA. These scripts make use of an iterative and interactive imaging procedure with the CLEAN algorithm, using Briggs weighting (with robustness = 0.5), multi-scale cleaning, and iterative masking with decreasing thresholds to deconvolve the inter-shell structures of the CSE. Compared to the imaging scripts of the delivered data products, our strategy employs more mask iterations with finer thresholds and the CLEAN masks are carefully adapted where necessary.

After the imaging process for the interferometric data, the TP single-dish data were added via feathering¹. For the final data products presented in Figs. 1 and 2, velocity binning to 1 km s^{-1} was applied during the imaging to increase the signal-to-noise ratio in the fainter parts of the shell.

3. Interpretation

3.1. Morphology of the detached shell

A first inspection of the B3 and B6 maps close to the systemic velocity of 24.5 km s^{-1} in Figs. 1 and 2 reveals a remarkably thin, overall spherically symmetric, detached CO shell of about $42.5''$ radius expanding at a velocity of about 19 km s^{-1} . At a distance of 260 pc this corresponds to an expansion age of about 2700 yr and a physical radius of 0.05 pc. The shell appearance is quite similar in both CO lines. The detached shell centre coincides with the stellar position within the measurement errors.

On closer inspection, the detached shell shows some fine, filamentary structures down to the resolution limit of about $1.5''$. In several regions the shell is split into two basically unresolved filaments differing in radius by up to $5''$. This splitting is seen in many of the velocity channels and seems to be a general property of the shell as it is supported by the B6 spectral scan movie in Fig. A.1. Figure 3 makes this even more evident by plotting the CO($J = 2-1$) emission of the detached shell close to systemic velocity in polar coordinates. While at other velocities the details of the shell change, the overall filamentary structure remains.

The partially split structure is further seen through a comparable phenomenon at the extreme velocity channel maps both in Figs. 1 and 2, and in the integrated spectrum close to the stellar position in Fig. 4. The latter reveals a split in velocity by

¹ Although feathering of single-dish to interferometric data is known to be problematic and in most cases slightly incorrect, up to now no other, more reliable methods to combine single-dish data in the visibility plane are currently under development. The authors are aware of the fact that the resulting images may contain artefacts, but thorough analysis suggests that the TP inclusion via this process does not alter the data significantly.

F. Kerschbaum et al.: The remarkable detached shell of U Antliae

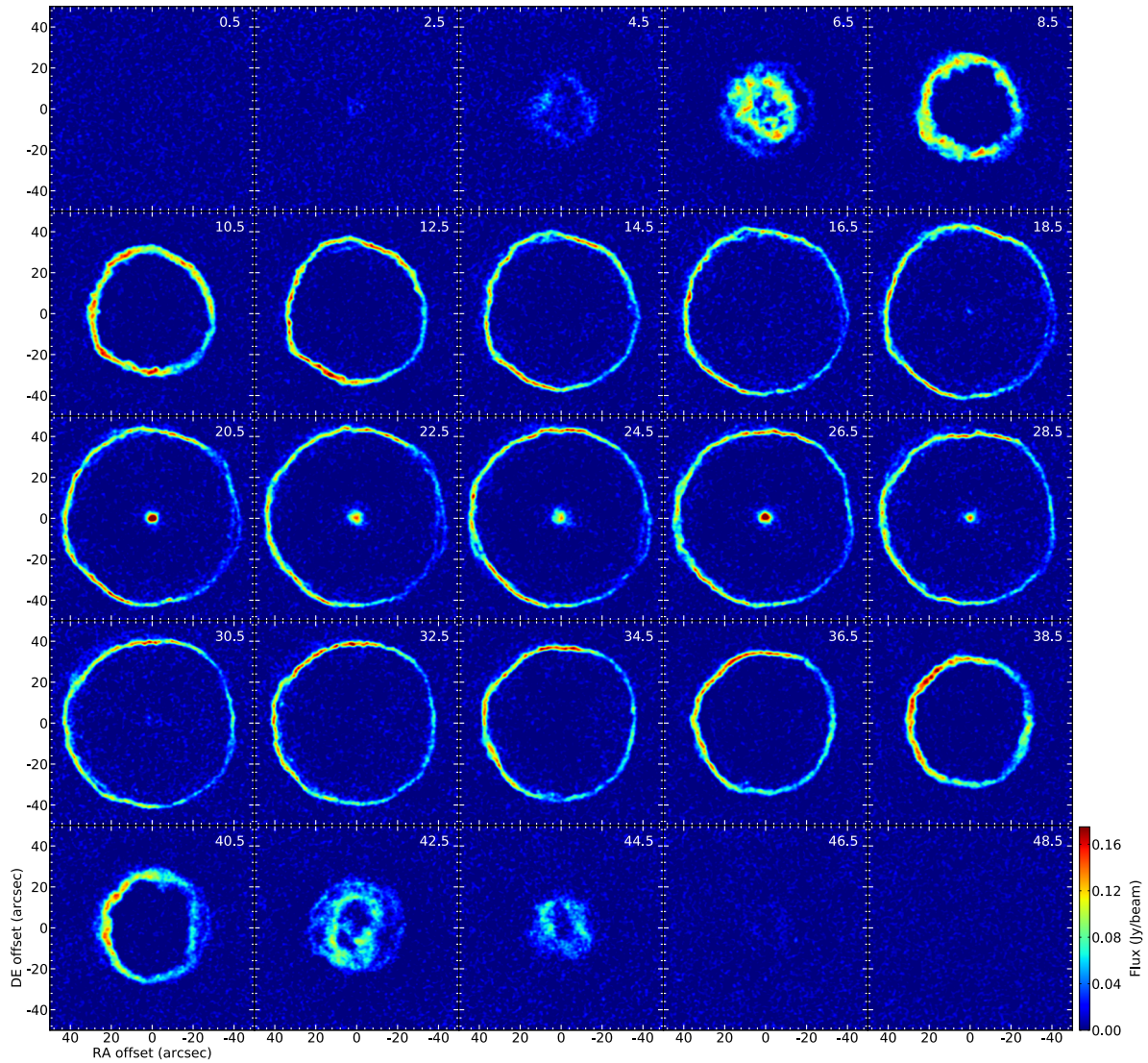


Fig. 1. ALMA (MA+ACA+TP) observations of $^{12}\text{CO}(1-0)$ towards U Ant. The central LSR velocity in units of km s^{-1} of each subpanel is indicated in the respective upper right corners. The velocity resolution is binned to 1 km s^{-1} . The colour bar to the right gives the flux density scale.

about 3 km s^{-1} at both velocity extremes. This split is also responsible for the double ring structure seen in the middle panel of Fig. 4, which shows enlarged 0.65 km s^{-1} resolution velocity channel maps at $\pm 18.5 \text{ km s}^{-1}$ relative to the systemic velocity. The illustration on the right side of Fig. 4 visualizes the geometrical situation when selecting a velocity channel map at the extreme velocity of the “inner” shell filament leading to a spatially separate cut through the “outer” shell filament, consistent with the data shown in the middle panel where a filled circle is surrounded by a ring.

The question is whether we see the same phenomenon in the channel maps and in the spectrum? A plausible interpretation is that the splitting into filaments is a result of the supersonic collision of a fast wind resulting from the thermal pulse and a slower normal AGB wind. The gas at the interface heats up and

expands outwards resulting in the creation of a reverse shock (moving towards the star) and a forward shock (expanding into the pre-thermal pulse material). Depending on the gas densities and velocities, the thin shell that forms from this supersonic interaction can be subject to dynamical and/or thermal instabilities (e.g. Mohamed et al. 2012, 2013). The filamentary structure we observe may result from the growth of such instabilities.

This is further supported by the coincidence that a velocity splitting as observed in the extreme velocity channels shown in Fig. 4 and discussed above could also explain the spatial splitting into filaments of up to $5''$ in the stellar velocity channel image over a timescale comparable to the geometric expansion age of the shell (i.e. 2700 yr).

Mohamed et al. (2012) consider the collision of a stellar wind emanating from a runaway star with the flow from the

A&A 605, A116 (2017)

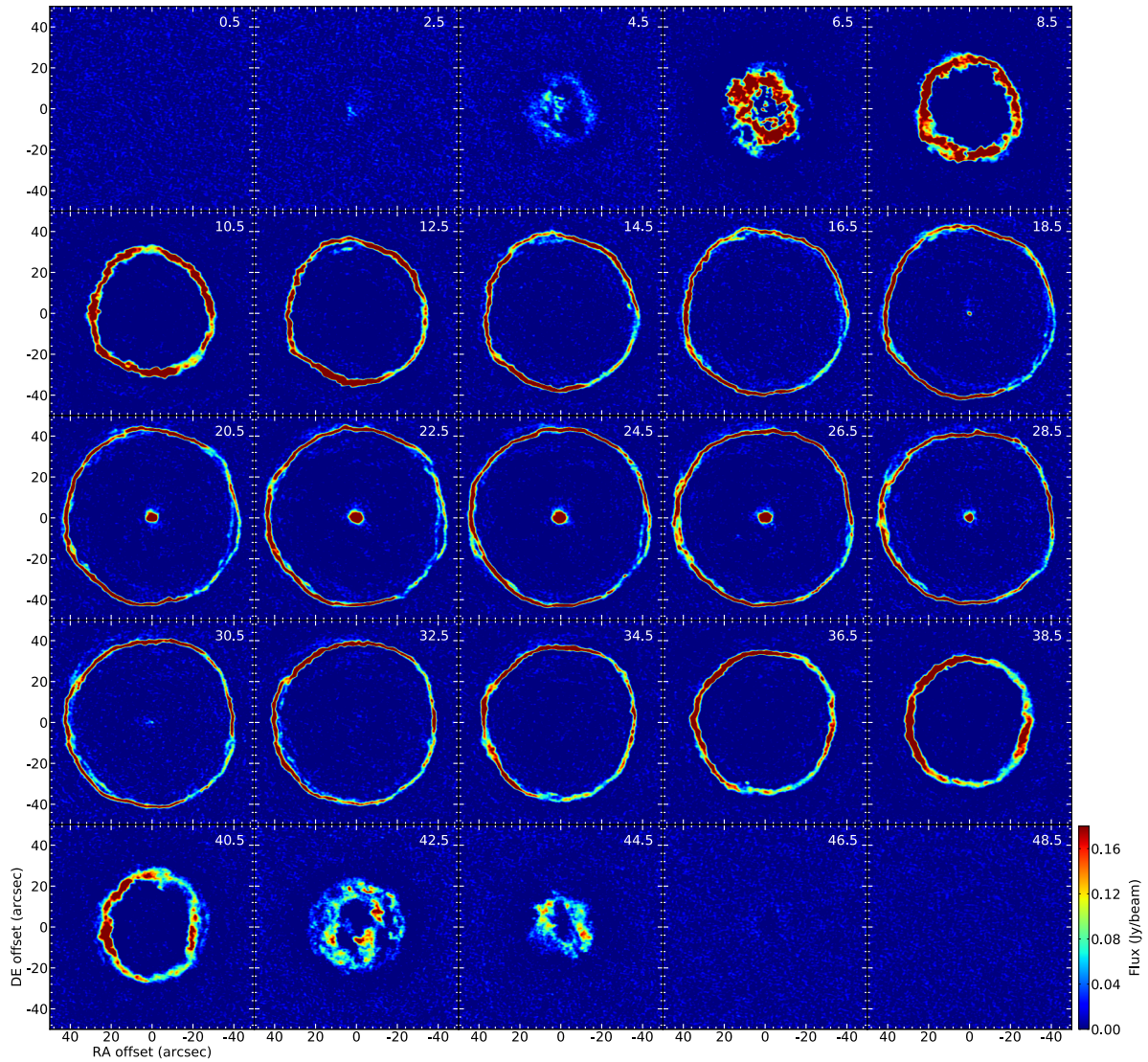


Fig. 2. Same as Fig. 1 for the $^{12}\text{CO}(2-1)$ line.

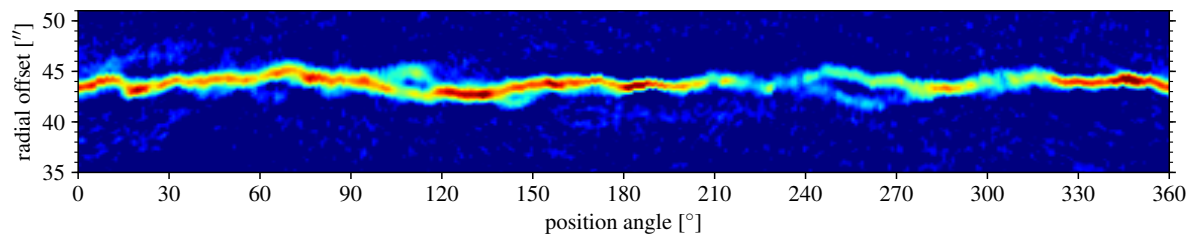


Fig. 3. ALMA (MA+ACA+TP) observations of $^{12}\text{CO}(2-1)$ towards U Ant spectrally integrated close to the systemic velocity ($23.5\text{--}25.5\text{ km s}^{-1}$), mapped to polar coordinates, and shown only for radial distances close to the detached shell (compare also Fig. 5 for a similar representation of the whole envelope incl. dust emission).

F. Kerschbaum et al.: The remarkable detached shell of U Antliae

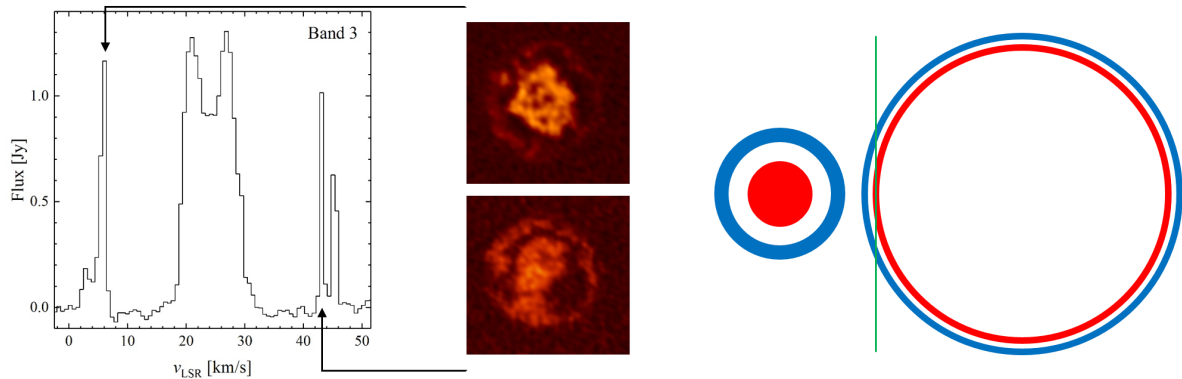


Fig. 4. *Left:* integrated B3 $^{12}\text{CO}(1-0)$ spectrum obtained in a circular, $7''$ wide region centred on U Ant. *Middle:* enlarged 0.65 km s^{-1} resolution velocity channel maps at $\pm 18.5 \text{ km s}^{-1}$ relative to the systemic velocity. *Right:* illustration of the geometry when selecting special velocity channel maps of a double shell structure, first as seen by the observer as in the middle maps and second in a hypothetical side view with the green line indicating the spatial cut corresponding to the chosen velocity channel.

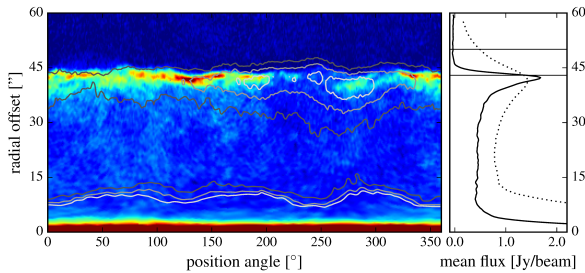


Fig. 5. U Ant $^{12}\text{CO}(2-1)$ spectrally integrated data mapped to polar coordinates over plotted with PACS $70 \mu\text{m}$ contours. The graph to the right depicts azimuthally averaged flux in the ALMA (full) and the *Herschel* (dashed) data. The two horizontal lines at 43 and $50''$ indicate the radial positions of shells 3 and 4 as discussed in Maercker et al. (2010).

ISM. The collision produces the same type of double-shocked structure described above and their “slow” models have similar gas dynamical properties to our study. In their Fig. B.2., the emissivity cross-section map due to rotational transitions of CO demonstrates how the molecular emission in the forward shock differs from that in the reverse shock; the emission is strong in the denser, shocked stellar wind and weaker in the shocked ambient medium.

The growth of instabilities (e.g. Rayleigh-Taylor instabilities) is also demonstrated and results in mixing between the two layers and the formation of filamentary substructure when projected on the sky (e.g. see their Fig. 12). The 3D appearance of these instabilities is comparable in structure to the filaments we observe. A definite, physical interpretation of the detached shell fine structure has to await full hydrodynamical simulations foreseen for an upcoming paper.

One can also compare our gas shell morphology with that of the dust. Figure 5 shows spectrally integrated (moment 0) $^{12}\text{CO}(2-1)$ data, mapped onto polar coordinates with *Herschel* PACS $70 \mu\text{m}$ contours (Kerschbaum et al. 2010; Cox et al. 2012). Overall, the spatial distributions are quite similar and resemble each other even in several details, indicating a strong coupling between gas and dust.

Nevertheless, it should be noted that the brightest regions in dust emission at position angles between 160 and 300°

correspond to an overall fainter region in gas emission – something that was already evident when comparing the PACS data to earlier single dish CO measurements of U Ant (Olofsson et al. 1996). This partial anti-correlation is surprising since possible photodissociation effects would act the other way round with a positive correlation by the shielding from dust. Moreover, Fig. 5 indicates that the molecular gas shell as observed by ALMA is co-spatial with the gas dominated shell 3 at $43''$ of Maercker et al. (2010) and not their dust shell 4 further out.

In Cox et al. (2012) a U Ant space velocity of 36 km s^{-1} , with respect to the ISM, at a projected position angle of 285.8° was derived, as well as a $5.3'$ stand-off-distance of a possible bow shock. In Fig. 5 this position angle corresponds to a region of somewhat smaller detached shell radius. The very different spatial scales ($5.3'$ versus the $43''$ shell radius) nevertheless make a connection unlikely. One should also note that we see no signs of shells 1 and 2 in our ALMA CO data. So far this remains a mystery since something is clearly seen in the Na data (but not in the K data) of Maercker et al. (2010).

Moreover, all our global spectra are asymmetric, with the blue-shifted side emitting more strongly. The profiles are surprisingly similar to those of R Scl (Maercker et al. 2016). This asymmetry was noted already by Olofsson et al. (1996) for R Scl, U Ant, and S Sct. The star TT Cyg seems to be an exception. Keeping in mind the still small sample size, however, this may be a pure coincidence.

3.2. Recent and older mass loss

When zooming in closer to the star, it is evident from our maps (Figs. 1, 2, and 6) that the detached shell is not completely hollow. There is new present-day mass loss confined to a region of about $6''$ in radius. There may even be slight deviations from spherical symmetry, unfortunately at the limit of the spatial resolution as indicated by our ALMA beam size in Fig. 6.

As seen in Fig. 7, this central region, covered by a $15''$ aperture, shows much smaller expansion velocities of only 4.7 and 4.2 km s^{-1} in B3 and B6, respectively, than the spectra that were produced by using a $110''$ aperture covering the whole emitting region. An expansion age of the present-day mass loss of less than 1600 yr can be estimated from these numbers.

This very low present-day expansion velocity is well in line with earlier findings on DR Ser, V644 Sco (Schöier et al. 2005),

A&A 605, A116 (2017)

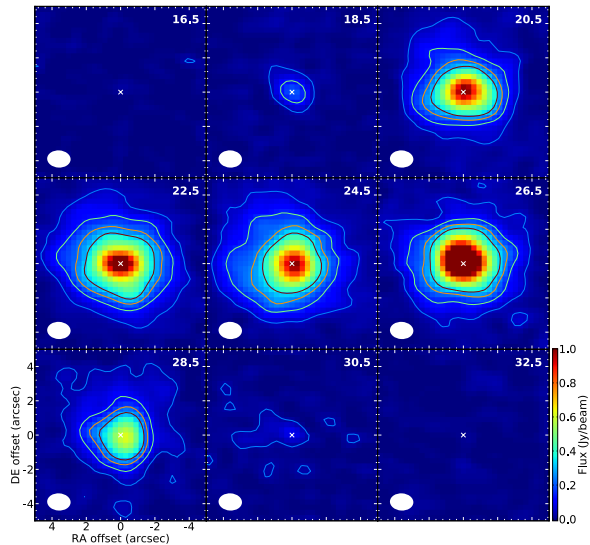


Fig. 6. ALMA observations in the $^{12}\text{CO}(2-1)$ line of central regions of selected velocity sub panels of Fig. 2 (see Fig. 2 for further description).

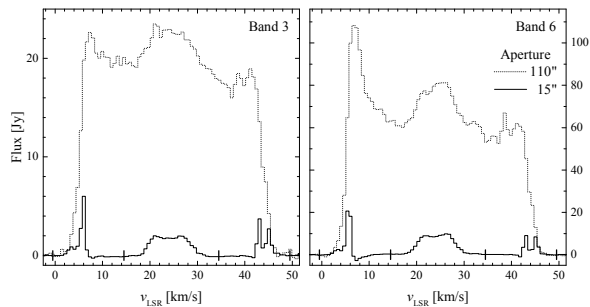


Fig. 7. Spatially integrated $^{12}\text{CO}(1-0)$ and $^{12}\text{CO}(2-1)$ spectra using two different aperture diameters fitting the whole emitting region and only the region showing new mass loss close to the star.

TT Cyg (Olofsson et al. 2000), and S Sct (Olofsson et al. 1996), and as expected from the interpulse expansion velocity evolution predicted by Vassiliadis & Wood (1993). The relatively high present-day expansion velocity of U Cam (Lindqvist et al. 1999) could be explained by its very young detached shell (only 700 yr as compared to the several thousands of most of the others). The binary R Scl may also be a special case (Maercker et al. 2016).

Schöier et al. (2005) performed a radiative transfer analysis of single-dish CO data on U Ant in order to derive the present-day mass-loss rate and the mass of the detached shell. We use the same method and code here to model the ALMA data as well as the existing single-dish data in a preliminary analysis (for reasons given below). Following Schöier et al. (2005), where the details of the modelling are described, we assume a CO abundance with respect to H_2 of 10^{-3} , and for the shell a kinetic temperature of 200 K (not well constrained). A present-day mass-loss rate of $4 \times 10^{-8} M_{\odot} \text{yr}^{-1}$ (twice that of Schöier et al. 2005) and a shell mass of $2 \times 10^{-3} M_{\odot}$ (consistent with Schöier et al. 2005) result in a reasonably good fit to all the data, including the ALMA radial brightness distributions of the $J = 1-0$ and $2-1$ lines, in Figs. 8 and 9.

The good fit to the radial brightness distributions of the ALMA data (lower panels of Fig. 8) indicates that the Mamon et al. (1988) results for the photodissociation of CO that are used in the model give a good estimate of the size of the CO envelope produced by the present-day wind for the adopted mass-loss rate. The line intensity contrast between the red- and blue-shifted peaks of the shell emission cannot be reproduced by the model. Its origin probably lies in the large-scale distribution of CO gas in the detached shell, although the very similar appearance of the CO detached shell emission also towards R Scl and S Sct may point to another explanation (Olofsson et al. 1996).

Taken at face value, the results suggest that the mass-loss rate has declined considerably since the creation of the shell until the present day. It is presently impossible to say whether this is similar or different to the evolution of the mass-loss rate around R Scl. In the case of R Scl, the binary-induced spiral made it possible to detect the extended component of the post-pulse wind (i.e. right after the pulse) that may just disappear below the detection threshold without the binary interaction. To have a definite say on this, as well as to improve the modelling of the observed data, requires a much more detailed analysis, for example, a substantial amount of emission from material between the star and the detached shell may be missing due to photodissociation of CO; a consideration of this is planned for a forthcoming paper.

The mass-loss rate during the shell formation is more difficult to estimate since the shell structure has most likely been affected by hydrodynamical effects during the expansion, which may affect the width of the shell as well as its expansion velocity. Noting these problems and assuming a connection between shell formation and thermal pulses (Olofsson et al. 1990), we adopt the timescale of the high-luminosity phase during a thermal pulse, a few $\times 10^2$ yr (Karakas & Lattanzio 2007), as the timescale of the shell formation. In this way, we estimate an average mass-loss rate during the ejection of the shell of the order of $\approx 10^{-5} M_{\odot} \text{yr}^{-1}$.

4. Conclusion

Spatial and spectral high resolution molecular gas observations from ALMA help us to better understand both the mass-loss morphology and the time evolution of mass loss in the detached shell around the carbon star U Ant. The detached shell is remarkably thin and overall spherically symmetric. Its size and expansion velocity indicate a short high mass-loss period about 2700 yr ago lasting only a few hundred years. When looking into the details of the shell, a filamentary substructure becomes visible that is also accompanied by velocity substructures. The barely resolved filaments are confined to a detached shell width of a differential expansion age of only 150–300 yr. These timescales fall in the same range as that of high mass loss during a thermal pulse of ≈ 200 yr (Vassiliadis & Wood 1993) further supporting a short high mass-loss ejection period. The high mass-loss period of U Ant can be characterized by an expansion velocity of the order of 19 km s^{-1} and a mass-loss rate of up to $\approx 10^{-5} M_{\odot} \text{yr}^{-1}$.

These simple conclusions neglect the maybe dominating effects of instabilities in the interaction zone of the fast, dense wind from the thermal pulse that swept up a slower, less dense wind lost prior to the helium-shell flash. The latter may have had similar properties to the low-velocity, present-day wind we observe close to the star. The presence of instabilities in the detached shell is supported by the morphological similarity of the filaments with comparable structures seen in interaction zones of

F. Kerschbaum et al.: The remarkable detached shell of U Antliae

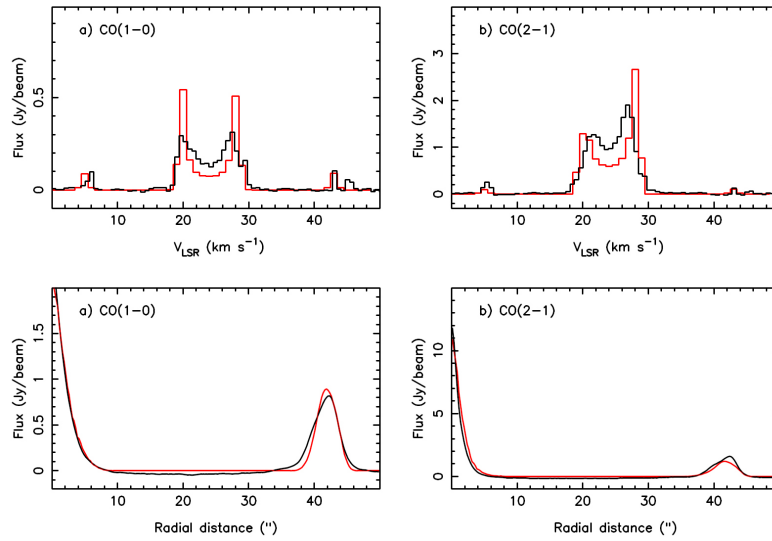


Fig. 8. Upper panels: ALMA $^{12}\text{CO}(1-0)$ and $^{12}\text{CO}(2-1)$ line spectra extracted at the stellar position (1.7'' and 1.2'' annuli, respectively). The red lines show the global best-fit model as discussed in the text. Lower panels: ALMA radial intensity profiles in the $^{12}\text{CO}(1-0)$ and $^{12}\text{CO}(2-1)$ lines over-plotted with our best-fit model.

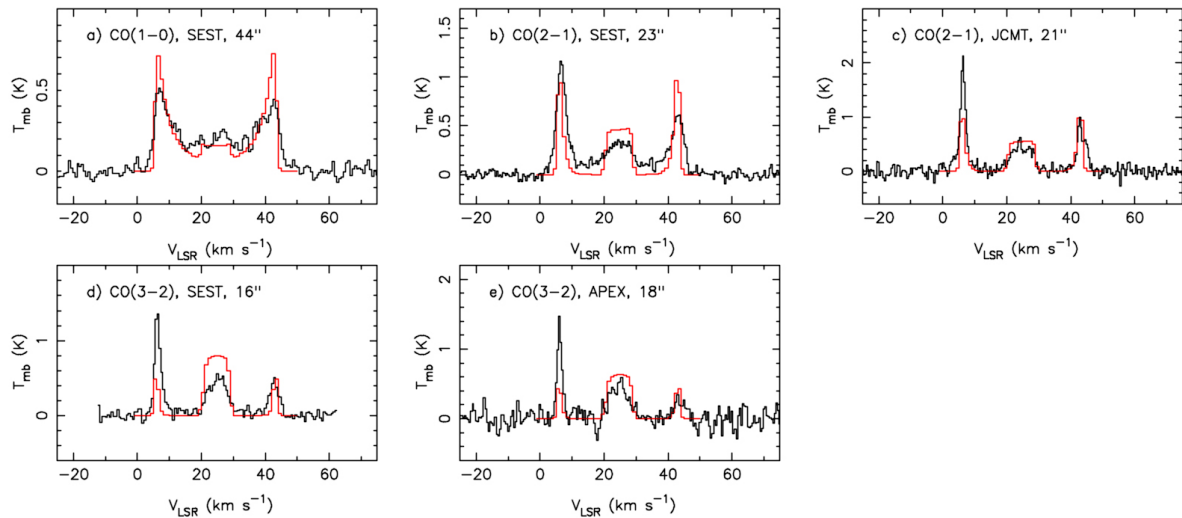


Fig. 9. Single dish observations towards U Ant (Schöier et al. 2005) with transition, telescope, and respective beam sizes indicated. The red lines show the global best-fit model as discussed in the text.

stellar winds with the ISM. Only full hydrodynamical models will be able to clarify the filaments origin.

The present-day mass loss with a gas expansion velocity of $\approx 4.5 \text{ km s}^{-1}$ and a mass-loss rate of $4 \times 10^{-8} M_{\odot} \text{ yr}^{-1}$ lies at the low end of AGB mass-loss characteristics and seems to have been of that order already for the last 1600 yr. Both the expansion velocity difference, and the difference in mass-loss rate between the present-day and the shell ejection epoch are in general agreement with the corresponding evolutionary changes predicted by Vassiliadis & Wood (1993) for the interpulse period.

When comparing U Ant to other detached shell objects that have spatially high resolution observations of their circumstellar CO emission, TT Cyg and R Scl, the emission towards U Ant and TT Cyg is consistent with a rapid decline to low gas expansion

velocities and mass-loss rates following the thermal pulse. The observations of R Scl indicate a more gradual evolution of the mass-loss characteristics in this source. However, it is only because of the binary-induced spiral shape that this slow decline is made visible in the case of R Scl. Without the spiral shape, the emission around R Scl created by the slowly declining mass-loss rate and expansion velocity would likely look very similar to that of U Ant and TT Cyg.

Acknowledgements. F.K. and M.B. acknowledge funding by the Austrian Science Fund FWF under project number P23586. M.B. further acknowledges funding through the uni:docs fellowship of the University of Vienna. M.M., H.O., and W.V. acknowledge financial support from the Swedish Research Council. C.P. is supported by the Belgian Fund for Scientific Research F.R.S.-FNRS.

A&A 605, A116 (2017)

References

- Cox, N. L. J., Kerschbaum, F., van Marle, A.-J., et al. 2012, [A&A](#), **537**, A35
- González Delgado, D., Olofsson, H., Schwarz, H. E., Eriksson, K., & Gustafsson, B. 2001, [A&A](#), **372**, 885
- González Delgado, D., Olofsson, H., Schwarz, H. E., et al. 2003, [A&A](#), **399**, 1021
- Izumiura, H., Kester, D. J. M., de Jong, T., et al. 1995, [Ap&SS](#), **224**, 495
- Karakas, A., & Lattanzio, J. C. 2007, [PASA](#), **24**, 103
- Kerschbaum, F., Ladjal, D., Ottensamer, R., et al. 2010, [A&A](#), **518**, L140
- Lindqvist, M., Olofsson, H., Lucas, R., et al. 1999, [A&A](#), **351**, L1
- Maercker, M., Olofsson, H., Eriksson, K., Gustafsson, B., & Schöier, F. L. 2010, [A&A](#), **511**, A37
- Maercker, M., Mohamed, S., Vlemmings, W. H. T., et al. 2012, [Nature](#), **490**, 232
- Maercker, M., Vlemmings, W. H. T., Brunner, M., et al. 2016, [A&A](#), **586**, A5
- Mamon, G. A., Glassgold, A. E., & Huggins, P. J. 1988, [ApJ](#), **328**, 797
- Mayer, A., Jorissen, A., Kerschbaum, F., et al. 2011, [A&A](#), **531**, L4
- Mohamed, S., Mackey, J., & Langer, N. 2012, [A&A](#), **541**, A1
- Mohamed, S., Mackey, J., & Langer, N. 2013, in *EAS Pub. Ser.* 60, eds. P. Kervella, T. Le Bertre, & G. Perrin, 243
- Olofsson, H., Carlstrom, U., Eriksson, K., Gustafsson, B., & Willson, L. A. 1990, [A&A](#), **230**, L13
- Olofsson, H., Bergman, P., Eriksson, K., & Gustafsson, B. 1996, [A&A](#), **311**, 587
- Olofsson, H., Bergman, P., Lucas, R., et al. 2000, [A&A](#), **353**, 583
- Olofsson, H., Maercker, M., Eriksson, K., Gustafsson, B., & Schöier, F. 2010, [A&A](#), **515**, A27
- Ramstedt, S., Mohamed, S., Vlemmings, W. H. T., et al. 2014, [A&A](#), **570**, L14
- Schneider, R., Valiante, R., Ventura, P., et al. 2014, [MNRAS](#), **442**, 1440
- Schöier, F. L., Lindqvist, M., & Olofsson, H. 2005, [A&A](#), **436**, 633
- Vassiliadis, E., & Wood, P. R. 1993, [ApJ](#), **413**, 641
- Waters, L. B. F. M., Loup, C., Kester, D. J. M., Bontekoe, T. R., & de Jong, T. 1994, [A&A](#), **281**, L1

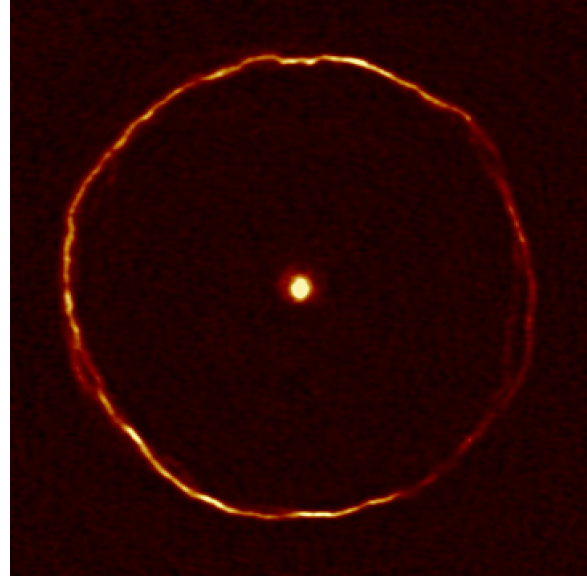


Fig. A.1. Single velocity step of the full $^{12}\text{CO}(2-1)$ animated velocity scan ([online movie](#)). The velocity resolution and step size is 0.65 km s^{-1} .

Appendix A: Additional figure

A full resolution animated velocity scan of the $^{12}\text{CO}(2-1)$ maps (compare Fig. 2) is shown in Fig. A.1. It repeatedly scans through all velocity channels at steps of 0.65 km s^{-1} in order to visualize the 3D structure of the detached shell. To more clearly show simultaneously the filamentary structures and the morphology of the region near the star, the movie uses nonlinear colour scales. Figure 2 shows the linear flux scales.

Part III

Publications with contributions

Chapter 8

The CO envelope around W Aquilae (Paper V)

Title: *The circumstellar envelope around the S-type AGB star W Aql: Effects of an eccentric binary orbit*

Authors: S. Ramstedt, S. Mohamed, W.H.T Vlemmings, T. Danilovich, **M. Brunner**, E. De Beck, E.M.L. Humphreys, M. Lindqvist, M. Maercker, H Olofsson, F. Kerschbaum, and G. Quintana-Lacaci

Year: 2017

Journal: Astronomy and Astrophysics,

DOI: <https://doi.org/10.1051/0004-6361/201730934>

Credit: Ramstedt et al. 2017, A&A, 605, A126, reproduced with permission © ESO

In this publication the molecular circumstellar envelope of the S-type AGB star W Aql is analysed by studies of the $^{12}\text{CO}(3-2)$ emission, observed with ALMA with subarcsecond resolution. W Aql is a known binary star, for which wind-binary interaction was shown already by earlier studies of the dusty circumstellar emission observed in thermal emission in the infrared with Herschel/PACS. The high resolution ALMA observations make it possible to investigate the wind-binary interaction also in molecular gas emission and extract wind properties from that. Additionally to 3D radiative transfer modelling, providing a mass-loss rate, 3D smooth particle hydrodynamic models are generated to analyse the wind-shaping mechanism in the binary system and infer binary orbit parameters from that. The analysis of this object is part of a larger study of binary AGB stars with different binary separations, which should provide an overview picture on how strongly binarity influences AGB winds.

Personal contribution: I contributed to this publication by engaging in the discussion about data processing related issues as well as scientific interpretation of the results.

A&A 605, A126 (2017)
 DOI: [10.1051/0004-6361/201730934](https://doi.org/10.1051/0004-6361/201730934)
 © ESO 2017

**Astronomy
&
Astrophysics**

The circumstellar envelope around the S-type AGB star W Aql

Effects of an eccentric binary orbit

S. Ramstedt¹, S. Mohamed^{2,3,4}, W. H. T. Vlemmings⁵, T. Danilovich⁶, M. Brunner⁷, E. De Beck⁵,
 E. M. L. Humphreys⁸, M. Lindqvist⁵, M. Maercker⁵, H. Olofsson⁵, F. Kerschbaum⁷, and G. Quintana-Lacaci⁹

¹ Department of Physics and Astronomy, Uppsala University, 75236 Uppsala, Sweden
 e-mail: sofia.ramstedt@physics.uu.se

² South African Astronomical Observatory, PO Box 9, 7935 Observatory, South Africa

³ Astronomy Department, University of Cape Town, 7701 Rondebosch, South Africa

⁴ South Africa National Institute for Theoretical Physics, Private Bag X1, 7602 Matieland, South Africa

⁵ Dept. of Earth and Space Sciences, Chalmers University of Technology, Onsala Space Observatory, 439 92 Onsala, Sweden

⁶ Instituut voor Sterrenkunde, KU Leuven, Celestijnenlaan 200D, 3001 Leuven, Belgium

⁷ Dept. of Astrophysics, University of Vienna, Türkenschanzstr. 17, 1180 Vienna, Austria

⁸ ESO, Karl-Schwarzschild-Str. 2, 85748 Garching bei München, Germany

⁹ Instituto de Ciencia de Materiales de Madrid, CSIC, c/ Sor Juana Inés de la Cruz 3, 28049 Cantoblanco, Madrid, Spain

Received 4 April 2017 / Accepted 19 June 2017

ABSTRACT

Context. Recent observations at subarcsecond resolution, now possible also at submillimeter wavelengths, have shown intricate circumstellar structures around asymptotic giant branch (AGB) stars, mostly attributed to binary interaction. The results presented here are part of a larger project aimed at investigating the effects of a binary companion on the morphology of circumstellar envelopes (CSEs) of AGB stars.

Aims. AGB stars are characterized by intense stellar winds that build CSEs around the stars. Here, the CO($J = 3 \rightarrow 2$) emission from the CSE of the binary S-type AGB star W Aql has been observed at subarcsecond resolution using ALMA. The aim of this paper is to investigate the wind properties of the AGB star and to analyse how the known companion has shaped the CSE.

Methods. The average mass-loss rate during the creation of the detected CSE is estimated through modelling, using the ALMA brightness distribution and previously published single-dish measurements as observational constraints. The ALMA observations are presented and compared to the results from a 3D smoothed particle hydrodynamics (SPH) binary interaction model with the same properties as the W Aql system and with two different orbital eccentricities. Three-dimensional radiative transfer modelling is performed and the response of the interferometer is modelled and discussed.

Results. The estimated average mass-loss rate of W Aql is $\dot{M} = 3.0 \times 10^{-6} M_{\odot} \text{ yr}^{-1}$ and agrees with previous results based on single-dish CO line emission observations. The size of the emitting region is consistent with photodissociation models. The inner $10''$ of the CSE is asymmetric with arc-like structures at separations of $2\text{--}3''$ scattered across the denser sections. Further out, weaker spiral structures at greater separations are found, but this is at the limit of the sensitivity and field of view of the ALMA observations.

Conclusions. The CO($J = 3 \rightarrow 2$) emission is dominated by a smooth component overlaid with two weak arc patterns with different separations. The larger pattern is predicted by the binary interaction model with separations of $\sim 10''$ and therefore likely due to the known companion. It is consistent with a binary orbit with low eccentricity. The smaller separation pattern is asymmetric and coincides with the dust distribution, but the separation timescale (200 yr) is not consistent with any known process of the system. The separation of the known companions of the system is large enough to not have a very strong effect on the circumstellar morphology. The density contrast across the envelope of a binary with an even larger separation will not be easily detectable, even with ALMA, unless the orbit is strongly asymmetric or the AGB star has a much larger mass-loss rate.

Key words. stars: AGB and post-AGB – circumstellar matter – binaries: general – submillimeter: stars

1. Introduction

Stars with a main-sequence initial mass between $0.8\text{--}8 M_{\odot}$ will evolve up the asymptotic giant branch (AGB) before nuclear burning is finally extinguished and the stars die (Habing & Olofsson 2003). The gas and dust expelled from the stars by the intense AGB wind (Willson 2000) is later lit up by the hard radiation from the exposed stellar cores and form planetary nebulae (PNe). Several findings suggest that not all stars in the full AGB mass range will form PNe. For example, the range of measured carbon isotopic ratios is much smaller for PNe than for AGB stars (e.g. Ramstedt & Olofsson 2014).

In recent decades there has been intense research to find out how and when the complex morphologies seen among the majority of PNe arise. Interacting winds (e.g. Kwok 2002; Steffen et al. 2013), rotation (Dorfi & Hoefner 1996; García-Segura et al. 2016), global magnetic fields (García-Segura et al. 2005), and binary (or large planet) interaction (Nordhaus & Blackman 2006; De Marco 2009; Staff et al. 2016) have been proposed as possible shaping agents for stars already on the AGB, and/or during the transition. Recently, the community has reached some consensus that interaction with a binary companion is required to explain the morphologies exhibited by most PNe (De Marco 2014), thereby suggesting

A&A 605, A126 (2017)

that PNe formation is more common among binary stars (e.g. Moe & De Marco 2006).

It is likely – and recent, high spatial resolution observations have also shown (e.g. Maercker et al. 2012; Maun et al. 2013; Cernicharo et al. 2015; Kim et al. 2017) – that the shaping of the circumstellar material will start on the (late) AGB. Circumstellar wind dynamics in binary systems with a mass-losing primary are therefore a very active field of research (e.g. Kim et al. 2015; Toupin et al. 2015). To provide observational constraints for recently developed 3D hydrodynamical models (e.g. Mohamed & Podsiadlowski 2012), we have designed a project for ALMA to observe the CO gas distribution and kinematics around known binary AGB stars. Resolved images of the binary pair are available for the initial sample stars, R Aqr, α Cet (Mira), W Aql, and π^1 Gru, and the sources cover extensive ranges in the important modelling parameters, i.e. binary separation, $a \sim 20$ –400 AU, and AGB wind expansion velocity, $v_e \approx 10$ –100 km s⁻¹. Initial results have been published in Ramstedt et al. (2014, on Mira), Ramstedt et al. (2015, also on W Aql, and π^1 Gru); and Doan et al. (2017, on π^1 Gru).

This paper focuses on the S-type AGB star W Aql. S-type stars are classified by the presence by ZrO bands and are thought to represent an intermediate evolutionary stage where the atmospheric C/O-ratio is close to 1. W Aql has a known companion at a separation of $a = 0.46''$ (Ramstedt et al. 2011) or ≈ 180 AU, and the distance to the system is estimated to 395 pc (Danilovich et al. 2014). Several resolved observations of the system and the circumstellar material exist. The dust emission at 11.15 μ m from the inner arcsecond around W Aql was measured using the three-element Infrared Spatial Interferometer (ISI) in 2004 (Tatebe et al. 2006). The observations showed brighter emission on the east side of the source indicating dust excess very close to the star ($0''.5 \sim 200$ AU at $D = 395$ pc). Assuming a typical outflow velocity of 20 km s⁻¹, Tatebe et al. (2006) suggest that a dust shell has been expelled from the star “within the last 35 years” (from 2004). The dust distribution on a $1'$ scale around W Aql was imaged by Ramstedt et al. (2011) using polarimetry to detect the dust scattered light. This revealed an asymmetric dust distribution around the star with more dust on the south-west side. The first resolved *Hubble* Space Telescope (HST¹) image of the binary pair was also presented. The companion was later classified by Danilovich et al. (2015) as a F8 to G0 main-sequence star. Danilovich et al. (2015) established that the known companion has an effective temperature in the range 5900–6170 K and a mass of 1.04–1.09 M_\odot . They find a mass for the AGB star of 1.04–3 M_\odot . The thermal dust emission from W Aql (on even larger scales) was imaged by *Herschel*/PACS as part of the Mass-loss of Evolved StarS (MESS) key program (Groenewegen et al. 2011). Mayer et al. (2013) investigated the large-scale dust distribution, and found that the south-west dust asymmetry also extends to larger scales.

Danilovich et al. (2014) modelled the molecular line emission from W Aql assuming a spherically symmetric circumstellar envelope (CSE), and derived the abundances of several chemically important molecules (including the first detection of NH₃ in an S-type star) and a mass-loss rate of $\dot{M} = 4.0 \times 10^{-6} M_\odot \text{ yr}^{-1}$. In this paper the 1D CO radiative transfer model is further constrained by the ALMA data. The data is presented in Sect. 2, and the 1D radiative transfer modelling to estimate the average mass-loss rate in Sect. 3.1. The 3D models used to analyse the wind shaping effects due to the companion are introduced in Sects. 3.2 and 3.3. In Sect. 4 the results from the observations

Table 1. Current position (J2000.0) and continuum flux density at 338 GHz measured from the ALMA data.

Source	RA	Dec	S_ν
W Aql	19:15:23.379	−07:02:50.38	$29 \pm 3 \text{ mJy}$

and the models are given, and further discussed in Sect. 5. Finally, conclusions are drawn in Sect. 6.

2. Observations

W Aql was observed with ten Atacama Compact Array (ACA) 7 m antennas on 6 March 2014. It was also observed on 20 March 2014 with 33, and on 14 April 2014 with 34 main array 12 m antennas. The main array observations were performed as a ten-pointing mosaic covering an area of approximately $30'' \times 30''$. The same area was covered by the ACA in three mosaic pointings. Finally, it was observed with three 12 m antennas of the Total Power (TP) array on the 12 June 2015. The correlator was set up with four spectral windows ~ 2 GHz in width centred on 331, 333, 343, and 345 GHz to cover the ¹²CO and ¹³CO $J = 3 \rightarrow 2$ lines in the same setting. The total observing time was 23 min for the ACA, and 7.25 min and 7.3 min for the 12 m array on the first and second run, respectively, and 67 min total time for the TP array. Baseline lengths range from 15 to 558 m for the main array, and from 9 to 49 m for the ACA. This results in a maximum recoverable scale of $\sim 7''$ for the main array and $\sim 12''$ for the ACA. The restoring beam of the TP observation is $18''.84 \times 18''.84$ at 345.2 GHz. Calibration was carried out following standard procedure. The quasar J1911-2006 was used as complex gain calibrator; quasar J1924-2914 was used as bandpass calibrator; and Ceres, Titan, and quasar J1924-292 were used as flux calibrators. Total power observations are calibrated using standard single-dish observing procedures with regular pointing checks and focus calibration. The intensity scale is converted from Kelvin to Jansky using conversion factors of 46.723, 48.568, 47.036, and 48.196 across the four different spectral windows. The main array data was combined with the ACA data, which was weighted by a factor of 0.25 to account for the lower sensitivity of the 7 m antennas, and the combined data was imaged. The combined main array+ACA visibilities were finally combined with the TP visibility data using the CASA task SD2VIS². A continuum image was made using the emission free channels from all spectral windows, but the continuum was too weak to be used for self-calibration of the offset mosaic pointings. The position and measured continuum flux density at 338 GHz is determined from image fitting and given in Table 1. Final imaging was done after subtracting the continuum and averaging to reach a spectral resolution of 2 km s⁻¹. The beam of the final images has a full width at half maximum of $0''.47 \times 0''.41$, and a position angle of 65.3° . The rms noise level in the emission-free channels reaches 15 mJy/beam. Previous ¹²CO $J = 3 \rightarrow 2$ line emission observations with APEX (Ramstedt et al. 2009) measured a peak intensity of $\sim 145 \text{ Jy}$ showing that the same amount of flux was recovered by the combined ALMA observations (Fig. 1, left). The ¹²CO $J = 3 \rightarrow 2$ line emission is centred at a local standard of rest (LSR) velocity of $v_{\text{LSR}} = -25.5 \text{ km s}^{-1}$.

¹ HST Proposal 10185, PI: Raghvendra Sahai.

² Developed at the Nordic ALMA ARC: www.oso.nordic-alma.se

S. Ramstedt et al.: The circumstellar envelope around the S-type AGB star W Aql

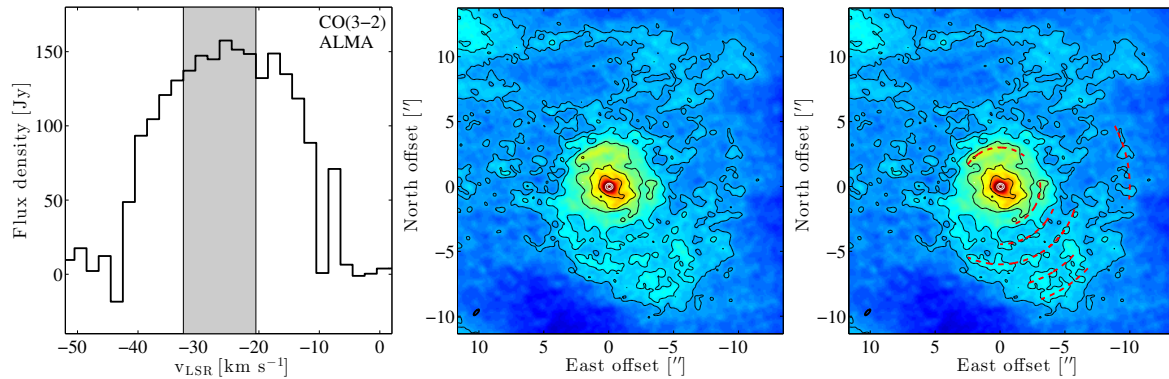


Fig. 1. *Left:* ALMA CO($J = 3 \rightarrow 2$) emission line at 2 km s^{-1} spectral resolution. The dip at $v_{\text{LSR}} = -10 \text{ km s}^{-1}$ is due to a bad channel (see Appendix A) and is not a real feature. The grey shaded area shows the averaged velocity range to create the image to the right. *Middle:* image average of the central channels of the line (grey shaded area in left plot). The image shows arc-like structures and increased emission on the south-west and west sides of the star. Black contours are drawn at 5, 10, 20, 30, and 40σ (where σ is measured over the emission-free channels). The white contours show the position of the AGB star from the continuum emission at 338 GHz. The beam is drawn in the lower left corner. *Right:* same as middle image with arcs outlined by red dashed lines.

3. Analysis

3.1. Determining the average mass-loss rate

Danilovich et al. (2014) modelled all the available single-dish CO rotational lines of W Aql (up to $J = 25 \rightarrow 24$ in the vibrational ground state, $v = 0$) using the non-LTE, non-local Monte Carlo radiative transfer code described in Schöier & Olofsson (2001), and assuming a distance of 395 pc. The radiative transfer code assumes a spherically symmetric CSE created by a constant mass-loss rate. For a further description on the assumptions made for the W Aql model in particular and the code in general see Danilovich et al. (2014) and Schöier & Olofsson (2001), respectively.

The model by Danilovich et al. (2014) is further constrained here by the brightness distribution derived from the CO($J = 3 \rightarrow 2$) map from ALMA. The CO envelope size was previously based on the photodissociation models by Mamon et al. (1988), Stanek et al. (1995). Now the brightness distribution provides direct constraints on the size of the CO envelope, which can be treated as a free parameter. The CO($J = 3 \rightarrow 2$) brightness distribution is derived by smoothing the full image cube to a resolution of $0''.6$ using imsmooth in CASA. Then the brightness distribution is measured by the integrated line flux (within a $0''.6$ beam) at increasing distances from the centre (determined by the position of W Aql A) in four directions (north, east, south, and west) and finally averaged over direction. The corresponding brightness distribution (using the same beam size and radii) is calculated from the radiative transfer modelling results and compared to the observed values until a fit is found (Fig. 2). The error in the measured line flux is assumed to be 10% with the variation across the different directions taken into account.

3.2. Hydrodynamical modelling

W Aql was modelled using the Evolved Stellar Interactions with GADGET in 3D (^{3D}ESI-Gadget code), which is based on a modified version of the collisionless and gasdynamical cosmological code GADGET2 (Springel 2005). The fluid equations are solved using smoothed particle hydrodynamics (SPH), a Lagrangian method particularly suited to studying flows with arbitrary geometries. Modules include radiative cooling, stellar

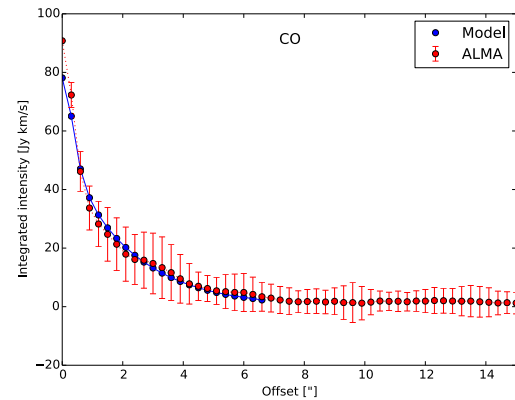


Fig. 2. Comparison between the direction-averaged CO($J = 3 \rightarrow 2$) brightness distribution from the ALMA observations (red dots with error bars) and that derived from the radiative transfer model assuming a spherically symmetric CSE (blue dots).

Table 2. Properties assumed in the hydrodynamic models.

Parameter	Assumed value
M_{AGB}	$2 M_{\odot}$
$M_{\text{companion}}$	$1 M_{\odot}$
R_{AGB}	$400 R_{\odot}$
T_{AGB}	3000 K
\dot{M}_{AGB}	$3 \times 10^{-6} M_{\odot} \text{ yr}^{-1}$
$v_{\infty \text{AGB}}$	16.5 km s^{-1}
a	180 AU
P_{orb}	1395 yr
e	0.2 and 0.6

winds, and binary interactions (Mohamed & Podsiadlowski 2007; Mohamed et al. 2012).

The parameters assumed for the models are given in Table 2; the stars are treated as point masses, and two different eccentricities for the binary orbit were assumed – $e = 0.2$ and $e = 0.6$. The

A&A 605, A126 (2017)

stellar wind from the AGB star was simulated by periodically injecting particles at a boundary given by the surface of the star. An acceleration parameter was added to the momentum equation to ensure that a smooth continuous wind with a terminal velocity of 16.5 km s^{-1} was produced. It was not possible to resolve the surface of the companion; this was instead treated as an accretion boundary (the boundary radius is set to 1 AU) where particles lose mass as they approach the companion and are removed from the simulation once they are 1% of their original mass. The wind particles are injected into initial vacuum conditions, thus the outermost arc is denser than it would be otherwise. Each simulation was run for long enough to ensure that this region is outside the observed ALMA field of view. After $\approx 11\,800$ yr of evolution, 6×10^6 particles had been injected. The initial mass of the particles is determined empirically so that it leads to the estimated mass-loss rate. They all have the same initial mass and the mass of the AGB star does not change as these particles are injected. Over the timescales considered, the amount of mass injected is insignificant (relative to the stellar mass). The output from these high-resolution models was then gridded using the SPH cubic spline kernel to a 512^3 grid in order to be used as input for the post-processing radiative transfer routine.

3.3. Post-processing radiative transfer

The output from the hydrodynamical model, i.e. 512^3 grids of the H_2 number density, the temperature, and the velocity distributions, is used as input to calculate the expected CO line emission. The non-LTE, non-local 3D radiative transfer code LIME (Line Modelling Engine, Brinch & Hogerheijde 2010) is used to calculate the CO level populations and solve the radiative transfer equations. Grid points are distributed across the computational volume using Delauney triangulation and the probability for placing a grid point is weighted with the density. Each grid cell is the corresponding Voronoi cell where the local conditions (density, temperature, excitation, etc.) are constant across each cell. For the calculations presented here, 100 000 grid points were used in a volume with a radius of 15 000 AU. A constant CO/ H_2 fractional abundance of 6.0×10^{-4} is assumed for the S-type star. The molecular excitation is calculated including 41 rotational transitions in the vibrational ground state and first excited state. Higher energy levels are not expected to be significantly populated. Collisions with H_2 are included assuming an ortho-to-para ratio of 3. Collisional rate coefficients, as well as energy levels and radiative transition probabilities, are taken from Schöier et al. (2005)³. For the continuum thermal dust emission, amorphous silicate grains are assumed (Justtanont & Tielens 1992).

The output images from the radiative transfer model are produced over 100 channels using a spectral resolution of 1 km s^{-1} , and a spatial resolution of $0''.2$. The source distance is assumed to be 395 pc. Finally, the uv-coverage of the combined ALMA arrays is taken into account by running this image through the ALMA simulator using the array configurations at the time of the W Aql observations (in Cycle 1).

4. Results

4.1. Wind properties

The average mass-loss rate during the creation of the CSE probed by the observations is estimated to

$\dot{M} = 3.0 \times 10^{-6} M_{\odot} \text{ yr}^{-1}$. The line widths are best fitted by a slowly accelerating velocity field which reaches the terminal expansion velocity of $v_{\infty} = 16.5 \text{ km s}^{-1}$ at $r \sim 2 \times 10^{16} \text{ cm}$, i.e. about 100 times the inner radius of the (modelled) CSE. This agrees well with previous estimates of the average mass-loss rate during the creation of the CSE around W Aql. Also, the size of the CSE required to produce the CO(3–2) brightness distribution (Fig. 2) agrees with the results from the model by Mamon et al. (1988).

4.2. Circumstellar morphology

The channel maps of the CO($J = 3 \rightarrow 2$) emission around W Aql (see Appendix A) shows a circumstellar CO emission distribution quite similar to that seen around R Scl and other stars (e.g. Maercker et al. 2016). The emitting region starts out small and essentially circular at the blue edge of the line, reaches maximum size at the line centre where several prominent arc-like structures are seen, and then shrinks again toward the red line edge. The small-scale structure seen closer to the line centre is more well-defined, while the emission appears rather smooth closer to the line edges. Unlike R Scl, W Aql is not surrounded by a spherically symmetric thin gas shell. Figure 1 (middle, right) shows the image averaged over the central channels of the line (Fig. 1, left). The strength of the brightness distributions in the four different directions over which it was measured vary only marginally (Sect. 3.1), indicating that most of the line emission comes from a smooth extended component. In Fig. 1 (middle, right), however, the emission appears slightly brighter and less smooth on the west side and in particular on the south-west side of the source. There are prominent arc-like structures close to the star (within $\pm 3''$), while these structures become less well-defined further out. In Fig. 1, right, the arc-like structures are marked since the contrast between the arcs and the background is weak. The full imaged area reaches about $20''$ from the position of the continuum source, but structures beyond $\sim 12''$ are less reliable, due to the rapidly declining image quality when moving away from the image centre.

Figure 3 shows position-velocity (PV) diagrams generated over a narrow slit (9 pixels) across the north-south and east-west directions at a position angle (PA) of 0° and 90° . The right diagram is generated along the apparent binary axis as it appears in the resolved HST image (at PA = 35° , Ramstedt et al. 2011). In the PV diagrams, the asymmetry is even more pronounced, and the arc-like structures on the west and south-west sides (marked in Fig. 1) appear more clearly. The contrast is weak, but there is a hint at an arc periodicity of about $3\text{--}4''$ on both the east and west sides in the middle PV diagram at PA = 90° . In the central-channel image in Fig. 1, middle and right, the arc-like structures appear clearest along the north-east-south-west diagonal, or along the binary axis, which is also shown in the PV-diagram at PA = 35° (Fig. 3, far right) where the arcs are separated by $2\text{--}3''$. However, it should be noted that the orientation of the orbit is not known and the direction of the binary axis in the HST image is only as it appears projected onto the plane of the sky.

4.3. Binary interaction model results

Figure 4 shows the results from the LIME radiative transfer model. The far left image is the output image modelled at $0''.2$ resolution before being convolved with the response of the interferometer, and generated over the central channels

³ <http://home.strw.leidenuniv.nl/~moldata/>

S. Ramstedt et al.: The circumstellar envelope around the S-type AGB star W Aql

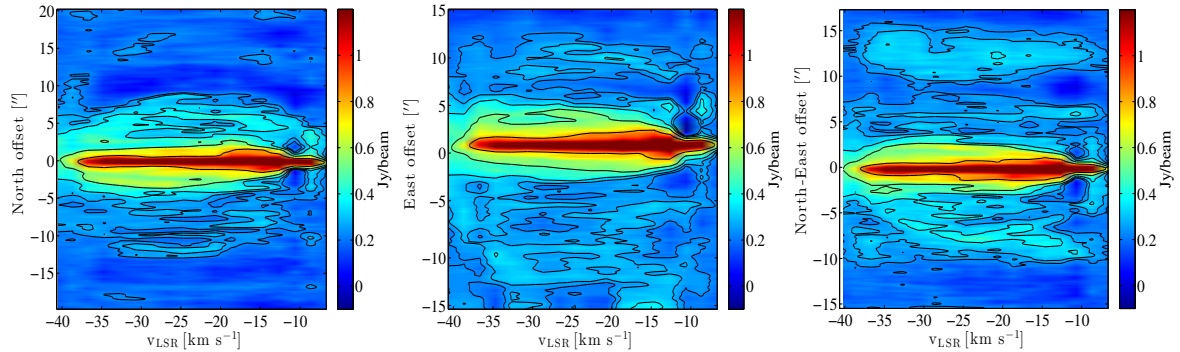


Fig. 3. *Left:* position-velocity diagram across the north-south direction ($PA = 0^\circ$). The contours are drawn at 3, 5, 10, 20, and 40σ (where σ is measured over the emission-free channels). *Middle:* position-velocity diagram across the east-west direction ($PA = 90^\circ$) showing the brighter and more structured emission on the west side of the stars. *Right:* position-velocity diagram along the binary axis ($PA = 35^\circ$) showing the structure within the south-west bright emission (Fig. 1).

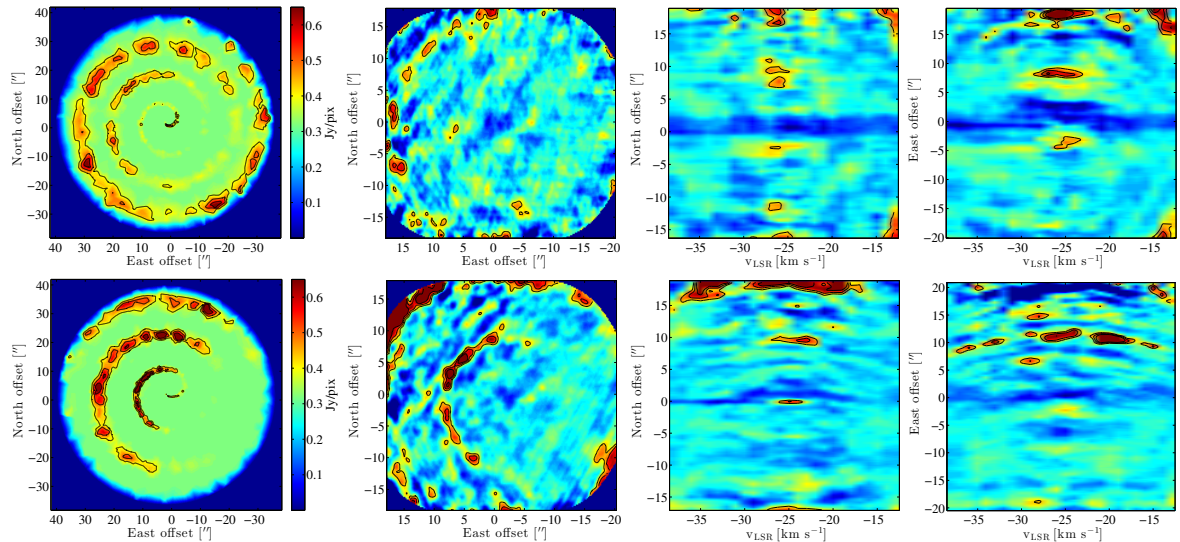


Fig. 4. Results from the radiative transfer modelling of the two hydrodynamical models with different orbital eccentricities. The *upper row* shows the results from the $e = 0.2$ model. The *lower row* shows the results from the $e = 0.6$ model. The *far left* image shows the output of the full model over the central channels (analogous to Fig. 1) without taking the response of the interferometer into account. The *middle left* image shows the output from the ALMA simulator. The *two right* images show PV-diagrams generated perpendicular to the model binary axis ($PA = 0^\circ$) and along it ($PA = 90^\circ$), respectively. The contours are drawn at 35, 50, 75%-fractions of the peak emission.

(analogous to Fig. 1). As seen in previous publications (Mastrodemos & Morris 1998; Mohamed & Podsiadlowski 2012; Kim et al. 2015), the binary companion will shape a spiral pattern in the outflowing CSE of the AGB star. For a system with the same properties as W Aql (orbital period = 1394/5 yr, $v_{\text{exp}} = 16.5 \text{ km s}^{-1}$), the arc separation will be 10–12". The emission contrast between the arcs and the interarc regions is a factor of ≤ 2 for the $e = 0.2$ model and ≤ 3 for the $e = 0.6$ model. The model binary axis is along the east-west direction.

The middle left image in Fig. 4 shows the emission as it would be seen by ALMA using the same main array, ACA, and TP configurations as used for the W Aql observations in Cycle 1 (we note that the image size is different to that in the far left image). The full channel maps are shown in Figs. A.2 and A.3. This shows particularly well the difficulty in recovering weakly contrasting features even with ALMA, and also how insufficient

cleaning can introduce false features, which emphasizes that weak emission structures should not be overinterpreted. This image was generated using the CASA task *simanalyze* without the careful, iterative, multiscale cleaning used when imaging the real data, and therefore the fidelity is worse than in the W Aql images in Figs. 1, 3, and A.1.

The two right images show PV diagrams generated from the middle left image taking the interferometer response into account. The middle right diagram shows the emission distribution along an axis perpendicular to the model binary axis ($PA = 0^\circ$); the far right diagram shows the emission along the binary axis ($PA = 90^\circ$). The diagrams show the brightest ("real") arcs in the image together with some weak (false) features. When the observational set-up from Cycle 1 is used, the PV diagrams show that only one or two arc-like structures ($\sim 10''$) with larger separations can be detected, and that a larger area would have to be

A&A 605, A126 (2017)

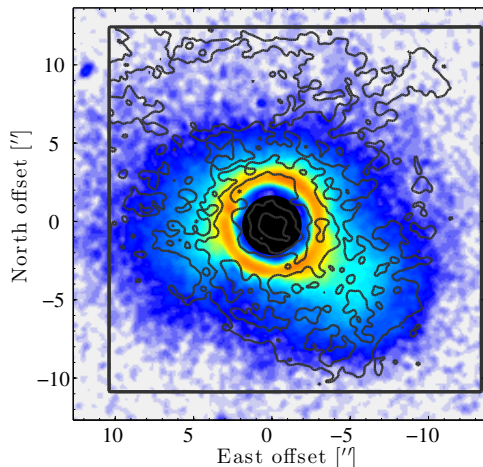


Fig. 5. CO($J = 3 \rightarrow 2$) emission from ALMA (grey contours) overlaid on the R -band dust-scattered emission image from PolCor (Ramstedt et al. 2011).

mapped in order to draw firm conclusions about the eccentricity of the orbit of the two resolved companions in the W Aql system.

The upper row of Fig. 4 shows the results from the $e = 0.2$ model, and the lower row shows the results from the $e = 0.6$ model. A difference compared to a circular orbit (see e.g. Maercker et al. 2012) introduced when varying the eccentricity is that the distribution of circumstellar material across the rotation axis will be asymmetric and there will be more material on the periastron side. The contrast across the rotation axis will grow with eccentricity, as will the contrast between the arcs and the interarc regions (see above and Fig. 4). Also, as seen in Fig. 4, the arc separation on the apastron side is larger when the eccentricity is larger.

5. Discussion

5.1. Comparison to previous resolved observations of the CSE around W Aql

The dust shell detected by Tatebe et al. (2006) would not be resolved by the ALMA observations, but it is possible that it is an inner extension of the arcs seen close to the star (see Fig. 1).

The dust-scattered emission over about $1'$ around W Aql imaged by Ramstedt et al. (2011, using the PolCor instrument) showed that the circumstellar dust is distributed asymmetrically around the star with more dust on the south-west side. Figure 5 shows the CO emission contours from Fig. 1 overlaid on the PolCor image. The figure shows that the dust and CO gas distributions overlap on these scales, and that the south-west emission (density) enhancement appears in both images. The small-scale structures, or arcs, seen in the central-channel CO line image (Fig. 1) are not seen in the scattered-light R -band image since the arcs, which appear at different velocity channels (Appendix A), are smeared in the dust emission image.

The large-scale morphology of the circumstellar dust around W Aql has been studied in detail by Mayer et al. (2013) using images from *Herschel*/PACS. The dust distribution appears elliptical with brighter emission reaching further from the star along the east-west axis (to $40\text{--}45'' \sim 16\,000$ AU at $D = 395$ pc). More diffuse emission extends further on the west side, but is not apparent on the east side where the emission appears truncated by a large arc-like feature, possibly a bow-shock (although

not aligned with the space motion as calculated by Mayer et al. 2013). The inner region of the PACS images (overlapping with the region mapped by ALMA) shows a slight elongation to the south-west, but there is also bright emission on the east side which does not have an apparent counterpart in the gas emission images. By assuming an orbital period ≤ 1000 yr and a wind velocity of 20 km s^{-1} , Mayer et al. (2013) estimate an expected arc separation of $12''.5$ and try to fit the PACS data with different Archimedean spirals with some success. Figure 3 (right) shows the PV diagram of the ALMA data along $PA = 0^\circ$, i.e. the north-south direction, and although the emission contrast is very weak and the image fidelity decreases beyond $\sim 12''$, recurring arcs of a similar periodicity to that suggested by Mayer et al. (2013) are seen.

5.2. Comparison to the binary interaction models

The hydrodynamical models using the known parameters of the W Aql system as input, and assuming a constant mass-loss rate and expansion velocity, produce a large spiral pattern with $\sim 10''$ spiral-arm separation. The main difference between the two models with different eccentricities is the contrast between the arcs of the spiral on the apastron versus periastron side. From the $e = 0.2$ -model there is almost no contrast between the two sides, while the $e = 0.6$ model essentially lacks arcs on the apastron side (Fig. 4). The inner $10''$ of the W Aql CSE show a clear contrast between the west and east sides, with smoother declining emission on the east side and arc-like structures at separations of $2\text{--}3''$ perpendicular to the apparent binary axis (Figs. 1, middle and right, and 3, left and right). This close arc pattern is not seen in the models because no process that could produce density variations on a timescale of ~ 200 yr was included.

There is a hint of arc-like structures at larger separations in the observations (best seen in the $PA = 90^\circ$ PV diagram, Fig. 3, middle), but the contrast between the smooth component and the arcs is very weak (about a factor of 2, in agreement with the $e = 0.2$ model) and they appear in the outer regions where the image is less reliable. There is no apparent asymmetry between the brightness of arcs with larger separations when comparing the north and south sides, but it is difficult to evaluate using the current data. As already mentioned above, a deeper and larger image would be necessary in order to draw firm conclusions about the orbit eccentricity of the known companion in the W Aql system.

5.3. Circumstellar gas envelope of W Aql

To summarize, the CO($3\text{--}2$) line emission from the W Aql system is entirely dominated by a smooth symmetric component (Fig. 2) from the gas envelope generated by an average mass-loss rate estimated to $\dot{M} = 3.0 \times 10^{-6} M_\odot \text{ yr}^{-1}$, i.e. rather high for an S-type star (Ramstedt et al. 2009). Superimposed on the smooth component, there appears to be a double arc pattern in the CSE of W Aql. It is likely that the arcs at greater separations ($10''$) are caused by the gravitational pull on the circumstellar gas by the known companion at $0''.46$. There is no apparent asymmetry between the arc-like structures at greater separations on different sides of the system, as seen in the $e = 0.6$ model, and the contrast between the arcs and interarc region agrees with the output from the $e = 0.2$ model, but this is also difficult to evaluate with the current data set. The closer arcs, marked in Fig. 1 (right), could be formed via a number of different processes: a second closer companion (or a massive planet) with an eccentric orbit, a recent change in the wind velocity (which would have to decrease by a factor of 3–4), mass-loss-rate variations, etc. Density

S. Ramstedt et al.: The circumstellar envelope around the S-type AGB star W Aql

variations over the same timescale are also seen in the carbon star IRC+10216 (e.g. Leão et al. 2006). In that star, the optically thick CSE could block heat from escaping the dust formation region and thereby stop grain formation temporarily, causing episodic mass loss on the same timescales (Eriksson et al. 2014); however, in the S-type CSE of W Aql, this is a less likely explanation. The pulsation/convection timescale is much shorter than the arc-formation timescale, and therefore is probably not the cause of the arcs at smaller separations. The inner arc structure is clearly asymmetric, and co-incident with the previously imaged dust emission enhancement. It is possible that the disappearing SiO masers of W Aql (Ramstedt et al. 2012) hint that a disruption of the inner CSE ($<5 R_*$) is occurring, which could lend weight to the presence of an additional, closer companion. If this is the case, then the third body approached sufficiently close to the star to disrupt the SiO maser zone during 2010–2011, but this is highly speculative. Closer imaging and monitoring of the system to look for dust formation variations (Ohnaka et al. 2016) or a third system body would be very interesting and would help to understand the shaping of the W Aql CSE.

6. Conclusions

The observations of W Aql are part of a project with the aim of achieving a better understanding of how a binary companion will shape the expanding CSE around a mass-losing AGB star by observing stars with a known binary companion. The idea is that this would provide better constraints for the models of the interaction, as opposed to the more common strategy of inferring the companion from the shape of the CSE alone. However, even when the separation is known, this has proven perhaps more complicated than initially hoped (Ramstedt et al. 2014; Doan et al. 2017), and additional information about the systems, orbits, more exact distances, properties of the companion, etc., are required to fully understand the systems and to explain the shaping processes.

In the W Aql system, the circumstellar gas distribution is moderately affected by the interaction with the companion, which is also to be expected given the relatively large separation between the two stars (close to 200 AU at 395 pc). Instead, the distribution of the circumstellar material is mostly smooth, and the envelope has been formed by an average mass-loss rate of $\dot{M} = 3.0 \times 10^{-6} M_{\odot} \text{ yr}^{-1}$. The arcs with larger separations ($\sim 10''$) are probably due to the known companion and, within the limitations of the data, consistent with a circular or possibly low-eccentricity orbit. An even weaker density contrast, as would be expected from a companion at an even larger separation, would be very difficult to detect, even with ALMA. In addition, the inner region of the CSE around the W Aql system is asymmetric and shows an arc pattern with a separation of $2\text{--}3''$, predominately on the south-west side of the sources and overlapping with the previously mapped dust emission. The physical processes behind the south-west asymmetry and the arcs at smaller separations are not known, and cannot be easily linked to any known properties of the system.

Acknowledgements. The authors would like to thank the staff of the Nordic ALMA ARC node for their support, availability, and continuous efforts in helping produce maximum quality data products. This paper makes use of the following ALMA data: ADS/JAO.ALMA#2012.1.00524.S. ALMA is a partnership of ESO (representing its member states), NSF (USA), and NINS (Japan), together with NRC (Canada) and NSC and ASIAA (Taiwan), in cooperation with the Republic of Chile. The Joint ALMA Observatory is operated by ESO, AUI/NRAO, and NAOJ. S.M. is grateful to the South African National Research

Foundation (NRF) for a research grant. W.V. acknowledges support from ERC consolidator grant 614264. T.D. acknowledges support from the ERC consolidator grant 646758 AEROSOL and the FWO Research Project grant G024112N. G.Q.L. acknowledges support from the European Research Council under the European Union's Seventh Framework Programme (FP/2007–2013)/ERC Grant Agreement No. 610256 (NANOCOSMOS).

References

- Brinch, C., & Hogerheijde, M. R. 2010, *A&A*, **523**, A25
 Cernicharo, J., Marcelino, N., Agúndez, M., & Guélin, M. 2015, *A&A*, **575**, A91
 Danilovich, T., Bergman, P., Justtanont, K., et al. 2014, *A&A*, **569**, A76
 Danilovich, T., Olofsson, G., Black, J. H., Justtanont, K., & Olofsson, H. 2015, *A&A*, **574**, A23
 De Marco, O. 2009, *PASP*, **121**, 316
 De Marco, O. 2014, in Asymmetrical Planetary Nebulae VI Conference, 122
 Doan, L., Ramstedt, S., Vlemmings, W. H. T., et al. 2017, *A&A*, **605**, A28
 Dorfi, E. A., & Hoefner, S. 1996, *A&A*, **313**, 605
 Eriksson, K., Nowotny, W., Höfner, S., Aringer, B., & Wachter, A. 2014, *A&A*, **566**, A95
 García-Segura, G., López, J. A., & Franco, J. 2005, *ApJ*, **618**, 919
 García-Segura, G., Villaver, E., Manchado, A., Langer, N., & Yoon, S.-C. 2016, *ApJ*, **823**, 142
 Groenewegen, M. A. T., Waelkens, C., Barlow, M. J., et al. 2011, *A&A*, **526**, A162
 Habing, H. J., & Olofsson, H. 2003, *Asymptotic Giant Branch Stars* (New York, Berlin: Springer)
 Justtanont, K., & Tielens, A. G. G. M. 1992, *ApJ*, **389**, 400
 Kim, H., Liu, S.-Y., Hirano, N., et al. 2015, *ApJ*, **814**, 61
 Kim, H., Trejo, A., Liu, S.-Y., et al. 2017, *Nature Astron.*, **1**, 0060
 Kwok, S. 2002, in *Interacting Winds from Massive Stars*, eds. A. F. J. Moffat, & N. St-Louis, *ASP Conf. Ser.*, **260**, 245
 Leão, I. C., de Laverny, P., Mékarnia, D., de Medeiros, J. R., & Vandame, B. 2006, *A&A*, **455**, 187
 Maercker, M., Mohamed, S., Vlemmings, W. H. T., et al. 2012, *Nature*, **490**, 232
 Maercker, M., Vlemmings, W. H. T., Brunner, M., et al. 2016, *A&A*, **586**, A5
 Mamon, G. A., Glassgold, A. E., & Huggins, P. J. 1988, *ApJ*, **328**, 797
 Mastrodemos, N., & Morris, M. 1998, *ApJ*, **497**, 303
 Mauron, N., Huggins, P. J., & Cheung, C.-L. 2013, *A&A*, **551**, A110
 Mayer, A., Jorissen, A., Kerschbaum, F., et al. 2013, *A&A*, **549**, A69
 Moe, M., & De Marco, O. 2006, *ApJ*, **650**, 916
 Mohamed, S., & Podsiadlowski, P. 2007, in 15th European Workshop on White Dwarfs, eds. R. Napiwotzki, & M. R. Burleigh, *ASP Conf. Ser.*, **372**, 397
 Mohamed, S., & Podsiadlowski, P. 2012, *Balt. Astron.*, **21**, 88
 Mohamed, S., Mackey, J., & Langer, N. 2012, *A&A*, **541**, A1
 Nordhaus, J., & Blackman, E. G. 2006, *MNRAS*, **370**, 2004
 Ohnaka, K., Weigelt, G., & Hofmann, K.-H. 2016, *A&A*, **589**, A91
 Ramstedt, S., & Olofsson, H. 2014, *A&A*, **566**, A145
 Ramstedt, S., Schöier, F. L., & Olofsson, H. 2009, *A&A*, **499**, 515
 Ramstedt, S., Maercker, M., Olofsson, G., Olofsson, H., & Schöier, F. L. 2011, *A&A*, **531**, A148
 Ramstedt, S., Vlemmings, W., Mohamed, S., Choi, Y. K., & Olofsson, H. 2012, in *Cosmic Masers – from OH to H₂O*, eds. R. S. Booth, W. H. T. Vlemmings, & E. M. L. Humphreys, *IAU Symp.*, **287**, 260
 Ramstedt, S., Mohamed, S., Vlemmings, W. H. T., et al. 2014, *A&A*, **570**, L14
 Ramstedt, S., Vlemmings, W. H. T., & Mohamed, S. 2015, in *Revolution in Astronomy with ALMA: The Third Year*, eds. D. Iono, K. Tatematsu, A. Wootten, & L. Testi, *ASP Conf. Ser.*, **499**, 331
 Schöier, F. L., & Olofsson, H. 2001, *A&A*, **368**, 969
 Schöier, F. L., van der Tak, F. F. S., van Dishoeck, E. F., & Black, J. H. 2005, *A&A*, **432**, 369
 Springel, V. 2005, *MNRAS*, **364**, 1105
 Staff, J. E., De Marco, O., Wood, P., Galaviz, P., & Passy, J.-C. 2016, *MNRAS*, **458**, 832
 Stanek, K. Z., Knapp, G. R., Young, K., & Phillips, T. G. 1995, *ApJS*, **100**, 169
 Steffen, W., Koning, N., Esquivel, A., et al. 2013, *MNRAS*, **436**, 470
 Tatebe, K., Chandler, A. A., Hale, D. D. S., & Townes, C. H. 2006, *ApJ*, **652**, 666
 Toupin, S., Braun, K., Siess, L., Jorissen, A., & Price, D. 2015, in *Why Galaxies Care about AGB Stars III: A Closer Look in Space and Time*, eds. F. Kerschbaum, R. F. Wing, & J. Hron, *ASP Conf. Ser.*, **497**, 225
 Willson, L. A. 2000, *ARA&A*, **38**, 573

A&A 605, A126 (2017)

Appendix A: Channel maps

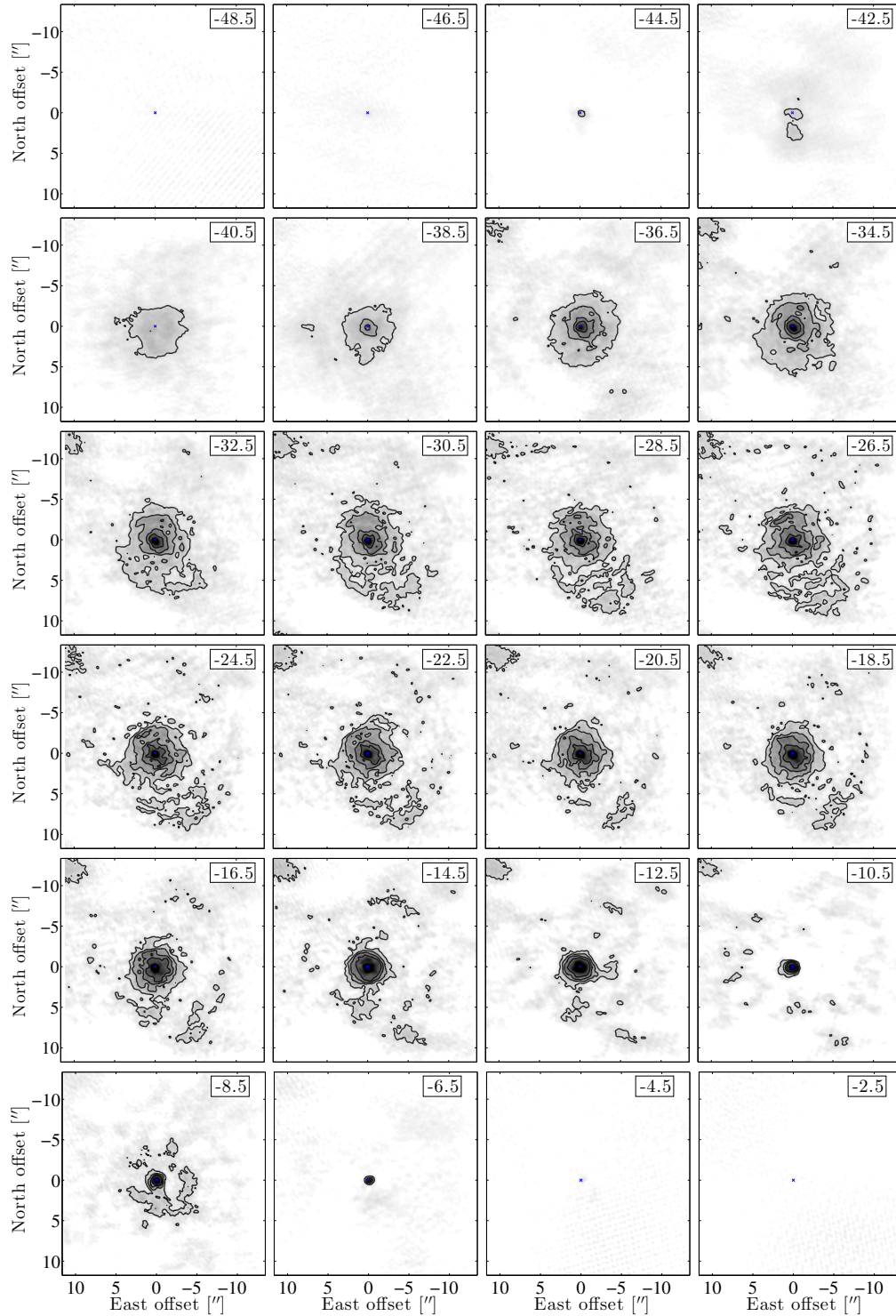


Fig. A.1. ALMA CO(3-2) channel maps. The LSR velocity of each channel is given in the upper right corner legend. Contours are given at 10, 20, 30, and 40σ , where σ has been measured in the emission-free channels. The blue cross marks the peak of the continuum emission.

S. Ramstedt et al.: The circumstellar envelope around the S-type AGB star W Aql

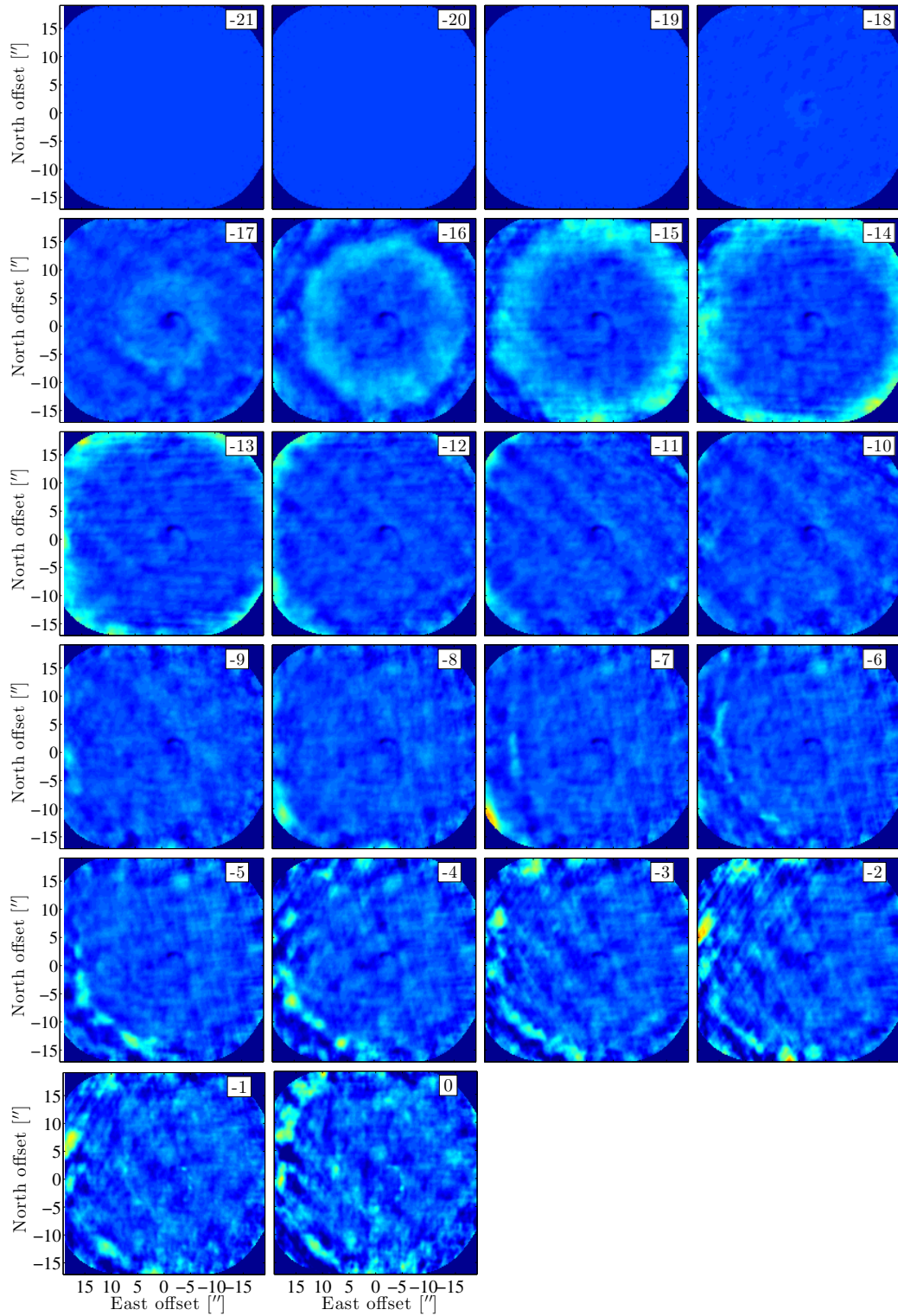


Fig. A.2. Channel maps from the model with $e = 0.2$ (see text for explanation). The velocity relative to the line centre of each channel is given in the upper right corner legend. Only the blue-shifted emission is shown since the maps are completely symmetric around the line centre.

A&A 605, A126 (2017)

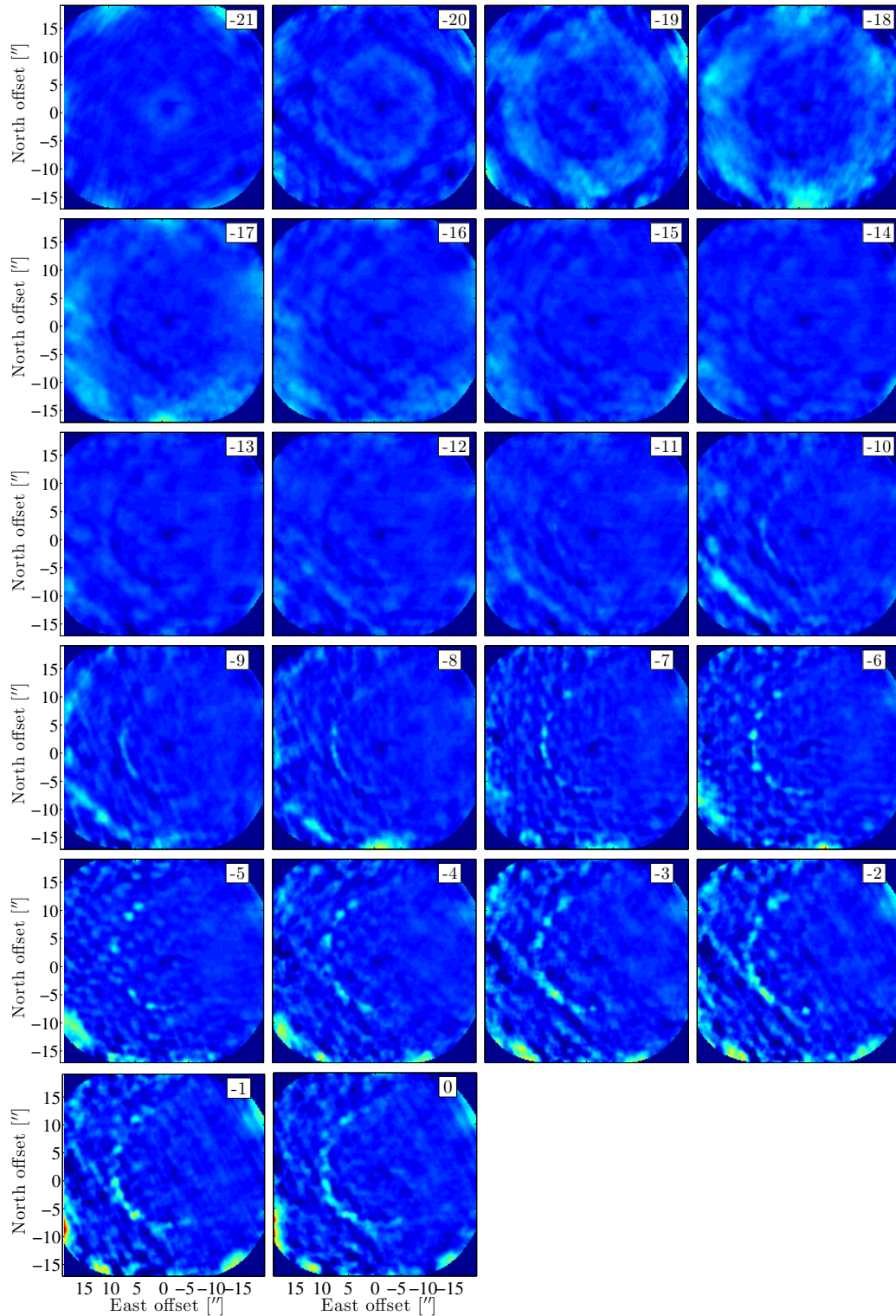


Fig. A.3. Channel maps from the model with $e = 0.6$ (see text for explanation). The velocity relative to the line centre of each channel is given in the upper right corner legend. Only the red-shifted emission is shown since the maps are completely symmetric around the line centre.

Chapter 9

The CO envelope around R Sculptoris (Paper VI)

Title: *A detailed view of the gas shell around R Sculptoris with ALMA*

Authors: M. Maercker, W.H.T Vlemmings, **M. Brunner**, E. De Beck, E.M. Humphreys, F. Kerschbaum, M. Lindqvist, H. Olofsson, and S. Ramstedt

Year: 2016

Journal: Astronomy and Astrophysics

DOI: <https://doi.org/10.1051/0004-6361/201527128>

Credit: Maercker et al. 2016, A&A, 586, A5, reproduced with permission © ESO

In this publication the molecular circumstellar envelope of the carbon rich AGB star R Sculptoris is analysed by studies of the $^{12}\text{CO}(1-0)$, $^{12}\text{CO}(2-1)$ and $^{12}\text{CO}(3-2)$ emission, observed with ALMA and single-dish telescopes. R Scl is surrounded by a detached shell created through a thermal pulse, and additionally a binary induced spiral is connecting the present-day stellar wind with the detached shell. With ALMA, the different emission components of the CSE can be resolved and analysed separately, allowing us to investigate the mass-loss history of this particular object in detail. Radiative transfer modelling is performed to determine the mass-loss properties of the shell as well as the subsequent mass-loss period. Contrary to previous theories, we find that the post-pulse mass-loss rate does not decline rapidly but rather with a gradual decline, which results in a smoothly filled shell, underlying to the imprinted spiral structure. These results have impact on our understanding of the mass return to the ISM as well as the observational interpretation of other detached shell objects.

Personal contribution: I contributed on a fundament level to this publication by refining the ALMA data reduction process for the investigated datasets, improving the image quality and reducing imaging artefacts introduced by the imaging process. Additionally, I was actively contributing to the scientific discussion and analysis of the modelling results.

A&A 586, A5 (2016)
 DOI: 10.1051/0004-6361/201527128
 © ESO 2016

**Astronomy
&
Astrophysics**

A detailed view of the gas shell around R Sculptoris with ALMA

M. Maercker¹, W. H. T. Vlemmings¹, M. Brunner², E. De Beck¹, E. M. Humphreys³,
 F. Kerschbaum², M. Lindqvist¹, H. Olofsson¹, and S. Ramstedt⁴

¹ Department of Earth and Space Sciences, Chalmers University of Technology, Onsala Space Observatory, 43992 Onsala, Sweden
 e-mail: maercker@chalmers.se

² Department of Astrophysics, University of Vienna, Türkenschanzstr. 17, 1180 Vienna, Austria

³ European Southern Observatory, Karl-Schwarzschild-Straße 2, 85748 Garching, Germany

⁴ Department of Physics and Astronomy, Uppsala University, Box 516, 75120 Uppsala, Sweden

Received 5 August 2015 / Accepted 17 November 2015

ABSTRACT

Context. During the asymptotic giant branch (AGB) phase, stars undergo thermal pulses – short-lived phases of explosive helium burning in a shell around the stellar core. Thermal pulses lead to the formation and mixing-up of new elements to the stellar surface. They are hence fundamental to the chemical evolution of the star and its circumstellar envelope. A further consequence of thermal pulses is the formation of detached shells of gas and dust around the star, several of which have been observed around carbon-rich AGB stars.

Aims. We aim to determine the physical properties of the detached gas shell around R Sculptoris, in particular the shell mass and temperature, and to constrain the evolution of the mass-loss rate during and after a thermal pulse.

Methods. We analyse $^{12}\text{CO}(1-0)$, $^{12}\text{CO}(2-1)$, and $^{12}\text{CO}(3-2)$ emission, observed with the Atacama Large Millimeter/submillimeter Array (ALMA) during Cycle 0 and complemented by single-dish observations. The spatial resolution of the ALMA data allows us to separate the detached shell emission from the extended emission inside the shell. We perform radiative transfer modelling of both components to determine the shell properties and the post-pulse mass-loss properties.

Results. The ALMA data show a gas shell with a radius of $19\frac{1}{2}$ expanding at 14.3 km s^{-1} . The different scales probed by the ALMA Cycle 0 array show that the shell must be entirely filled with gas, contrary to the idea of a detached shell. The comparison to single-dish spectra and radiative transfer modelling confirms this. We derive a shell mass of $4.5 \times 10^{-3} M_{\odot}$ with a temperature of 50 K. Typical timescales for thermal pulses imply a pulse mass-loss rate of $2.3 \times 10^{-5} M_{\odot} \text{ yr}^{-1}$. For the post-pulse mass-loss rate, we find evidence for a gradual decline of the mass-loss rate, with an average value of $1.6 \times 10^{-5} M_{\odot} \text{ yr}^{-1}$. The total amount of mass lost since the last thermal pulse is $0.03 M_{\odot}$, a factor four higher compared to classical models, with a sharp decline in mass-loss rate immediately after the pulse.

Conclusions. We find that the mass-loss rate after a thermal pulse has to decline more slowly than generally expected from models of thermal pulses. This may cause the star to lose significantly more mass during a thermal pulse cycle, which affects the lifetime on the AGB and the chemical evolution of the star, its circumstellar envelope, and the interstellar medium.

Key words. stars: AGB and post-AGB – binaries: general – stars: carbon – stars: evolution – stars: mass-loss

1. Introduction

The chemical evolution of evolved stars between $0.8\text{--}10 M_{\odot}$ on the asymptotic giant branch (AGB) is driven by thermal pulses (TP). Thermal runaway burning of helium in a shell around the dormant carbon–oxygen core leads to a mixing of the inner layers of the star, resulting in an intricate nucleosynthetic network and the production of new heavy elements (e.g. Karakas & Lattanzio 2007). These elements are mixed to the surface of the star through deep convection during the third dredge-up after the pulse and are incorporated into the stellar wind. The winds from AGB stars replenish the interstellar medium (ISM) with this newly processed material (e.g. Schneider et al. 2014). The stellar mass loss is high enough (up to $10^{-4} M_{\odot} \text{ yr}^{-1}$) to eventually terminate the evolution of the star on the AGB with most of the stellar mass lost to the ISM (e.g. Herwig 2005). As such, AGB stars are significant contributors to the chemical evolution of the ISM and galaxies. The material is included in molecular clouds where new stars and planets are formed.

The phase of rapid helium burning during a TP cycle lasts only a few hundred years (Vassiliadis & Wood 1993). Although

the helium luminosity experiences a large increase, the surface luminosity only increases slightly. However, this increase in luminosity leads to additional radiation pressure on the dust grains in the upper atmosphere of the star and, combined with a lower temperature and larger radius, results in an increased mass-loss rate and expansion velocity. After He-burning ceases, the surface luminosity, and hence the mass-loss rate and expansion velocity, decrease again (Steffen & Schönberner 2000; Mattsson et al. 2007).

An indication of highly variable mass loss from AGB stars was first observed in CO emission in the form of detached shells around carbon AGB stars, and a formation connected to TPs was suggested (Olofsson et al. 1988, 1990). Since then, detached shells of dust and gas around ~ten carbon AGB stars have been observed. The strongest argument for the connection between detached-shell sources and TPs are the detection statistics that are based on a volume-limited sample of carbon stars (Olofsson et al. 1993). No detached CO shells have been observed around oxygen-rich (M-type) AGB stars, where dust opacity effects possibly prevent the formation of a shell during the TP (e.g. Bladh et al. 2015). The formation mechanism

A&A 586, A5 (2016)

is also fundamentally different from the shells observed around high-mass evolved stars, where photoionization creates confined shells (Mackey et al. 2014). Thermal emission from the dust in detached shells was first observed in the far-infrared by IRAS (van der Veen & Habing 1988; Waters et al. 1994; Izumiura et al. 1997), and more recently by AKARI and *Herschel* (Kerschbaum et al. 2010; Izumiura et al. 2011; Cox et al. 2012; Mećina et al. 2014). Most of these shells are likely connected to TPs. The images make it possible to determine the dust temperature in the detached shells and, to some extent, the sizes of the shell. Observations of dust scattered, stellar light in the optical have given a detailed view of the dust distribution in the shells, most recently in scattered polarised light of the detached shell sources R Scl and V644 Sco (González Delgado et al. 2001, 2003; Olofsson et al. 2010; Maercker et al. 2010, 2014; Ramstedt et al. 2011). In comparison to single-dish (SD) observations of CO line emission and images of dust in the far infrared, the optical observations of dust scattered light provide information at high angular resolution. Observations at high-angular resolution of the detached gas shells in CO emission have only been done for the detached shell sources TT Cyg (Olofsson et al. 2000) and U Cam (Lindqvist et al. 1999) using the Plateau de Bure Interferometer, and R Scl (Maercker et al. 2012) using the Atacama Large Millimeter/submillimeter Array (ALMA). The observations clearly show the detached shells around TT Cyg and U Cam at $35''$ and $7''.3$, respectively. No emission is detected between the shells and the present-day mass-loss, implying that the mass-loss rate decreased significantly after the TP, leading to the formation of an expanding shell that is not connected to the present-day mass-loss (and hence detached). The recent observations with ALMA during Cycle 0 imaged the detached shell around R Scl in $^{12}\text{CO}(3-2)$ emission at high angular resolution ($\approx 1''.4$ beam; Maercker et al. 2012), showing a clumpy structure and slight deviations from spherical symmetry in the shell. In addition to the detached shell, the data also show a spiral structure that connects the shell with the present-day mass-loss. The spiral is formed by the interaction of the stellar wind with a previously unknown binary companion, and allows us to determine the evolution of the mass-loss rate and expansion velocity since the last TP. These are the first *observational* constraints of the behaviour of the stellar mass loss during and after a TP. While the evolution generally fits with theoretical predictions, it is clear that the mass-loss rate must decrease significantly slower than predicted by models. These observations already show that the shell around R Scl is not entirely detached. Comparing the distribution of the gas shell with images of polarised, dust scattered stellar light shows that the dust and gas have an almost identical distribution in the shell, implying a common evolution of the dust and gas shells since the last TP (Maercker et al. 2014).

Maercker et al. (2012) only discuss the ALMA observations of $^{12}\text{CO}(3-2)$ observed towards R Scl, and focus on the hydrodynamical modelling of the spiral structure. We here present the full set of ^{12}CO observations of the circumstellar environment around R Scl, concentrating on the overall CO emission. In Sect. 2 we present the ALMA observations of $^{12}\text{CO}(1-0)$, $^{12}\text{CO}(2-1)$, and $^{12}\text{CO}(3-2)$. We also present new SD observations of $^{12}\text{CO}(2-1)$ and $^{12}\text{CO}(3-2)$ taken with the Atacama Pathfinder Experiment telescope (APEX). In Sect. 3 we describe our analysis strategy and the results, and in Sect. 4 we discuss what this implies for the physical properties of the gas shell and its origin. Our conclusions are finally presented in Sect. 5.

In previous publications, the shells of gas found around carbon AGB stars are referred to as *detached* shells. At least in the case of R Scl there are clear signs that the shell is in fact not

Table 1. Summary of the reduced image cubes of the ALMA observations of the circumstellar environment of R Scl.

Transition	Beam	θ_{max}	Δv [km s $^{-1}$]	rms [mJy/beam]
$^{12}\text{CO}(1-0)$	$3''.8 \times 2''.8$	$18''$	1.5	7.3
$^{12}\text{CO}(2-1)$	$2''.1 \times 1''.7$	$11''$	1.0	6.4
$^{12}\text{CO}(3-2)$	$1''.6 \times 1''.2$	$7''$	0.5	16.0

Notes. θ_{max} gives the maximum recoverable scale, and the rms is measured in line-free channels in the final reduced images. The absolute calibration uncertainty is $\approx 10\text{--}20\%$.

detached; Sects. 2.4 and 3.3. Throughout the paper we will therefore refer to the *shell* around R Scl, meaning the thin shell of dust and gas found at $19''.5$ from the star. We will refer to the gas *between* the shell and the star as the circumstellar envelope (CSE).

2. Observations

2.1. R Sculptoris

R Scl is a semi-regular pulsating carbon AGB star with a pulsation period of approximately 370 days. Current distance estimates are very uncertain, ranging from 266 pc (revised H β line, Knapp et al. 2003) to 370 pc (using *K*-band Period-Luminosity relationships; Knapp et al. 2003; Whitelock et al. 2008). Integrating the spectral energy distribution of R Scl and assuming a distance of 370 pc gives a luminosity of $L = 5200 L_{\odot}$ – a reasonable value for carbon AGB stars. We will use 370 pc throughout this paper, noting the high uncertainty in this value. Maercker et al. (2012) use a distance of 290 pc, adopting a value that was erroneously calculated from a period-luminosity relationship in Schöier et al. (2005). This does not affect the main conclusions in Maercker et al. (2012), but changes the estimated age of the shell around R Scl from 1800 yr to 2300 yr. The estimated mass-loss rates also slightly increase.

The stellar velocity is determined from molecular line observations to be $v_{\text{LSR}}^* = -19 \text{ km s}^{-1}$. R Scl is surrounded by a thin shell of dust and gas. The radius and width of the shell were measured with high precision in images of dust scattered, stellar light, to be $19''.5 \pm 0''.5$ and $2'' \pm 1''$ (Olofsson et al. 2010; Maercker et al. 2014), respectively, and the dust-shell radius and width were found to coincide nearly exactly with the shell of gas observed in $^{12}\text{CO}(3-2)$ with ALMA (Maercker et al. 2014).

2.2. ALMA early science observations

R Scl was observed during ALMA Cycle 0 using the compact configuration of the main array. The main target of the observations were the $^{12}\text{CO}(1-0)$ line in Band 3, the $^{12}\text{CO}(2-1)$ line in Band 6, and the $^{12}\text{CO}(3-2)$ line in Band 7. The parameters of the final reduced images are given in Table 1. Channel maps of the three ^{12}CO transitions are shown in Figs. 1 to 3. The observational setup is summarised in Table 2 and described below. In Cycle 0 ALMA did not offer the Atacama compact array (ACA) yet, and the data are hence limited by the largest observable scales in the respective transitions. The spectral setup in Cycle 0 allowed us to define (with some restrictions) four spectral windows (spw) with the same bandwidth (BW) and channel width. In all bands pointed mosaics were observed to cover

M. Maercker et al.: A detailed view of the gas shell around R Sculptoris with ALMA

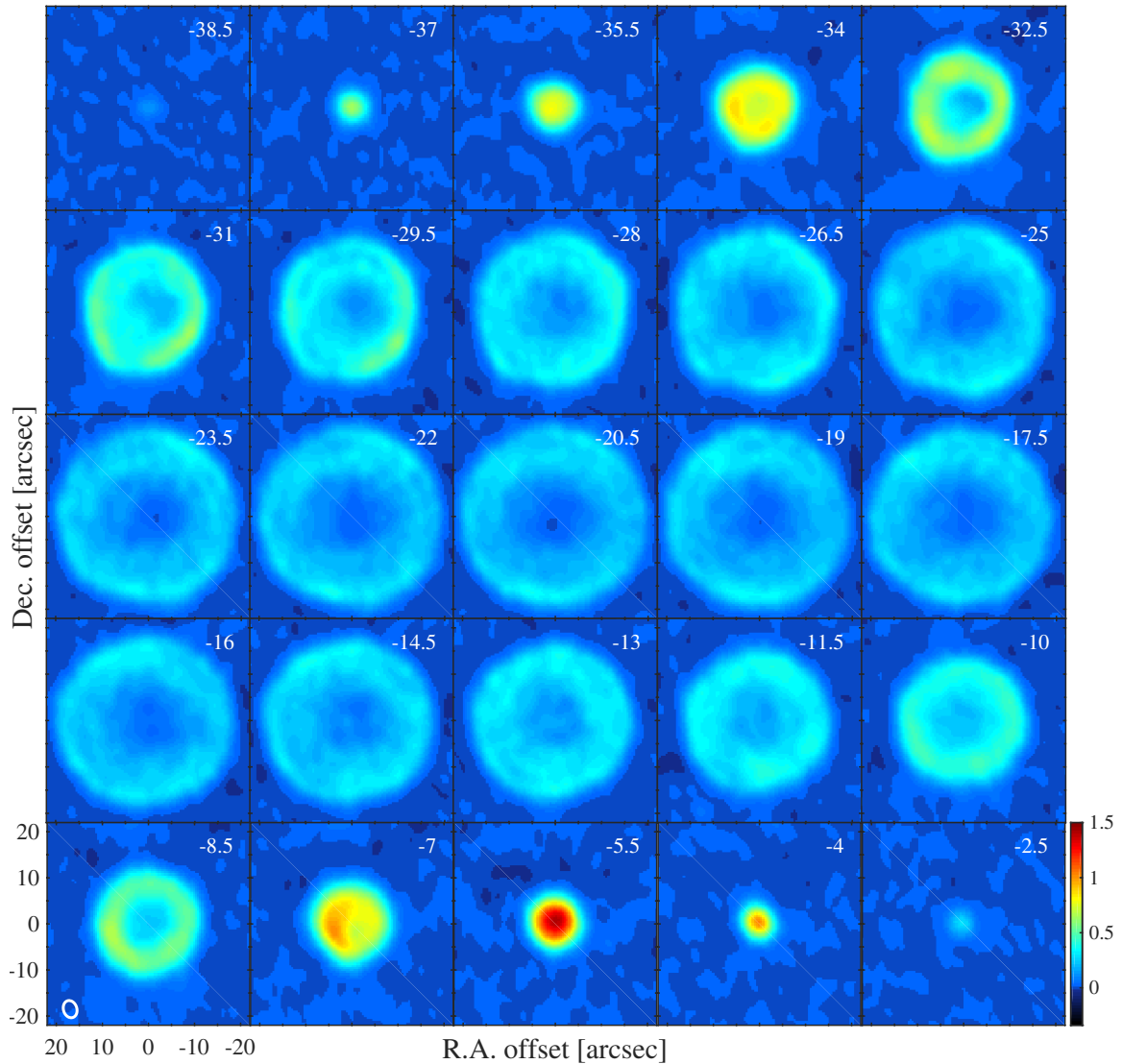


Fig. 1. ALMA observations of $^{12}\text{CO}(1-0)$ towards R Scl. The bin size of each panel is 1.5 km s^{-1} . The color scale is given in Jy/beam. The beam ellipse is given in the lower left corner.

the entire area of the detached shell. The observations are divided into individual scheduling blocks (SBs). The delivered data was re-reduced to improve the data quality using version 4.1 of the Common Astronomy Software Application (CASA), making use of python scripts to automate the calibration process. The SBs are calibrated separately and then combined for the respective bands. After calibration, imaging of the CO emission lines was carried out with the CLEAN algorithm using natural weighting and binning the spectra. The complex structures of the CO envelope were masked in an iterative procedure with decreasing thresholds in CLEAN. *Band 3*: observations of the $^{12}\text{CO}(1-0)$ emission line at 115.27 GHz were carried out between Jan. 23 and Jan. 25 2012. The dataset contains two SBs, taken in the two consecutive nights. Unfortunately, water vapour radiometer (WVR) measurements with sufficient quality were

only available for one of the SBs, meaning that rapid atmospheric variations were only corrected for half of the data. One SB revealed very low quality data of the flux calibrator Callisto. Therefore the flux densities of the calibrators were adopted from the other SB. However, the entire spectral window containing the $\text{CN}(N = 1-0)$ emission had to be excluded from further investigation because of a very low signal-to-noise ratio, making the data unusable.

Band 6: observations of the $^{12}\text{CO}(2-1)$ emission line at 230.54 GHz were carried out on Oct. 1 2011. The dataset contains two SBs.

Band 7: observations of the $^{12}\text{CO}(3-2)$ emission line at 345.80 GHz were carried out between Oct. 3 and Oct. 19 2011. The dataset contains a total of seven SBs. One SB did not contain

A&A 586, A5 (2016)

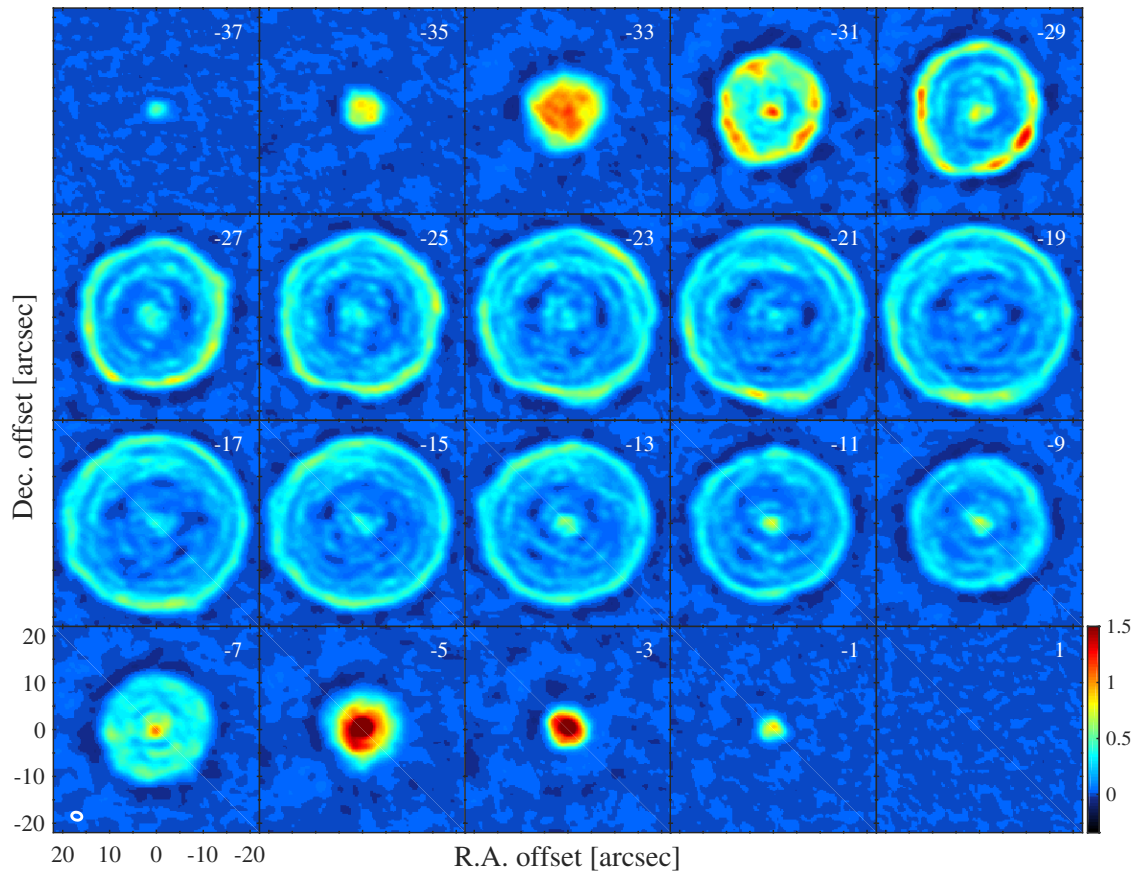


Fig. 2. ALMA observations of $^{12}\text{CO}(2-1)$ towards R Scl. The bin size of each panel is 1.0 km s^{-1} . Panels with a spacing of 2 km s^{-1} are shown. The color scale is given in Jy/beam. The beam ellipse is given in the lower left corner.

flux calibrator measurements, forcing us to use the flux calibration data from the other SBs.

2.3. Single-dish observations

In order to estimate the amount of extended emission that goes beyond the largest recoverable scales in the ALMA observations, we compare the ALMA spectra to SD spectra. For the $^{12}\text{CO}(1-0)$ transition we use spectra from the Swedish-ESO submillimeter telescope (SEST, with a beam full width half maximum (FWHM) of $44''$; Olofsson et al. 1996) and the IRAM 30 m telescope (with a beam FWHM of $22''$; Olofsson et al. 1993).

For the $^{12}\text{CO}(2-1)$ and $^{12}\text{CO}(3-2)$ transitions we observed two on-the-fly (OTF) maps with APEX. The observations were done using the APEX-1 and APEX-2 receivers for $^{12}\text{CO}(2-1)$ and $^{12}\text{CO}(3-2)$, respectively (Vassilev et al. 2008). The beam FWHM is $27''$ in the $^{12}\text{CO}(2-1)$ transition and $18''$ in the $^{12}\text{CO}(3-2)$ transition. The maps are sampled at $\approx 1/3$ of the beam-widths and cover areas of $45'' \times 45''$ and $54'' \times 54''$, respectively. The total on-source integration of respectively 12.5 min and 13.5 min resulted in rms values of 0.07 K and 0.18 K. Figure 4 shows the SD observations. Spectra were extracted from the pixel in the APEX OTF maps centred on the star, giving a spectrum equivalent to a single

pointing on the star with the beam of APEX at the respective frequency. The observations are summarised in Table 3.

2.4. Interferometer vs. single-dish observations and extended emission

Figure 4 shows a comparison of observed SD spectra with the equivalent ALMA spectra extracted from maps that were smoothed to the same respective beams using the task *imsmooth* in CASA. Depending on the frequency and array configuration, the interferometer will resolve out flux coming from spatial scales that are larger than the largest recoverable scale (Table 2), leading to negative features in the images. The comparison to the SD spectra shows that the ALMA observations miss flux in all the observed emission lines:

The front and back of the shell:

One would expect the least amount of flux to be lost at the extreme velocities, where the emission only comes from the front and back caps of the shell and is comparatively compact, while the emission may be more extended at the v_{LSR}^* due to an extended envelope (see below). For $^{12}\text{CO}(1-0)$ we see that this is indeed the case, where we recover all emission at projected velocities $|v_{\text{LSR}} - v_{\text{LSR}}^*| > 11$, while we only recover

M. Maercker et al.: A detailed view of the gas shell around R Sculptoris with ALMA

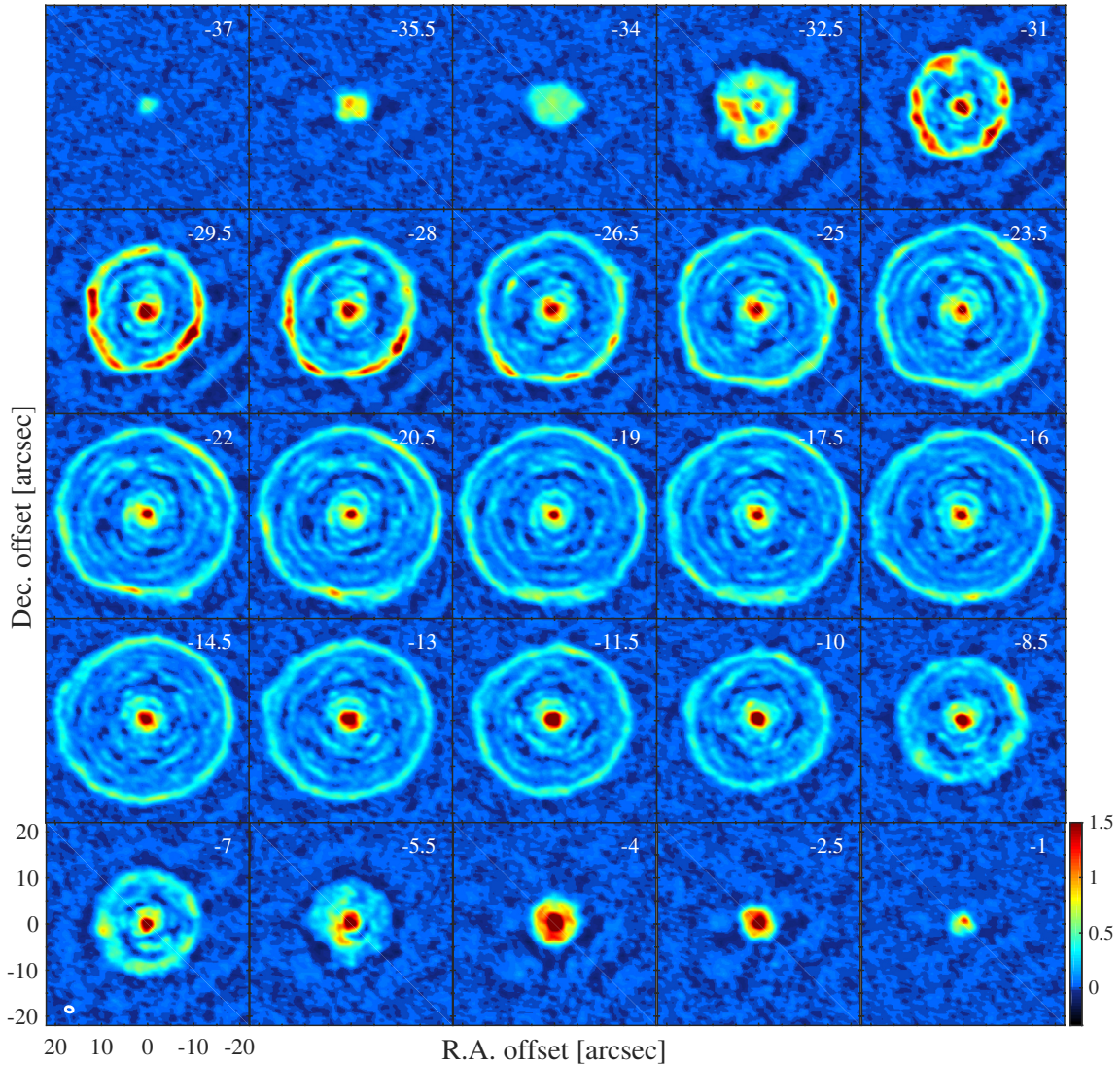


Fig. 3. ALMA observations of $^{12}\text{CO}(3-2)$ towards R Scl. The bin size of each panel is 0.5 km s^{-1} . Panels with a spacing of 1.5 km s^{-1} are shown. The color scale is given in Jy/beam. The beam ellipse is given in the lower left corner. These data were first presented in [Maercker et al. \(2012\)](#).

about 60–70% of the flux at the v_{LSR}^* . For the $^{12}\text{CO}(2-1)$ transition the observations recover $\approx 70\%$ of the flux at the extreme velocities, while only $\approx 35\%$ is recovered at the v_{LSR}^* . Finally, 60–70% of the flux is recovered at all velocities for the $^{12}\text{CO}(3-2)$ line¹.

At the extreme velocities the geometry of the shell (expansion velocity, shell thickness, and turbulent velocity) causes the caps to have an apparent size that can be larger than the largest recoverable scales. For a shell radius of $R_{\text{sh}} = 19''.5$, a shell width of $\Delta R_{\text{sh}} = 2''$ ([Maercker et al. 2014](#)), and an expansion velocity of $v_{\text{sh}} = 14.3 \text{ km s}^{-1}$, the size of the cap at the extreme velocity would be $\approx 18''$ at 1.5 km s^{-1} resolution

in $^{12}\text{CO}(1-0)$, $\approx 15''$ at 1 km s^{-1} resolution in $^{12}\text{CO}(2-1)$, and $\approx 11''$ at 0.5 km s^{-1} resolution in $^{12}\text{CO}(3-2)$. For $^{12}\text{CO}(2-1)$ and $^{12}\text{CO}(3-2)$ this is indeed larger than the maximum recoverable scale, explaining the lost flux.

The CSE and shell:

The amount of flux lost in the different transitions at the v_{LSR}^* constrains the extended emission of the CSE. In the $^{12}\text{CO}(1-0)$ emission (Fig. 1) the shell can barely be discerned and the spiral shape observed in $^{12}\text{CO}(3-2)$ ([Maercker et al. 2012](#)) disappears almost entirely. Instead the ALMA observations show a bowl-like shape with no emission at the stellar position. This can be explained with a shell that is entirely filled with $^{12}\text{CO}(1-0)$ emission, with a low contrast between the extended emission and the small-scale structure (i.e. the shell and spiral). While the SD

¹ Note that [Vlemmings et al. \(2013\)](#) estimate that only 25% of the flux is recovered for the $^{12}\text{CO}(3-2)$ line. This is however due to an erroneous main-beam correction of the APEX data in [De Beck et al. \(2010\)](#).

A&A 586, A5 (2016)

Table 2. Summary of ALMA observations of the circumstellar environment of R Scl.

ALMA Band	BW [MHz]	Resolution [MHz]	No. of mosaic pointings	t_{tot} [min]	Calibrators bandpass	flux	ν_{spw} [GHz]
3 (84–116 GHz)	937.5	0.244	7	64	J0522-364 J040353-360513	Callisto	101.5: continuum 112.6: CN(N=1–0) 113.1: continuum 114.5: $^{12}\text{CO}(1-0)$
6 (211–275 GHz)	1857.0	0.488	23	90	3c454.3	Neptune	215.25: SiO(5–4) 217.11: continuum 230.25: $^{12}\text{CO}(2-1)$ 232.10: continuum
7 (275–373 GHz)	1875.0	0.488	45	155	3c454.3 J0403-360	Neptune	331.17: $^{13}\text{CO}(3-2)$ 333.02: continuum 343.30: CS(7–6) 345.15: $^{12}\text{CO}(3-2)$

Notes. BW is the total bandwidth, t_{tot} the total on-source time in the map, and ν_{spw} the central frequency of the respective spectral windows (with observed lines or continuum indicated). Calibrators are for all spectral windows in the respective bands.

observations detect all the extended emission inside the shell, the ALMA observations resolve-out the flux at large scales, leading to the observed bowl-like shape. In the $^{12}\text{CO}(2-1)$ emission (Fig. 2) the shell is more pronounced and the spiral shape can be seen. However, the structure still lies on top of an overall bowl-like shape, with the present-day mass loss only barely detected. Such an observed intensity distribution can be explained by slightly less extended $^{12}\text{CO}(2-1)$ emission, and a higher contrast between the small-scale structures and the extended emission (i.e. less flux gets resolved out compared to the $^{12}\text{CO}(1-0)$ emission, and the small-scale structures are more pronounced). In the $^{12}\text{CO}(3-2)$ emission (Fig. 3) the shell, spiral, and present-day mass loss are clearly visible, and the lost flux is apparent in the form of negative features around the observed structure. This implies a relatively limited extent of the $^{12}\text{CO}(3-2)$ emission that is centrally peaked. The maximum recoverable scales for the different transitions in Table 2 give an indication of the minimum size of the emitting regions for the individual lines, while the beam FWHMs of the SD spectra give a rough upper limit (depending on whether the line profiles are spatially resolved or unresolved). This confirms that the $^{12}\text{CO}(1-0)$ emission must extend almost out to the shell, causing the smooth distribution and lack of central emission observed in the ALMA data, while the $^{12}\text{CO}(2-1)$ emitting region is limited to radii up to $\approx 13''$ – $15''$, and the $^{12}\text{CO}(3-2)$ emission comes from a radius up to $\approx 10''$. Extended emission from ^{12}CO reaching out to the shell means that the shell is in fact not detached, but instead filled with significant amounts of molecular gas.

In Fig. 5 we use a toy model to simulate extended regions of emission and their effect on the ALMA observations. We create ad-hoc intensity distributions with no underlying physical model to fit the above described scales and reproduce the observed images. The toy-images consist of a clumpy shell with a radius of $19.5''$ and a width of $2''$, a spiral with 4.5 evenly spaced spiral windings, and extended emission in the form of discs with radii of $\approx 18''$, $\approx 14''$, and $\approx 9''$ for the $^{12}\text{CO}(1-0)$, $^{12}\text{CO}(2-1)$, and $^{12}\text{CO}(3-2)$ transitions, respectively, and with a Gaussian drop-off at the edge with $\sigma = 6''$.

Simulations in CASA, using the ALMA Cycle 0 compact configuration in the three bands, show that the observed features can indeed be explained by a shell and spiral shape where the

Table 3. Summary of single-dish (SD) observations towards R Scl.

Transition	Telescope	FWHM	$I_{\text{vlsr,SD}}$ [Jy/beam]	$I_{\text{vlsr,ALMA}}$ [Jy/beam]
$^{12}\text{CO}(1-0)$	SEST	$44''$	28 ± 1.0	20
$^{12}\text{CO}(1-0)$	IRAM	$22''$	11 ± 1.5	6.5
$^{12}\text{CO}(2-1)$	APEX	$27''$	75 ± 1.5	27
$^{12}\text{CO}(3-2)$	APEX	$18''$	50 ± 2.5	30

Notes. I_{vlsr} gives the measured flux at the stellar v_{LSR} SD observations. The absolute calibration uncertainty for the SD observations is 20%. For comparison, the measured flux at the stellar v_{LSR} measured in the ALMA observations convolved with the respective SD FWHM (Sect. 2.4 and Fig. 4) is also given.

shell is filled with extended emission of varying size (decreasing from $^{12}\text{CO}(1-0)$ to $^{12}\text{CO}(3-2)$). The toy model qualitatively shows the effects of different intensity distributions, explaining the observations, and serves only as a rough estimate of the spatial scales of the emission. The implications this has for the density distribution within the shell, and hence the evolution of the mass-loss rate during and after the TP, are discussed in Sect. 3.3.

3. Analysis and results

We extract the shell emission from the ALMA observations, allowing us to analyse the shell and CSE separately. Our analysis and results focus on the properties of the shell and on the information we can gain about the distribution of the molecular gas of the CSE to constrain the recent mass-loss evolution. We do not treat the spiral. A detailed analysis of the spiral shape observed in $^{12}\text{CO}(3-2)$ was done using hydrodynamical models (Maercker et al. 2012). Any additional detailed analysis of the CSE structure would require high spatial-resolution observations of the spiral shape to constrain essential parameters such as the binary separation, the shape of the inner spiral, and the contrast between the spiral and inter-spiral material. Such observations are in progress during the current ALMA Cycle (Cycle 2).

M. Maercker et al.: A detailed view of the gas shell around R Sculptoris with ALMA

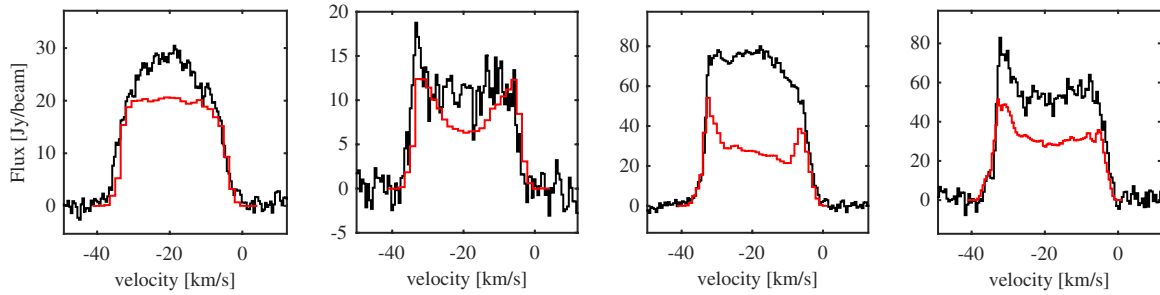


Fig. 4. SD observations towards R Scl (from left to right): SEST CO(1–0), IRAM 30 m CO(1–0), APEX CO(2–1), and APEX CO(3–2). The FWHM of the SD beams are 44", 22", 27", and 18", respectively. The red spectra show the ALMA observations of the respective transitions convolved with Gaussian beams to give the FWHM from the respective telescopes.

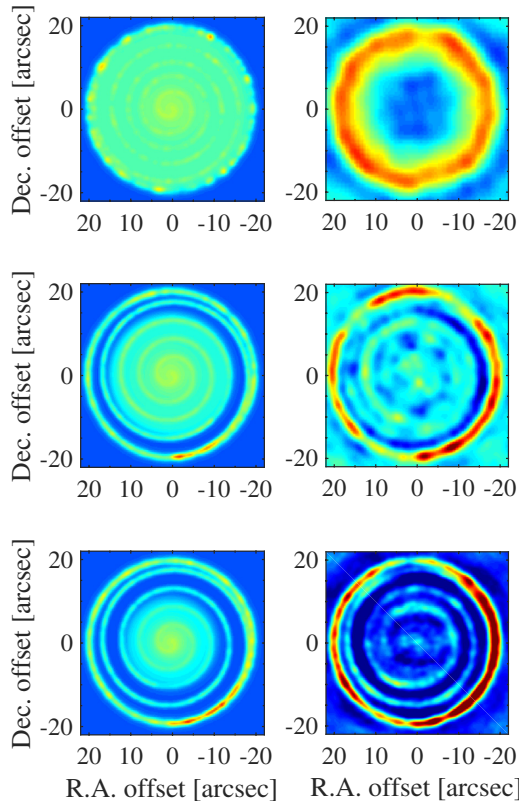


Fig. 5. Qualitative analysis of the effect of extended emission on the ALMA Cycle 0 observations of ALMA. The left columns shows toy-models of the emission from the shell around R Scl and extended emission inside the shell at the v_{LSR}^* for the $^{12}\text{CO}(1-0)$, $^{12}\text{CO}(2-1)$, and $^{12}\text{CO}(3-2)$ transitions (top to bottom, respectively). The right column shows the resulting simulated observations using the ALMA Cycle 0 compact configuration of the main array (simulated using the CASA simulator).

3.1. The shell morphology

The shell morphology is best described based on the $^{12}\text{CO}(3-2)$ images, where the ALMA observations give the highest spatial resolution. Overall the shell has a spherical appearance in all velocity channels. Fitting a spherically symmetric shell with a

radius of 18".5 expanding at 14.3 km s^{-1} reproduces the *observed* size of the shell in all channels (Maercker et al. 2012). Limb brightening along the inner edge of the shell slightly moves the peak inwards (Maercker et al. 2010; Olofsson et al. 2010), and the radius measured in the ALMA data is consistent with the 19".5 measured in polarised, dust-scattered light of the shell around R Scl (Maercker et al. 2014).

However, clear deviations from a perfect sphere are apparent. This was already observed in the dust observations (Maercker et al. 2014), which show an almost identical distribution to the $^{12}\text{CO}(3-2)$ from ALMA. In particular there is a flattening of the southern part of the shell at the v_{LSR}^* . The shell also appears strongly disrupted in this region. The same structures can also be seen in the $^{12}\text{CO}(2-1)$ maps, and to some degree in the $^{12}\text{CO}(1-0)$ maps, where the lower angular resolution, however, smoothes most features out.

A speculative interpretation of this is an interaction of the binary companion with the stellar wind as the shell is created. The interaction distorts the shell from a spherically symmetric shape, while leaving the shell undisturbed on the opposite side. As the shell expands, the effect of the binary companion is reduced. At the end of the pulse, when the mass-loss rate and expansion velocity start to decline, the spiral formed by the post-pulse mass-loss connects to the shell at position angle $\text{PA} \approx 90^\circ$ (with $\text{PA} = 0^\circ$ being North, and the PA increasing counter-clockwise). If true, the flattened and disrupted southern part of the shell would indicate the onset of the TP, while the point at which the spiral attaches to the shell marks the end of the TP. The estimated binary period is based on the present-day expansion velocity of the wind and the separation of the inner spiral windings (Maercker et al. 2012) and depends on the estimated distance to the source. Adjusting for the larger distance used here, the binary period is estimated to be 445 yr (Maercker et al. 2012). The fraction of the shell affected by the binary companion would be $\approx 40\%$ of one revolution, translating into a TP timescale of $\approx 180 \text{ yr}$.

Whether this is a viable scenario has to be tested through detailed hydrodynamical modelling. The morphology of the shell depends on the mass-loss properties, the masses of the stars, and the timescales. ALMA Cycle 2 data will give us the necessary resolution and sensitivity to constrain these critical parameters and to calculate a detailed model of the shell and spiral formation.

3.2. The shell emission

In order to analyse the emission from the shell we extract regions in the channel maps for all three transitions

A&A 586, A5 (2016)

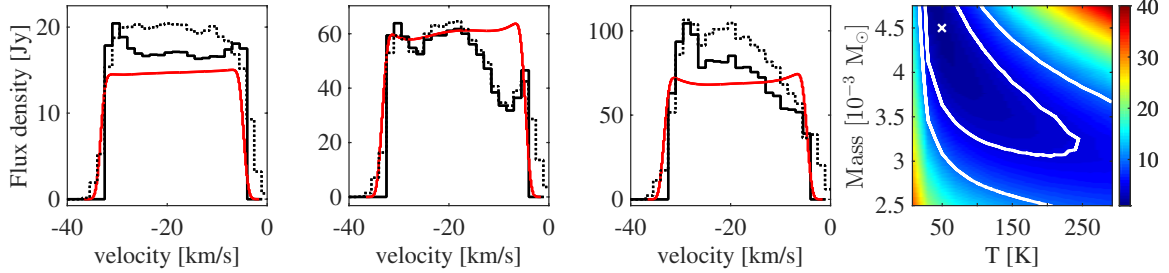


Fig. 6. ALMA ^{12}CO observations of the shell for $^{12}\text{CO}(1-0)$, $^{12}\text{CO}(2-1)$, and $^{12}\text{CO}(3-2)$ (black lines, panels 1–3, respectively). The data are extracted from annuli within $\pm 3''$ from the projected radius of the shell in each velocity bin in the images smoothed to $4''$ resolution. For comparison, the black dotted lines show the emission integrated over the entire image for each velocity bin instead (i.e. also containing emission from the CSE). The red lines show the best-fit model of the shell only. The right panel shows the χ^2 map of the radiative transfer models of the shell with shell-mass vs. shell temperature. The colour scale gives the χ^2 value, the white cross indicates the best-fit model. The white contours give the 1σ and 2σ levels (the 3σ contours fall outside of the plotted range).

assuming a shell-radius of $19''.5$ and an expansion velocity of 14.3 km s^{-1} (Maercker et al. 2012, 2014). In order to ensure that the same regions are extracted in each transition, we smoothed the images to a spatial resolution of $4''$ and a velocity resolution of 1.5 km s^{-1} . Although the FWHM of the shell is only $2''$, the spatial and spectral resolution cause a widening of the shell in the images, and the shell emission is extracted from a ring with width $\pm 3''$ centred on the shell. The resulting spectra are shown in Fig. 6 and are compared to the spectra integrated over the entire images.

For a homogeneous spherically symmetric shell one would expect a flat spectrum, i.e. each velocity channel probes the same number of CO molecules in the shell. However, in particular for $^{12}\text{CO}(2-1)$ and $^{12}\text{CO}(3-2)$, it is clear that the shell has a clumpy structure and an asymmetric distribution of CO between the front and the back of the shell. Further, close to the extreme velocities it becomes increasingly difficult to differentiate between shell emission and emission originating from the rest of the CSE. This is particularly true in the case of R Scl where the emission inside the shell has a velocity gradient that gradually decreases from 14.3 km s^{-1} in the shell to its present-day value of 10.5 km s^{-1} (Maercker et al. 2012).

In order to determine the mass and temperature in the shell, we calculated a grid of 1-dimensional radiative transfer models based on the monte-carlo technique (Schöier & Olofsson 2001). Each shell has a Gaussian density distribution with a radius of $19''.5$, a FWHM of $2''$, and a constant expansion velocity of 14.3 km s^{-1} . We assume a fractional abundance of ^{12}CO of $f(^{12}\text{CO}) = 4.3 \times 10^{-4}$ relative to H_2 (Olofsson et al. 1993). This value was derived using the elemental composition given by Lambert et al. (1986). The temperature is assumed to be constant throughout the shell. The grid is calculated for shell-masses between $2.5 \times 10^{-3} M_{\odot}$ to $4.75 \times 10^{-3} M_{\odot}$ in steps of $0.25 \times 10^{-3} M_{\odot}$ and temperatures between 10 K to 290 K in steps of 20 K. For each model we determine the best-fit model (Fig. 6) by minimising the χ^2 value

$$\chi^2 = \left(\frac{I_{\text{obs},i} - I_{\text{mod},i}}{\sigma_{\text{obs},i}} \right)^2, \quad (1)$$

where $I_{\text{obs},i}$ is the integrated intensity of the observation i , $I_{\text{mod},i}$ is the modelled intensity, $\sigma_{\text{obs},i}$ is the uncertainty in the observation is assumed to be 20%, and the sum goes over all transitions. The best-fit model gives a shell-mass of $(4.5 \pm 1.5) \times 10^{-3} M_{\odot}$ at a temperature of $50^{+200}_{-20} \text{ K}$. Note that the radiative transfer model

assumes a spherically symmetric, smooth shell, and hence can not reproduce asymmetries within the shell. The observed and modelled line profiles may therefore differ significantly. In the optically thin limit, the integrated intensity still gives a good measure of the total mass and temperature in the shell. The upper limit in the shell mass is only sampled by few points, and hence not included in the χ^2 map in Fig. 6. The fractional ^{12}CO abundance further assumes that no ^{12}CO has been photodissociated. Decreasing $f(^{12}\text{CO})$ leads to an increase in the estimated shell mass and a decrease in the shell temperature. For optically thin lines the increase in mass would scale roughly linearly with $f(^{12}\text{CO})$. The lines in our best-fit model have tangential optical depths of $\tau_{\text{tan}} \sim 1$, meaning that the shell mass clearly would be affected by a change in $f(^{12}\text{CO})$, making the estimated shell mass a lower limit. However, for the mass-loss rate during the creation of the shell ($2.3 \times 10^{-5} M_{\odot} \text{ yr}^{-1}$, see below), models of photodissociation predict the half-abundance radius of CO to be significantly larger than the radius of the shell (on the order of $40\text{--}50''$; Stanek et al. 1995). A clumpy medium will further protect the ^{12}CO in the shell from dissociation (while still allowing photodissociation in the CSE; see Sect. 3.3), and we do not expect the photodissociation to affect the abundance of ^{12}CO in the shell significantly. We thus consider the estimated mass to be the correct shell mass within the uncertainties.

The estimate of the mass in the gas shell is consistent with previous estimates from Schöier et al. (2005) based on SD data alone ($M_{\text{shell}} = 2.5 \times 10^{-3} M_{\odot}$). More recently, Olofsson et al. (2015) model the emission of CI from the shell based on SD observations with APEX. Their detection of CI is consistent with the estimated C/O-ratio of R Scl, assuming solar abundances of oxygen, that all neutral carbon comes from the photodissociation of carbon-bearing molecules except for the CO, and there is very limited ionisation of C. They determine the physical parameters of the shell using SD spectra of ^{12}CO , including high J-transitions observed with HIFI. Assuming $f(^{12}\text{CO}) = 10^{-3}$, their resulting shell mass is $(2 \pm 1) \times 10^{-3} M_{\odot}$, with a temperature of $100^{+200}_{-70} \text{ K}$. Hence, using essentially independent methods (interferometry vs. SD observations and an independent consistency check with CI observations), and adjusting for the difference in $f(^{12}\text{CO})$, the same shell masses and temperatures are derived.

The analysis of the $^{13}\text{CO}(3-2)$ emission observed with ALMA suggests that at least parts of the shell must have temperatures that are lower than the derived 50 K (Vlemmings et al. 2013). The measured $^{12}\text{CO}/^{13}\text{CO}$ ratio shows regions in which additional ^{13}CO is formed due to chemical fractionation.

M. Maercker et al.: A detailed view of the gas shell around R Sculptoris with ALMA

This process however requires temperatures lower than 35 K. We only model the temperature of a smooth, homogeneous shell, while a clumpy structure will affect the radiative transfer and decouple the connection between mass and temperature. Olofsson et al. (2015) in principle manage to find a satisfying fit for even lower temperatures than 50 K, albeit for unrealistically high shell masses. Shell temperatures of ≈ 10 K require masses approaching $1 M_{\odot}$. Although this may in principle be possible, the consistency of a shell mass of a few times $10^{-3} M_{\odot}$ with various dust estimates (e.g. González Delgado et al. 2003; Schöier et al. 2005; Olofsson et al. 2010) makes a total mass in excess of $0.1 M_{\odot}$ unlikely (Olofsson et al. 2015).

While the shell is likely confined by collision with a previous, slower wind (e.g. Steffen & Schönberner 2000; Schöier et al. 2005; Mattsson et al. 2007), the mass-loss rate of the previous wind must have been very low (less than a few $10^{-6} M_{\odot} \text{ yr}^{-1}$). The half-abundance radius due to photodissociation of ^{12}CO lies outside the shell for higher mass-loss rates, but no signs of the spiral structure can be observed outside of the shell. A significant amount of mass outside of the shell would have further led to a deceleration of the shell, which is not observed (Maercker et al. 2012). Hence, we believe that only a minor amount of mass from the previous mass-loss has been swept up in the shell. Assuming a shell-creation time of $\approx 200^{+100}_{-50}$ yr (Vassiliadis & Wood 1993, consistent with the ALMA observations) then leads to a mass-loss rate of $(2.3^{+1.7}_{-1.3}) \times 10^{-5} M_{\odot} \text{ yr}^{-1}$ during the creation of the shell.

3.3. The recent evolution of the stellar wind

In order to constrain the physical parameters of the CSE inside the shell, we convolved the best-fit model of the shell with the SD beams of the respective transitions (Fig. 7, top), and subtract it from the SD observations. The emission from the shell, extracted from the ALMA images, is additionally convolved with the SD beams and compared to the model to ensure that the right flux is subtracted. We find that the clumpy structure is generally smoothed out significantly in the SD observations, giving a good fit of the model to the observations. Using the model instead of the ALMA observations has the advantage that *only* the shell is subtracted, while the observations may still contain additional velocity components that do not belong to the shell. In difference to the hydrodynamical modelling of the $^{12}\text{CO}(3-2)$ observations (Maercker et al. 2012), we here focus on the overall extended emission from the CSE, instead of the detailed structure.

The shell-subtracted SD observations (Fig. 7, bottom) now contain the emission from the CSE without the shell, allowing us to model the mass loss since the creation of the shell. We model the subtracted SD spectra with a single, constant mass-loss rate, while in fact the mass-loss rate likely has varied since formation of the shell. As such we are only modelling an *average* mass-loss rate inside the shell. A varying mass-loss rate will however affect the density distribution and the emission regions of different CO transitions, making it difficult to find a consistent model for all observed lines. Likewise, the half-abundance radius assumes a constant wind and we are only determining an *average* radius for the emitting region. Further, the amount of photodissociation inside the shell is not clear as there likely is significant shielding by the shell itself. Finally, the models are very degenerate between the chosen mass-loss rate, half-abundance radius, temperature profile, and velocity profile.

Due to these limitations we only derive a model that fits the subtracted SD spectra assuming reasonable parameters for the temperature and velocity profiles, and loosely constraining

the radius of the emitting region by the limits given by the observed scales in the ALMA data (see Sect. 2.4). The derived mass-loss rate serves as an indication of the average mass-loss rate since the formation of the shell.

Assuming a constant mass-loss rate results in a $1/r^2$ density distribution. The fractional abundance is assumed to follow

$$f(r) = f_0 \exp\left(-\ln(2)\left(\frac{r}{R_{1/2}}\right)^a\right), \quad (2)$$

where f_0 is the initial fractional abundance, $R_{1/2}$ is the half-abundance radius, and $a = 2.5$ (Mamon et al. 1988). For the kinetic temperature we assume a power-law of the form $T_{\text{kin}}(r) = T_0 \times (r/R_0)^{\beta}$ with $\beta = -0.85$. R_0 is the inner radius of the CSE, assumed to lie at 3 times the stellar radius (assuming a blackbody with an effective temperature of 2300 K and luminosity of $5200 L_{\odot}$). The velocity increases gradually from 3 km s^{-1} to 14.3 km s^{-1} to take into account both the acceleration of the wind in the inner CSE, as well as the time evolution of the terminal wind velocity since creation of the shell.

Using the above assumptions, we manage to model the $^{12}\text{CO}(1-0)$ transition observed with SEST and the $^{12}\text{CO}(2-1)$ transition observed with APEX using a mass-loss rate of $1.6 \times 10^{-5} M_{\odot} \text{ yr}^{-1}$ and a half-abundance radius of $7''.2$. A ^{12}CO radius that is smaller than the shell indicates that the shell is clumpy, and allows for the penetration of photodissociating radiation into the CSE. The resulting emitting region for $^{12}\text{CO}(1-0)$ is indeed not very centrally peaked and extends out to $\approx 18''$, while the $^{12}\text{CO}(2-1)$ emission is more peaked and only extends out to $\approx 15''$. The $^{12}\text{CO}(3-2)$ emission is the most compact, extending out to a radius of $\approx 11''$. These results are consistent with the limits set by the ALMA and SD data (Sect. 2.4). While the extent of the emitting region in the different transitions is an effect of the excitation conditions, the best-fit model overestimates the emission in the $^{12}\text{CO}(1-0)$ line observed with IRAM and the $^{12}\text{CO}(3-2)$ emission observed with APEX, in particular at the v_{LSR}^* . For the $^{12}\text{CO}(1-0)$ transition the beam of the IRAM observations probes a much smaller region than the SEST observations ($27''$ in diameter vs. $44''$), and hence are dominated by the more recent mass loss from R Scl. The APEX $^{12}\text{CO}(3-2)$ observations also are dominated by the recent mass loss, both due to more centrally peaked $^{12}\text{CO}(3-2)$ emission, as well as due to a smaller beam size ($18''$). These two transitions can be modelled with the same half-abundance radius but a mass-loss rate of $3.5 \times 10^{-6} M_{\odot} \text{ yr}^{-1}$, consistent with a continuously declining mass-loss rate since the last TP. The present-day mass-loss rate is estimated to be $\approx 3 \times 10^{-7} M_{\odot} \text{ yr}^{-1}$ based on HCN models (Schöier et al. 2005). Additional photodissociation of molecules in the inner wind due to binary interaction (Vlemmings et al. 2013) likely makes this estimate a lower limit, with the true present-day mass-loss rate being closer to $10^{-6} M_{\odot} \text{ yr}^{-1}$.

Hence, modelling of the shell-subtracted SD data gives a rough picture in which the mass-loss rate decreases gradually by more than an order of magnitude from when the shell was created to today. The mass-loss rate derived by fitting the lines that probe the largest extent of the CSE is only slightly lower than the shell mass-loss rate, implying that the mass loss most likely did not drop very quickly after creation of the shell. In principle it would be possible to attempt to derive a more quantitative evolution of the mass-loss rate since the creation of the shell by modelling a variable mass-loss rate that decreases over time. However, the limits set by the SD spectra are relatively uncertain, and the degeneracies of the model (mass-loss rate, CO photodissociation, temperature profile) are not easily constrained.

A&A 586, A5 (2016)

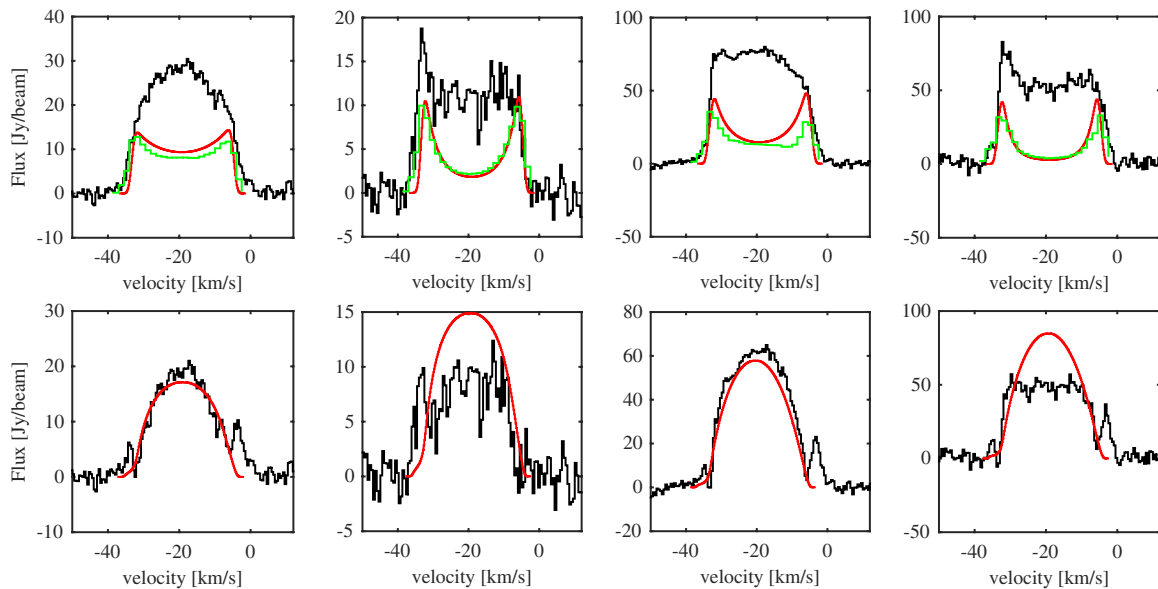


Fig. 7. *Top:* SD spectra (black, from left to right: SEST $^{12}\text{CO}(1-0)$, IRAM $^{12}\text{CO}(1-0)$, APEX $^{12}\text{CO}(2-1)$, and APEX $^{12}\text{CO}(3-2)$) with the best-fit shell model convolved with the respective beams (red). The green spectra show the shell emission extracted from the ALMA data and convolved with the respective SD beams. *Bottom:* SD spectra after subtracting the best-fit shell models. The red lines show the best-fit model fit to the shell-subtracted SD observations to constrain the average mass-loss rate since creation of the shell.

The loss of extended flux in the current ALMA data prevents using these observations to effectively constrain the mass-loss rate evolution, while the lack of intermediate baselines makes combination with the SD data very uncertain. The ALMA Cycle 2 observations of R Scl will contain Atacama Compact Array (ACA) observations, together with high-resolution main-array observations, and will make a more detailed description of the spiral around R Scl and measure the emission on all spatial scales possible. This together with detailed hydrodynamical modelling will set stronger constraints on the recent mass-loss evolution and the creation of the shell around R Scl.

3.4. An additional velocity component

In the ^{12}CO maps observed with ALMA (Figs. 1 to 3) there is clear emission at velocities $\pm 18 \text{ km s}^{-1}$ relative to the v_{LSR}^* . The expansion velocity of the shell is $14.3 \pm 0.5 \text{ km s}^{-1}$, while the present-day expansion velocity is constrained to less than 10.5 km s^{-1} by HCN and high-J ^{12}CO line profiles (Schöier et al. 2005; Olofsson et al. 2015). The additional velocity component also becomes evident in the SD spectra after subtracting the shell model (most prominently as a red-shifted peak; Fig. 7). The ALMA maps show that the emission is centred on the star. However, it is not clear what the origin of this higher-velocity component is. The ratio of the high-velocity components between the observed transitions implies that the emission comes from a warm region close to the star. The ratio between the blue and red-shifted parts of this component further indicates emission from an optically thick outflow. A possible explanation would be the onset of a bipolar outflow. If this were an extended outflow, it would have to be exactly along the line of sight, which is unlikely. A compact bipolar outflow would be possible along any direction as long as it does not extend further than the spatial resolution of the $^{12}\text{CO}(3-2)$ map, i.e. $\approx 1''.4$. At a distance

of 370 pc this corresponds to a physical size of $\approx 500 \text{ AU}$ in diameter. An alternative explanation may be a recent increase in expansion velocity of a spherical mass-loss. Whether this comes along with an increase in mass-loss rate is uncertain, but it would imply that the evolution of the post-pulse expansion velocity and mass-loss is not necessarily a smooth function of time.

It is not clear which (if any) of the above scenarios can explain the additional emission at higher velocities observed in the ^{12}CO lines. The high spatial-resolution data with ALMA from Cycle 2 will resolve the inner CSE of R Scl with a spatial resolution of $0''.2$. This will help in identifying the origin of the higher-velocity emission.

4. Discussion

For over two decades, the observed, geometrically thin gas shells around a handful of AGB stars have been connected to TPs. Their formation has been described both theoretically (Steffen et al. 1998; Steffen & Schönberner 2000; Mattsson et al. 2007) and observationally (e.g. Olofsson et al. 1990, 1996, 2010; Schöier et al. 2005; Maercker et al. 2010, 2012, 2014). It is generally assumed that the increase in mass-loss rate and expansion velocity during a TP leads to a higher-mass shell interacting with a low-density, slower pre-pulse wind, confining the shell and preventing it from very quickly dispersing due to internal pressure. After the TP, the mass-loss rate and expansion velocity drop drastically, only slowly recovering to values similar to the pre-pulse mass-loss during the remainder of the TP cycle. The sudden drop in mass-loss rate and expansion velocity leads to the shell detaching entirely from the present-day mass loss, leaving an essentially empty shell. The TP cycle starts with a high mass-loss-rate phase which lasts a few hundred years, followed by an inter-pulse time of several ten thousand years, depending on the mass of the star (Karakas & Lattanzio 2007). In order

M. Maercker et al.: A detailed view of the gas shell around R Sculptoris with ALMA

to form a detached shell, a sufficient change between the pre-pulse and pulse mass-loss rates in combination with a change in expansion velocity is required (Mattsson et al. 2007). The parameters derived in this paper imply a change in mass-loss rate of more than an order of magnitude, accompanied by a change in expansion velocity. The creation of the shell around R Scl is hence consistent with formation during a TP.

However, instead of showing a detached shell without (significant) ^{12}CO emission between the shell and the present-day mass loss, the ALMA observations of the shell around R Scl show a continuous mass-loss rate evolution with a significantly slower decline over time. This leads to a *filled* shell rather than a detached shell. The derived mass of the shell combined with estimated TP timescales implies a relatively high mass-loss rate during creation of the shell. Based on the expansion velocity, the age of the shell is ≈ 2300 yr, over which the mass-loss rate has slowly decreased by an order of magnitude. This is consistent with the hydrodynamical modelling of the observed spiral shape seen in the $^{12}\text{CO}(3-2)$ maps (Maercker et al. 2012). Hence, employing two different and independent methods of analysis (detailed hydrodynamical modelling of the structure seen in one transition vs. radiative transfer of the overall emission in all three transitions), we arrive at the same conclusion. The models form a shell during a TP, with a subsequent linear decline of the mass-loss rate to the present-day value. Assuming a TP mass-loss rate of $2.3 \times 10^{-5} M_{\odot} \text{ yr}^{-1}$ for 200 yr and a linear decline to the present-day value of $10^{-6} M_{\odot} \text{ yr}^{-1}$ over an additional 2100 yr, the total mass lost by R Scl since the onset of the most recent TP is $0.03 M_{\odot}$. If the mass-loss rate instead had evolved according to the classical scenario (i.e. with a sudden drop after the TP), the total mass lost would only have been $\approx 0.007 M_{\odot}$.

As the total amount of mass lost during the TP cycle increases monotonically during AGB evolution, the determined mass can be used to roughly estimate the evolutionary stage of R Scl, depending on the (unknown) main-sequence mass. For a $3 M_{\odot}$ star (main-sequence mass) at solar metallicity typical inter-pulse timescales once the third dredge-up has set in are $\approx 60\,000$ yr. Using the values derived for R Scl, and assuming that the present-day mass-loss rate remains constant for the remainder of the TP cycle at $10^{-6} M_{\odot} \text{ yr}^{-1}$, this implies that up to $0.09 M_{\odot}$ will be lost in total during the most recent TP cycle, placing R Scl at the end of the TP-AGB (Karakas & Lattanzio 2007). A $4.5 M_{\odot}$ star (main-sequence mass) on the other hand has typical inter-pulse timescales of $\approx 10\,000$ yr. In this case only a total of $0.04 M_{\odot}$ will be lost in the most recent TP cycle, and R Scl would have only evolved about halfway along the TP-AGB (Karakas & Lattanzio 2007).

Our results show that a significant fraction of the mass during a TP cycle will be lost immediately after the pulse due to a relatively slow decline from the thermal-pulse mass-loss rate. The total amount of mass lost during the TP-cycle limits the lifetime on the AGB and hence the number of TPs a star can experience. The mass of the stellar hydrogen envelope will also have a profound effect on the nucleosynthetic processes inside the star (e.g. hot bottom burning). The evolution of the mass-loss rate throughout the TP-cycle therefore also strongly affects the chemical evolution of the star, and the enrichment of the CSE and ISM.

5. Conclusions

We present the full set of ALMA Cycle 0 observations of ^{12}CO towards the carbon AGB star R Scl. The observations clearly resolve the shell around R Scl and reveal a spiral structure

induced by a binary companion. The data allow us to separate the shell from the extended emission inside the shell and analyse both components separately. Radiative transfer modelling of the shell and the present-day mass loss constrains the mass in the shell and average mass-loss rate since the formation of the shell. The results are consistent with a shell creation during a TP with a subsequent decline of the mass-loss rate. In particular we find that

- contrary to what was believed so far, the shell around R Scl is entirely filled with gas and as such is not detached,
- the shell is consistent with an increase in mass-loss rate and expansion velocity during a TP, leading to a two-wind interaction with a previous, slower wind,
- the estimated shell mass-loss rate is $2.3 \times 10^{-5} M_{\odot} \text{ yr}^{-1}$ for a period of ≈ 200 yr, while the post-pulse mass-loss rate is on average $1.6 \times 10^{-5} M_{\odot} \text{ yr}^{-1}$ during the last ≈ 2100 yr, and goes at least as low as $3.5 \times 10^{-6} M_{\odot} \text{ yr}^{-1}$ in recent years,
- the derived mass-loss rates imply that the decline in mass-loss rate after the pulse must have been significantly slower than previously assumed, and
- the amount of mass lost during a TP cycle may be significantly higher than previously assumed, strongly affecting the lifetime on the AGB, and the chemical evolution of the star, CSE, and ISM.

Additionally, we observe a higher-velocity component centred on the star for which we cannot find an obvious explanation. ALMA Cycle 2 observations at high-angular resolution will give a more complete picture of the spiral structure close to the star and include ACA observations to recover also the extended flux. The data will be essential for deriving a more accurate mass-loss rate evolution since the creation of the shell and will allow us to effectively constrain hydrodynamical models.

Acknowledgements. This paper makes use of ALMA data from project No. ADS/JAO.ALMA#2011.0.00131.S. ALMA is a partnership of ESO (representing its member states), the NSF (USA) and NINS (Japan), together with the NRC (Canada) and NSC and ASIAA (Taiwan), in cooperation with the Republic of Chile. The Joint ALMA Observatory is operated by ESO, AUI/NRAO and NAOJ. M.M. has received funding from the People Programme (Marie Curie Actions) of the EU's FP7 (FP7/2007-2013) under REA grant agreement No. 623898.11. W.V. acknowledges support from Marie Curie Career Integration Grant 321691 and ERC consolidator grant 614264. F.K. and M.B. acknowledge funding by the Austrian Science Fund FWF under project number P23586. M.B. further acknowledges funding through the ESO Director General's Discretionary Fund and the uni:docs fellowship of the University of Vienna. H.O. acknowledges financial support from the Swedish Research Council.

References

- Bladh, S., Höfner, S., Aringer, B., & Eriksson, K. 2015, *A&A*, **575**, A105
 Cox, N. L. J., Kerschbaum, F., van Marle, A.-J., et al. 2012, *A&A*, **537**, A35
 De Beck, E., Decin, L., de Koter, A., et al. 2010, *A&A*, **523**, A47
 González Delgado, D., Olofsson, H., Schwarz, H. E., Eriksson, K., & Gustafsson, B. 2001, *A&A*, **372**, 885
 González Delgado, D., Olofsson, H., Schwarz, H. E., et al. 2003, *A&A*, **399**, 1021
 Herwig, F. 2005, *ARA&A*, **43**, 435
 Izumiura, H., Waters, L. B. F. M., de Jong, T., et al. 1997, *A&A*, **323**, 449
 Izumiura, H., Ueta, T., Yamamura, I., et al. 2011, *A&A*, **528**, A29
 Karakas, A., & Lattanzio, J. C. 2007, *PASA*, **24**, 103
 Kerschbaum, F., Ladjal, D., Ottensamer, R., et al. 2010, *A&A*, **518**, L140
 Knapp, G. R., Pourbaix, D., Platais, I., & Jorissen, A. 2003, *A&A*, **403**, 993
 Lambert, D. L., Gustafsson, B., Eriksson, K., & Hinkle, K. H. 1986, *ApJS*, **62**, 373
 Lindqvist, M., Olofsson, H., Lucas, R., et al. 1999, *A&A*, **351**, L1
 Mackey, J., Mohamed, S., Gvaramadze, V. V., et al. 2014, *Nature*, **512**, 282
 Maercker, M., Olofsson, H., Eriksson, K., Gustafsson, B., & Schöier, F. L. 2010, *A&A*, **511**, A37

A&A 586, A5 (2016)

- Maercker, M., Mohamed, S., Vlemmings, W. H. T., et al. 2012, *Nature*, **490**, 232
- Maercker, M., Ramstedt, S., Leal-Ferreira, M. L., Olofsson, G., & Floren, H. G. 2014, *A&A*, **570**, A101
- Mamon, G. A., Glassgold, A. E., & Huggins, P. J. 1988, *ApJ*, **328**, 797
- Mattsson, L., Höfner, S., & Herwig, F. 2007, *A&A*, **470**, 339
- Mečina, M., Kerschbaum, F., Groenewegen, M. A. T., et al. 2014, *A&A*, **566**, A69
- Olofsson, H., Eriksson, K., & Gustafsson, B. 1988, *A&A*, **196**, L1
- Olofsson, H., Carlstrom, U., Eriksson, K., Gustafsson, B., & Willson, L. A. 1990, *A&A*, **230**, L13
- Olofsson, H., Eriksson, K., Gustafsson, B., & Carlstrom, U. 1993, *ApJS*, **87**, 267
- Olofsson, H., Bergman, P., Eriksson, K., & Gustafsson, B. 1996, *A&A*, **311**, 587
- Olofsson, H., Bergman, P., Lucas, R., et al. 2000, *A&A*, **353**, 583
- Olofsson, H., Maercker, M., Eriksson, K., Gustafsson, B., & Schöier, F. 2010, *A&A*, **515**, A27
- Olofsson, H., Bergman, P., & Lindqvist, M. 2015, *A&A*, **582**, A102
- Ramstedt, S., Maercker, M., Olofsson, G., Olofsson, H., & Schöier, F. L. 2011, *A&A*, **531**, A148
- Schneider, R., Valiante, R., Ventura, P., et al. 2014, *MNRAS*, **442**, 1440
- Schöier, F. L., & Olofsson, H. 2001, *A&A*, **368**, 969
- Schöier, F. L., Lindqvist, M., & Olofsson, H. 2005, *A&A*, **436**, 633
- Stanek, K. Z., Knapp, G. R., Young, K., & Phillips, T. G. 1995, *ApJS*, **100**, 169
- Steffen, M., & Schönberner, D. 2000, *A&A*, **357**, 180
- Steffen, M., Szczerba, R., & Schoenberner, D. 1998, *A&A*, **337**, 149
- van der Veen, W. E. C. J., & Habing, H. J. 1988, *A&A*, **194**, 125
- Vassilev, V., Meledin, D., Lapkin, I., et al. 2008, *A&A*, **490**, 1157
- Vassiliadis, E., & Wood, P. R. 1993, *ApJ*, **413**, 641
- Vlemmings, W. H. T., Maercker, M., Lindqvist, M., et al. 2013, *A&A*, **556**, L1
- Waters, L. B. F. M., Loup, C., Kester, D. J. M., Bontekoe, T. R., & de Jong, T. 1994, *A&A*, **281**, L1
- Whitelock, P. A., Feast, M. W., & van Leeuwen, F. 2008, *MNRAS*, **386**, 313

Chapter 10

Measuring the distance to R Sculptoris (Paper VII)

Title: *An independent distance estimate to the AGB star R Sculptoris*

Authors: M. Maercker, **M. Brunner**, M. Mecina, and E. De Beck

Year: 2017

Journal: Astronomy and Astrophysics

DOI: <https://doi.org/10.1051/0004-6361/201732057>

Credit: Maercker et al. 2018, A&A, 611, A102, reproduced with permission © ESO

In this publication an innovative observational method is used to improve the distance estimate to the carbon rich AGB star R Scl. The distance to astronomical object is mostly associated with a very high uncertainty, based on the imprecise measurement methods available. Even – or especially – for AGB stars well within our Galaxy, this can be a problem, because their physical properties might even aggravate the measurement uncertainties. On the other hand, an accurately known distance is required to determine intrinsic stellar properties such as the real luminosity of a star, which is an essential input to modelling strategies such as radiative transfer modelling. Therefore it is vital to determine distances to intensively studied objects carefully. We use the well known, semi-regular variability of R Scl to determine the delay of the luminosity maximum measured between the star and the shell to determine the linear radius of the shell. In combination with the accurately measured angular separation of the shell, we determine the linear distance to R Scl. The new results agree with previous measurements and calculations, but have a significantly smaller uncertainty.

Personal contribution: For this project I contributed on a fundamental level by assisting in one and executing another full observational set at the ESO NTT telescope in La Silla, Chile. I was actively involved in the development and technical setup of the observational method and also engaged in the scientific analysis of the results.

A&A 611, A102 (2018)
<https://doi.org/10.1051/0004-6361/201732057>
 © ESO 2018

**Astronomy
&
Astrophysics**

An independent distance estimate to the AGB star R Sculptoris

M. Maercker¹, M. Brunner², M. Mecina², and E. De Beck¹

¹ Department of Space, Earth and Environment, Chalmers University of Technology, Onsala Space Observatory, 43992 Onsala, Sweden

e-mail: maercker@chalmers.se

² Department of Astrophysics, University of Vienna, Türkenschanzstr. 17, 1180 Vienna, Austria

Received 6 October 2017 / Accepted 22 November 2017

ABSTRACT

Context. Distance measurements to astronomical objects are essential for understanding their intrinsic properties. For asymptotic giant branch (AGB) stars it is particularly difficult to derive accurate distance estimates. Period-luminosity relationships rely on the correlation of different physical properties of the stars, while the angular sizes and variability of AGB stars make parallax measurements inherently inaccurate. For the carbon AGB star R Sculptoris, the uncertain distance significantly affects the interpretation of observations regarding the evolution of the stellar mass loss during and after the most recent thermal pulse.

Aims. We aim to provide a new, independent measurement of the distance to R Sculptoris, reducing the absolute uncertainty of the distance estimate to this source.

Methods. R Scl is a semi-regular pulsating star, surrounded by a thin shell of dust and gas created during a thermal pulse ≈ 2000 years ago. The stellar light is scattered by the dust particles in the shell at a radius of $\approx 19''$. The variation in the stellar light affects the amount of dust-scattered light with the same period and amplitude ratio, but with a phase lag that depends on the absolute size of the shell. We measured this phase lag by observing the star R Scl and the dust-scattered stellar light from the shell at five epochs between June–December 2016. By observing in polarised light, we imaged the shell in the plane of the sky, removing any uncertainty due to geometrical effects. The phase lag gives the absolute size of the shell, and together with the angular size of the shell directly gives the absolute distance to R Sculptoris.

Results. We measured a phase lag between the stellar variations and the variation in the shell of 40.0 ± 4.0 days. The angular size of the shell is measured to be $19'.1 \pm 0'.7$. Combined, this gives an absolute distance to R Sculptoris of 361 ± 44 pc.

Conclusions. We independently determined the absolute distance to R Scl with an uncertainty of 12%. The estimated distance is consistent with previous estimates, but is one of the most accurate distances to the source to date. In the future, using the variations in polarised, dust-scattered stellar light, may offer an independent possibility to measure reliable distances to AGB stars.

Key words. stars: AGB and post-AGB – stars: distances – stars: evolution – techniques: polarimetric

1. Introduction

The asymptotic giant branch (AGB) star R Scl is a semiregular pulsating, carbon-rich star in the last stages of its life. During the AGB, low-mass stars shed most of their stellar envelopes in a strong, slow wind that enriches the interstellar medium with stellar processed material formed during thermal pulses (TPs). AGB stars contribute to the chemical evolution of galaxies and provide up to 70% of the total dust budget (Schneider et al. 2014).

Estimating correct distances to AGB stars is notoriously difficult. Parallax measurements of nearby AGB stars are hampered by the fact that the size of the star itself, typically a few AU in radius, is comparable to or larger than the parallax. Additionally, bright features on the surface of the stars and/or varying extinction due to the dust circumstellar envelope lead to extremely unreliable parallaxes. Even the *Gaia* mission, which will measure parallaxes to stars in the Milky Way with unprecedented precision, will suffer from this problem. Phase lag measurements from OH masers, on the other hand, are limited to sources with OH maser emission, that is oxygen-rich stars (e.g. van Langevelde et al. 1990). Groenewegen et al. (2012) determined the distance to the AGB star CW Leo through phase lag measurements in features observed in thermal emission with *Herschel*/SPIRE. Although this estimate provides

an independent measurement of the distance, it relies on an assumed geometry when deriving the absolute distance.

Studies of R Scl show that it is possible to observationally study the evolution of the mass-loss rate and expansion velocity during and after a thermal pulse (Maercker et al. 2012, 2016). However, the estimated distance is a major source of uncertainty. It affects the measured absolute sizes of the detached shell, and hence all evolutionary timescales, for example the total age of the shell. It further plays an important role in the dust and molecular radiative transfer, affecting the total measured dust and molecular masses.

We present observations with ESO Faint Object and Spectrometer Camera, v.2 (EFOSC2; Buzzoni et al. 1984) on the ESO/NTT telescope at La Silla observatory to image the detached shell of dust around the carbon AGB star R Scl. The goal of the observations is to determine the distance to R Scl by measuring the phase lag Δt between the stellar variability and the variability in the detached shell due to dust-scattered stellar light. The shell around R Scl was created during the brief increase in mass-loss rate and expansion velocity during a TP, and has a simple spherical geometry with a well-defined angular radius of $\approx 19''$ and a width of $\approx 2\text{--}3''$ (González Delgado et al. 2001, 2003; Olofsson et al. 2010; Maercker et al. 2014). In polarised light, the shell appears as a ring (González Delgado et al. 2003;

A&A 611, A102 (2018)

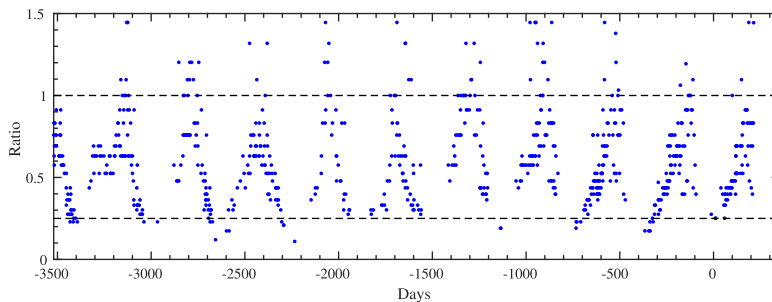


Fig. 1. Light curve of R Scl based on V-band observations from AAVSO and relative to a magnitude of $m_V = 6.5$ (i.e. ratio 1 in the figure). Observations are shown for the last ten years, relative to June 1st, 2016 (JD 2457540.5). The dashed lines indicate the minimum and maximum values corresponding to a min-to-max ratio of 0.25 (i.e. a magnitude amplitude of 0.75 magnitudes).

Maercker et al. 2014) with an absolute radius of $c \times \Delta t$, where c is the speed of light and Δt the measured phase lag (e.g. Sparks 1994). Combined with the angular size of the shell, this then directly gives an independent estimate of the distance to R Scl.

In Sect. 2 we present the EFOSC2 observations and describe the pulsation properties of R Scl. Section 3 presents the measured variability in R Scl and the detached shell, the resulting light curves, and the estimated distance. The results are discussed in Sect. 4, and related to previous measurements of the distance to R Scl. Conclusions and implications for future observations and other detached shell objects are presented in Sect. 5.

2. Observations

2.1. The light curve of R Scl

R Scl is a carbon-rich, semi-regular pulsating AGB star (Samus et al. 2009). Wittkowski et al. (2017) fit a sine curve to the last ten pulsation periods, and derive a period of 376 days. Their curve has an amplitude of 0.7 mag in V-band. However, looking at the most recent periods (Fig. 1), a magnitude amplitude in the pulsation of 0.75 mag appears more likely, corresponding to a min-to-max ratio in the brightness of 0.25. Using a sine curve to fit the pulsations reproduces the observed magnitudes reasonably well (Fig. 2). Variations in the light curve between different periods are difficult to predict, and the deviations from a sine curve lead to an added uncertainty in the estimated distance. We assume a sine curve with $P = 376$ days and an amplitude of 0.75 mag for fitting the observed light curve in R Scl and the shell.

2.2. EFOSC observations

In order to measure the variability in the star, R Scl was observed during five epochs between June 2016 and December 2016, that is sampling approximately half a pulsation period of R Scl (see Sect. 2.1). For each epoch, observations were scheduled to be carried out on three consecutive nights to ensure that useable data was obtained for each epoch. Given the sky conditions, we managed to observe useful data during one night in Epoch 1, and two nights in Epochs 2 and 4. Epochs 3 and 5 have the full three nights of measurements. EFOSC2 was used in direct imaging, polarisation, and coronagraphic mode, using the standard ESO V-band filter (V#641), a customised neutral density filter, and a customised V-band filter including an adhesive polarising film (Table 1). The pixel scale of EFOSC2 on the NTT is $0''.24 \times 0''.24$. The field of view is $4' \times 4'$.

In order to eliminate the uncertainty due to absolute flux calibration, we measured the variation of the star and the detached

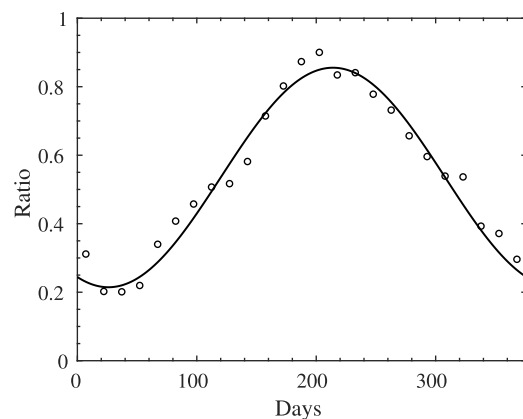


Fig. 2. Final ten periods folded and binned by 25 days (circles), together with a sinus function fit to the data. The sin-function has a period of 376 days and an amplitude of 0.75 magnitudes.

shell relative to four background stars spread throughout the field of view (Fig. 3). This reduces any uncertainty due to different pointings on the sky for observations of flux calibrators, decreasing the uncertainty in our distance estimate.

2.3. Direct observations of R Scl

We observed R Scl directly using the ESO V-band filter (V#641), centred at $\lambda_V = 547.6$ nm with a width $\Delta\lambda_V = 113.2$ nm. In V-band, R Scl has a peak magnitude of $m_V \approx 6.5$ (Fig. 1). In direct observations through broadband filters, EFOSC2 will saturate immediately for a star with this magnitude. In order to reduce the direct stellar light, we observed R Scl through a neutral density filter (ND3), reducing the brightness of the star by a factor of 10^3 . The ND3 filter was entered in the grism wheel, in front of the V#641 filter. Observations combining the ND3 and V#641 filters were used to measure the variation in R Scl directly.

2.4. Polarised observations of the detached shell

In order to accurately measure the phase lag to R Scl, it is necessary to know the correct angular size of the detached shell. This is best done in polarised dust-scattered stellar light. The stellar light is polarised as it is scattered by the dust grains in the detached shell, and the polarisation is strongest when the angle between the incident light and scattered light is 90 degrees. In polarised light the detached shell hence appears as

M. Maercker et al.: An independent distance estimate to the AGB star R Sculptoris

Table 1. Filters and coronagraphs used in the observations, central wavelengths (λ) and filter widths ($\Delta\lambda$).

Filter	λ [nm]	$\Delta\lambda$ [nm]	Comments
V-pol	550	88	including adhesive polarising film
V#641	548	113	–
ND3	–	–	neutral density filter, reduction by 1000
Coronagraph	–	–	8'' coronagraphic spot

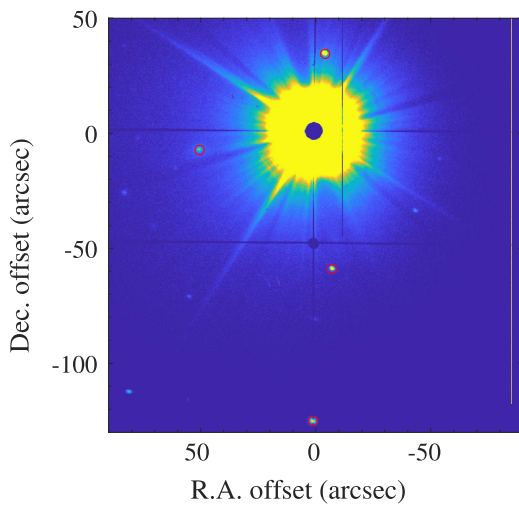


Fig. 3. 180'' \times 180'' part of the field observed with EFOSC2 in the V#641 filter. The background stars used to scale the brightness of R Scl and the shell are marked with red circles.

a ring, with a radius that corresponds to the angular size of the shell. This method has been used repeatedly to observe the detached shells around carbon stars (González Delgado et al. 2003; Maercker et al. 2010, 2014; Ramstedt et al. 2011). The intensity of the polarised light varies with the brightness of the central star, with the same period and the same ratio between minimum and maximum brightness. By using polarised light observations, we therefore can both accurately measure the angular size of the shell, as well as the variation in intensity in the shell.

Without the ND3 filter, the brightness of the central star requires the use of a coronagraph. EFOSC2 offers two coronagraphic spots with diameters of 4'' and 8''. The shell around R Scl has a radius of $\approx 20''$, and we used the larger of the two spots to effectively block the direct stellar light without affecting the measurements of the shell (Fig. 4).

The usual setup of EFOSC2 in polarimetric mode uses an imaging filter, a half-wave or quarter-wave plate, and a wollaston prism splitting the image into two strips 10'' or 20'' wide, with one polarisation each. All these elements together take up the available filter and grism wheels in EFOSC2, and it is not possible to use the coronagraphic spots in polarisation mode in any standard setup. Additionally, since the shell around R Scl has a radius of $\approx 20''$, the splitting of the image into narrow strips is

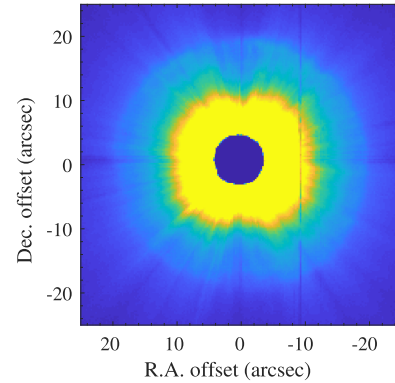


Fig. 4. All epochs of R Scl combined in total intensity.

not ideal, making it impossible to cover the entire shell in one image.

In order to avoid the problems with the standard polarisation setup, we used a customised V-band filter, with an adhesive, polarising film (V-pol). This made it possible to use EFOSC2 in standard coronagraphic mode using the half-wave plate, and with the V-pol filter inserted in the filter wheel. The observations provided polarised images at four polarisation angles (0°, 45°, 90°, and 135°). These could then be combined to produce images in total and polarised intensity (e.g. Maercker et al. 2010, 2014; Ramstedt et al. 2011). The polarised intensity images were used to measure the variation of the scattered light in the shell (Fig. 5).

2.5. Observing strategy

The variation in brightness of the star and shell is measured relative to background stars in the image. Ideally, the background stars are measured in the same image as the star and shell, reducing any uncertainties due to changing sky conditions. However, due to the strong contrast in brightness between R Scl, the background stars, and the shell, this was not possible. The use of the ND3 filter for the direct observations of R Scl makes it impossible to also detect the shell or background stars in the same image. In order to reduce the uncertainty due to varying sky conditions, the background stars were observed between observations in polarisation mode and observations with the ND3 filter. A typical sequence of observations is presented in Table 2.

Domeflats were observed during the day by the daytime operator. All images were then flatfielded, background subtracted, clipped, median combined, and scaled to 1 s to give coronagraphic images at each polarisation angle in the V-pol filter, coronagraphic images in total intensity in the V#641 filter, and direct images of R Scl in the V#641 + ND3 filters in counts s⁻¹.

Depending on the visibility of R Scl throughout the observing period, we usually managed to observe 2–3 sets per night. In some epochs not all sets could be used, due to varying weather conditions. Figures 4 and 5 show all epochs of R Scl combined in total intensity and polarised intensity, respectively.

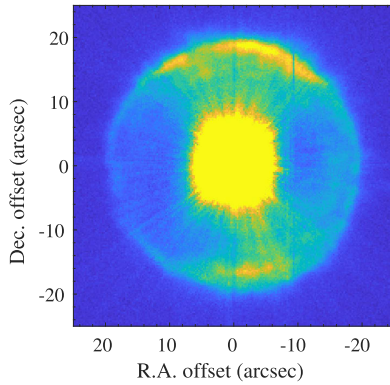
Flux standards were also observed for a basic consistency check, confirming the magnitude of R Scl. Since the absolute calibration is less certain than the relative calibration against background stars, and not required in this study, we do not present any absolute flux calibration.

A&A 611, A102 (2018)

Table 2. Typical observing sequence for R Scl.

Set	Filter	Coronagraph	Polarisation	Exposures	Product
1	V-pol	yes	yes	6 × 30 s	Polarised intensity from shell
2	V#641	yes	no	6 × 30 s	Total intensity from background stars
3	V#641 + ND3	no	no	3 × 15 s	Total intensity from R Scl

Notes. Exposure times are representative values typically used, but were adjusted based on the prevailing observing conditions. Per observing night two to three sequences were observed.

**Fig. 5.** All epochs of R Scl combined in polarised intensity.

3. Results

3.1. Brightness ratios

The brightness of the point sources (i.e. R Scl and the background stars) was measured through aperture photometry in the ND3 + V#641 and V#641 images. The apertures were 20 pixels and 15 pixels for R Scl and the background stars, respectively. The sky background was subtracted, defined by the average of counts in annuli of 25–35 pixels and 16–25 pixels for R Scl and the background stars, respectively. The resulting brightness is given in counts s⁻¹ for R Scl (I_{RScl}) and the background stars (I_{bg}), and the uncertainty for each measurement (σ_{RScl} and σ_{bg}) is determined by the rms in the background region. An average value was calculated for the four background stars. The results are presented in Table 3.

For the shell we created azimuthally averaged radial profiles of the polarised intensity for each observation set. The radial profiles have a spatial resolution of one pixel (i.e. 0''.24). Figure 6 shows an example of such a profile from December 2016. The peak at 18''.5 due to the detached shell can clearly be seen, and is consistent with previous, similar observations with PolCor (Maercker et al. 2014). The increase in emission at smaller radii is due to the remaining stellar psf, more recent mass loss, and additional scattering at the edge of the mask. Due to limb brightening in the shell, the true peak of the shell lies at a slightly larger radius than the peak in the radial profile. Figure 6 shows the theoretical profile expected from a thin shell assuming a Gaussian density distribution with $R = 19''.2$ and $FWHM = 2''.7$ (the profile only considers the shell, i.e. no emission from inside the shell due to more recent mass loss). The theoretical profile is calculated using an analytical formula for dust scattering, assuming isotropic scattering by the dust grains (Heney & Greenstein 1941; Draine 2003; Maercker et al. 2010).

The light curve of the shell is measured by fitting a theoretical profile to the observed radial profiles, adjusting the radius and peak intensity I_{shell} to determine two parameters: the peak intensity in the radial profile and the radius of the Gaussian distribution. This method has been used previously for R Scl and other detached shell sources (Maercker et al. 2010, 2014). We note that the shell is not perfectly symmetric. In particular, there is a flattening of the shell in the south. This has been observed in previous observations in dust scattered light, and is consistent with observations in CO line emission (Maercker et al. 2012, 2014, 2016). The asymmetric structures mainly affect the measured width of the shell, and not the average radius. Excluding the flattened feature from the average profile increases the measured radius by $\approx 0''.1$, significantly less than the assumed error in the measured average radius (Sect. 4.1, and Maercker et al. 2014). The error in the peak brightness σ_{shell} is determined by the rms value in that radial bin (defined as $\sigma_{\text{lm}} / \sqrt{N_{\text{bin}}}$, where N_{bin} is the number of bins included in the average value of that radial bin and σ_{lm} is the overall rms across the image). The measured peak intensities with uncertainties and radii are presented in Table 3.

For each set of observations the ratio between measurements was formed

$$r_{\text{RScl}} = \frac{I_{\text{RScl}}}{I_{\text{bg}}}, \quad (1)$$

and the uncertainty in the ratio was determined through standard error propagation:

$$\sigma_r = r_{\text{RScl}} \times \sqrt{\frac{\sigma_{\text{RScl}}^2}{I_{\text{RScl}}^2} + \frac{\sigma_{\text{bg}}^2}{I_{\text{bg}}^2}}. \quad (2)$$

And the equivalent was done for I_{shell} . The ratios of each epoch are averaged to give the final ratios R_{RScl} and R_{shell} (with respective errors) for the star and the shell, respectively.

3.2. Light curve fitting

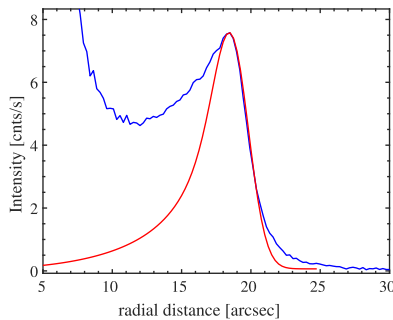
In order to determine the phase lag between the stellar pulsations and the brightness of the shell, we fit a sine curve to the observed data points. The sine curve is fixed to have a period of 376 days, and minimum to maximum ratio of 0.25. This leaves two free parameters when fitting the sine curve to the observations: a shift in days (i.e. the x -direction), and a shift in the average ratio (i.e. the y -direction). The difference in shift in days between the light curves fit to R_{RScl} and R_{shell} gives the phase lag, and hence the absolute size of the shell. Together with the angular size of the shell, this gives the distance to R Scl.

Figure 7 shows the observed light curves for R Scl and the shell. The sources of uncertainties in the measured ratios are discussed in more detail in Sect. 4.1.

M. Maercker et al.: An independent distance estimate to the AGB star R Sculptoris

Table 3. Observations of R Scl, four background stars, the polarised shell, and the shell radius.

Day	Set	R Scl		BG-S1		BG-S2		BG-E		BG-N		BG-AVG		Shell		Radius ["]
		I_{RScl}	σ_{RScl}	$I_{\text{bg-S1}}$	$\sigma_{\text{bg-S1}}$	$I_{\text{bg-S2}}$	$\sigma_{\text{bg-S2}}$	$I_{\text{bg-E}}$	$\sigma_{\text{bg-E}}$	$I_{\text{bg-N}}$	$\sigma_{\text{bg-N}}$	I_{bg}	σ_{bg}	I_{shell}	σ_{shell}	
Epoch 1 – June																
16	set 2	41 622	9.0	1911.9	602.3	1338.4	611.9	1002.2	637.7	3777.3	643.6	2007	312	1.5	0.04	19.0
<i>Ratio</i>		$R_{\text{RScl}} = 20.7 \pm 3.2$			$R_{\text{shell}} = 0.75 \pm 0.11$											
Epoch 2 – July																
46	set 1	50 555	13.2	1593.8	43.6	1269.2	24.3	829.8	39.4	2892.3	97.2	1646	29	1.8	0.06	19.0
	set 2	60 003	14.0	1960.5	27.4	1452.4	14.9	978.9	31.0	4008.3	92.1	2100	26	1.5	0.05	19.5
48	set 1	58 118	15.5	1375.9	63.6	1254.5	36.4	872.0	44.9	3664.4	190.5	1792	52	1.5	0.10	19.0
	set 2	59 887	14.8	1705.9	45.2	1378.8	21.9	912.3	42.3	3918.7	145.6	1979	40	1.6	0.07	19.0
	set 3	61 277	12.9	1724.5	39.5	1434.5	19.9	911.4	43.6	4365.8	172.3	2109	46	1.9	0.08	19.0
<i>Ratio</i>		$R_{\text{RScl}} = 30.1 \pm 0.3$			$R_{\text{shell}} = 0.88 \pm 0.02$											
Epoch 3 – September I																
96	set 1	95 159	23.7	2232.4	27.2	1540.5	11.8	903.9	54.4	5374.8	132.7	2513	37	4.4	0.10	19.1
	set 2	95 814	27.7	2098.7	27.6	1444.7	12.1	893.8	37.8	4345.2	136.0	2196	36	4.4	0.10	19.1
97	set 1	99 705	23.5	2161.0	33.8	1567.8	18.0	965.5	41.6	4633.3	143.6	2332	39	4.4	0.09	19.2
	set 2	98 577	22.2	2184.2	28.2	1369.9	13.7	946.6	45.4	3345.6	121.3	1962	33	4.5	0.11	19.2
98	set 1	98 347	34.6	2158.0	35.1	1546.2	17.6	944.4	37.3	4511.4	128.5	2290	35	4.5	0.10	19.2
	set 2	98 382	32.0	2206.6	27.5	1385.2	12.3	1047.7	41.2	4011.0	115.4	2163	32	4.7	0.11	19.1
<i>Ratio</i>		$R_{\text{RScl}} = 43.8 \pm 0.3$			$R_{\text{shell}} = 2.01 \pm 0.02$											
Epoch 4 – September II																
107	set 1	103 100	31.7	1535.9	104.5	1344.4	48.0	911.2	82.5	3524.7	250.7	1829	72	4.4	0.12	19.1
	set 2	102 010	31.7	1722.3	79.0	1448.7	38.3	813.2	80.0	3305.5	252.2	1822	70	4.6	0.13	19.0
	set 3	100 470	28.3	1562.2	85.0	1448.9	29.5	1031.1	60.3	4349.7	287.5	2098	77	4.6	0.12	19.0
108	set 1	101 510	36.0	1901.2	79.0	1509.1	37.7	1053.3	71.9	3653.6	201.7	2029	58	4.7	0.13	19.0
	set 2	103 140	41.3	1943.3	75.1	1565.3	33.8	891.8	67.7	4892.4	219.1	2323	61	4.9	0.12	19.1
	set 3	102 920	47.9	1990.6	64.7	1491.1	29.9	908.8	70.4	3209.8	196.1	1900	55	5.0	0.13	19.1
	set 4	98 752	54.2	1855.4	74.2	1518.3	28.4	1111.9	55.4	4435.4	246.7	2230	66	4.7	0.13	19.1
<i>Ratio</i>		$R_{\text{RScl}} = 50.8 \pm 0.7$			$R_{\text{shell}} = 2.33 \pm 0.04$											
Epoch 5 – December																
195	set 1	125 730	43.8	1680.1	65.8	1235.0	29.9	820.5	68.3	2892.6	160.1	1657	47	7.7	0.16	19.1
	set 2	117 520	46.3	1483.4	85.7	1290.7	28.4	1028.3	52.3	3935.4	203.7	1934	57	7.5	0.16	19.2
196	set 1	119 830	29.9	1807.3	52.6	1241.1	18.9	911.9	50.1	3778.4	163.3	1935	45	7.6	0.15	19.2
	set 2	113 920	28.5	1663.1	69.5	1282.3	22.3	805.3	50.4	4101.3	187.8	1963	52	7.4	0.15	19.2
197	set 1	122 550	42.3	2128.5	43.5	1258.3	18.1	745.0	57.2	2517.8	150.2	1662	42	8.2	0.16	19.2
	set 2	116 960	40.9	1616.1	52.6	1328.2	20.6	738.9	49.5	4239.7	180.8	1981	49	7.6	0.15	19.2
<i>Ratio</i>		$R_{\text{RScl}} = 64.9 \pm 0.7$			$R_{\text{shell}} = 4.16 \pm 0.06$											

Notes. The measurements are given in counts s⁻¹. The days are relative to June 1, 2016 (JD 2457540.5).**Fig. 6.** Azimuthally averaged radial profile of the observed polarised intensity from the second set of observations on December 15, 2016 (blue). The expected radial profile from a shell with $R = 19.2''$ and $\text{FWHM} = 2''.7$ (red).

In order to fit the sine curve to the data points, we created grids of sine curves varying the days and average ratios, and determine the χ^2 -value for each fit:

$$\chi^2 = \frac{1}{N_i} \times \sum \frac{(R_i - F_i)^2}{\sigma_{R,i}}, \quad (3)$$

where N_i is the number of points, R_i are the observed ratios, F_i the model value in point i , and $\sigma_{R,i}$ the uncertainty in the observed ratio. The resulting χ^2 -maps are shown in Fig. 8. The uncertainty in the shift in days for the light curve of R Scl and the shell are ± 2.6 and ± 3.1 days, respectively. The resulting shift in the light curves between R Scl and the shell is 40.0 ± 4.0 days, corresponding to an absolute distance between the star and shell of 6900 ± 690 AU. The average angular size of the measured peak is $19''.1 \pm 0''.1$. However, comparing to earlier measurements of the shell radius (e.g. Maercker et al. 2014, and references therein), the uncertainty in the shell radius is likely larger. Here we adopt the uncertainty of $\pm 0''.7$ from Maercker et al. (2014). This leads to a distance to R Scl of 361 pc, with a measurement uncertainty of ± 39 pc. The absolute uncertainty is likely higher (Sect. 4.1).

4. Discussion

4.1. Observational uncertainties

The uncertainty in the measured fluxes for R Scl in the ND3 + V#641 filter combination is generally $\approx 0.05\%$. The uncertainty in the measured flux averaged between the four background stars in the V#641 filter is $\approx 2\%$. With the exception of the first epoch (June 17, 2016) the uncertainty in the ratio R_{RScl} is

A&A 611, A102 (2018)

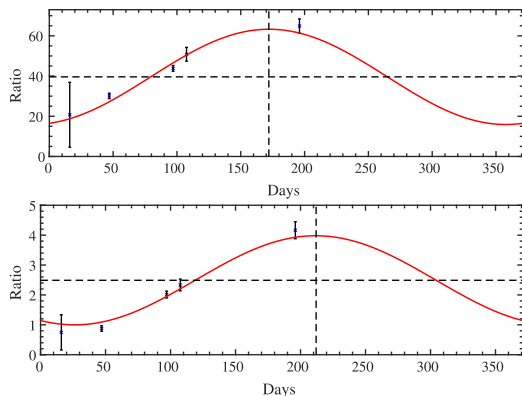


Fig. 7. Observed light curves for R Scl (*top*) and the detached shell (*bottom*). The days are relative to June 1, 2016 (JD 2457540.5). The intensity of R Scl is reduced by a factor 1000 by the ND3 filter. The values of the ratio for the shell however were multiplied by a factor 1000 for the sake of readability. For *both panels* the errors were multiplied by five for visualisation. The dashed lines show the best-fit ratio and peak of the light curve for this period.

$\approx 1\%$ for each epoch. The one night of observations in Epoch 1 still had unstable weather, leaving us with only one set of useful observations, and an uncertainty of $\approx 15\%$ for this measurement. The uncertainty in the measured peak intensities in polarised light of the shell is $\approx 2\text{--}4\%$. The error in the measured ratios R_{shell} is $\approx 2\%$.

In principle it would have been possible to measure the brightness of the background stars directly in the total intensity images of the V-pol observations (making them simultaneous with the polarised observations). However, the transmission of the V-pol filter with the polarising film applied was $\approx 50\%$ of the V#641 filter, reducing the signal-to-noise of these observations and hence increasing the relative error to $\sim 10\%$. We therefore chose to use the V#641 observations of the background stars also for the ratios with the shell emission.

The total error in the distance due to these observational uncertainties lies at 11% . Additional uncertainties that can affect the distance estimate are the assumed pulsation period and amplitude. Decreasing and increasing the pulsation period by 5 days changes the estimated distance to 357 pc and 368 pc, respectively. A change in amplitude in the fitted sine curves to 0.7 mag and 0.8 mag gives best-fit distances of 340 pc and 380 pc, respectively. The true uncertainty in the distance is therefore likely larger than 39 pc. Using the range of possible distances due to changes in the period and amplitude as an indication, we add uncertainties of ± 5 pc and ± 20 pc, respectively. Adding these uncertainties in quadrature, the total uncertainty in the estimated distance then becomes 44 pc.

The fractional uncertainty in the distance to R Scl (12%) is comparable to the uncertainty in the distance to CW Leo, also determined through phase lag measurements (123 ± 14 pc, that is 11% ; Groenewegen et al. 2012), with the difference that our method does not have to make any assumptions on the geometry of the source. Adding more epochs to the observations of R Scl may somewhat reduce the fractional uncertainty. Adding two more observations approximately one year after our observations, and assuming similar observational uncertainties, reduces the fractional uncertainty to $\approx 8\%$. In particular, the effect of

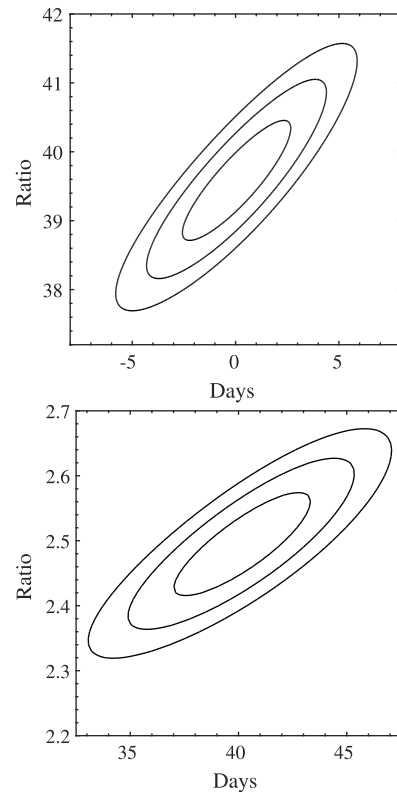


Fig. 8. χ^2 maps from sine curves fit to the observed ratios for R Scl (*top*) and the shell (*bottom*). The shift in days is given relative to the best-fit model for R Scl.

the uncertainty in the amplitude of the variation is reduced to ± 10 pc.

An unfortunate fact is that we had to use a neutral density filter to observe R Scl directly, and that the total intensity observations through the V-pol filter had a relatively large error compared to the V#641 observations. Ideally one would measure R Scl directly, the polarised shell, and the background stars in the same exposure.

When observing the polarised, dust-scattered stellar light around AGB stars with the PolCor instrument (Ramstedt et al. 2011; Maercker et al. 2014), the coronagraphic spots were neutral density spots that would reduce the direct stellar light to different degrees. In PolCor observations this allows for a careful placement of the star behind the mask, reducing the artefacts in the images. In these observations, one cycle of all polarisations angles would allow us to create images in polarised and total intensity that would contain the direct star light, the shell, and the background stars from the same exposures. Unfortunately the field of view of PolCor is too small to contain any of the background stars used here.

4.2. Comparison to other distance estimates to R Scl

Table 4 presents earlier estimates of the distance to R Scl, mainly based on (P - L) relationships. All measurements, with the exception of the HIPPARCOS distance, lie within our estimated

M. Maercker et al.: An independent distance estimate to the AGB star R Sculptoris

Table 4. Distance estimates to R Scl from the literature compared to our estimate.

D [pc]	σD [pc]	Method	Reference
360	–	($P-L$) relationship for Mira variables	Groenewegen & Whitelock (1996)
370	–70/+100	($P-L$) relationship for SR variables	Knapp et al. (2003)
340	–70/+100	($P-L$) relationship for Mira variables	Knapp et al. (2003)
266	–45/+66	revised HIPPARCOS	van Leeuwen (2007)
370	–	($P-L$) relationship for Mira variables	Whitelock et al. (2008)
350	–50/+50	SED fitting to hydrostatic atmosphere models	Sacuto et al. (2011)
361	–44/+ 44	Phase lag measurements in the detached shell	This paper

distance of $361 \text{ pc} \pm 44 \text{ pc}$, including the estimate based on spectral energy distribution (SED) fitting to hydrostatic atmosphere models by Sacuto et al. (2011). Interestingly, the HIPPARCOS distance is the only one that is not consistent with any of the other measurements, but has the smallest uncertainty. The difficulty with measuring distances to AGB stars using parallaxes is that the angular size of the star is comparable to the parallax itself. For a diameter of 2 AU, the stellar disk of R Scl would have an angular size of $\approx 5 \text{ mas}$ at the distance of 380 pc, while the revised parallax is only 3.76 mas. Time-variable features on the stellar disk, and/or obscuration due to the dusty circumstellar envelope, might easily disturb the measured parallax. Most recently, the stellar disk of R Scl has been observed and shown to exhibit such asymmetric features (Wittkowski et al. 2017).

In general, ($P-L$) relationships give relatively large errors, and rely on empirical relationships for large samples of sources. This increases the uncertainty for individual cases. Fitting the SED to hydrostatic models of the atmosphere treats R Scl individually. However, this method relies on assumptions about the stellar atmosphere, and the underlying model uncertainties.

Our distance estimate is completely independent from the methods used by previous estimates. Further, the method itself does not make very critical or complicated assumptions, and is very straight-forward to measure and apply. The uncertainty of 12% is one of the lowest uncertainties measured, along with the distance determined through hydrostatic atmosphere models (Sacuto et al. 2011).

5. Conclusions

We have provided an independent distance estimate to the carbon AGB star R Scl. At $361 \text{ pc} \pm 44 \text{ pc}$, our distance is consistent with most previous distance estimates, however with a lower uncertainty. The absolute size of the detached shell around R Scl was measured by determining the phase lag between brightness variations in the star due to the stellar pulsations to the variation in brightness in the detached shell due to dust-scattered stellar light. By observing the shell in polarised light, geometrical uncertainties are eliminated, as the scattering will polarise the light preferentially in the plane of the sky, causing the detached shell to appear as a well-defined ring in the polarised images. By measuring the variation in intensity relative to background stars in the same field of view, calibration uncertainties are also removed. Except for the pulsation period and amplitude, the method does not make any assumptions regarding the characteristics of the star. As such, it provides one of the most reliable distance estimates to date. The agreement between our estimated distance, and the distance estimate through SED fitting

of hydrostatic atmosphere models (Sacuto et al. 2011), adds to the reliability of both methods.

With this distance in hand, one of the largest uncertainties in models of the shell around R Scl is reduced. The assumed distance to R Scl affects all absolute sizes and time scales derived from the observations of the detached shell (Maercker et al. 2012, 2016). Only with a correct distance is it possible to properly constrain hydrodynamical models of the evolution of the shell, and hence its connection to thermal pulses and the evolution of the wind throughout the thermal-pulse cycle.

We are currently developing a new version of the PolCor instrument with a larger field of view, and an improved image quality. When finished, it will be possible to measure the star, shell, and background stars in the same exposures, reducing the error even further.

Besides R Scl, there are six additional detached shell sources known (Schöier et al. 2005; Ramstedt et al. 2011; Maercker et al. 2014), with shell radii ranging between $\approx 7''$ and $60''$. This method could be applied to these sources as well.

If the new PolCor instrument meets the expected improved image quality, it may also be possible to use this method to determine the distance to regular dusty envelopes around AGB stars. Also here the polarised observations give the distribution of the dust in the plane of the sky, reducing any confusion due to geometrical effects. As long as a dusty feature can be clearly identified, the variation in intensity compared to the stellar pulsations will give the absolute distance of the dusty feature to the star, and hence the distance to the star from Earth. The results for R Scl indicate that, together with SED fitting of atmospheric models, phase lag measurements in dust-scattered stellar light might provide one of the most reliable distance estimates to individual AGB stars.

Acknowledgements. M. Maercker acknowledges support from the Swedish Research Council under grant number 2016-03402. M.B. acknowledges funding through the uni:docs fellowship of the University of Vienna, and funding by the Austrian Science Fund FWF under project number P23586. E.D.B. acknowledges funding by the Swedish National Spaceboard. We acknowledge with thanks the variable star observations from the AAVSO International Database contributed by observers worldwide and used in this research.

References

- Buzzoni, B., Delabre, B., Dekker, H., et al. 1984, *The Messenger*, **38**, 9
- Draine, B. T. 2003, *ApJ*, **598**, 1017
- González Delgado, D., Olofsson, H., Schwarz, H. E., Eriksson, K., & Gustafsson, B. 2001, *A&A*, **372**, 885
- González Delgado, D., Olofsson, H., Schwarz, H. E., et al. 2003, *A&A*, **399**, 1021
- Groenewegen, M. A. T., & Whitelock, P. A. 1996, *MNRAS*, **281**, 1347

A&A 611, A102 (2018)

- Groenewegen, M. A. T., Barlow, M. J., Blommaert, J. A. D. L., et al. 2012, [A&A](#), **543**, L8
- Heney, L. G., & Greenstein, J. L. 1941, [ApJ](#), **93**, 70
- Knapp, G. R., Pourbaix, D., Platais, I., & Jorissen, A. 2003, [A&A](#), **403**, 993
- Maercker, M., Olofsson, H., Eriksson, K., Gustafsson, B., & Schöier, F. L. 2010, [A&A](#), **511**, A37
- Maercker, M., Mohamed, S., Vlemmings, W. H. T., et al. 2012, [Nature](#), **490**, 232
- Maercker, M., Ramstedt, S., Leal-Ferreira, M. L., Olofsson, G., & Floren, H. G. 2014, [A&A](#), **570**, A101
- Maercker, M., Vlemmings, W. H. T., Brunner, M., et al. 2016, [A&A](#), **586**, A5
- Olofsson, H., Maercker, M., Eriksson, K., Gustafsson, B., & Schöier, F. 2010, [A&A](#), **515**, A27
- Ramstedt, S., Maercker, M., Olofsson, G., Olofsson, H., & Schöier, F. L. 2011, [A&A](#), **531**, A148
- Sacuto, S., Aringer, B., Hron, J., et al. 2011, [A&A](#), **525**, A42
- Samus, N. N., Kazarovets, E. V., Pastukhova, E. N., Tsvetkova, T. M., & Durevich, O. V. 2009, [PASP](#), **121**, 1378
- Schneider, R., Valiante, R., Ventura, P., et al. 2014, [MNRAS](#), **442**, 1440
- Schöier, F. L., Lindqvist, M., & Olofsson, H. 2005, [A&A](#), **436**, 633
- Sparks, W. B. 1994, [ApJ](#), **433**, 19
- van Langevelde, H. J., van der Heiden, R., & van Schooneveld, C. 1990, [A&A](#), **239**, 193
- van Leeuwen, F. 2007, [A&A](#), **474**, 653
- Whitelock, P. A., Feast, M. W., & van Leeuwen, F. 2008, [MNRAS](#), **386**, 313
- Wittkowski, M., Hofmann, K.-H., Höfner, S., et al. 2017, [A&A](#), **601**, A3

Part IV

Conclusions and outlook

Chapter 11

Conclusions

This dissertation studied circumstellar gas and dust structures of CSEs around AGB stars of different evolutionary stages and during different episodes of mass-loss variation. The presented publications cover four different AGB stars from S-type to C-type stars and aim to resolve their CSEs with high angular and spectral resolution, observed with the world's most powerful submillimeter interferometer ALMA. Each observation represents a snapshot of the mass-loss history and can be seen as puzzle piece of the larger picture of stellar evolution.

All findings of the presented publications are in accordance with the common evolutionary theory of AGB stars evolving from M- to S- to C-type, and thermal pulses driving this evolution through the dredge-up of carbon. For the S-type star W Aql, this is underlined by the coincidental detection of carbon- and oxygen-rich molecules in the CSE, which further supports that S-type stars represent a transition stage between oxygen- and carbon-rich AGB stars. The derived abundances of the molecular species of CS, H¹³CN, SiO, and SiS, as well as associated isotopic ratios, are in accordance with previous studies. W Aql is in a confirmed binary system and large-scale maps of the CO emission have shown that there is significant wind-binary interaction, resulting in a spiral-like structure. We find that a deviation from symmetry is also visible in the compact parts of the molecular emission of the above listed molecules.

Moving on in the evolutionary sequence of increasing C/O ratio with time, the high spatial resolution observations of the molecular CSE around the carbon-rich AGB star TX Psc with a C/O ratio of just above 1, reveal a detached shell, which is linked to the presence of thermal pulses. Not only have all previously detected detached shells been found around stars with significantly higher C/O ratios, but also the geometry of the detached shell around TX Psc is remarkable. Instead of a spherically symmetric detached shell, the shell around TX Psc is of elliptical shape, with an axis ratio of 1.3 between the semi-major and semi-minor axis. The present-day wind follows the same ellipticity. The most likely explanation for this ellipticity is the presence of stellar rotation of the order of 2 km/s, which is significantly above the theoretical rotation velocity of solitary AGB stars. We come to the conclusion that a secondary object of the order of the mass of a brown dwarf has to be present in the close vicinity of TX Psc to be able to transfer enough angular momentum to the star for such a rotation rate. The size of the detached shell of TX Psc and the expansion velocities lead to an estimated age of the shell of roughly 2600 years, which is on the same order of magnitude as other detached shells. Nevertheless, the irregular structure of the shell itself, with many clumps and filaments, hints at a slightly different formation history as the more regular and spherical shells of R Scl and U Ant. One possible theory for this is that as subsequent thermal pulses shape the CSE, the density increases, and thermal pulses later in the path of stellar evolution will run into denser media, where they are more efficiently shaped into smoother structures. This would explain why the shell around TX Psc, which is most likely experiencing one of its

first thermal pulses, making it a carbon-rich AGB star, is more “fluffy” than the shells around more evolved carbon stars such as R Scl and U Ant.

The CSE and in particular the detached shell around the carbon star R Scl has been previously studied in high resolution CO emission and revealed a very symmetrical and spherical detached shell, which is connected to the present-day wind by a spiral, introduced by a binary companion. In the course of this thesis, we modelled the dusty counterpart of the molecular detached shell to calculate the dust shell mass with respect to different dust properties. We come to the conclusion that the geometry of the dust grains has the strongest influence on the total dust mass in the shell around R Scl. Typical grain geometries used in models are solid spheres, hollow spheres, elliptical grains, as well as fluffy and irregularly shaped grains. Dust parameters such as the grain size, addition of chemical elements apart from amorphous carbon, and differently calculated and measured opacities, do not influence the total dust shell mass significantly, in comparison to the grain geometry. We also detected an excess in submillimeter emission in the SED of R Scl, which cannot be explained by our models. Similar excess emission has been observed for the detached shell sources U Ant, DR Ser, and V644 Sco (Maercker et al. 2018), hinting at a common cause for this submillimeter excess, which has yet to be studied in detail.

The star with the highest C/O ratio, studied in the sample of this thesis, is U Ant. The detached shell around U Ant is spherically symmetric, but a sort of double-shell structure is seen for the first time. This could either hint to dynamic instabilities during the formation of the shell, or the presence of a reverse shock.

For all stars in the observed sample, the dust and gas distributions seem to be co-spatial, with the exception of additional shell-like structures seen in dust emission for U Ant, where no molecular counterparts have been detected. Additionally, the dust emission in the detached shell around U Ant is significantly brighter in one quadrant of the shell, and this brightness in dust emission is correlated with a weakness in molecular CO emission. This partial anti-correlation is not yet explained sufficiently.

Overall, this thesis provides individual snapshots of the geometry and mass-loss history during AGB stellar evolution, which can be used to investigate the evolutionary sequence of these stars. It also serves as base for the future investigation of similar AGB stars, adding more and more pieces to the puzzle of AGB mass-loss evolution.

Chapter 12

Outlook

The availability of ALMA as high-resolution interferometer has been a huge booster for the study of AGB CSEs in the last few years, and still only a relatively small sample of AGB stars has been intensely observed with ALMA. The future proposing cycles will undoubtedly bring forth more and more detailed observations of these objects, allowing us to slowly build up a larger sample of CSEs, which have been observed with the same sensitivity, resolution, and image quality. Until now, there is probably a bias towards observing the “odd” objects, which are targets that are easier to justify. Despite the high sensitivity of ALMA, we are still far away from a statistically relevant sample of AGB stars observed at this quality, due to the long observing times needed to cover extended CSEs in mosaic observations. Fortunately, a very large sample of AGB and CSEs stars has been observed and classified with *Herschel*, and this sample now serves as a basis of selection for further high-resolution observations. The AGB community is also trying to push a larger survey of AGB CSEs with intermediate resolution, using only the compact ACA.

In the near future, it will become more and more important to understand and model which small-scale structures that we observe in CSEs are actually intrinsically formed by the AGB star itself, by the interaction with the surrounding medium, or by dynamical instabilities within the stellar wind, and which structures only arise due to the interaction with companions. Only then, fully consistent models can be developed to derive significant mass-loss rates and return rates to the cosmic cycle of matter.

losing through you
what seemed myself, i find
selves unimaginably mine.

E.E. Cummings

Acknowledgements / Danksagung

This is finally it. The point to step back and take a look at all the accomplishments, struggles, and experiences throughout the last 10 years, leading up to this point. And the point to realise that none of this would have happened without every single one of you who supported me, motivated me, built me up when I was down, and had an open ear for my problems along the way. As everything in life, also my studies were filled with times of pure joy and fun, regularly followed by periods of frustration and despair – but luckily I was never left alone during the more exhausting parts of this journey. The last 10 years have shaped my personality, mind, and perception of the world like nothing else, and although I would have to lie if I'd say I regret nothing, I am extremely thankful that I have ended up where I am right now. A tiny bit wiser, and a lot richer in experience – professionally and personally.

Science requires networking, collaborations, and teamwork – and I'm thankful for all the opportunities and paths that have opened up to me during my work in the AGB working group at the department for astrophysics of the University of Vienna. Thank you, Franz, for supervising me, connecting me with the scientific community, and introducing me to ALMA early on in my studies, which sparked my interest to dive deeper into the space of this research topic. Thanks also to everyone else in the working group, still here or already gone, who enriched my work-life in one way or another. Thanks also especially to Marko, who was stuck in an office with me until the very end, and who had to regularly endure my outbursts of frustration or complete randomness. For refreshingly random and weird conversations I also want to thank Philip, Michi, Andi, Roli, Gioia, Birgit, Ruth, and everyone else who has taken my mind off work sometimes when it was necessary to just fool around for a bit.

My deepest gratitude goes to everyone in the evolved stars working group at the Onsala Space Observatory, Sweden, who reminded me over and over again how much fun it can be to do science, and regularly helped me find my motivation and productivity to finish this thesis. Matthias, thank you so much for acting like a second supervisor and letting me in on all the cool projects that you have been working on in the last years! My visits to Onsala were always extremely rewarding, and especially the observing runs at La Silla reminded me of why I started to study astronomy in the first place. This definitely was the cherry on the cake of my PhD – thanks for that opportunity!

A big thank you also goes to Liz, who supervised me during my short stay at ESO, Garching, which was another very rewarding experience in my career.

Now to my friends – old (I know, we all refuse to be old...) and new – who were there for me, cared for me, distracted me from my work when I needed it most, and have not been mad at me for neglecting them a bit when time was short on my hands. Thank you for constantly reminding me that what I do is actually cool, even when it felt quite insignificant to me. Thanks for being there, and thanks for being you. All of you enrich my life and inspire me to be my best self. There is no other way to thank you than by saying I love you all, and you deserve the biggest of all hugs (come and redeem that next time around).

There have been a couple of close companions in my life throughout the last years, who have all helped me to become the person that I am today. You have lifted me up, kicked my

ass when it was needed, told me everything would be alright when it sometimes wasn't, and made sure that I always had a safe space to retreat to, when I was fed up with the world. Thank you for sharing a part of my life with me and making it brighter and richer by your presence. You will stay in my heart.

The last part of this acknowledgements is reserved for the bunch of people that have had to stick with me for all my 29 years of life: my family. My deepest thanks goes to my parents for encouraging me to explore the world and giving me all the freedom to develop a mind of my own. Thank you for making my studies possible and not questioning my weird career choice too much. Thank you, Mama, for always being on my side, being there for me, and trusting in what I do. Thank you, Papa, for keeping in touch even during the busy times of our lives, and always sharing a funny anecdote. Dear brother, thank you for being awesome. I appreciate it a lot that we do so many fun things together and have not lost touch. A big thank you also goes to my amazing aunt, Margit, who is so much fun to be around and always reminds me of the good things in life. Thank you, Großmutter, for supporting me and always feeding me with delicious food or keeping my mind sharp with a round of Scrabble (or two). Thank you, Großvater, for sharing your interests in physics with me, even though I was a bit too young to appreciate it properly at that time. And last but not least, thank you, Omi, for all the fun hours in Unterach, either playing cards, eating sweets, or just fooling around before going to bed (way too late). The stars will always be brighter, lying there on the warm terrace at summertime.

I would not be here, finishing my dissertation as I write these last words, without all of you! Thank you for believing in me, even when I didn't. You are my stars.

Zusammenfassung

Am Ende ihres Lebens befinden sich Sterne mit Massen zwischen ungefähr 0.8 und 8 Sonnenmassen (M_{\odot}) in der sogenannten Asymptotic Giant Branch (AGB) Phase, in der sie starke Sternwinde entwickeln. AGB Sterne tragen maßgeblich zur Produktion von chemischen Elementen bei, die im Sterninneren und besonders in Wasserstoff- und Helium-Schalen durch Nukleosyntheseprozesse gebildet werden. Die dadurch gebildeten und schon bestehenden Elemente können im Weiteren in den kühlen Schichten der Sternatmosphäre Moleküle bilden. Die Sternwinde werden durch Strahlungsdruck auf Staubteilchen in der Sternatmosphäre, die sich in dichten und kühlen Regionen aus Molekülen bilden, angetrieben. Als Folge bilden sich enorm große zirkumstellare Hüllen (CSEs) aus molekularem Gas und Staub rund um AGB Sterne. Die Form der Sternwinde und CSEs kann durch zeitliche Variationen der Massenverlustrate, die Interaktion des Sternwindes mit dem umgebenden Medium oder früheren Winden, oder der Gravitations-Wechselwirkung mit einem massereichen Objekt im Sternorbit wesentlich beeinflusst werden. Aus diesem Grund treten CSEs in viele verschiedenen Geometrien auf, die Information über die Massenverlustgeschichte und die Dynamik des Sternwinds in sich tragen.

Das Ziel dieser Dissertation ist die Erforschung der Massenverlustgeschichte und Geometrie von CSEs von AGB Sternen in unterschiedlichen Phasen der Sternentwicklung, und die Untersuchung von verschiedenen Beobachtungen einer kleinen Auswahl von AGB CSEs bezüglich der Entstehungsszenarien. Die präsentierten Beobachtungen wurden mit dem Atacama Large Millimeter/submillimeter Array (ALMA) durchgeführt, das derzeit die höchste räumliche Auflösung und Sensitivität im Millimeter/submillimeter Wellenlängenbereich ermöglicht. Mit der Beobachtungstechnik der Interferometrie können wir die beobachteten CSEs mit bisher unerreichter Auflösung abbilden, bis hin zu kleinsten dynamischen Instabilitäten im Sternwind. Unsere Auswahl der beobachteten AGB Sterne umfasst W Aql, TX Psc, R Scl, und U Ant, gereiht nach aufsteigendem Kohlenstoff-zu-Sauerstoff (C/O) Verhältnis. Das C/O Verhältnis wird verwendet um den Entwicklungsstatus von AGB Sternen zu beschreiben und geht von M- zu S- zu C-Typ. Wir untersuchen einen S-Typ Stern (W Aql) und drei C-Typ Sterne in dieser Dissertation und legen den Fokus besonders auf die Analyse von sogenannten Detached Shells, die bisher nur um C-Typ Sterne gefunden wurden. Die ALMA Beobachtungen werden durch Beobachtungen im fernen Infrarot mit dem *Herschel* Space Telescope und des Einzelteleskops APEX im Submillimeter Bereich ergänzt. Die Modellierung der Beobachtungsdaten wurde mit Modellen zum Strahlungstransport von Moleküllinien (W Aql), geometrischen Modellen mit *Shape* (TX Psc), und Modellen zum Strahlungstransport von Staubteilchen (R Scl) durchgeführt. Wir stellen fest, dass die Molekülhäufigkeiten um W Aql den chemischen Modellen einer gemischten Kohlenstoff- und Sauerstoff-Chemie um S-Typ Sternen entsprechen. Um TX Psc entdecken wir die erste elliptische Detached Shell, deren Form durch erhebliche und unerwartete Sternrotation, angetrieben durch ein sekundäres Objekt im Umlauf, erklärt werden kann. Wir modellieren die Staubmasse in der Detached

Shell um R Scl und finden heraus, dass diese maßgeblich durch die Geometrie der Staubeilchen beeinflusst wird, und weniger durch die restlichen Staubparameter. Wir präsentieren die ersten hochauflösten Bilder der Detached Shell um U Ant, die eine komplexe Feinstruktur zeigt. Basierend auf unserer Auswahl scheint die Morphologie der beobachteten Detached Shells nahezulegen, dass diese mit zunehmender Entwicklung der C-Typ AGB Sterne räumlich genauer begrenzt werden.

Bibliography

- Asplund, M., Grevesse, N., Sauval, A. J., & Scott, P. 2009, *ARA&A*, 47, 481
- Bergeat, J. & Chevallier, L. 2005, *A&A*, 429, 235
- Bogdanov, M. B. 1997, *Astronomy Letters*, 23, 784
- Busso, M., Gallino, R., & Wasserburg, G. J. 1999, *ARA&A*, 37, 239
- Cox, N. L. J., Kerschbaum, F., van Marle, A.-J., et al. 2012, *A&A*, 537, A35
- Cruzalebes, P., Lopez, B., Bester, M., Gendron, E., & Sams, B. 1998, *A&A*, 338, 132
- Cutri, R. M., Skrutskie, M. F., van Dyk, S., et al. 2003, *VizieR Online Data Catalog*, 2246, 0
- Danilovich, T., Bergman, P., Justtanont, K., et al. 2014, *A&A*, 569, A76
- Danilovich, T., Olofsson, G., Black, J. H., Justtanont, K., & Olofsson, H. 2015, *A&A*, 574, A23
- De Marco, O. & Izzard, R. G. 2017, *PASA*, 34, e001
- Decin, L., Cherchneff, I., Hony, S., et al. 2008, *A&A*, 480, 431
- Feast, M. W. & Whitelock, P. A. 2000, *MNRAS*, 317, 460
- González Delgado, D., Olofsson, H., Schwarz, H. E., Eriksson, K., & Gustafsson, B. 2001, *A&A*, 372, 885
- González Delgado, D., Olofsson, H., Schwarz, H. E., et al. 2003, *A&A*, 399, 1021
- Griffin, M. J., Abergel, A., Abreu, A., et al. 2010, *A&A*, 518, L3
- Groenewegen, M. A. T., Waelkens, C., Barlow, M. J., et al. 2011, *A&A*, 526, A162
- Habing, H. J. & Olofsson, H., eds. 2003, *Asymptotic giant branch stars*
- Herwig, F. 2005, *ARA&A*, 43, 435
- Heske, A. 1990, *A&A*, 229, 494
- Heske, A., te Lintel Hekkert, P., & Maloney, P. R. 1989, *A&A*, 218, L5
- Höfner, S. & Olofsson, H. 2018, *A&A Rev.*, 26, 1
- Högbom, J. A. 1974, *A&AS*, 15, 417
- Jorissen, A., Mayer, A., van Eck, S., et al. 2011, *A&A*, 532, A135

- Karakas, A. I. & Lattanzio, J. C. 2014, PASA, 31, e030
- Keenan, P. C. & Boeshaar, P. C. 1980, ApJS, 43, 379
- Kerschbaum, F., Ladjal, D., Ottensamer, R., et al. 2010, A&A, 518, L140
- Klotz, D., Paladini, C., Hron, J., et al. 2013, A&A, 550, A86
- Knapp, G. R., Pourbaix, D., Platais, I., & Jorissen, A. 2003, A&A, 403, 993
- Lebzelter, T. & Hron, J. 2003, A&A, 411, 533
- Maercker, M., Khouri Silva, T., De Beck, E., et al. 2018, submitted to A&A
- Maercker, M., Mohamed, S., Vlemmings, W. H. T., et al. 2012, Nature, 490, 232
- Maercker, M., Olofsson, H., Eriksson, K., Gustafsson, B., & Schöier, F. L. 2010, A&A, 511, A37
- Maercker, M., Ramstedt, S., Leal-Ferreira, M. L., Olofsson, G., & Floren, H. G. 2014, A&A, 570, A101
- Maercker, M., Vlemmings, W. H. T., Brunner, M., et al. 2016, A&A, 586, A5
- Mayer, A., Jorissen, A., Kerschbaum, F., et al. 2013, A&A, 549, A69
- Min, M., Dullemond, C. P., Dominik, C., de Koter, A., & Hovenier, J. W. 2009, A&A, 497, 155
- Olofsson, H., Bergman, P., Eriksson, K., & Gustafsson, B. 1996, A&A, 311, 587
- Olofsson, H., Carlstrom, U., Eriksson, K., Gustafsson, B., & Willson, L. A. 1990, A&A, 230, L13
- Olofsson, H., Eriksson, K., Gustafsson, B., & Carlstrom, U. 1993, ApJS, 87, 267
- Olofsson, H., Maercker, M., Eriksson, K., Gustafsson, B., & Schöier, F. 2010, A&A, 515, A27
- Pilbratt, G. L., Riedinger, J. R., Passvogel, T., et al. 2010, A&A, 518, L1
- Poglitsch, A., Waelkens, C., Geis, N., et al. 2010, A&A, 518, L2
- Ramstedt, S., Maercker, M., Olofsson, G., Olofsson, H., & Schöier, F. L. 2011, A&A, 531, A148
- Ramstedt, S., Schöier, F. L., Olofsson, H., & Lundgren, A. A. 2008, A&A, 487, 645
- Rybicki, G. B. & Hummer, D. G. 1991, A&A, 245, 171
- Schöier, F. L., Lindqvist, M., & Olofsson, H. 2005, A&A, 436, 633
- Schöier, F. L. & Olofsson, H. 2001, A&A, 368, 969
- Siringo, G., Kreysa, E., Kovács, A., et al. 2009, A&A, 497, 945

van Leeuwen, F. 2008, VizieR Online Data Catalog, 1311, 0

Wasatonic, R. P. 1997, Journal of the American Association of Variable Star Observers (JAAVSO), 26, 1

Whitelock, P. A., Feast, M. W., & van Leeuwen, F. 2008, MNRAS, 386, 313

Yamashita, Y. 1972, Annals of the Tokyo Astronomical Observatory, 13, 169

Appendix A

Appendix

A.1 Reprint permission

The following page includes the official reprint permission from A&A for the publications presented in this thesis.

Astronomy and Astrophysics

Editor in Chief: T. Forveille

T. Forveille

Astronomy & Astrophysics
Observatoire de Paris
61, avenue de l'Observatoire
75014 Paris, France

Tel.: 33 0(1) 43 29 05 41
Fax: 33 0(1) 43 29 05 57
e-mail: aanda.paris@obspm.fr
Web: <http://www.aanda.org>

merging
Annales d'Astrophysique
Arkiv for Astronomi
Bulletin of the Astronomical Institutes
of the Netherlands
Bulletin Astronomique
Journal des Observateurs
Zeitschrift fur Astrophysik
Bulletin of the Astronomical Institutes
of Czechoslovakia

Paris, June 5, 2018

Reprint Permission

Material:

Article by Brunner et al. 2018, A&A, in press, DOI 10.1051/0004-6361/201832724
Article by Brunner et al. 2018, A&A, 614, A17
Article by Maercker et al. 2018, A&A, 611, A102
Article by Kerschbaum et al. 2017, A&A, 605, A116
Article by Ramstedt et al. 2017 A&A, 605, A126
Article by Maercker et al. 2016, A&A, 586, A5

To be used in:

PhD thesis entitled "Circumstellar Envelopes of Asymptotic Giant Branch Stars: Evolution and Geometry of Mass-Loss", University of Vienna

Permission granted to:

Magdalena Brunner
magdalena.brunner@univie.ac.at

I hold copyright on the material referred to above, and hereby grant permission for its use as requested herewith.

The article should be reproduced in the same format as that published in A&A (for example, in an appendix). In particular, the present permission rules do not allow copy-and-pasting parts of the article into the main text of the thesis.

Credit should be given as follows:

Credit: Author, A&A, vol, page, year, reproduced with permission © ESO.



Thierry Forveille
A&A Editor-in-Chief

Sponsored by Argentina, Armenia, Austria, Belgium, Bulgaria, Chile, Croatia, Czech Republic, Denmark, Estonia, Finland, France, Germany, Greece, Hungary, Italy, Lithuania, Netherlands, Norway, Poland, Portugal, Slovak Republic, Spain, Sweden, and Switzerland.

Produced and distributed by EDP Sciences for ESO.

A.2 CV

The following pages include my professional CV.

Magdalena Brunner

Curriculum Vitae

Ullmannstrasse 52/9
1150 Vienna, Austria
☎ (+43) 699 112 35 001
✉ magdalena.brunner@univie.ac.at



Studies & Education

- Since 10/2014 **Doctoral Studies**, *Department of Astrophysics*, University of Vienna.
Focus on observations and modeling of evolved stars
- 2010 – 2013 **Master of Science**, *Department of Astrophysics*, University of Vienna.
Degree achieved with distinction
- 2007 – 2010 **Bachelor of Science**, *Department of Astrophysics*, University of Vienna.
Degree achieved with distinction
- 1999 – 2007 **Secondary School**, *BG/BRG Purkersdorf*, Lower Austria.
 - Completed with distinction
 - Focus subjects: Geometry, Informatics
 - Repeated participation in the “Chemistry Olympiad”

Master Thesis

- Title *ALMA data reduction of R Sculptoris*
- Supervisors Franz Kerschbaum & Helmut Dannerbauer
- Description This thesis focused on the details of the ALMA data reduction process, based on the example of the circumstellar envelope around the evolved star R Sculptoris.

Bachelor Thesis

- Title *Habitability of exoplanets*
- Supervisors Rudolf Dvorak
- Description This thesis explored the necessary requirements for exoplanets to be habitable, focusing on the influence of the eccentricity of the exoplanet’s orbit on the habitability.

Employment History

University/Scientific

- 2018 **FWF project assistant: “Herschel und das unsichtbare Ende des Regenbogens”**, *Department of Astrophysics*, University of Vienna, Austria.
PI: Franz Kerschbaum
- 2014 – 2018 **Prae-doc position**, *Department of Astrophysics*, University of Vienna, Austria.
Supervisor: Franz Kerschbaum

- 02 – 03/2014 **Scientific Internship**, *European Southern Observatory (ESO)*, Garching, Germany.
Unpaid associate under the Director General's Discretionary Fund for 2 months of internship
(main topic: ALMA data reduction)
- 2013 – 2014 **Research Assistant**, *Department of Astrophysics, University of Vienna*, Austria.
Supervisor: Franz Kerschbaum
- Part-time Jobs and Internships**
- 2010 – 2011 **Wien-Ticket**, *Ticket Center*, Vienna.
Sales and customer care
- 09 – 10/2007 **Bentour-Travel**, *Travel Agency*, Vienna.
Customer care, postal administration, information management
- 07/2004 & **SAP Austria**, Vienna.
07/2005 Internship in Human Resources department

Fellowships, Awards & Grants

- 01 – 06 2018 Abschlussstipendium, University of Vienna (finishing scholarship)
- 2014 – 2017 uni:docs Fellowship, University of Vienna (PhD program)

Computer skills

- Basic IRAF
- Intermediate FORTRAN90, PYTHON, MS Office
- Advanced CASA, L^AT_EX

Special Skills & Qualities

- Social team-minded, communicative, self-organized, creative, quick comprehension
- Technical operating small & intermediate telescopes (e.g. 80 cm Cassegrain “vlt” at University of Vienna & 1.5 m RC at Leopold Figl Observatory), DSLR photography

Languages

- German **Mothertongue**
- English **Excellent** *Professionally fluent in speaking and writing*
- Spanish **Basic** *Basic words and phrases only*

Research Interests

- Theoretical **Stellar Evolution.** Asymptotic Giant Branch stars
- Observational **Sub-mm/Radio Interferometry.** ALMA
- Experimental **Single photon detection of faint signals.** Development/employment of single-photon detection system at the University telescopes

Teaching

- 2014 – 2016 **Occasional lecturer**, *Department of Astrophysics, University of Vienna*, Casual teaching of sub-mm interferometry and ALMA for master students.

- 2012 – 2013 **Supervising tutor**, *Department of Astrophysics, University of Vienna*, In charge of 3 practical courses for Bachelor students.
- Observing at the 80 cm University telescope
 - Basics of data reduction and photometry with IRAF
 - Galaxy classification on photometric plates

Public Outreach

- 10/2016 **Observations of Red Giants with ALMA**, *Lecture Series: "Nachts auf der Sternwarte ..."*, Department of Astrophysics, University of Vienna.
Public talk
- 10/2016 **Observations of Red Giants with ALMA**, *"Astrotreff"*, Wiener Arbeitsgemeinschaft für Astronomie (WAA), Vienna.
Invited public talk
- 07&08/2015 **Wie alt sind Rote Riesen und Weiße Zwerge?**, *"Kinderuni 2015"*, University of Vienna.
Talk at University event for children
- Since 2015 **"Nachts auf der Sternwarte ..."**, Department of Astrophysics, University of Vienna, Participating (and since 2016 leading) member of the organising committee.
Monthly public lecture series at the observatory
- Since 2009 **"Lange Nacht der Forschung"**, Department of Astrophysics, University of Vienna, Working at different science stations.
Regular public science event

Research Stays & Observations

- 09/2016 **New Technology Telescope (NTT)**, *ESO, La Silla, Chile*, Observations of the carbon AGB star R Sculptoris.
2 full + 3 half nights, PI: Matthias Maercker
- 06/2016 **New Technology Telescope (NTT)**, *ESO, La Silla, Chile*, Observations of the carbon AGB star R Sculptoris.
3 half nights, PI: Matthias Maercker
- 07 – 09/2010 **University Observatory**, *Vienna*, Observations at the 80 cm University telescope; 2 color follow-up observations of the Kepler-satellite field to detect and classify variable stars.

Conference Participation & Meetings

- 06/2017 **COASTARS 2017 - Connecting Observational and theoretical studies of AGB STARS**, *Chalmers Technical University, Gothenburg, Sweden*.
- 07/2016 **European Week of Astronomy and Space Science**, *Eugenides Foundation, Athens, Greece*.
- 03/2016 **"Evolved stars with ALMA" Meeting**, *Chalmers University of Technology, Gothenburg, Sweden*.
Preparing and discussing ALMA proposal ideas and projects.

- 02/2016 **Evolved Stars Get-Together**, *Chalmers University of Technology, Gothenburg, Sweden*.
Meeting and networking of international young researchers in the evolved stars community.
- 07/2015 **Stellar End Products: The low mass - high mass connection**, *ESO, Garching, Germany*.
- 06/2015 **The Physics of Evolved Stars**, *Nice, France*.
- 07/2014 **Why galaxies care about AGB stars III**, *Department of Astrophysics, University of Vienna, Vienna*.
- 10/2012 **8th IRAM Millimeter Interferometry School**, *IRAM Institute, Grenoble, France*.
- 06/2012 **German ALMA Community Days 2012**, *Argelander Institute for Astronomy, Bonn, Germany*.
- 09/2011 **"The History and Philosophy of Astrobiology" Symposium**, *Lund University, Sweden*.

Conference Contribution

- Oral Presentation **"Modeling the dusty circumstellar envelope of R Scl"**, *"COASTARS 2017" Conference*, 12.06. - 16.06.2017, Gothenburg, Sweden.
- Oral Presentation **"ALMA's view on AGB stars: Studies of W Aquilae and TX Piscium"**, *"European Week of Astronomy and Space Science" Conference*, 04.07. - 08.07.2016, Eugenides Foundation, Athens, Greece.
- Poster Presentation **"The ALMA view on W Aquilae: Observations and Modeling of Molecules in the Circumstellar Envelope"**, *"Stellar End Products: The low mass - high mass connection" Conference*, 06.07. - 10.07.2015, ESO, Garching, Germany.
2nd place of poster award
- Poster Presentation **"A Spiral Goes Viral - Observations and Modeling of R Sculptoris"**, *"Why Galaxies Care About AGB Stars III" Conference*, 28.07. - 01.08.2014, University of Vienna, Austria.
2nd place of poster award
- Poster Presentation **"OSETI - Search for Extraterrestrial Intelligence within Optical Wavelengths"**, *"The History and Philosophy of Astrobiology" Symposium*, 27.09. - 28.09.2011, Lund University, Sweden.

Publications

M. **Brunner**, M. Maercker, M. Mecina, T. Khouri, and F. Kerschbaum. Modelling the carbon AGB star R Sculptoris - Constraining the dust properties in the detached shell based on far-infrared and sub-millimeter observations. *A&A*, 614:A17, June 2018. DOI: 10.1051/0004-6361/201732065.

M. **Brunner**, T. Danilovich, S. Ramstedt, I. Marti-Vidal, E. De Beck, W. H. T. Vlemmings, M. Lindqvist, and F. Kerschbaum. Molecular line study of the S-type AGB star W Aquilae. ALMA observations of CS, SiS, SiO and HCN. *ArXiv e-prints*, June 2018. DOI: 10.1051/0004-6361/201832724.

M. Maercker, M. **Brunner**, M. Mecina, and E. De Beck. An independent distance

estimate to the AGB star R Sculptoris. *A&A*, 611:A102, April 2018. DOI: 10.1051/0004-6361/201732057.

S. Ramstedt, S. Mohamed, W. H. T. Vlemmings, T. Danilovich, M. **Brunner**, E. De Beck, E. M. L. Humphreys, M. Lindqvist, M. Maercker, H. Olofsson, F. Kerschbaum, and G. Quintana-Lacaci. The circumstellar envelope around the S-type AGB star W Aql. Effects of an eccentric binary orbit. *A&A*, 605:A126, September 2017. DOI: 10.1051/0004-6361/201730934.

F. Kerschbaum, M. Maercker, M. **Brunner**, M. Lindqvist, H. Olofsson, M. Mecina, E. De Beck, M. A. T. Groenewegen, E. Lagadec, S. Mohamed, C. Paladini, S. Ramstedt, W. H. T. Vlemmings, and M. Wittkowski. Rings and filaments: The remarkable detached CO shell of U Antliae. *A&A*, 605:A116, September 2017. DOI: 10.1051/0004-6361/201730665.

F. Kerschbaum, M. Maercker, M. **Brunner**, M. Lindqvist, H. Olofsson, M. Mecina, B. E. de, M. A. T. Groenewegen, E. Lagadec, S. Mohamed, C. Paladini, S. Ramstedt, W. H. T. Vlemmings, and M. Wittkowski. VizieR Online Data Catalog: ALMA FITS cubes of CO(1-0) and CO(2-1) (Kerschbaum+, 2017). *VizieR Online Data Catalog*, 360, August 2017.

M. Wittkowski, K.-H. Hofmann, S. Höfner, J. B. Le Bouquin, W. Nowotny, C. Paladini, J. Young, J.-P. Berger, M. **Brunner**, I. de Gregorio-Monsalvo, K. Eriksson, J. Hron, E. M. L. Humphreys, M. Lindqvist, M. Maercker, S. Mohamed, H. Olofsson, S. Ramstedt, and G. Weigelt. Aperture synthesis imaging of the carbon AGB star R Sculptoris. Detection of a complex structure and a dominating spot on the stellar disk. *A&A*, 601:A3, May 2017. DOI: 10.1051/0004-6361/201630214.

M. Maercker, W. H. T. Vlemmings, M. **Brunner**, E. De Beck, E. M. Humphreys, F. Kerschbaum, M. Lindqvist, H. Olofsson, and S. Ramstedt. A detailed view of the gas shell around R Sculptoris with ALMA. *A&A*, 586:A5, February 2016. DOI: 10.1051/0004-6361/201527128.

M. **Brunner**, M. Maercker, W. H. T. Vlemmings, M. Mečina, F. Kerschbaum, A. Mayer, and E. Humphreys. A Spiral Goes Viral: Observations and Modeling of the Circumstellar Envelope around R Sculptoris. In F. Kerschbaum, R. F. Wing, and J. Hron, editors, *Why Galaxies Care about AGB Stars III: A Closer Look in Space and Time*, volume 497 of *Astronomical Society of the Pacific Conference Series*, page 215, August 2015.

W. R. Leeb, J. Alves, S. Meingast, and M. **Brunner**. Simulated low-intensity optical pulsar observation with single-photon detector. *A&A*, 574:A9, February 2015. DOI: 10.1051/0004-6361/201424480.

P. Sowicka, G. Handler, R. Taubner, M. **Brunner**, V.-M. Passegger, F. Bauer, and E. Paunzen. Variable stars in the field of the young open cluster Roslund 2. In J. A. Guzik, W. J. Chaplin, G. Handler, and A. Pigulski, editors, *Precision Asteroseismology*, volume 301 of *IAU Symposium*, pages 495–496, February 2014. DOI: 10.1017/S1743921313015226.

W. H. T. Vlemmings, M. Maercker, M. Lindqvist, S. Mohamed, H. Olofsson, S. Ramstedt, M. **Brunner**, M. A. T. Groenewegen, F. Kerschbaum, and M. Wittkowski. ALMA observations of the variable $^{12}\text{CO}/^{13}\text{CO}$ ratio around the asymptotic giant branch star R Sculptoris. *A&A*, 556:L1, August 2013. DOI: 10.1051/0004-6361/201321821.

W. H. T. Vlemmings, M. Maercker, M. Lindqvist, S. Mohamed, H. Olofsson, S. Ramstedt, M. **Brunner**, M. A. T. Groenewegen, F. Kerschbaum, and M. Wittkowski. VizieR Online Data Catalog: ALMA observations of $^{12}\text{CO}/^{13}\text{CO}$ around R Scl (Vlemmings+, 2013). *VizieR Online Data Catalog*, 355, July 2013.

W. R. Leeb, A. Poppe, E. Hammel, J. Alves, M. **Brunner**, and S. Meingast. Single-Photon Technique for the Detection of Periodic Extraterrestrial Laser Pulses full access. *Astrobiology*, 13:521–535, June 2013. DOI: 10.1089/ast.2012.0951.